

AN ABSTRACT OF THE THESIS OF

Muhammad A. Daous for the degree of Doctor of Philosophy  
in Chemical Engineering presented on April 29, 1983

Title: MEASURING AND MODELING SOLIDS MOVEMENT IN A LARGE,

COLD FLUIDIZED-BED TEST FACILITY

Abstract approved: \_\_\_\_\_

Redacted for Privacy

Robert V. Mrazek \_\_\_\_\_

Solids movement in large-particle fluidized beds was studied in an 18 in x 18 in (46 cm x 46 cm) tube-filled, cold fluidized bed test facility. Direct measurement of local solid mass flux in two dimensions at various locations inside the bed was made possible by a new instrument developed in this study. This instrument can be installed as a part of the bed internal tube array and hence does not interfere with the solid flow field being measured. The instrument makes use of the magnetic property of solid and requires a bed media consisting entirely of magnetic solid particles. Iron particles with a mean particle diameter of 0.032 in (0.8 mm) and a density of 387 lb/ft<sup>3</sup> (6200 kg/m<sup>3</sup>) were used.

Experiments were conducted at room temperature and atmospheric pressure with air as the fluidizing gas. Two gas velocities above the minimum fluidization velocity were used. The net local solid movement and the gross solid circulation pattern inside the bed were deduced from the vertical and one horizontal component of the

local solid mass fluxes measured at various locations inside the bed. Two specific solid flow regions were found to exist. The net solids movement in the middle bubbling region of the bed was in the upward direction while adjacent to the bed walls the net solid movement was downward. The net lateral solid movement was not significant in the bubbling region of the bed. However, at the bottom of the bed this movement can be significantly enhanced by means of an uneven gas velocity distribution inside the bed.

A theoretical model for the gross solid circulation observed in a freely bubbling fluidized bed is proposed. The theory is based on material and momentum balances of the net solid circulating flow inside the bed with the assumption that the solid particulate phase behaves as an incompressible fluid of low viscosity. The model predictions for the vertical solid mass flux in the bubbling region of the bed show a reasonable agreement with the experimental results.

MEASURING AND MODELING SOLIDS MOVEMENT  
IN A LARGE, COLD FLUIDIZED-BED TEST FACILITY

by

Muhammad A. Daous

A THESIS

submitted to

Oregon State University

in partial fulfillment of  
the requirements for the  
degree of

Doctor of Philosophy

Completed April 29, 1983

Commencement June 1983

APPROVED:

Redacted for Privacy

\_\_\_\_\_  
Professor of Chemical Engineering in charge of major

Redacted for Privacy

\_\_\_\_\_  
Head of Department of Chemical Engineering

Redacted for Privacy

\_\_\_\_\_  
Dean of Graduate School

◁

Date thesis is presented April 29, 1983

Typed by Jane Doe for Muhammad A. Daous

## ACKNOWLEDGMENTS

Many people have contributed either directly or indirectly to this research project; I should like to mention several of them by name and express my appreciation to them:

To my major professor, Robert V. Mrazek for initiating this research project and choosing me to be a part of its team. His interest and guidance through the course of this work was invaluable.

To Dr. Thomas J. Fitzgerald who initiated the basic ideas of the instrumentation discussed in Chapter II.

To Riley T. Chan for his collaboration in the development of this instrumentation. His continued interest and enthusiasm for its success was unmatched.

To Richard Fobes, Manuk Colakyan, Steve Crane, and Dr. Goran Govanovic - all of whom have contributed in different ways to the success of this project.

To Professors Charles E. Wicks and Octave Levenspiel for their attention, friendliness and warmth during my stay at Oregon State University.

And finally to my family; my greatest appreciation and gratefulness to my wife, Zain for her patience, support and encouragement and to our little Yara for the joy she gives us.

This work was sponsored by a grant from the U.S. Department of Energy, Morgan Town Energy Technology Center, under contract number DE-AC 01-79 ET 13152.

## TABLE OF CONTENTS

	<u>Page</u>
1. INTRODUCTION	1
2. DEVELOPMENT OF THE MAGNETIC SOLID PARTICLES MASS FLOW METER	7
A. INTRODUCTION	7
B. PRELIMINARY DESIGN CONSIDERATIONS AND TESTS ON THE MAGNETIC SOLID PARTICLES FLOW METER	12
Initial Tests	14
Tests on Magnetic Saturation	21
Reducing Current Decay Time in the Write Coil	26
Reducing the Recording Pulse Width	28
Further Tests on the Magnetic Flow Meter	30
C. MODIFIED COIL DESIGNS TO FURTHER IMPROVE RESPONSE TIME AND ELIMINATE FLOW OBSTRUCTION	37
Unsuccessful Modified Coil Design	37
Successful Modified Coil Design	39
Modification in the Electronic Instrumentation	41
Computer Simulation of Magnetic Flux Lines	45
D. MAGNETIC FLOW METER CALIBRATION	51
Principles of Operation of L-Valve	54
Calibration Procedure	57
3. FLUIDIZED BED TEST FACILITY	62
A. FLUIDIZED BED AND BED MEDIA	62
Fluidized Bed	62
Bed Media	65
B. AIR SUPPLY SYSTEMS	66
C. THE PROBES	68
D. DATA ACQUISITION SYSTEM	71
4. SOLID PARTICLES MOVEMENT IN A FLUIDIZED BED, EXPERIMENTAL RESULTS	73
A. INTRODUCTION	73

## TABLE OF CONTENTS (Cont.)

	<u>Page</u>
B. EXPERIMENTAL DATA	75
Histogram Plots	78
C. GROSS SOLID CIRCULATION INSIDE THE BED	82
5. SOLID PARTICLES CIRCULATION INSIDE A FLUIDIZED BED: DEVELOPMENT OF A THEORETICAL MODEL	89
A. INTRODUCTION	89
B. THE TWO REGION MODEL BED FOR SOLID CIRCULATION	91
Assumptions of the Two Region Model Bed	94
Physical Parameters of the Two Region Model Bed	95
C. MATERIAL AND MOMENTUM BALANCES IN THE TWO REGION MODEL BED	97
Material Balance in the Wall Region	97
Material Balance in the Bubbling Region	99
x-Component of the Momentum Balance in the Wall Region	100
y-Component of the Momentum Balance in the Wall Region	101
x-Component of the Momentum Balance in the Bubbling Region	102
y-Component of the Momentum Balance in the Bubbling Region	102
Boundary Conditions	105
D. RESULTS OF CALCULATIONS AND LIMITS OF THE MODEL	108
Limits of the Model	128
E. COMPARISON BETWEEN MODEL PREDICTIONS AND EXPERIMENTAL RESULTS	130
6. SUMMARY AND CONCLUSIONS	135
BIBLIOGRAPHY	139
APPENDICES	
APPENDIX A - SCHEMATIC DRAWING OF THE ELECTRONIC INSTRUMENTATION OF THE MAGNETIC SOLID PARTICLE MASS FLOW METER	144
APPENDIX B - HISTOGRAM PLOTS OF RAW DATA	146

TABLE OF CONTENTS (Cont.)

	<u>Page</u>
APPENDIX C - NUMERICAL SOLUTION FOR SYSTEM OF DIFFERENTIAL EQUATIONS IN THE TWO REGION MODEL BED	183



## LIST OF FIGURES

<u>Figure</u>		<u>Page</u>
2.1	When the magnet is centered in the coil the emf in the coil produced by magnetic motion is minimal, since the rate of cutting of magnetic lines of force by the coil is minimal.	8
2.2a.	The lines of force around a long chain of aligned magnetic particles are not cut by the detector coil when the solids move in the same direction as the particle alignment.	10
2.2b.	Particles aligned off axis do produce lines of force which cut the detector coil as the solids move, however, the lines of force have opposite polarities and the net induced voltage in the coil is zero.	11
2.3.	Magnetizing coils are placed symmetric to the detector coil and wound in opposite directions so that the lines of force are concentrated in the vicinity of the detector coil.	12A
2.4.	Experimental set-up for the iron filled tube oscillating inside the coils of the magnetic flow meter by means of a motor and a set of pulleys.	15
2.5.	Block diagram of electronic instrumentation used in the initial tests on the magnetic solid flow meter.	16
2.6.	Timing diagram of control circuit used in the initial tests on the magnetic solid flow meter.	17
2.7.	Typical record of output signal for a sinusoidally varying velocity. Maximum excursion was 14 inches, frequency 0.88 Hz, sampling frequency 25 per second.	18
2.8.	Response signal as a function of amplifier power does not show saturation behavior at power level tested.	20
2.9.	Coil configurations.	22
2.10.	Magnetic saturation tests and calibration assembly.	24
2.11.	Typical saturation curve.	25
2.12.	Typical calibration curve for 1-1/2" folded "C" coil.	27

## LIST OF FIGURES (Cont.)

<u>Figure</u>	<u>Page</u>
2.13. Block diagram of driver amplifier to decrease current decay time and current level control.	29
2.14. Recording pulse (a) using a linear voltage amplifier, (b) using a current feed-back amplifier, (c) with "level switching" circuit.	31
2.15. Output signal vs. iron powder mass flux inside coils for series I.	33
2.16. Output signal vs. iron powder mass flux inside coils for series II.	34
2.17. Output signal vs. iron powder mass flux inside coils for series III.	35
2.18. "H" coil design for magnetic solid mass flow measurement.	38
2.19. The anti-parallel Write coil arrangement within the in-bed tube.	40
2.20. Schematic diagram of a new Write coil drive circuit.	42
2.21. Block diagram of the modified read coil analog amplification system and the sequential time control system.	43
2.22. Time sequence of the various functions of the modified electronic instrumentation.	44
2.23. One element of the triangular mesh generated by the computer program.	48
2.24. A cross-section of an in-bed tube with the write and read coils.	49
2.25. Generated mesh for the magnetic solid flow meter probe.	50
2.26. Flux lines distribution for the magnetic solid flow meter probe.	52
2.27. Flux lines distribution for the magnetic solid flow meter probe with iron region reduced in the y-direction.	53
2.28. Schematic of L-valve.	55

## LIST OF FIGURES (Cont.)

<u>Figure</u>	<u>Page</u>
2.29.      Output signal of a magnetic solid flow meter probe vs. iron powder mass flux in L-valve.	61
3.1.        A schematic diagram of the 18 in. x 18 in. scaled fluidized bed and related facility.	63
3.2.        The configuration of the distributor plate.	64
3.3.        Bed pressure drop vs. superficial gas velocity.	67
3.4.        The basic arrangement of dummy heat transfer tubes in the 18 in. x 18 in. scaled bed. The numbered tubes indicate the locations of the 14 instrumented tubes (probes) within the bed.	69
3.5.        Output signal from 14 identical magnetic solid flow meter probes vs. iron powder mass flux in L-valve.	70
3.6.        Block diagram of the Chemical Engineering Department minicomputer facility.	72
4.1.        Probe orientation in vertical and in horizontal solid flow measurement.	74
4.2.        Typical plot of the background signals for one of the 14 magnetic solid flow meter probes.	76
4.3.        The unequally spaced tube pattern used in experiment number 4.	79
4.4.        A plot of parts of the mass flux raw data collected using one of the 14 probes in one of the test runs.	80
4.5.        A sample histogram plot of mass flux raw data.	81
4.6.        The direction of the mean solid mass flux at 14 dif- ferent probe locations inside the bed for the first experiment. (The vector's length is proportional to the mean solid mass flux.)	83
4.7.        The direction of the mean solid mass flux at 14 dif- ferent probe locations inside the bed for the second experiment. (The vector's length is proportional to the mean solid mass flux.)	84

# LIST OF FIGURES (Cont.)

<u>Figure</u>		<u>Page</u>
4.8.	The direction of the mean solid mass flux at the four bottom probe locations inside the bed for the third experiment. (The vector's length is proportional to the mean solid mass flux.)	85
4.9.	The direction of the mean solid mass flux at the four bottom probe locations inside the bed for the fourth experiment. (The vector's length is proportional to the mean solid mass flux.)	86
5.1.	The solid gross circulation pattern inside the bed.	92
5.2.	The two region model bed.	93
5.3.	Solid mass flux through a fixed differential control volume in the two region model bed.	98
5.4a.	Vertical solid mass flux in the wall region of the model bed as a function of height in the bed and wall region thickness for $U_o = 3.25$ ft/sec and $\epsilon_1 = 0.49$ .	110
5.4b.	Vertical solid mass flux in the bubbling region of the model bed as a function of height in the bed and wall region thickness for $U_o = 3.25$ ft/sec and $\epsilon_1 = 0.490$ .	111
5.4c.	Net horizontal solid mass flux between the two regions of the model bed as a function of height in the bed and wall region thickness for $U_o = 3.25$ ft/sec and $\epsilon_1 = 0.49$ .	112
5.5a.	Vertical solid mass flux in the wall region of the model bed as a function of height in the bed and wall region thickness for $U_o = 3.25$ ft/sec and $\epsilon_1 = 0.520$ .	113
5.5b.	Vertical solid mass flux in the bubbling region of the model bed as a function of height in the bed and wall region thickness for $U_o = 3.25$ ft/sec and $\epsilon_1 = 0.520$ .	114
5.5c.	Net horizontal solid mass flux between the two regions of the model bed as a function of height in the bed and wall region thickness for $U_o = 3.25$ ft/sec and $\epsilon_1 = 0.520$ .	115

# LIST OF FIGURES (Cont.)

<u>Figure</u>		<u>Page</u>
5.6a.	Vertical solid mass flux in the wall region of the model bed as a function of height in the bed and wall region void fraction for $U_o = 3.25$ ft/sec.	116
5.6b.	Vertical solid mass flux in the bubbling region of the model bed as a function of height in the bed and wall region void fraction for $U_o = 3.25$ ft/sec.	117
5.6c.	Net horizontal solid mass flux between the two regions of the model bed as a function of height in the bed and wall region void fraction for $U_o = 3.25$ ft/sec.	118
5.7a.	Vertical solid mass flux in the wall region of the model bed as a function of height in the bed and wall region thickness for $U_o = 4.5$ ft/sec and $\epsilon_1 = 0.49$ .	119
5.7b.	Vertical solid mass flux in the bubbling region of the model bed as a function of height in the bed and wall region thickness for $U_o = 4.5$ ft/sec and $\epsilon_1 = 0.49$ .	120
5.7c.	Net horizontal solid mass flux between the two regions of the model bed as a function of height in the bed and wall region thickness for $U_o = 4.5$ ft/sec and $\epsilon_1 = 0.49$ .	121
5.8a.	Vertical solid mass flux in the wall region of the model bed as a function of height in the bed and wall region thickness for $U_o = 4.5$ ft/sec and $\epsilon_1 = 0.580$ .	122
5.8b.	Vertical solid mass flux in the bubbling region of the model bed as a function of height in the bed and wall region thickness for $U_o = 4.5$ ft/sec and $\epsilon_1 = 0.580$ .	123
5.8c.	Net horizontal solid mass flux between the two regions of the model bed as a function of height in the bed and wall region thickness for $U_o = 4.5$ ft/sec and $\epsilon_1 = 0.580$ .	124
5.9a.	Vertical solid mass flux in the wall region of the model bed as a function of height in the bed and wall region void fraction for $U_o = 4.5$ ft/sec.	125

# LIST OF FIGURES (Cont.)

<u>Figure</u>		<u>Page</u>
5.9b.	Vertical solid mass flux in the bubbling region of the model bed as a function of height in the bed and wall region void fraction for $U_o = 4.5$ ft/sec.	126
5.9c.	Net horizontal solid mass flux between the two regions of the model bed as a function of height in the bed and wall region void fraction for $U_o = 4.5$ ft/sec.	127
5.10.	Comparison between theoretical and measured values of vertical solid mass flux in the bubbling region of the bed for $U_o = 3.25$ ft/sec.	132
5.11.	Comparison between theoretical and measured values of vertical solid mass flux in the bubbling region of the bed for $U_o = 4.5$ ft/sec.	133
A.1.	Detailed schematic drawing of the electronic circuits of the magnetic solid particle mass flow meter.	145
B.1.	Frequency histogram plots for the data of the first experiment.	147
B.2.	Frequency histogram plots for the data of the second experiment.	161
B.3.	Frequency histogram plots for the data of the third experiment.	175
B.4.	Frequency histogram plots for the data of the fourth experiment.	179
C.1.	Fortran code for calculation procedure of the system of Eqs. (5-8) to (5-13).	184

## LIST OF TABLES

<u>Table</u>		<u>Page</u>
2.1	Output signal from magnetic solid mass flow detector for 3 frequencies and 4 amplifier power levels.	19
2.2	Average output signal from a magnetic solid mass flow meter probe for different downward mass flux of solid in the downcomer of the L-valve.	59
2.3	Average output signal from a magnetic-solid mass flow meter probe for different simulated upward mass flux of solid in the downcomer of the L-valve.	60
4.1	Summary of experimental conditions for solid-particles movement experiments.	77
5.1	Summary of dimensions of the model bed used in solid mass flux calculations.	109

## NOTATION

$A_t$	total cross-sectional area of the fluidized bed ( $\text{ft}^2$ )
$A_1, A_2$	cross-sectional area of the wall region and bubbling region of the two region model bed, respectively ( $\text{ft}^2$ )
$d_b$	effective bubble diameter (ft)
$d_p$	surface mean particle size (ft)
$g$	$= 32.174 \text{ ft/sec}^2$ , acceleration of gravity
$G_{1x}, G_{2x}$	horizontal solid mass flux in the wall region and bubbling region of the two region model bed, respectively ( $\text{lb}_m/\text{ft}^2 \cdot \text{sec}$ )
$G_{1y}, G_{2y}$	vertical solid mass flux in the wall region and bubbling region of the two region model bed, respectively ( $\text{lb}_m/\text{ft}^2 \cdot \text{sec}$ )
$H$	height of the freely bubbling fluidized bed (measured from distributor plate) (ft)
$H_{mf}$	bed height at minimum fluidization conditions (ft)
$L_B, L_W$	characteristic dimension of the bubbling region and wall region of a freely bubbling fluidized bed, respectively (ft) (see Figure 5.1)
$L_1, L_2$	thickness of the wall region and bubbling region of the two region model bed, respectively (ft) (see Figure 5.2)
$P_1, P_2$	pressure in the wall region and bubbling region of the two region model bed, respectively ( $\text{lb}_f/\text{ft}^2$ )
$\Delta P$	pressure drop ( $\text{lb}_f/\text{ft}^2$ )



$U_{br}$	rise velocity of a bubble with respect to emulsion phase (ft/sec)
$U_f$	upward velocity of gas through the emulsion (ft/sec)
$U_{mf}$	superficial gas velocity at minimum fluidizing conditions (ft/sec)
$U_o$	superficial gas velocity through the fluidized bed (ft/sec)
$V_{1x}, V_{2x}$	horizontal solid velocity in the wall region and bubbling region of the two region model bed, respectively (ft/sec)
$V_{1y}, V_{2y}$	vertical solid velocity in the wall region and bubbling region of the two region model bed, respectively (ft/sec)
$\epsilon_{av}$	average void fraction in the fluidized bed
$\epsilon_{mf}$	average void fraction in the fluidized bed at minimum fluidizing conditions
$\epsilon_1, \epsilon_2$	void fraction in the wall region and bubbling region of the two region model bed, respectively
$\rho_s$	solid density ( $\text{lb}_m/\text{ft}^3$ )
$\rho_1, \rho_2$	bulk density of the solid in the wall region and bubbling region of the two region model bed, respectively ( $\text{lb}_m/\text{ft}^3$ )

MEASURING AND MODELING SOLIDS MOVEMENT IN A LARGE,  
COLD FLUIDIZED BED TEST FACILITY

1. INTRODUCTION

Fluidized bed systems are noted for a number of highly useful properties, the more important being concerned with their excellent heat transfer characteristics and temperature control, continuity of operation, and the efficient handling of large quantities of fluid and solids in an excellent fluid-solid contact pattern. As a result, fluidized beds found numerous applications in the chemical, petrochemical, and other industries, and have received considerable attention in the chemical engineering research and literature. Most of these applications involved fine-particle systems (usually less than .5 mm in diameter). Fine-particle beds have been studied by many investigators and a large body of data on gas flow, heat transfer, solid mixing and other aspects of these systems is available in the literature.

Fluidized beds of large particles have only recently become a topic of investigation, primarily as a result of the increased interest in fluidized bed coal combustion. Fluidized bed combustors typically use large limestone particles (greater than .5 mm in diameter) to scavenge the sulfur dioxide produced by burning coal containing sulfur. Large-particle fluidization is also finding use in incineration of solid waste, hydrocarbon processing, separation of nuclear waste products and solvent extraction and drying.

Unfortunately, the performance of large-particle fluidized beds as chemical reactors cannot be predicted or described from existing data

and models of fine-particle beds. Major differences in the hydrodynamic behavior of the two fluidized bed systems come from the different nature of gas flow through and around ascending bubbles and from the different mechanism of solid mixing in the two bed systems.

The objective of this study is to provide fundamental data in the area of solid mixing and a better understanding of the characteristics of solid movement in a large-particle fluidized bed. Of particular interest is a fluidized bed combustor and the solid movement in the vicinity of fuel injection ports.

A fundamental understanding of this solid flow process is crucial to the design and operation of a fluidized bed combustor. For example, studies on coal devolatilization conducted at the University of Pennsylvania (1) showed that small particles (50-100  $\mu\text{m}$ ) which are usually present in a coal feed devolatilized at 800°C in less than a second, and larger particles (1000-1200  $\mu\text{m}$ ) were completely devolatilized in but a few seconds. Therefore, if coal fed into a fluidized bed combustor does not mix well in the horizontal plane during this time, a high concentration plume of volatiles will form in the bed precluding sulfur dioxide removal and limiting combustion efficiency. A plume model for coal combustion that treats this case has been developed by Park, et al. (2).

Two major problems, scale-up and instrumentation, have plagued investigators of solids flow in fluidized beds. Scale-up to large beds from experimental data obtained from small beds is still open to question. Van Deemter (3) has shown that vertical mixing in a fluidized bed is directly related to bed diameter. This is most probably due to differences in flow regimes, bubble sizes, bubble coalescence patterns

and gross circulation patterns as the bed diameter is changed. These hydrodynamic properties should also influence lateral mixing in the bed. Numerous investigators have shown that the ratio of bubble to bed dimensions influences the resulting behavior of the bed. Martin-Gautier and Pyle (4) showed that particle motion differs at small and large bubble Reynolds numbers, i.e., small and large bubbles. However, there has been very little experimental work done to determine the hydrodynamic behavior of a large utility-sized fluidized bed from the behavior of a cold smaller scaled bed. A recently published article by Fitzgerald and Crane (5) represents the first example of studies in this area. In their study they used four dimensionless groups<sup>1</sup>, first described by Scharff, et al. (6), as scale-up criteria and compared the behavior of large cork particles in a large cold bed fluidized by air with the behavior of small sand particles in a small scaled bed fluidized by Freon gas. They also compared the behavior of tungsten particles

---

<sup>1</sup> The four dimensionless groups are:

$\rho_s/\rho_g$	the ratio of solid density to gas density
$d_p/L$	the ratio of particle size to a characteristic bed dimension
$U^2/L G$	the ratio of superficial gas velocity squared to the product of the acceleration of gravity times a characteristic bed dimension
$d_p U_g \rho_g / \mu_g$	the particle Reynolds number: the ratio of the superficial gas velocity times particle size to the kinematic viscosity of the gas.

If one sets all of the above dimensionless numbers to be identical when comparing two beds, then both beds should have similar fluidization hydrodynamics.

in a small slugging bed fluidized by water with the behavior of large Styrofoam particles in a large-scaled slugging bed fluidized by air. Motion pictures taken of the cork-air bed vs. the sand-Freon bed and the tungsten-water vs. the Styrofoam-air bed showed similarities in bubble growth and solids flow patterns. They have also measured the pressure fluctuations across the beds and have compared the power spectral density of the pressure fluctuations. The results were quite similar to those predicted by the scale-up procedure.

The above results, although preliminary in nature, prompted the adoption of the same scale-up theory for this study. In trying to avoid a random design choice of a smaller scale cold fluidized bed in which to conduct the experiments of this study, and to help provide data that can be useful for future studies, the Babcock and Wilcox (38) 6 ft x 6 ft (183 cm x 183 cm) atmospheric fluidized bed combustor was chosen as a reference large-size hot bed. A scaled 18 in. x 18 in. (46 cm x 46 cm) cold bed was then used in all the experiments of this investigation.

Along with the scale-up question is the equally difficult problem of instrumentation to determine particle flow and mixing behavior within a fluidized bed. A variety of techniques have been used in the past. Most straightforward are the photographic techniques using a transparent wall in a two dimensional bed, e.g. Merry and Davidson (7), and Mori and Nakamura (8). However, results in two dimensional beds are not readily related to three dimensional beds, and the influence of bed size on solid flow cannot be properly studied in a two dimensional bed.

One experimental technique for studying mixing is to follow the motion of individually tagged particles. Kondukov et al. (9) studied

the movement of individual radioactively tagged particles using a three dimensional array of detectors. Leva (10), and more recently Chen (11) have used similar techniques. Merry and Davidson (7) used a small radio transmitter located in a much larger particle (called a "radio pill") in an attempt to follow overall particle phase motion.

Groups of tagged particles also have been used. Merrick and Highley (12) released a group of radioactive particles in the bed and measured the concentration of samples trapped at several bed locations at various times. Other investigators (13,14,15,16) introduced radioactive particles at one point in the bed and monitored their movements by radiation detectors at several points inside or outside the bed. Color tagged particles have been used also, e.g., Cranfield (17) prepositioned colored particles in the bed at some initial time. After a given period of fluidization the bed was suddenly defluidized and the new location of the colored particles was determined by excavating the bed. Magnetic tracer particles that can be separated from the rest of the bed material by a magnetic separating device have been used also. Fitzgerald, et al. (18) used such a technique along with 64 inductor probes to map the spread of tracer particles through a fluidized bed. Thermal tagging has been implemented by some researchers. A two-thermistor probe was described by Marsheck and Gomezplata (19) for measuring solids movement. The solids were heated by one thermistor and the temperature of the solids was sensed by a second thermistor a short distance from the first. From this measurement, the velocity component in the direction of the thermistors could be deduced.

A number of other different measurement techniques and instrumentations have been developed to provide direct information on local particle

velocities. Rezenbaum (20) described an instrument which makes use of a ball on a string. As the ball moves through the bed (presumably with the solids) the displacement of the string is measured and recorded. Another instrument, as described by Heertjes (21), et al., uses a needle at the end of a probe such that the measured stress on the needle is correlated with the velocity vector of the solids moving past the probe. Oki, et al. (22), and more recently Ishide, et al. (23), used a fiber-optics probe with correlation techniques to determine the velocity of particles moving along the face of the probe.

It can be seen from the above review that various techniques have been employed to study solids movement in fluidized beds. However, some of the above methods involve the insertion of rather large objects that are not part of the bed internals into the bed, which may distort the flow field being measured. In situ detection of radioactive tracers besides being hazardous, gives relatively "noisy" data because the intensity of radiation detected by a probe varies with the density of the bed media between the probe and the radioactive source. Thus, the occurrence of a bubble near a probe would increase the amount of radiation sensed by the detector and make the tracer appear to have moved closer to it. The single tagged particles technique can only give information about the motion of these particles and conditions at a single point in the bed and a massive amount of data must be taken to adequately characterize the temporal and spatial conditions in the bed. The methods using groups of tagged particles give indications of the spatial variations throughout the beds. However, they are restricted to relatively short duration transient experiments. Thus, it is uncertain how the results reflect the temporal behavior of a bed which is influenced

by the non-regular behavior of bubble arrays. In addition, these experimental methods require laborious and time consuming procedures between successive test runs.

A new instrumentation has been developed in this study that overcomes the limitation of previous experiments with groups of tagged particles and allows continuous or transient tests to be carried out. The new method makes use of the magnetic property of solids. However, unlike the magnetic tracer method implemented by Fitzgerald, et al. (18), which uses only about one percent magnetic solids in a bed of magnetically inert material, the new method uses a bed consisting entirely of magnetizable material. The use of such a bed was feasible for this study since magnetic solid particles that met our bed material density and size requirement were readily available and inexpensive.

With this new method, local solids mass flux at various locations inside the bed can be measured directly instead of being inferred from solids tracer concentration measurements. In addition, unlike the tracer measurements, the new method does not require that magnetic material be removed or sequestered at the end of each test run. Furthermore, the new instrumentation is installed as a part of the bed internal dummy heat-transfer tube bundle, and hence does not interfere with the solids flow field being measured.

A detailed description of the basic principle and development of the magnetic solid-particles mass-flow meter is given in the next chapter.



## 2. DEVELOPMENT OF THE MAGNETIC SOLID PARTICLES

### MASS FLOW METER

#### A. INTRODUCTION

The basic principle involved in the magnetic-solid flow meter is well known: a magnet moving past a coil sets up an emf in the coil which is proportional to the strength of the magnetic field and the velocity of the magnet relative to the coil. The emf is in fact proportional to the rate at which magnetic lines of force are cut by the detector coil,

$$\text{Emf} \propto N \frac{dB}{dx} \frac{dx}{dt} \quad \text{volts,} \quad (1)$$

where  $N$  is the number of turns in the coil,  $dB/dx$  is the spatial variation of magnetization along the magnet, and  $dx/dt$  is the magnet velocity.

A permanent bar magnet with dimensions comparable to the coil diameter causes a large induced emf when either end of the bar is moved through the coil. The sensitivity is minimal when the magnet is centered in the coil, since in this case the rate at which lines of force are cut approaches zero, or  $dB/dx$  in Eq. (1) approaches zero. This is illustrated in Figure 2.1.

Consider now the application of this principle to the detection of the motion of solid magnetic particles. At this point it is reasonable to ask whether the motion of the bed of uniformly magnetized particles would cause an emf to be induced in a pickup coil. Some of the magnetic particles will have random orientation. Their fields will tend to cancel

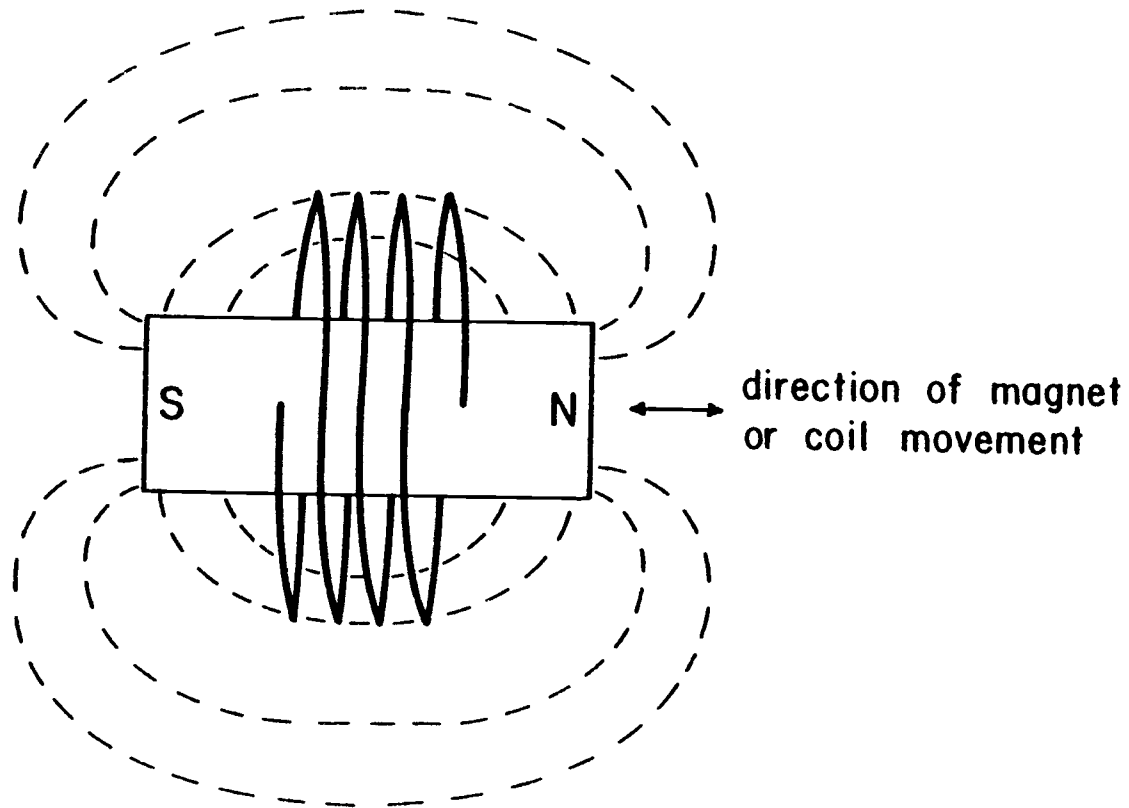


Figure 2.1.. When the magnet is centered in the coil the emf in the coil produced by magnetic motion is minimal, since the rate of cutting of magnetic lines of force by the coil is minimal.

and hence they can be ignored. The remainder of the particles however will be at least partially aligned with their north poles, for instance, all tending to point in the same direction. Close to every north pole there will be the south pole of a nearby particle and the lines of force between north and south poles will be mostly confined to the immediate neighborhood of the magnetic solids. A few lines will reach out to the pickup coil. If the particles are aligned in the direction of flow as shown in Figure 2.2A, then the lines of force near the coil will tend to be parallel to the direction of motion, and no lines of force will be cut as the solids move; hence, no emf will be induced in the detector coil. If the particles, however, are not aligned in the direction of motion, as shown in Figure 2.2B, then the lines of force which extend out to the pickup coil will be cut by the coil as the solids move past it. However, no net emf will be produced in the coil. One section of the coil is close to the net south pole of the solids; the other is closer to the net north pole of the solids. Each section of the coil will therefore produce an opposite emf, so the resultant emf in the coil is zero. This statement can be made more precisely in terms of line integrals of the magnetic field, but the effect is the same: no voltage is induced in a detecting coil by uniformly magnetized solids.

In order to make use of the moving magnet principle to measure solid mass flow, one needs a way to create a magnetic domain which is nonuniform. A nonuniform magnetic domain can be created locally by using a second magnetizing coil (a current carrying coil). When this magnetizer coil is turned off, the solid particles in the vicinity of the coil will remain partially magnetized (residual magnetism); and at least for a short time, they will maintain the orientation which they had while

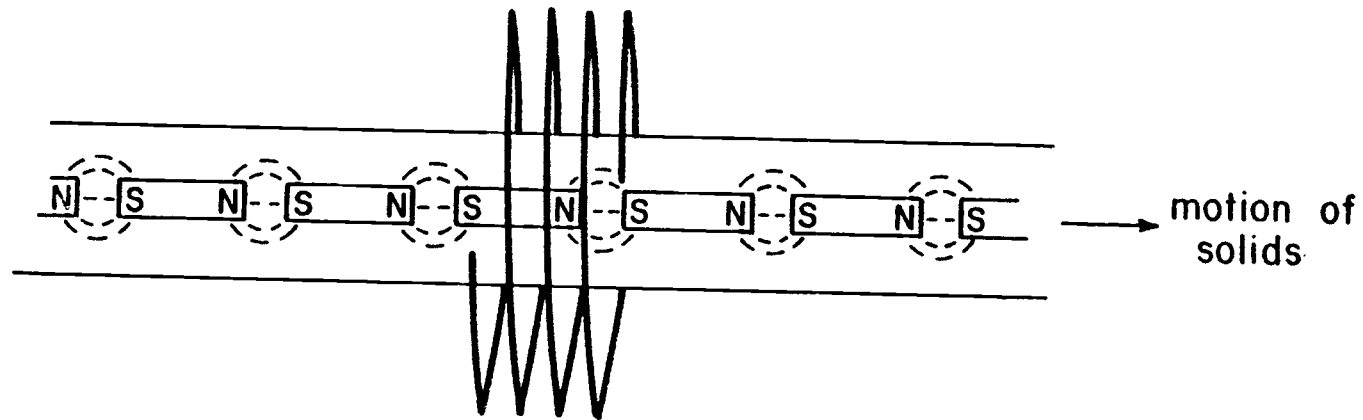


Figure 2.2A. The lines of force around a long chain of aligned magnetic particles are not cut by the detector coil when the solids move in the same direction as the particle alignment.

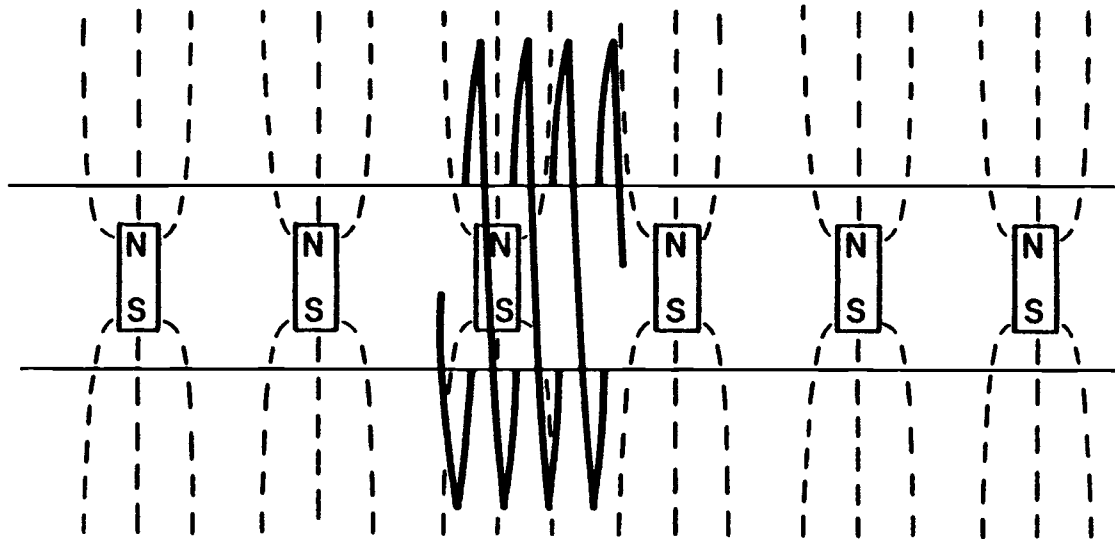


Figure 2.2B. Particles aligned off axis do produce lines of force which cut the detector coil as the solids move, however, the lines of force have opposite polarities and the net induced voltage in the coil is zero.

they were being magnetized. Movement of this array of magnetized particles will now induce an emf in the detector coil which can be used to determine the mass flow rate of the solids. Figure 2.3 shows an efficient arrangement of coils to accomplish particle magnetization and detection of motion. A magnetic field can be generated around coils A and C, which are wound in opposite directions, to produce a concentration of magnetic lines of force in the mid plane between the coils where detector coil B is placed. When the current in coils A and C is shut off, the moving magnetic solids in the vicinity will produce an emf in coil B which is proportional to the magnetic field strength of the now magnetized particles and the particles velocity normal to the plane of the detector coil, i.e., the emf is proportional to the solid mass flux.

B. PRELIMINARY DESIGN CONSIDERATIONS AND TESTS ON THE MAGNETIC  
SOLID PARTICLES FLOW METER

Before the magnetic-particle mass flow meter could be built and tested, it was necessary to consider more facts pertinent to the design and application of the flow meter.

As the particles move an appreciable distance from the position where they are magnetized, their orientation will change randomly so that the emf generated in the detector coil will no longer be a good indication of the solid mass flux through the detecting coil. Hence, the mass flow measurement can be made only during a short time interval just after the magnetization current in the magnetizing coil is cut off.

In order to obtain a subsequent reading, it is necessary to magnetize another set of solids. If many mass flow measurements are made in a

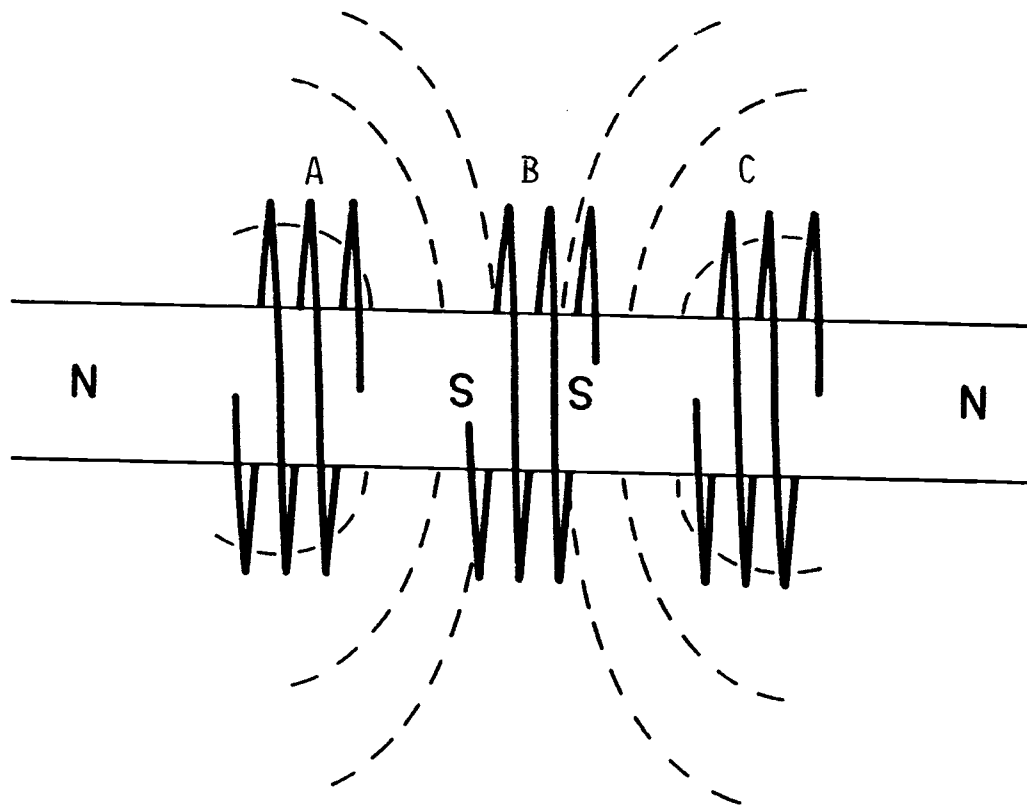


Figure 2.3. Magnetizing coils are placed symmetric to the detector coil and wound in opposite directions so that the lines of force are concentrated in the vicinity of the detector coil.

recirculating solids system such as a fluidized bed, then there will be a buildup of magnetized material in the system unless the solids are demagnetized. Some demagnetization will occur spontaneously, but it would be prudent to eliminate the residual magnetism in the particles as quickly as possible. This can be done rather easily by using an alternating current of decaying amplitude in the magnetizing coils to demagnetize the particles before they have a chance to move away from the coil. The sequence will then be: 1) unmagnetized moving solids are quickly magnetized by the magnetizing coils, 2) the magnetizing current is shut off and the solids mass flow is detected by the induced emf in the detector coil, 3) a decaying, alternating current in the magnetizing coils is then employed to demagnetize the solids. The overall cycle time from the beginning of magnetization to the end of the demagnetization should be short enough so that the particles will not have moved out of the range of influence of the coils.

There were two possible sources of error anticipated in applying magnetic particle flow measurement to fluidized bed systems. The first involved possible modification of the particle's velocity by magnetic forces, since the change in velocity of the solids is proportional to the time integral of the forces acting on them. Experiments with the magnetic flow meter, however, have shown that the magnetic forces acting on the particles are negligible compared to the mechanical forces, and hence the magnetization will have but a negligible effect on solids movement; besides, any magnetic force effect on the solids movement can be minimized by making the time duration during which the solids are subjected to magnetic forces as short as possible. The second possible source of error involved the magnetic inhomogeneity that would be caused



by bubbles in the fluidized bed. This effect was investigated both theoretically and experimentally and steps were taken to minimize such an effect.

### Initial Tests

The magnetic particle mass flow measuring device described above was first tested using the set-up shown in Figure 2.4. Particles were magnetized by a pair of record/erase coils arranged coaxially with opposite polarities so that the magnetic lines of force would be most dense at a plane midway between the two coils. Each coil was 2 inches in diameter and 1/2 inch thick. The spacing between the coils was 2 inches center to center. Each coil consisted of 40 turns of number 18 insulated copper wire giving an impedance at 2,000 hertz of approximately 5 ohms. The pick up or "READ" coil was 3 inches in diameter and was situated midway between the two record/erase (WRITE) coils. It consisted of 2,000 turns of number 36 insulated wire. A cardboard tube 1.5 inches in diameter was filled with 16-mesh iron particles and was pulled through the coils with a sinusoidally varying velocity by a mechanical drive system.

The electronic instrumentation used in conjunction with these two sets of coils is shown in block diagram form in Figure 2.5. Figure 2.6 shows the time sequence of record, read and erase pulses. The record signal was a simple pulse of one polarity. The duration of the pulse was approximately 0.5 milli-seconds. The erase signal was a 2 kHz square wave with an exponentially decaying envelope of about 20 milliseconds length. Figure 2.7 shows a typical output trace. The sinusoidally varying velocity is clearly represented in the output, indicating good

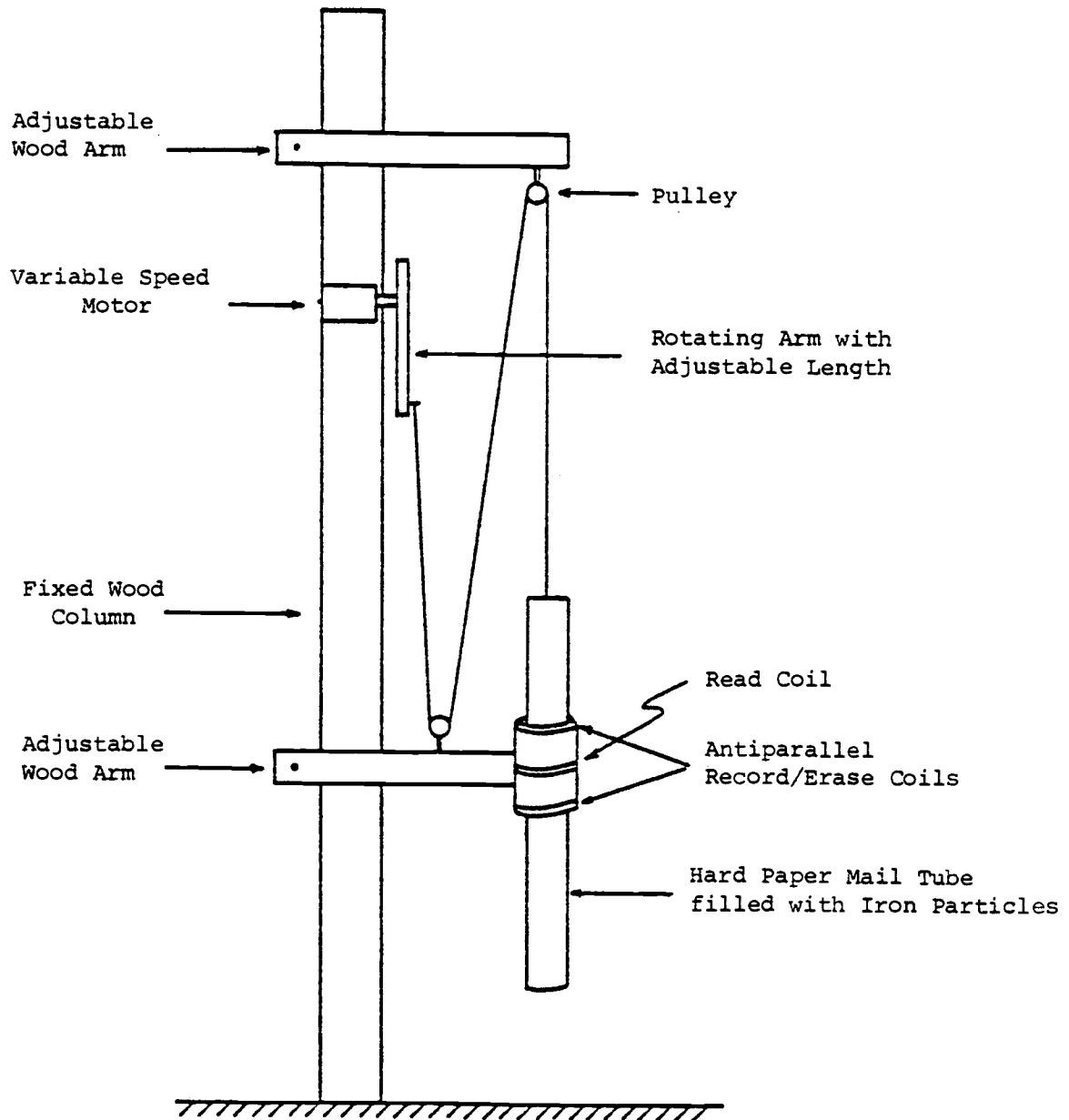


Figure 2.4. Experimental set up for the iron filled tube oscillating inside the coils of the magnetic flow meter by means of a motor and a set of pulleys.

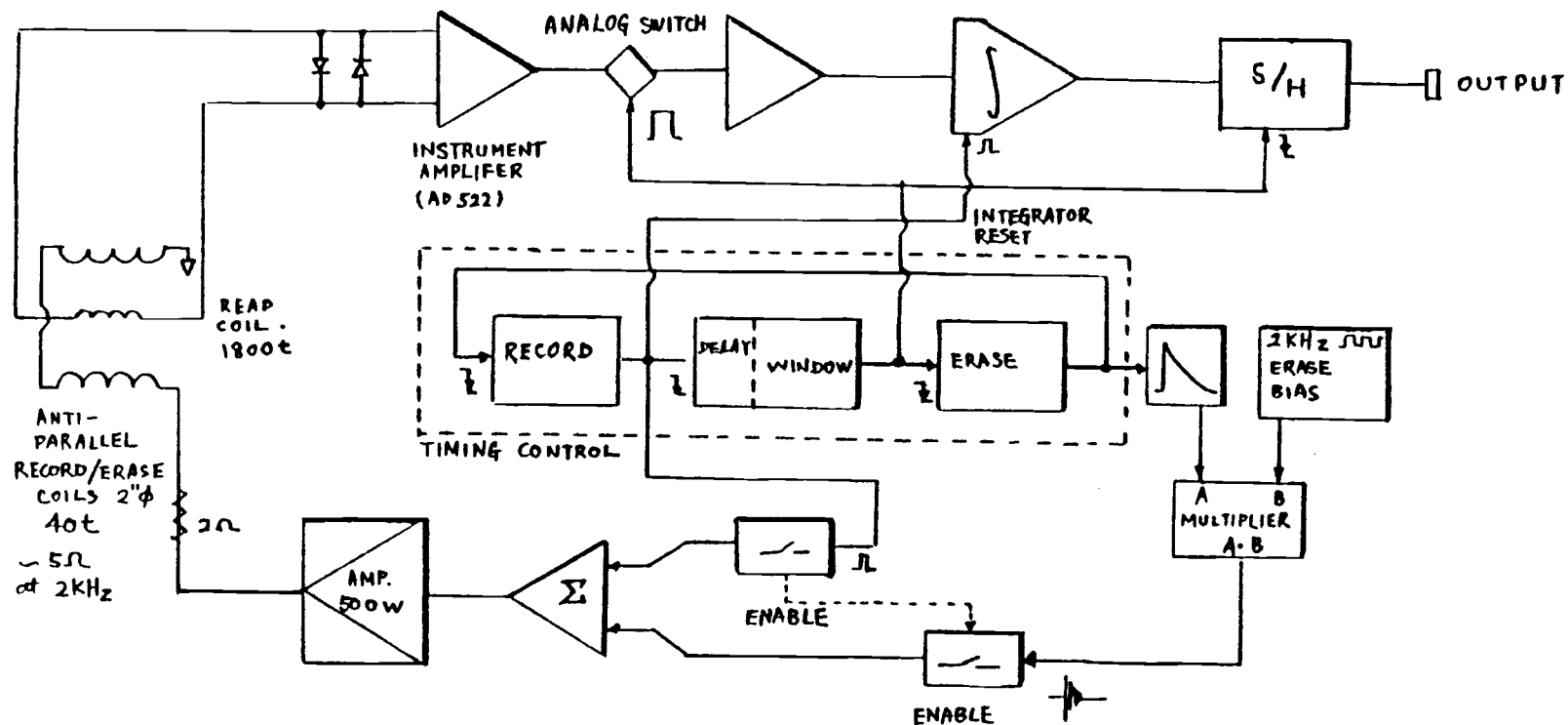
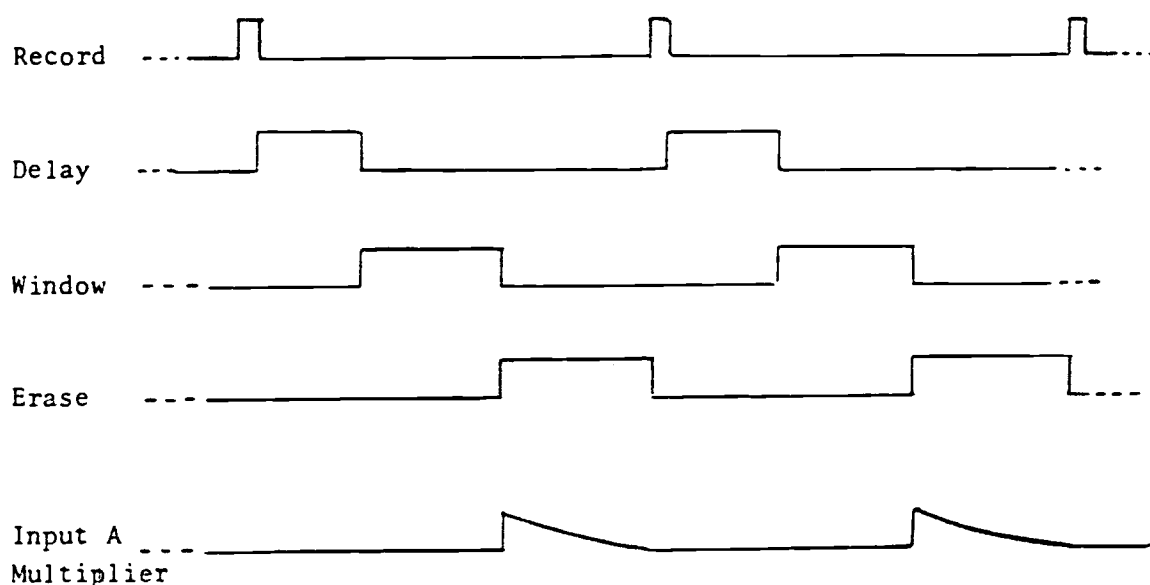



Figure 2.5. Block diagram of electronic instrumentation used in the initial tests on the magnetic solid flow meter.



Notes: 1. The sequence, Record → Delay → Window → Erase → Record-----, is controlled by the trailing edge of the preceeding function, indicated by (  ) on the block diagram.

2. Individual pulse widths are adjustable independently; the cycle time is the total time of all functions.

3. Amplitudes of RECORD and ERASE signals are adjustable independently, as well as together by the attenuator of the POWER AMPLIFIER.

Figure 2.6. Timing diagram of control circuit used in the initial tests on the magnetic solid flow meter.

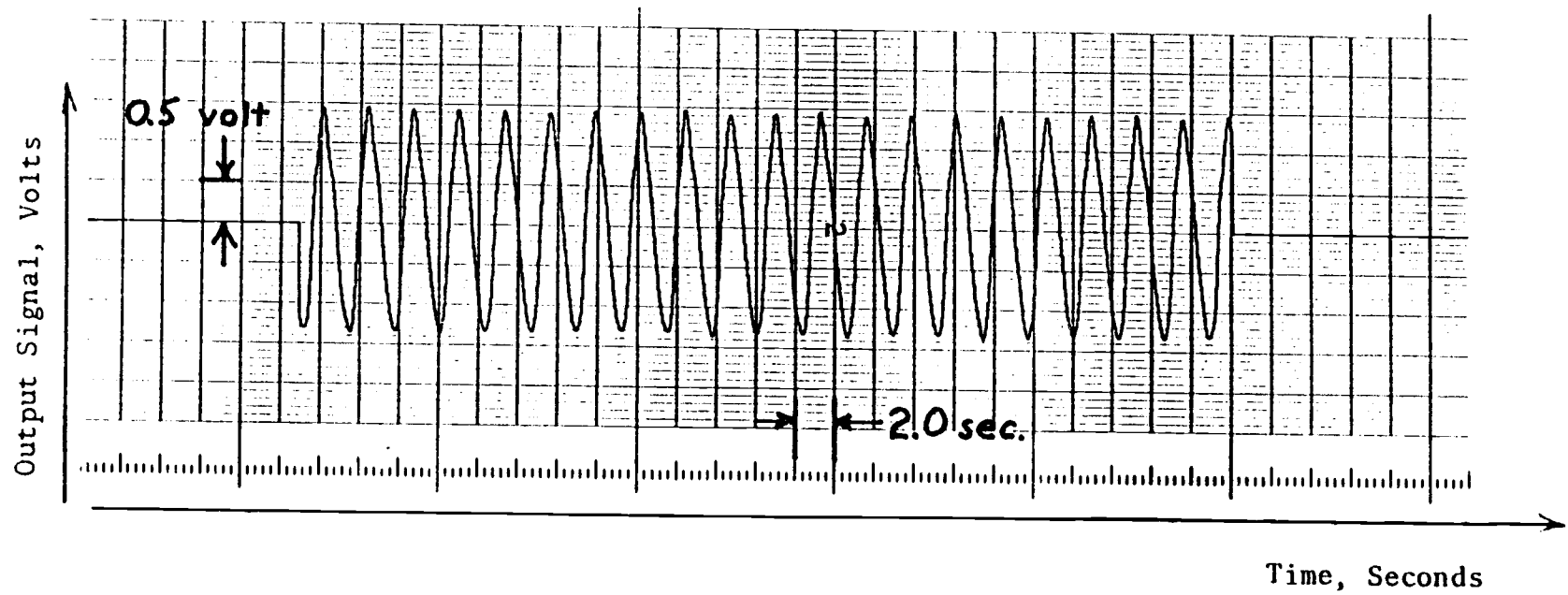


Figure 2.7. Typical record of output signal for a sinusoidally varying velocity. Maximum excursion was 14 inches, frequency 0.88 Hz, sampling frequency 25 per second.

linearity. Results for various velocities are tabulated below and shown in graphical form in Figure 2.8.

Distance Traveled by Iron Mass (Inches)	Frequency of Oscillation (Hz)	Record Amplifier Power (watts)	Output Signal Amplitude (volts)
14	0.5	50	0.8
14	0.5	100	1.2
14	0.5	150	1.6
14	0.5	200	2.3
14	0.73	50	1.4
14	0.73	100	1.75
14	0.73	150	2.3
14	0.73	200	3.0
14	0.88	50	1.6
14	0.88	100	2.1
14	0.88	150	2.6
14	0.88	200	3.6

Table 2.1. Output Signal from magnetic-solid mass flow detector for 3 frequencies and 4 amplifier power levels.

It can be seen that the output signals are proportional to the oscillating velocities, i.e., frequency (as they should be). The output level increases with amplifier power which indicates that saturation has not been achieved at the power levels used in this test. Saturation of material in the vicinity of the pick-up coil is necessary if one is to obtain a valid measure of the mass flux.

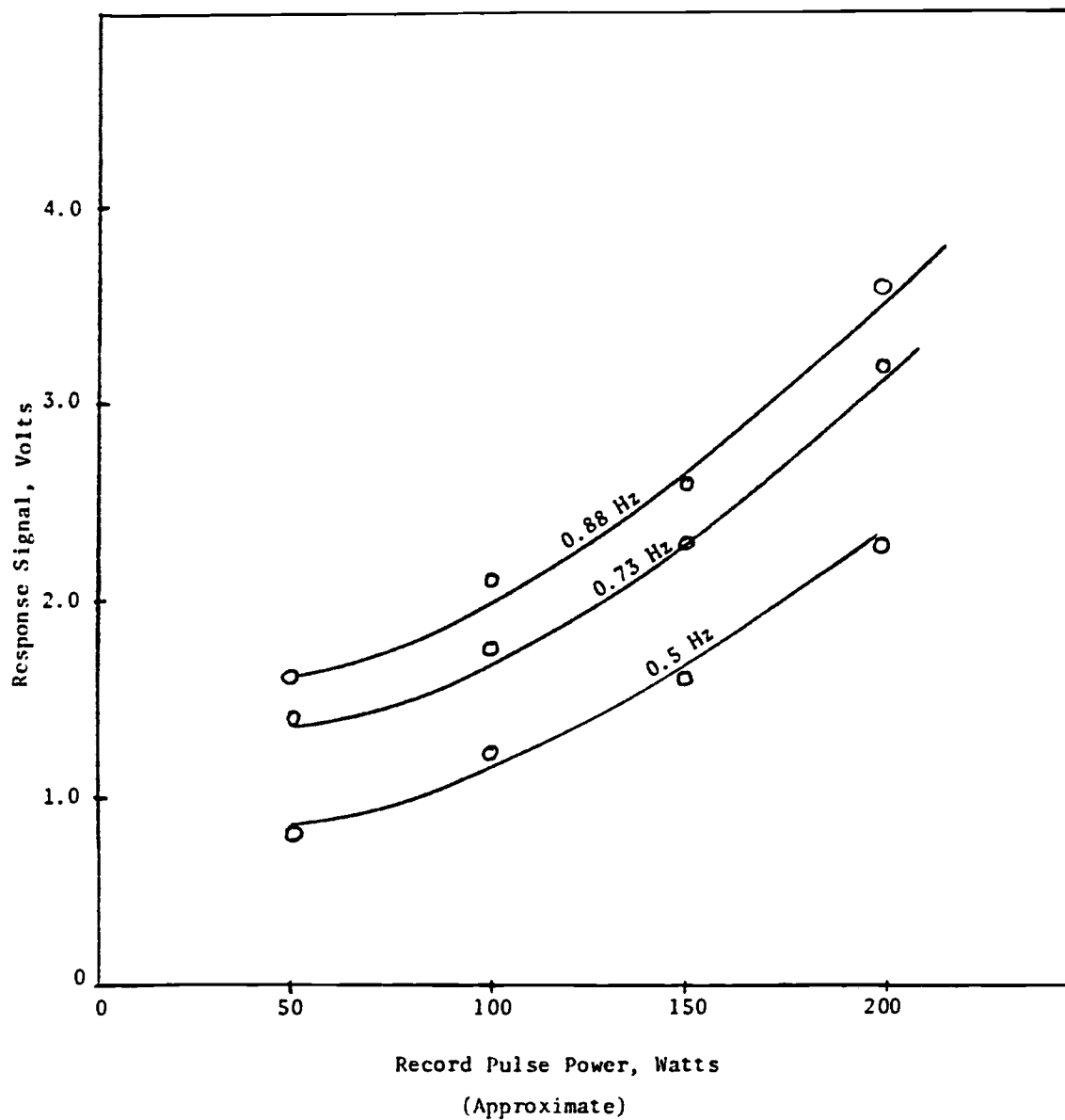


Figure 2.8. Response signal as a function of amplifier power does not show saturation behavior at power levels tested.

### Tests on Magnetic Saturation

Saturation of the magnetic material in the vicinity of the READ coil was later achieved by modifying the size of the coils and by increasing the magnetic field strength produced by the WRITE coil. The increase in the magnetic field strength was attained by increasing both the number of turns in the WRITE coil and its current input. The coil geometries were also modified to facilitate their installation in a tube-filled fluidized bed and to minimize solids flow obstruction inside the bed.

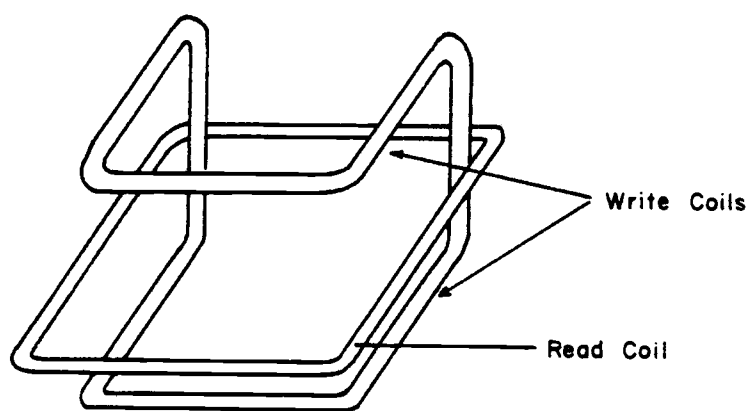
Two possible coil geometries were identified for this purpose, "the folded C-shaped" coil and the antiparallel set of coils.<sup>2</sup> These two geometries are shown in Figure 2.9. In both cases, the mass flow to be measured is along the axis of the READ coil, and as far as the mass flow measurement is concerned they should be equivalent. One of these two possible geometries - the "folded C" - was arbitrarily chosen to study the saturation of the magnetic material in the vicinity of the READ coil. This coil can be visualized as occupying eight edges of a cube 1.5 inches on an edge. The WRITE coil consisted of 90 turns of number 20 wire giving an impedance of approximately 1.5 ohms at 500 hertz. The READ coil was a 2" x 2" square coil of 2000 turns of number 36 wire.

The electronic instrumentation, and the sequence of RECORD, READ, and ERASE pulses were the same as used previously. However, the timing of these pulses was modified to allow data acquisition at a rate of 10 samples/second. The timing sequence is as follows:

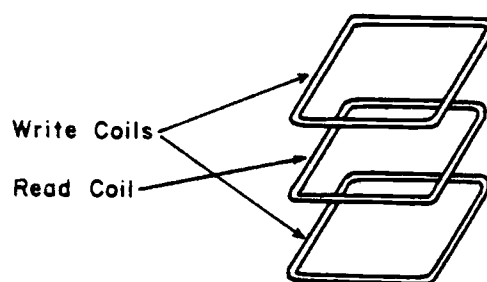
---

<sup>2</sup>An improved coil design that eliminated the interference of the coils in the solid flow inside the bed was later implemented in the solid mass flux measurements inside the bed (see next section). However, these coil designs still retain their potential use for different applications in solid mass flow measurements.





Folded "C" Configuration



Anti-parallel Configuration

Figure 2.9. Coil configurations.

Record pulse:	1 ms
First delay:	20 ms
Window:	3 ms
Erase pulse:	6 ms
Second delay:	<u>70 ms</u>
	100 ms

The device designed and used to produce a known movement of magnetizable material (iron powder) through the coils is shown in Figure 2.10. Sixteen-mesh iron powder was confined in a VINYL tube of either 3/4 inch or 1-inch diameter. The tube could be moved through the coils at a known linear velocity by a pulley system driven by a variable-speed motor. Knowledge of the length of the loop of VINYL tubing and the total mass of iron it contained allowed conversion from linear velocity to mass flux rate.

Magnetic saturation in the vicinity of the READ coil was established by monitoring field strength as a function of the power input used to magnetize the iron powder at a fixed tube velocity. Since the output signal from the READ coil is dependent upon the field strength, this was accomplished by simply measuring the output signal as a function of the WRITE-coil current input, and increasing the WRITE-coil current until two identical output readings were obtained. Any current above this level would produce the same output signal, and thus magnetic saturation was obtained. The results of a typical saturation test are depicted in Figure 2.11.

Mass flow measurements were then carried out at currents above the saturation threshold for both a 3/4-inch and a 1-inch tube filled with

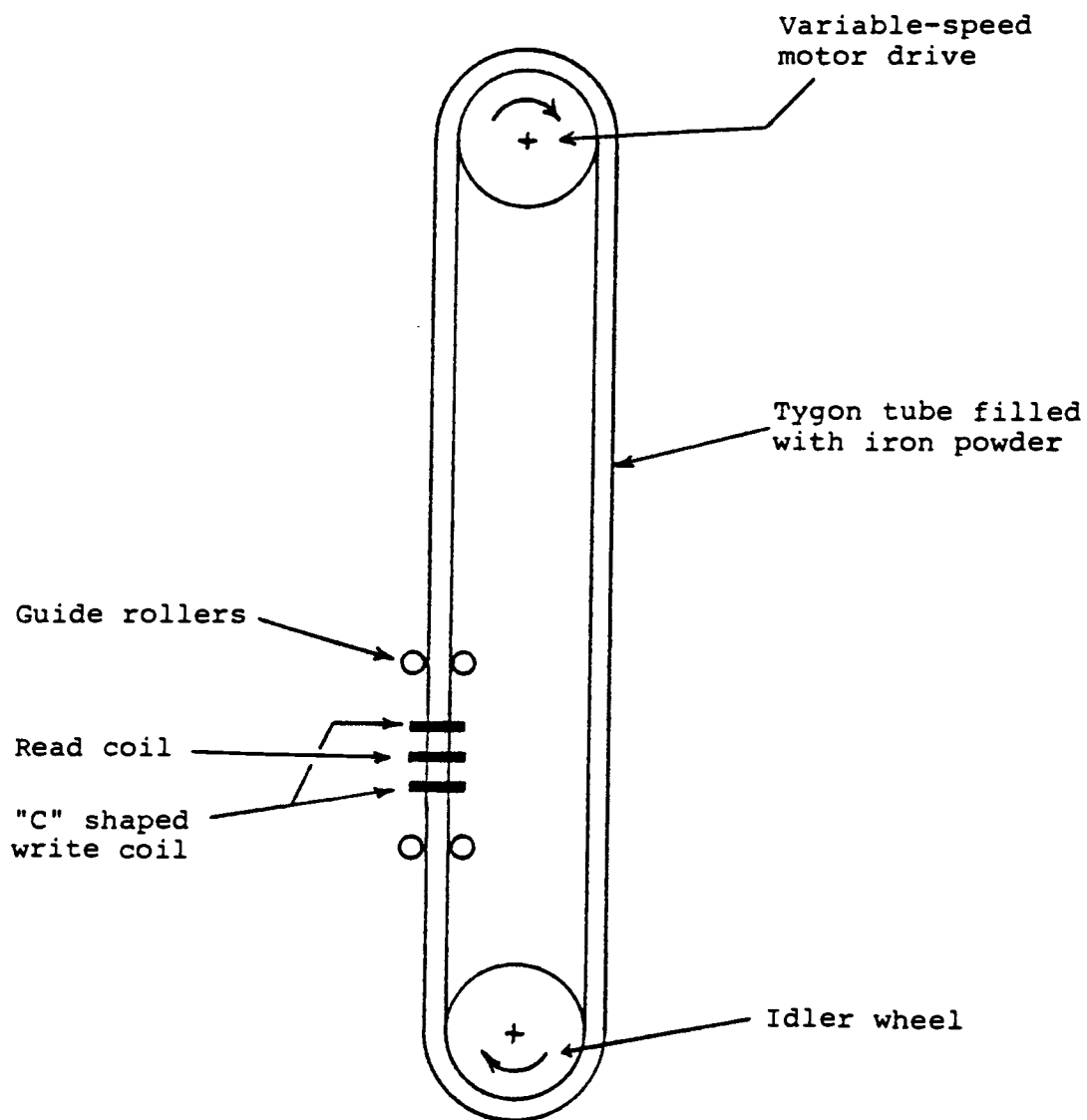
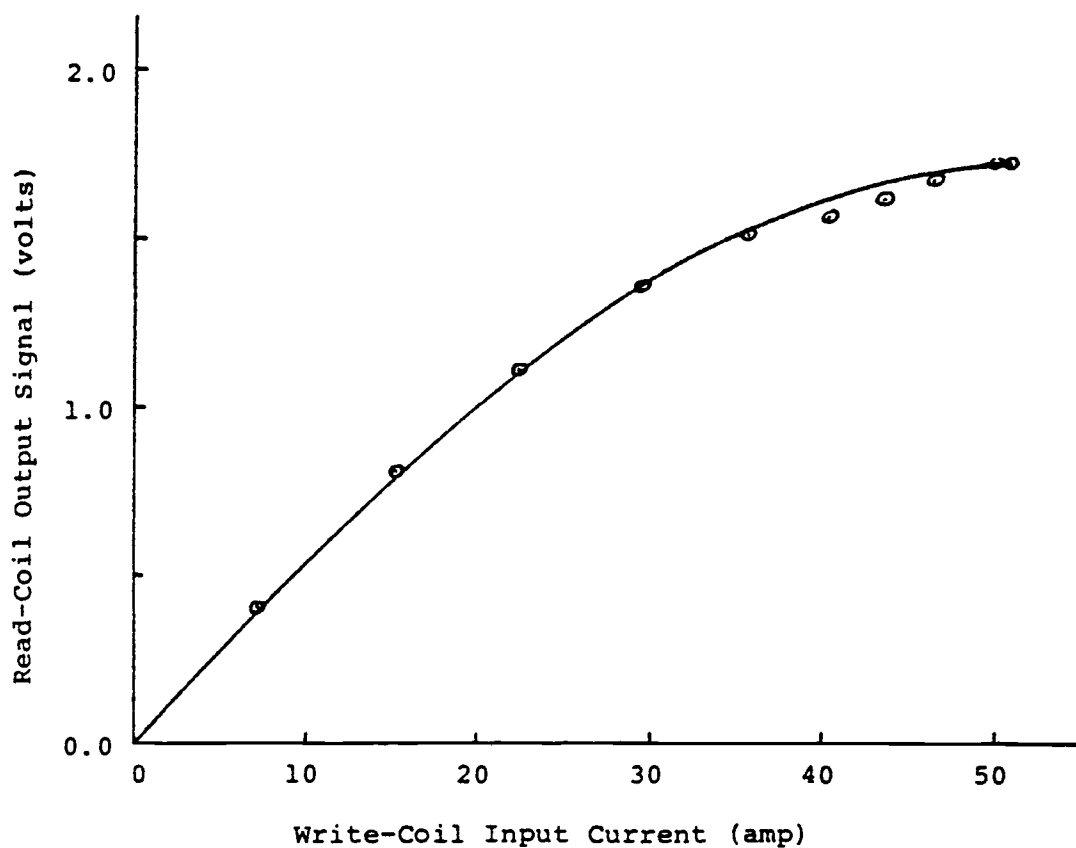


Figure 2.10. Magnetic saturation tests and calibration assembly.



Tube: 3/4 inch; 0.675 lb<sub>m</sub> iron powder/ft of tube

Mass flux: 16.70 lb<sub>m</sub>/ft<sup>2</sup>·sec

Coil: Folded "C"; 90 turns, #20 wire

Figure 2.11. Typical saturation curve.

iron powder moving through the coils. A range of linear velocities from 0 to 2.25 feet/second were used in both cases. For the same linear velocity in the two tubes, the ratio of mass flux for the larger tube to that for a smaller tube is 1.778. The results of these tests show, as expected, the output reading is indeed proportional to the iron-powder mass flux. These results are shown in Figure 2.12, and it can be seen from these data that the dependence of output signal upon mass flux is effectively linear for the range in mass flux of 18 to  $81 \text{ lb}_m/\text{ft}^2 \cdot \text{sec}$ . Some drop off occurs above a mass flux of  $81 \text{ lb}_m/\text{ft}^2 \cdot \text{sec}$ . If the three points on Figure 2.12 above a mass flux of  $81 \text{ lb}_m/\text{ft}^2 \cdot \text{sec}$  are excluded, a linear regression of the data produces the line shown, with a regression coefficient of 0.996.

The tests described above were carried out with iron powder inside the coils only. Further tests were needed to study the effect of iron powder surrounding the coils on the magnetic saturation of the material flowing through the coils. Before these tests were carried out, some modifications were made on the electronic instrumentation to shorten the response time between the application of the magnetizing pulse and the measuring of the induced voltage caused by the motion of the magnetized solids.

#### Reducing Current Decay Time in the WRITE Coil

When the magnetizing pulse is cut off, it is necessary to wait until the current in the WRITE coil decays to a sufficiently small value so that it is not picked up by transformer action in the READ coil. In previous experiments, the current pulse was produced by a linear voltage amplifier. At the end of the pulse the voltage dropped to zero and the

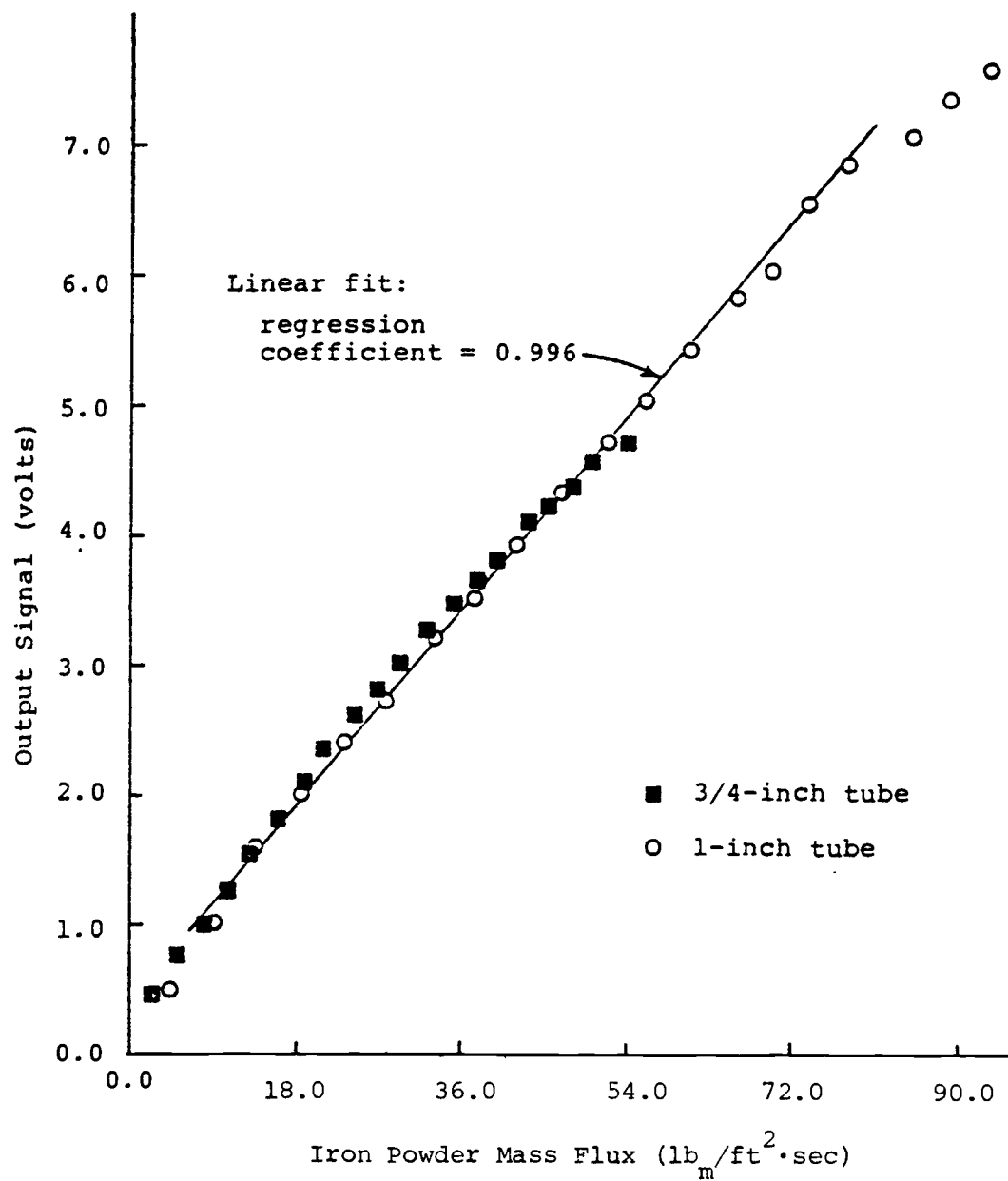


Figure 2.12. Typical calibration curve for 1 1/2" folded "C" coil.

current decayed exponentially down to zero with a time constant equal to the inductance of the coil divided by its resistance. The modification shown in Figure 2.13 improves the response of the amplifier by the use of current feedback instead of voltage feedback. An operational amplifier is used to drive the power amplifier. The feedback signal is the current through the WRITE coils. This current produces a small voltage, across a 0.1 ohm resistor, which is fed back to the negative input of the driver amplifier. At the end of the magnetizing pulse the signal input to the amplifier falls to zero but because of the inductance of the coil, the current does not immediately go to zero. Thus, a positive voltage appears at the negative input of amplifier A-1, thereby causing the output of amplifier A-3 to become negative. Because of the very large gain of the driver amplifier, the output from the power amplifier remains negative until the current falls to a very low value. The current then continues to decay all the way to zero but with a time constant which is equal to the inductance of the coil divided by its resistance and divided also by the gain of the driver amplifier. Figures 2.14a and 2.14b, respectively, show the record pulses using the linear voltage amplifier and the current feedback arrangement.

#### Reducing the Recording Pulse Width

The rise time of the recording pulse depends upon the inductance of the WRITE coils. When the coils are completely surrounded by iron, the inductance is high and the rise time is maximal. If there is less iron in the vicinity of the coils, then the inductance is smaller and the current in the WRITE coils reaches a saturating value in a shorter time. Once this saturating current has been established, there is no

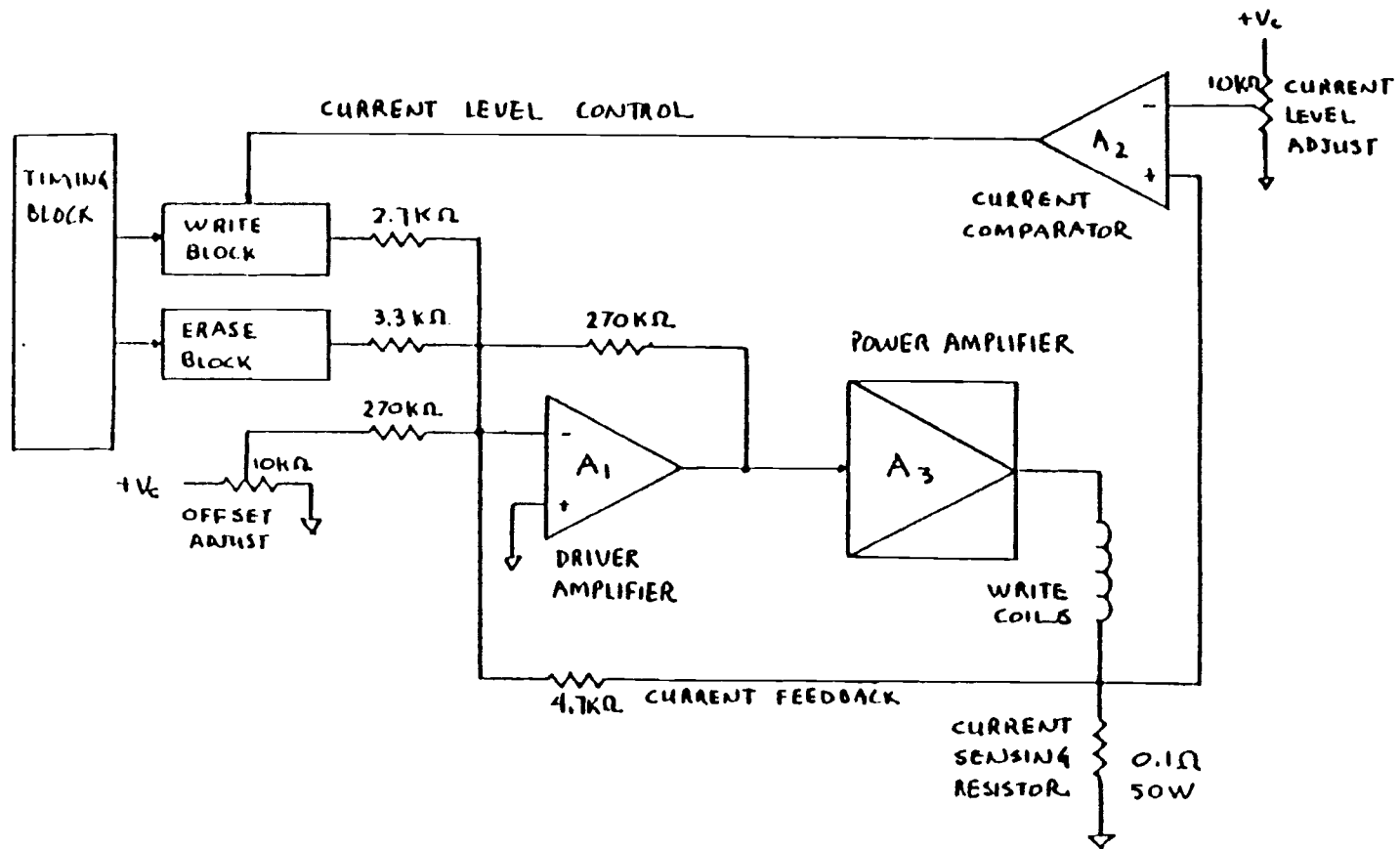


Figure 2.13. Block diagram of driver amplifier to decrease current decay time and current level control.



need to prolong the pulse. In order to take advantage of this effect, the electronics were modified so that the magnetizing pulse is switched off when the magnetizing current reaches a predetermined level, sufficient for saturating the iron in the vicinity of the WRITE coil. In order to protect the coil from possible overheating, the length of the recording pulse is limited to two milliseconds and the current will shut off after this time even if it has not reached the required saturating value. The shortened record pulse is shown in Figure 2.14c.

#### Further Tests on the Magnetic Flow Meter

Several series of tests were carried out in an effort to study and minimize the effect of the presence of solid particles outside of the coils. These tests were done with a set of antiparallel WRITE coils with a centered READ coil using the same apparatus described in the previous test. Samples of test results are given below. In all cases, a 1/2-inch i.d. VINYL tube filled with iron powder ( $0.316 \text{ lb}_m$  iron/ft of tube) was moved through both the READ and WRITE coils at a measured velocity. The particular test conditions and results are as follows:

#### Series I

WRITE Coils:	rectangular, 1.25" x 2.75"; 65 turns of #22 wire; 1.5" apart.
READ Coil:	centered, parallel to WRITE coils; 1.25" x 1.25"; 1000 turns of #34 wire.
Set A:	coils surrounded by air. current input: 80 amps current rise time: 0.68 ms Voltage drop across WRITE coils + 0.1 $\Omega$ resistor: 100 volts

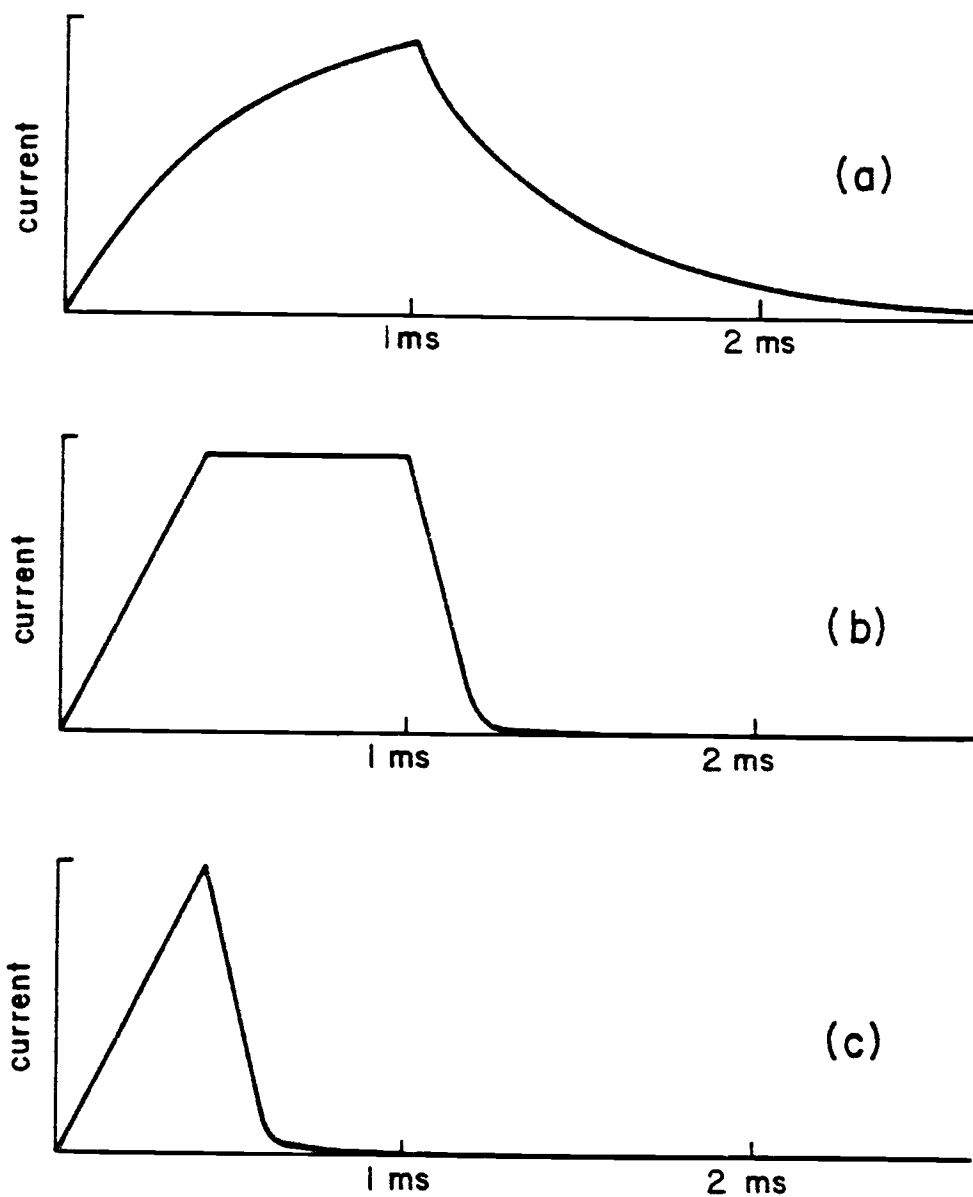


Figure 2.14. Recording pulse (a) using a linear voltage amplifier, (b) using a current feed-back amplifier, (c) with "level switching" circuit.

Set B: coils surrounded by iron powder.  
 current input: 80 amps  
 current rise time: 1.0 ms  
 voltage drop across WRITE coils + resistor:  
 112 volts.

The results of the tests in Series I are given in Figure 2.15.

### Series II

WRITE Coils: 1.25" square; 73 turns of #22 wire; 3" apart.

READ Coils: 1.25" square; centered parallel to ETIYR coils;  
 1000 turns of #34 wire.

Set A: coils surrounded by air.  
 current input: 80 amps  
 current rise time: 0.52 ms  
 voltage drop: 100 volts.

Set B: Coils surrounded by iron powder.  
 Current input: 80 amps  
 Current rise time: 0.92 ms  
 Voltage drop: 110 volts

The results of the tests in Series II are given in Figure 2.16.

### Series III

WRITE Coils: 1.25" square; 73 turns of #22 wire; 1.5" apart.

READ Coil: Rectangular, 1.25" x 1.75"; centered parallel to  
 WRITE coils; 1000 turns of #34 wire.

Set A: Coils surrounded by air.  
 Current input: 80 amps  
 Current rise time: 0.46 ms  
 Voltage drop: 100 volts

Set B: Coils surrounded by iron powder.  
 Current input: 80 amps  
 Current rise time: 0.8 ms  
 Voltage drop: 112 volts

The results of the tests in Series III are given in Figure 2.17.

The tests designated as Series III show for that coil design,  
 the output signal is unaffected by the media which surrounds the coils,

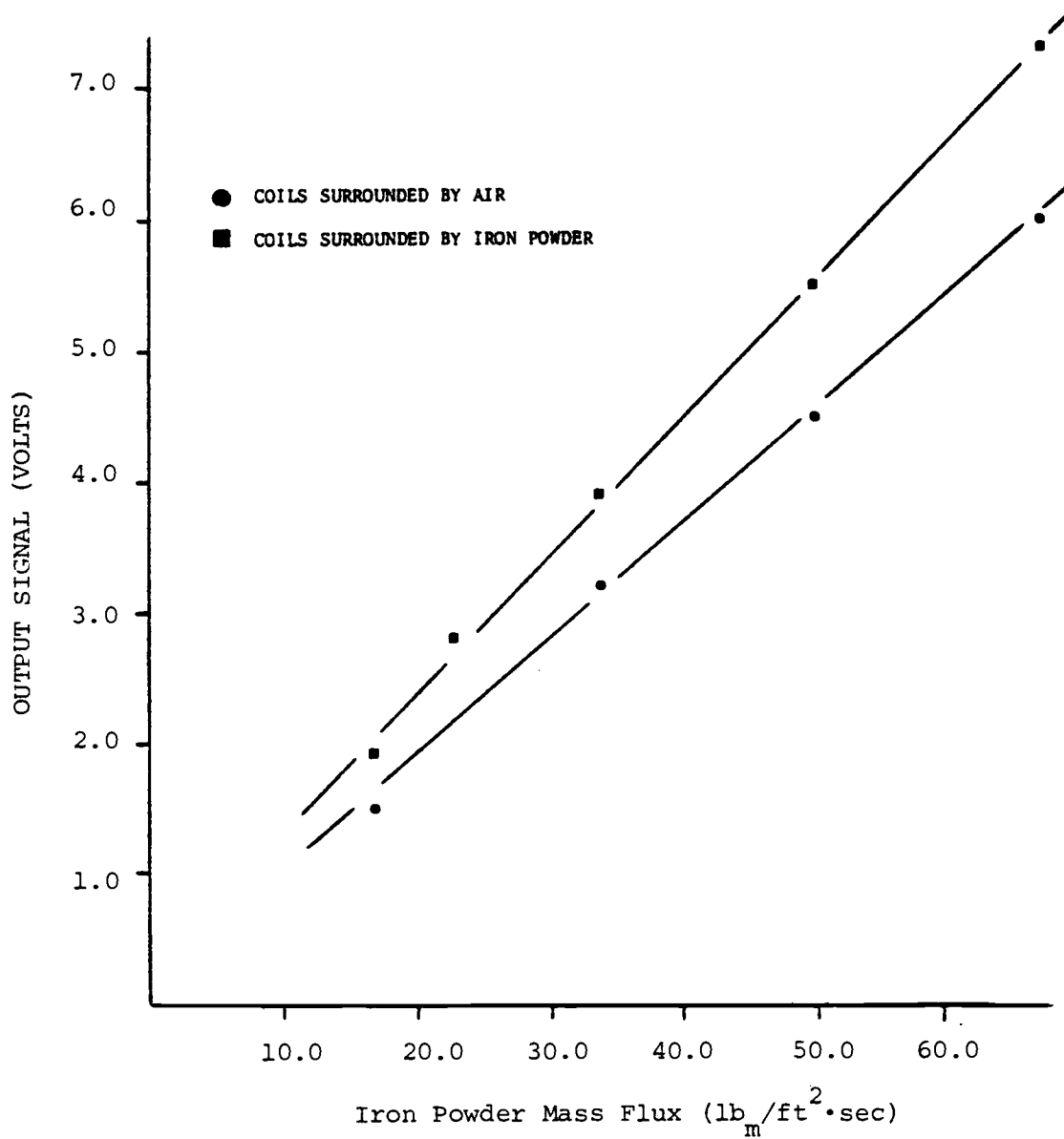


Figure 2.15. Output signal vs. iron powder mass flux inside coils for series I.

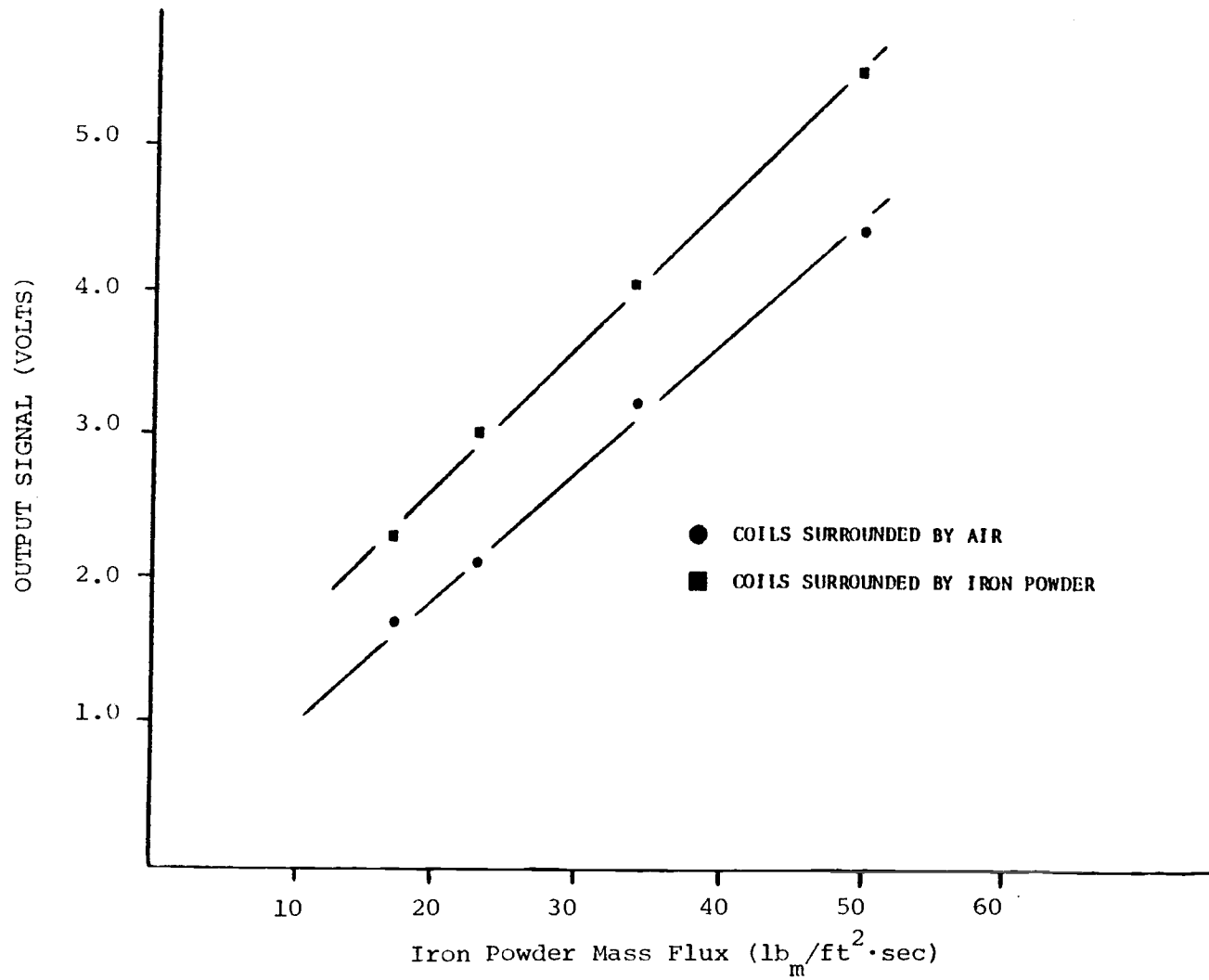


Figure 2.16. Output signal vs. iron powder mass flux inside coils for series II.

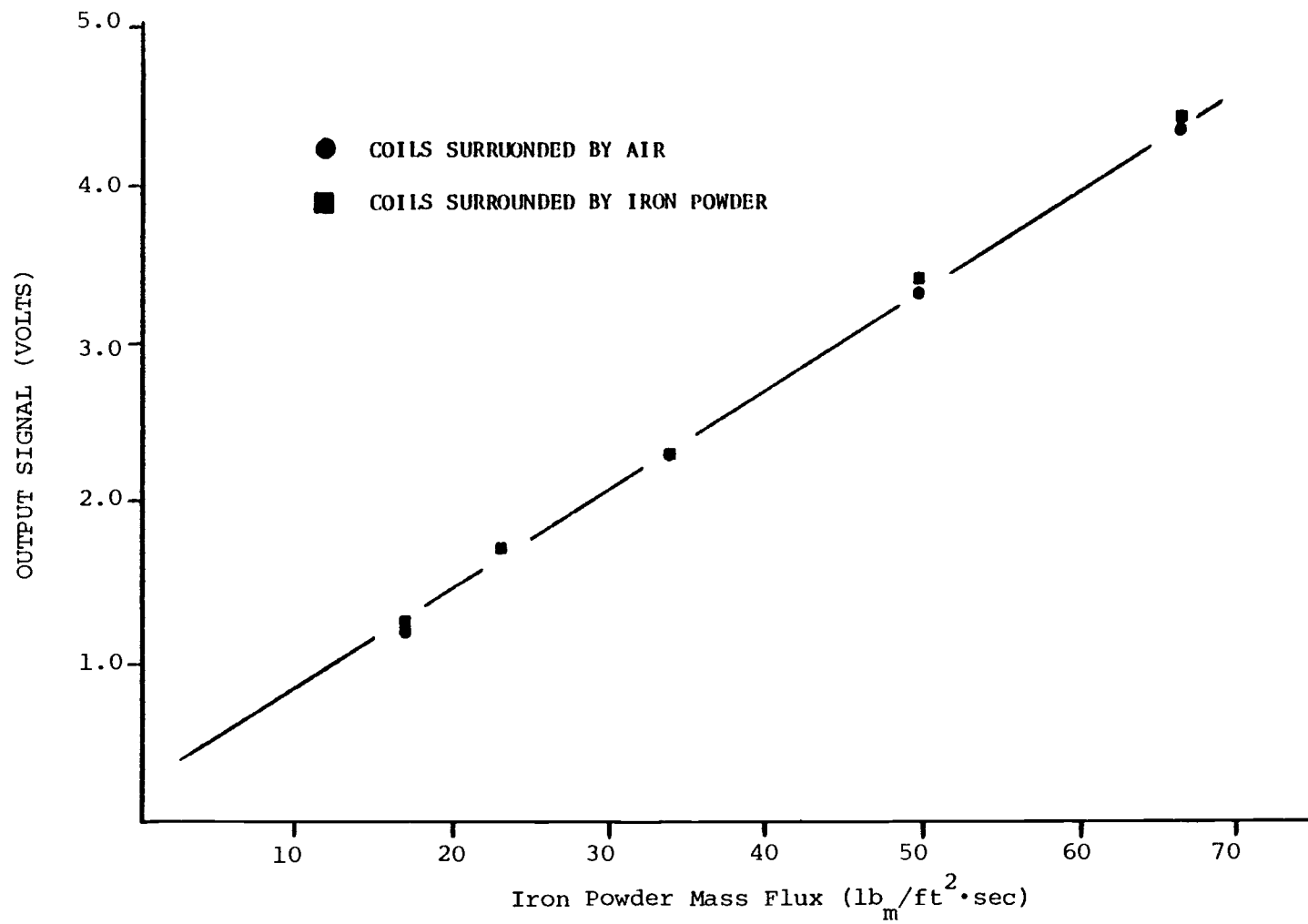


Figure 2.17. Output signal vs. iron powder mass flux inside coils for series III.

i.e., it makes no difference whether the coils are surrounded by air or iron powder. This is a necessary condition for consistent mass-flow measurements which are independent of the presence of a bubble outside the coils but in close proximity to them. Thus, the output signal represents only the mass flow of iron through the READ coil, and it is unaffected by the presence of iron outside of the coils, moving or stationary. These conclusions are only valid for the configuration designated in Series III of the tests.

The other two series of tests in which the WRITE coils were either further apart (Series II) or larger (rectangular; Series I) did not show positive results. In these cases, the differences between the output signals for the case of coils surrounded by air or coils surrounded by iron were significant. This is apparently caused by the inability to magnetically saturate the material contained in the region between the two WRITE coils within the limitations of our amplifiers.

In conclusion, the configuration used in Series III seemed to achieve the desired results. However, further modifications were considered to develop a configuration which does not interfere with solids movement at all, i.e., to incorporate the coils into a tube. In addition, the effect of not having the moving iron powder restrained was also investigated (i.e., what happens when the particles can rotate as they will in a fluidized bed?).

These modifications and others are the subject discussion in the next section.

C. MODIFIED COIL DESIGNS TO FURTHER IMPROVE RESPONSE TIME AND  
ELIMINATE FLOW OBSTRUCTION

Before the magnetic mass flow meter, described in the last section, could be used to give unambiguous results in an operating fluidized bed, one task remained. This was eliminating the presence of flow-obstructing coils, external to the in-bed tubes, which could affect the velocity of solids in the vicinity of the coils. This meant that the coil sizes and arrangement should be compatible with the size and arrangements of the in-bed tubes.

The first attempt to meet the above requirement in the design of the coils of the magnetic flow meter was not successful; a much lower signal to noise ratio was obtained with this design than was expected. A second design which also met the fluidized bed application requirements, had a very much increased and improved output signal which resulted from a flow of magnetic solid particles in the vicinity of the coils. A description of the two different coil designs follows.

Unsuccessful Modified Coil Design

The coil arrangement of this design is shown in Figure 2.18a. In this design all the coils...the record (WRITE) coil and the detector (READ) coils were located inside one of the in-bed tubes.

In this new arrangement, the coils were located in both the horizontal and vertical plane in the shape of an H. The upright legs of the H were the READ coils which were connected in parallel. The horizontal portion of the H was the WRITE coil. When energized, it created a magnetic field whose lines are shown in Figure 2.18b. When the magnetizing



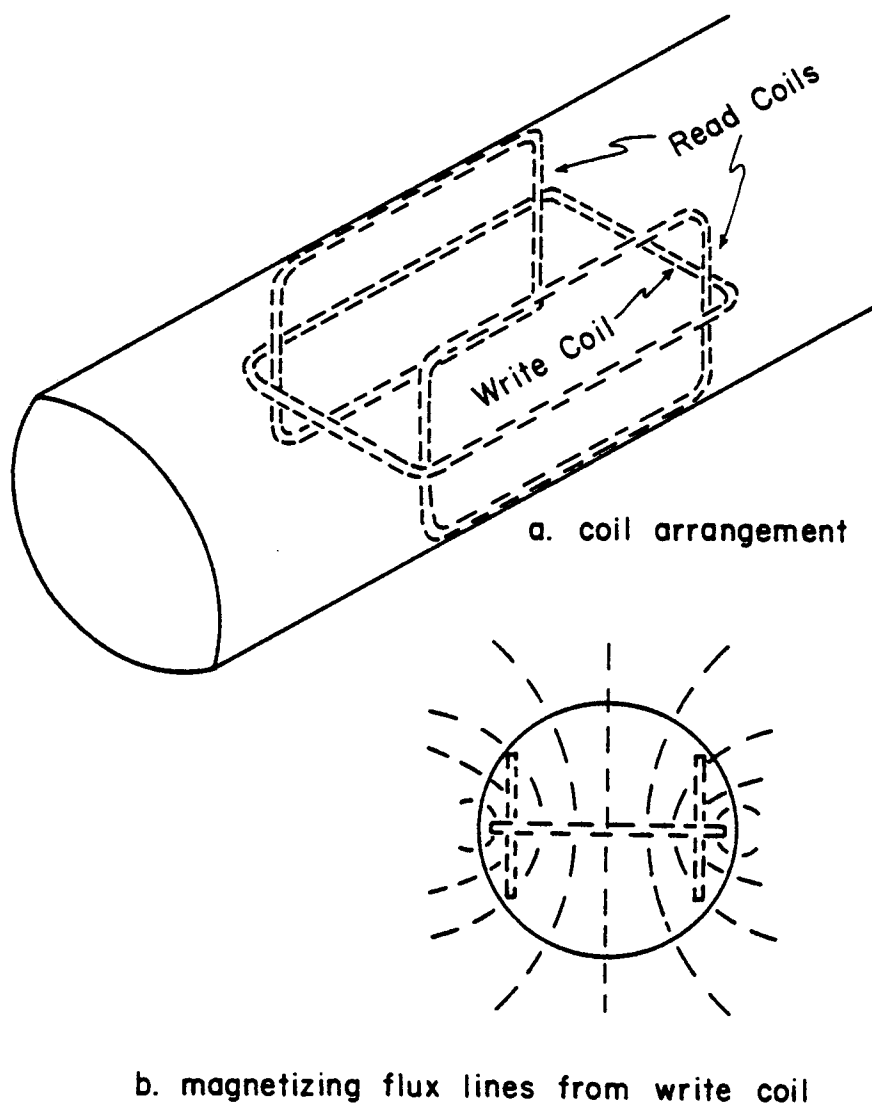


Figure 2.18. "H" coil design for magnetic solid mass flow measurement.

coil was no longer energized, the ferromagnetic material along the lines of force would retain its residual magnetism. The lines of force of this residual magnetic field should parallel the lines of force created by the WRITE coil. The READ coils were arranged to detect the upward (or downward) movement of solids next to the tube wall. Movement of the solids in either direction would result in the lines of force from the magnetized solids cutting the READ coil. Because the direction of the lines of force was reversed for the top and bottom leg of each READ coil, the induced voltages were added. The orientation of the READ coils at right angles to the WRITE coil had the advantage of minimizing the transformer pickup between them.

Tests made with the H coil, however, were not satisfactory. A much lower signal-to-noise ratio was obtained than was expected. The reason for this low signal was attributed to a less intense magnetic field in the vicinity of the coils than needed.

#### Successful Modified Coil Design

A different coil arrangement, which increased the magnetic field intensity, was designed and tested. In this new design the coils (WRITE and READ) were still located inside one of the in-bed tubes, but with a different arrangement as shown in Figure 2.19.

This new coil arrangement is similar to the anti-parallel coil arrangement described previously, but with the added advantage of compactness similar to that of the H-coil. A concentration of magnetic lines of force is still produced in the mid-plane between the two anti-parallel WRITE coils where the READ coil is placed. A further advantage of this compact coil design is that smaller coils inherently have lower

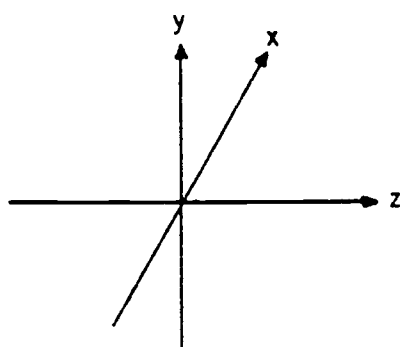
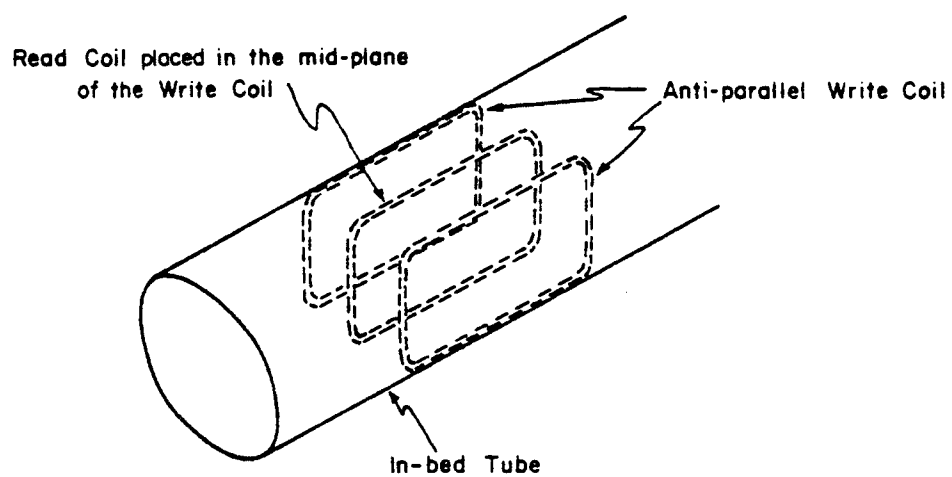


Figure 2.19. The anti-parallel write coil arrangement within the in-bed tube.

inductance. Because of this, the magnetizing current should rise to its maximum value in a shorter time, and it should also decay in a shorter time, thus enabling the magnetizing pulse to be shortened. The delay between magnetization and reading can also be shortened.

#### Modification in the Electronics Instrumentation

Before tests were conducted with the new coil design, several refinements were made in the electronics circuits of the magnetic solid particles mass flow meter to further improve the response time and the signal quality of the instrument.

A new WRITE coil drive circuit was designed and implemented with the compact coil design. This new circuit, shown in Figure 2.20, consists primarily of a set of 11 transistors connected in parallel in a common emitter switch mode. The WRITE coils connected as a collector load in the circuit have the effect of significantly reducing their inductive reaction to the current flow during the transient turn-off time of the WRITE pulse. This effect, in turn, further reduces the current decay time and oscillation in the coils during that period, compared to the previous circuit design (refer to Figure 2.13).

Figure 2.21 shows a block diagram of the modified READ coil analog amplification system and the sequential time control system of the magnetic-particles mass flow meter. In the analog amplification system, the READ coil is connected to a high quality, low noise audio amplifier through a pair of relay switches. The output of the amplifier is gated into an integrator; the smoothed signal is then sampled and held, and sent to the analog-to-digital converter of the data acquisition system. The sequential timing of these functions, with respect to each other and

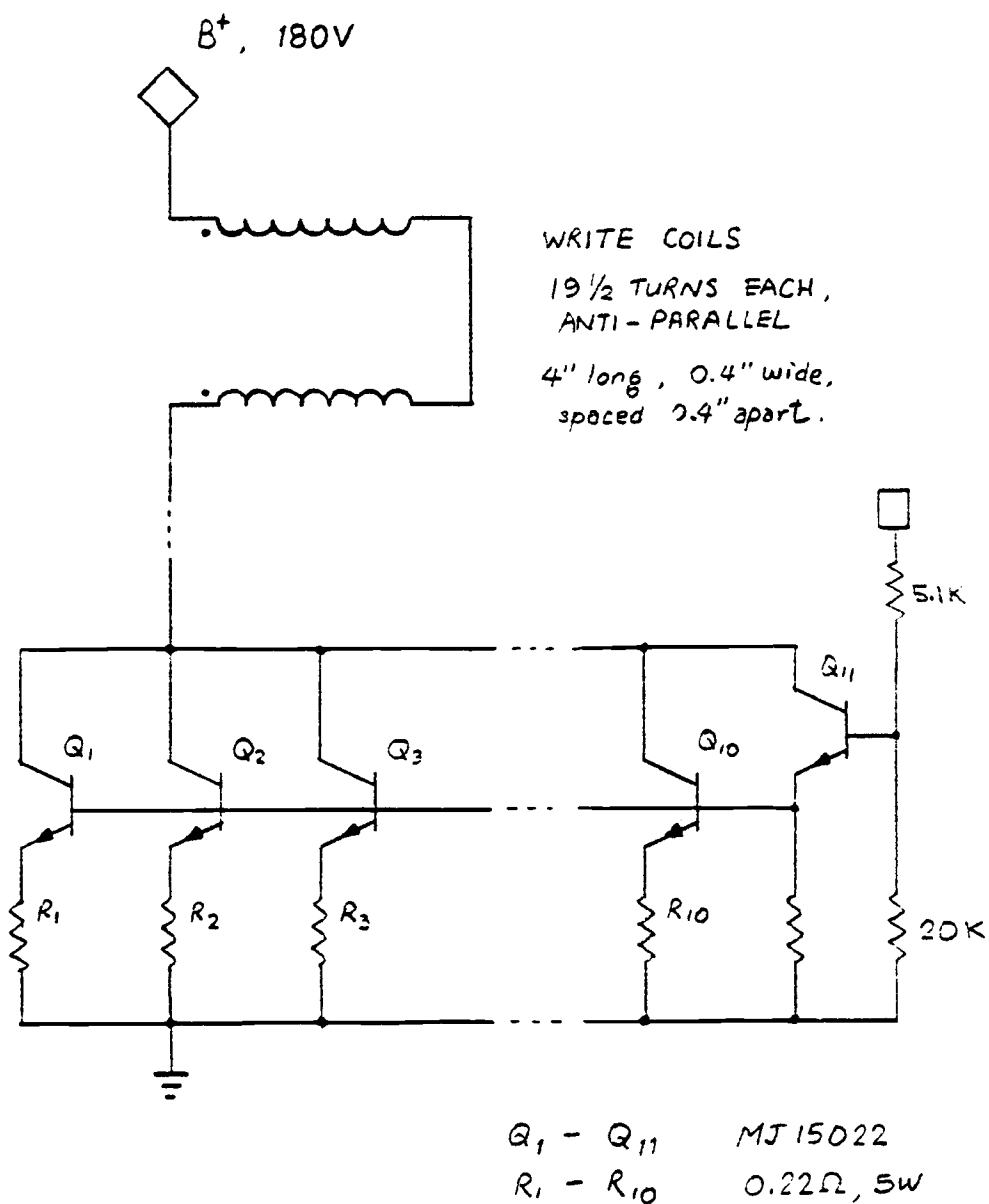


Figure 2.20. Schematic diagram of a new write-coil drive circuit.

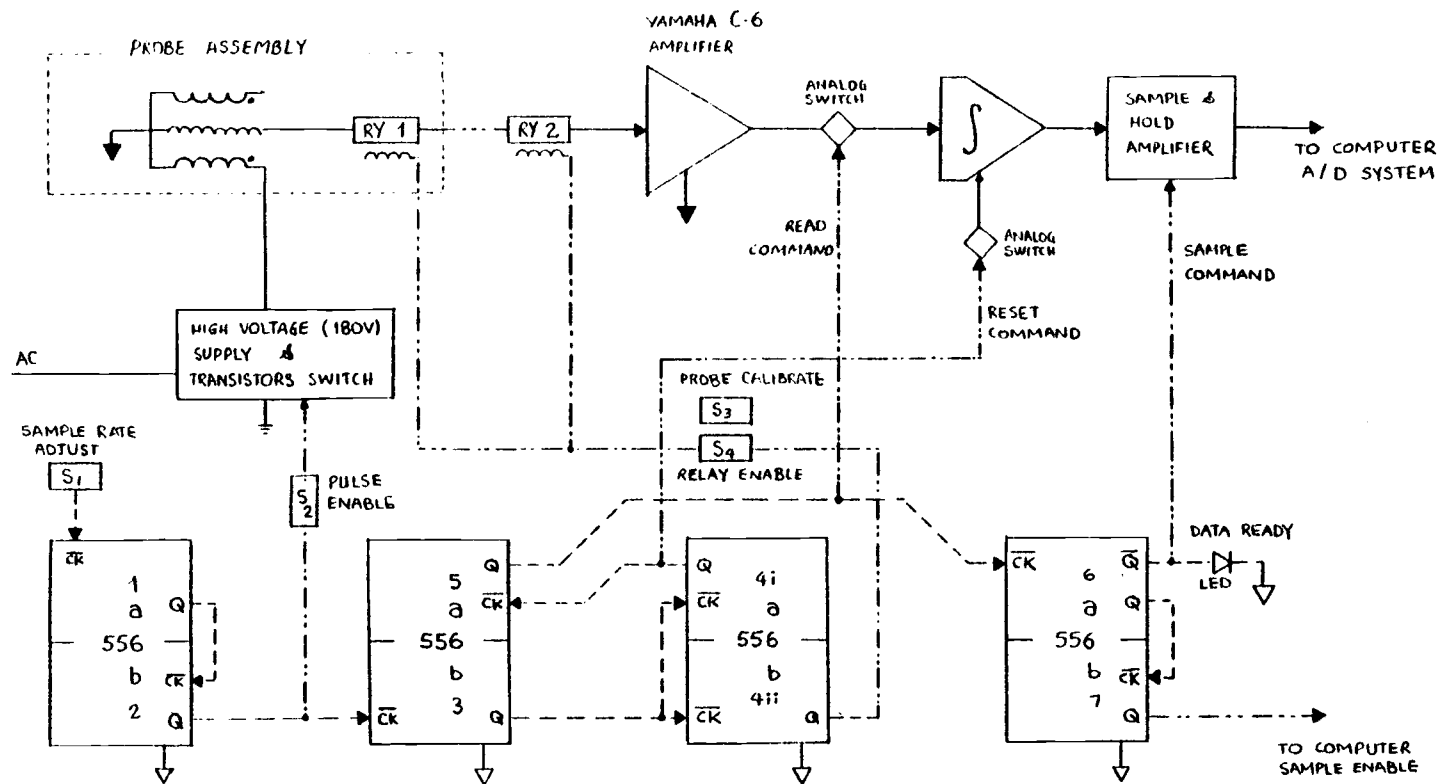


Figure 2.21. Block diagram of the modified read coil analog amplification system and the sequential time control system.

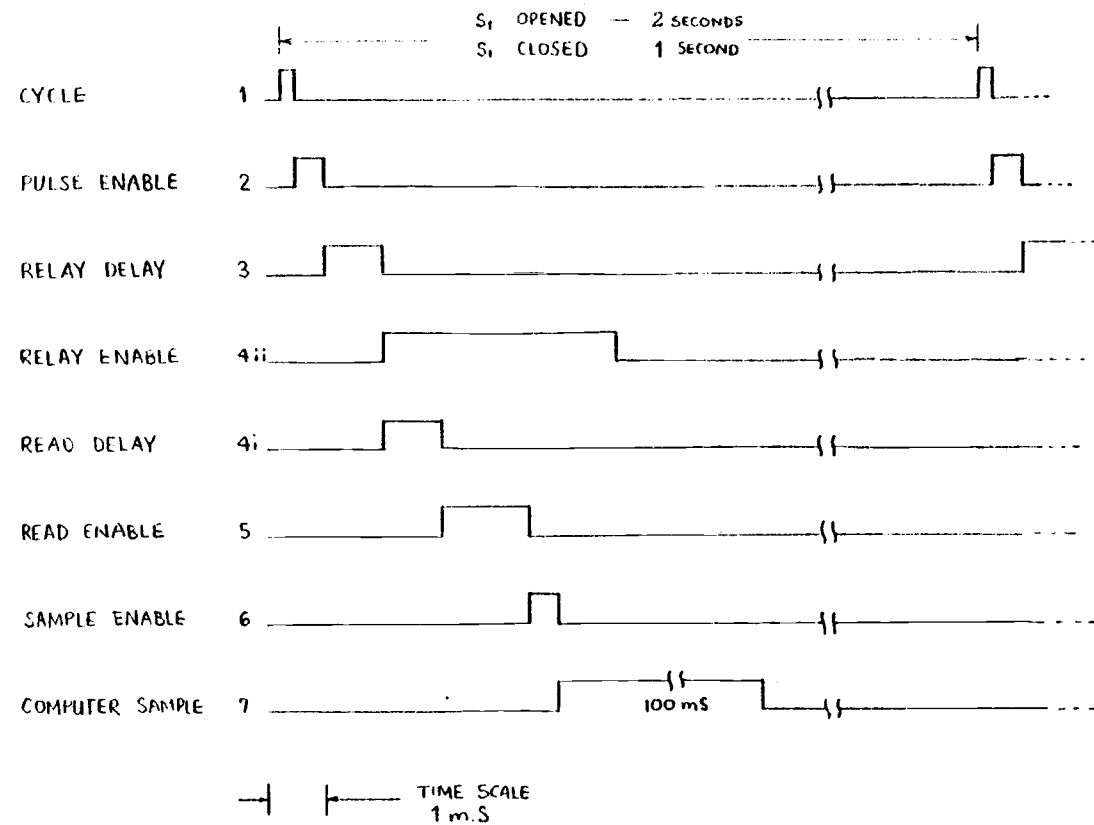


Figure 2.22. Time sequence of the various functions of the modified electronic instrumentation.

with respect to the function of the WRITE coil system, requires a precision timing control system to guarantee and maintain a reproducible output signal. This was provided by a system of 4 dual timers as illustrated in the block diagram. The timing sequence of the important functions of the electronics instrumentation is depicted in Figure 2.22.

A complete schematic drawing of the electronic instrumentation of the magnetic solid particles mass flow meter is given in Appendix A.

### Computer Simulation of Magnetic Flux Lines

A guide to the design and tests of the new coil arrangement has been provided by the use of a computer program<sup>3</sup> which is capable of simulating the physical characteristics of a two-dimensional magnet and finding the magnetic field and its gradients in these two dimensions. The program is divided into two separately executable programs: the mesh generator, MESH, and the magnetostatic program, FIELD. The purpose of MESH is to construct an irregular triangle mesh by interpolating between specified (by input) boundary points, and locating the internal mesh points of each region by a pseudo-equipotential method by assigning regional properties to each triangle. The purpose of FIELD is to solve the nonlinear Poisson's equation

$$\vec{\nabla} \cdot (\lambda \vec{\nabla} \psi) + \vec{S} = 0 \quad , \quad (2)$$

where  $\psi$  or its normal derivative is specified on the boundary,  $\lambda$  is a function of  $\psi$  or its derivatives and  $S$  is a function of position. For

---

<sup>3</sup>This computer program was obtained from Lawrence Berkeley Laboratory of the University of California in Berkeley. For a detailed description of the program and its use, see: Ref. (24).



magnetostatic problems the manner in which FIELD solves Eq. (1) is arrived at in the following fashion

$$\vec{B} = \mu \vec{H} = \vec{\nabla} \times \vec{A} , \quad (3)$$

where  $\mu$  is the permeability of the material, and  $\vec{A}$  is a magnetic vector potential.

The curl of the magnetic field intensity  $H$  is given by

$$\vec{\nabla} \times \vec{H} = 4\pi \vec{J} , \quad (4)$$

where  $J$  is the current density. Substituting  $H$  from Eq. (3) to Eq. (4) we obtain

$$\vec{\nabla} \times (1/\mu \vec{\nabla} \times \vec{A}) = 4\pi \vec{J} . \quad (5)$$

Since  $A$  and  $J$  have only one nonzero component, for two-dimensional problems, Eq. (5) reduces to

$$\vec{\nabla} \cdot (\gamma \vec{\nabla} A) = - 4\pi J , \quad (6)$$

where  $\gamma = 1/\mu$ .

The gradient of  $A$ , namely  $\vec{\nabla} A$ , is

$$\vec{\nabla} A = \vec{i} (\partial A / \partial x) + \vec{j} (\partial A / \partial y) , \quad (7)$$

and since  $\gamma$  depends on  $|\vec{\nabla} A|$ , it is convenient to consider  $\gamma$  as a function of  $B^2$  or

$$\gamma = F(B)^2 = F(|\vec{\nabla}A|^2) = F[(\partial A/\partial x)^2 + (\partial A/\partial y)^2] \quad (8)$$

The finite difference approximation in a triangular mesh is derived as

$$\sum_{i=1}^6 W_i (A_i - A) + 4\pi J = 0, \quad (9)$$

where  $A$  (see Figure 2.23) is the vector potential at point  $C$ ,  $A_i$  the vector potential at point  $C_i$  and the  $W_i$ 's are geometric factors called couplings, which depend also on  $\gamma$ .

This computer program, as mentioned before, works only for a two-dimensional magnet. To use it for a three-dimensional magnet, a plane of symmetry must exist in this magnet. Fortunately, such a plane does exist in our magnetic flow meter; this plane is the (y-z) plane shown in Figure 2.19. A cross section of the magnet flow meter at this plane is shown in Figure 2.24. The dotted portion of the circular cross section of the tube indicates a groove in the tube. This figure also shows the square geometry that the coil arrangement assumes in the tube. When the tube is totally surrounded by iron powder, the magnetic flow meter can then (for magnetic field calculation) be divided into three different regions as follows:

1. The iron region which is outside the protective shield and can extend as far out as the boundaries of the fluidized bed allow.
2. The WRITE coils region.
3. The nonmagnetic region inside the protective shield other than the WRITE coils region.

Figure 2.25 shows the mesh generated by the computer for the coil arrangement and the regions described above. Figure 2.26 shows a plot

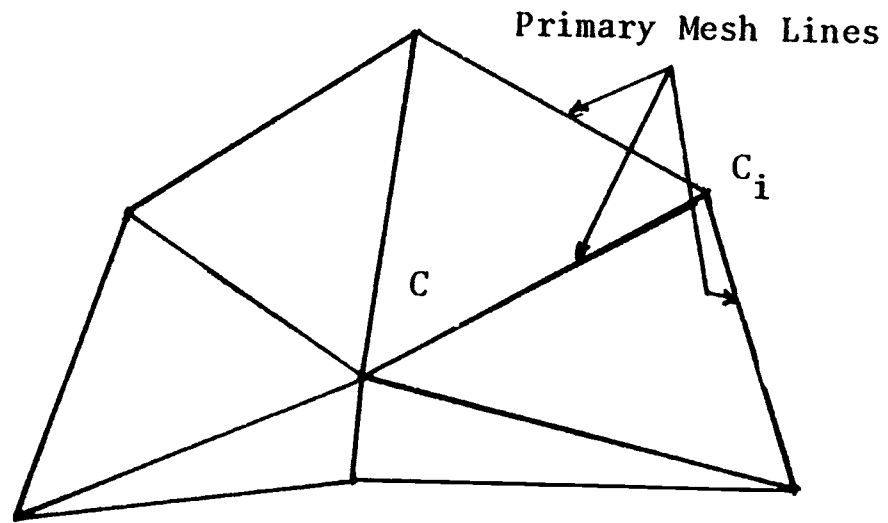


Figure 2.23. One element of the triangular mesh generated by the computer program.

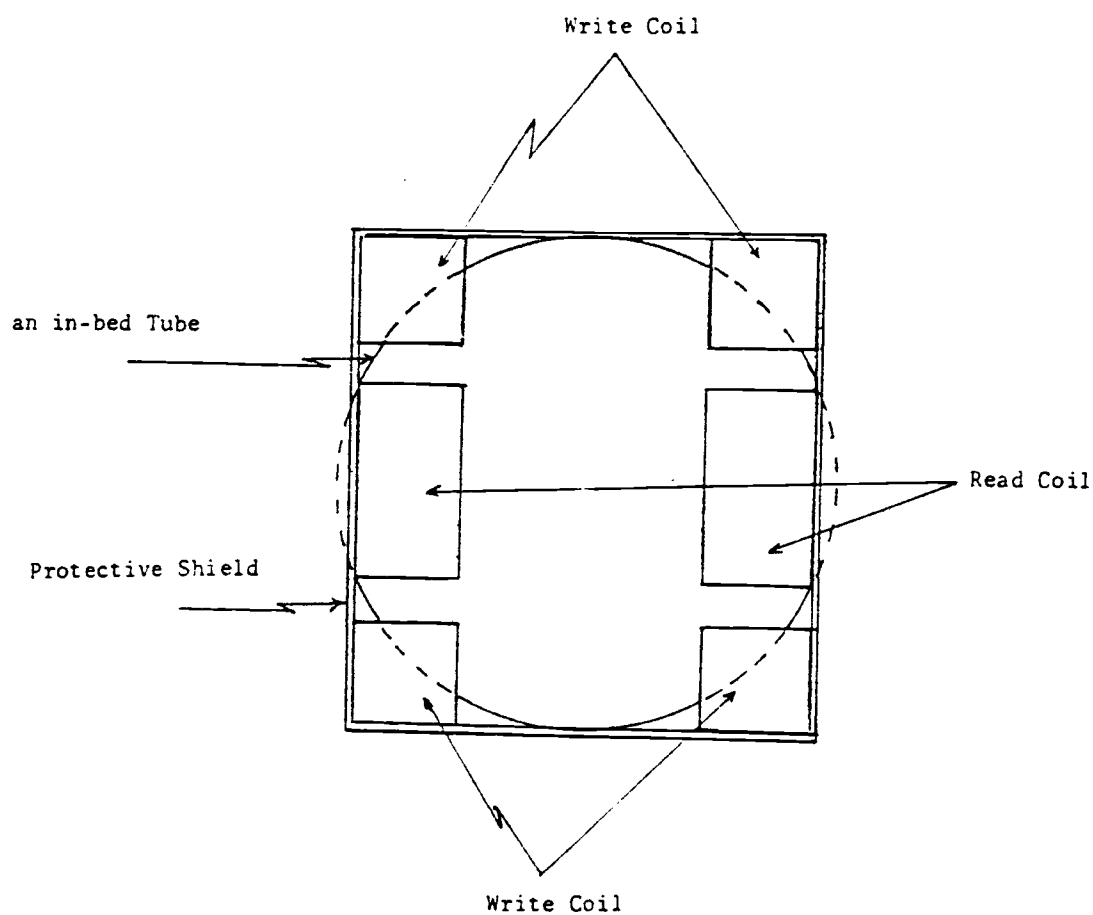


Figure 2.24. A cross-section of an in-bed tube with the write and read coils.

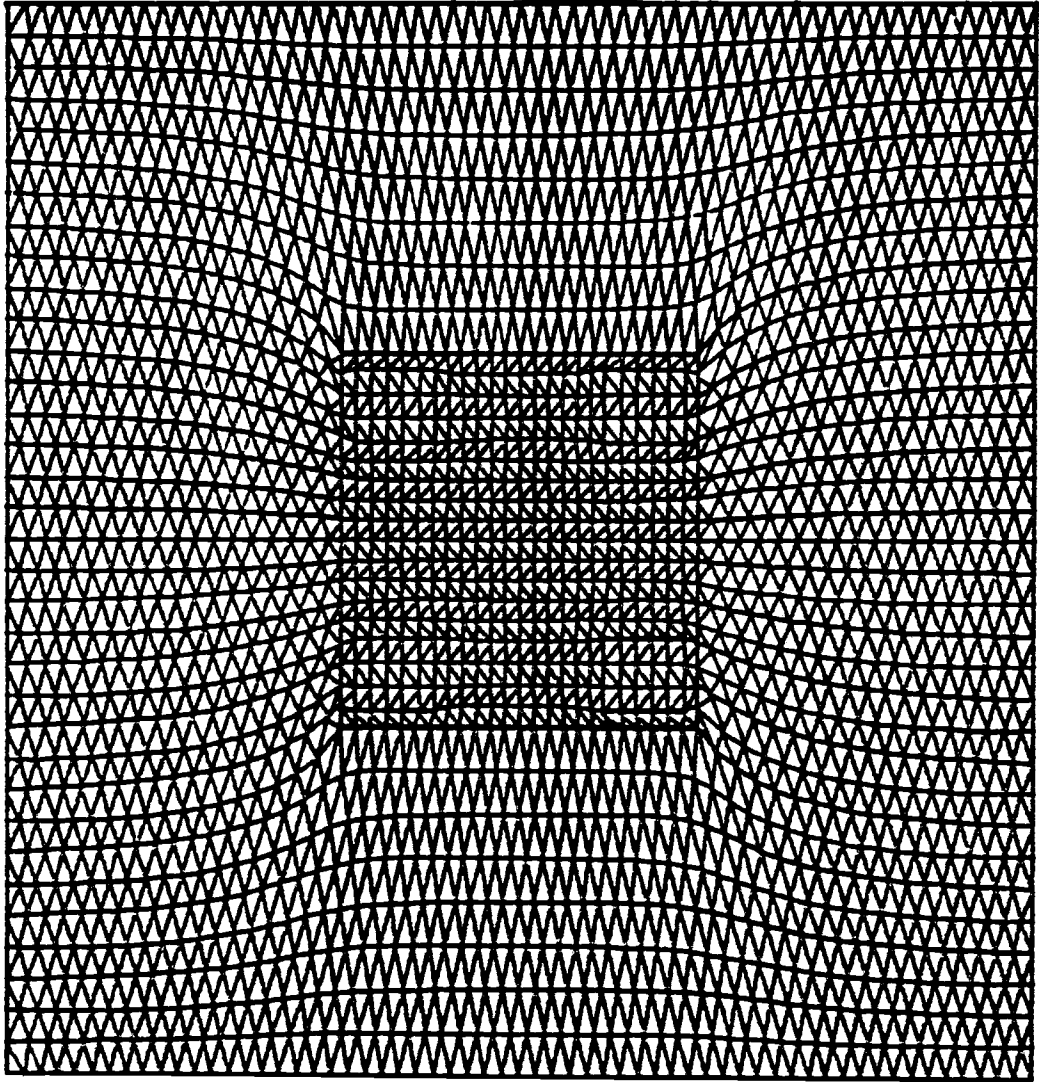


Figure 2.25. Generated mesh for the magnetic solid flow meter probe.

of the magnetic field generated by the program in the nonmagnetic region and in the surrounding magnetic iron powder. The figure shows a high magnetic-field intensity in the immediate vicinity of the WRITE coils, while it shows a less intense field further away from the coils. In fact, the magnetic field drops down by two orders of magnitude just 2 cm away from the WRITE coils. The reason for this rapid drop in the magnetic field intensity is the relatively lower permeability of iron powder caused by the presence of air gaps between the iron particles.

One of the important features of this computer program is its flexibility and ability to accept any conceivable arrangements and combination of exciting coils and magnetic and nonmagnetic media around them. This feature allowed simulation of different coil arrangements and the effect of the presence of air bubbles in different parts of the iron region surrounding the coils. Figure 2.27 shows a plot of a magnetic field similar to that in Figure 2.26, but with the iron region extending only 1.0 cm on each side of the coils in the x-direction. The plot shows that the magnetic field in the immediate vicinity of the coils is not affected by this change. Such simulation allowed estimation of the effective region of the WRITE coils and hence the pick-up region of the READ coil.

#### D. MAGNETIC FLOW METER CALIBRATION

A calibration method, suitable for the new magnetic solid flow meter discussed above, was adopted. An "L-valve", as studied by Knowlton and Hirsan (25) to feed limestone to atmospheric fluidized bed combustors, was used to calibrate the new probe.

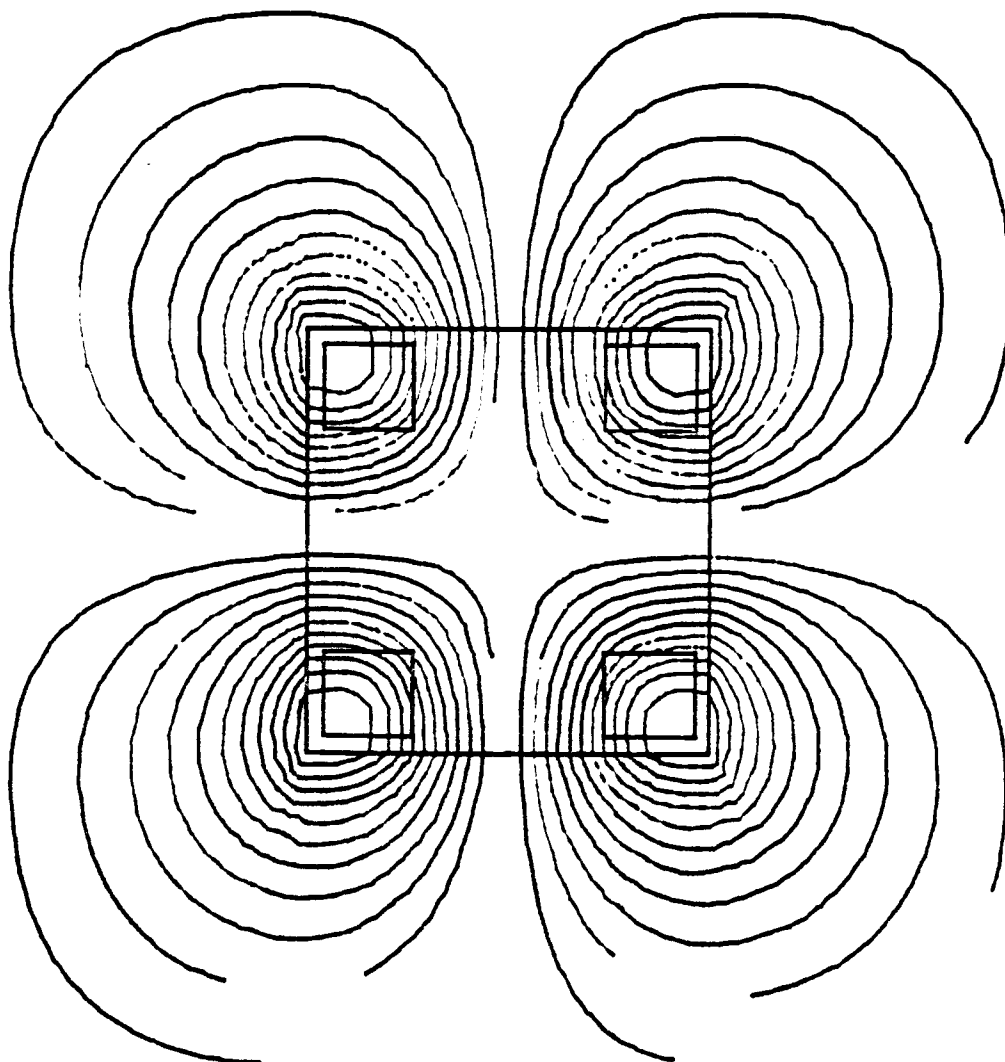


Figure 2.26. Flux lines distribution for the magnetic solid flow meter probe.

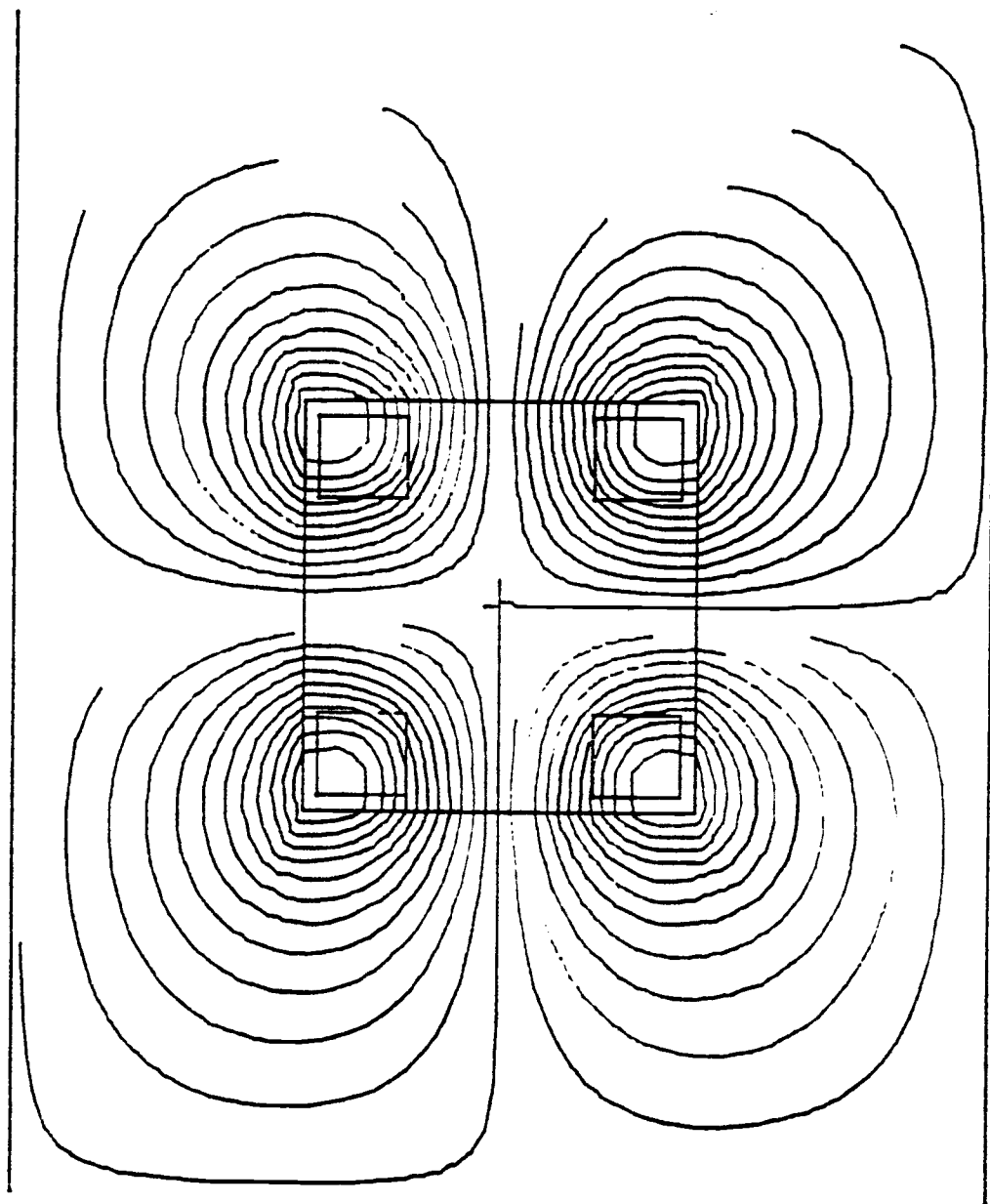


Figure 2.27. Flux lines distribution for the magnetic solid flow meter probe with iron region reduced in the Y-direction.



The apparatus consists (Figure 2.28) of a solids feed hopper at the top of the unit connected to a long stand pipe through which the iron powder passes in a gravity flow to the L-valve. Control aeration is added to the L-valve at a point just above the 90-degree section. The aeration gas causes the iron powder to flow through the 90-degree section into the horizontal section of the L-valve.

The magnetic solids flow meter was placed horizontally inside the downcomer. Calibration measurements were made by measuring the output signal from the READ coil of the magnetic probe at different solid flow rates. The solid flow rates were varied by changing the aeration gas flow rate.

#### Principles of Operation of the L-Valve

Knowlton has shown that the operation of the nonmechanical L-valve is dependent upon system pressure drop and geometry. Thus, a pressure balance must be maintained in the system such that the pressure drop in the horizontal section of the L-valve must equal the downcomer and hopper pressure drops.

$$\Delta P_{\text{downcomer}} + \Delta P_{\text{hopper}} = \Delta P_{\text{L-valve}} \quad (10)$$

The downcomer is the dependent part of the pressure drop loop; its pressure drop will adjust to exactly balance the pressure drop produced by the independent part of the loop, in this case the L-valve. However, there is a maximum pressure drop per unit length ( $\Delta P/L$ ) that the downcomer can develop. This value is the fluidized bed pressure drop per unit length  $(\Delta P/L)_{mf}$  for the material being used.

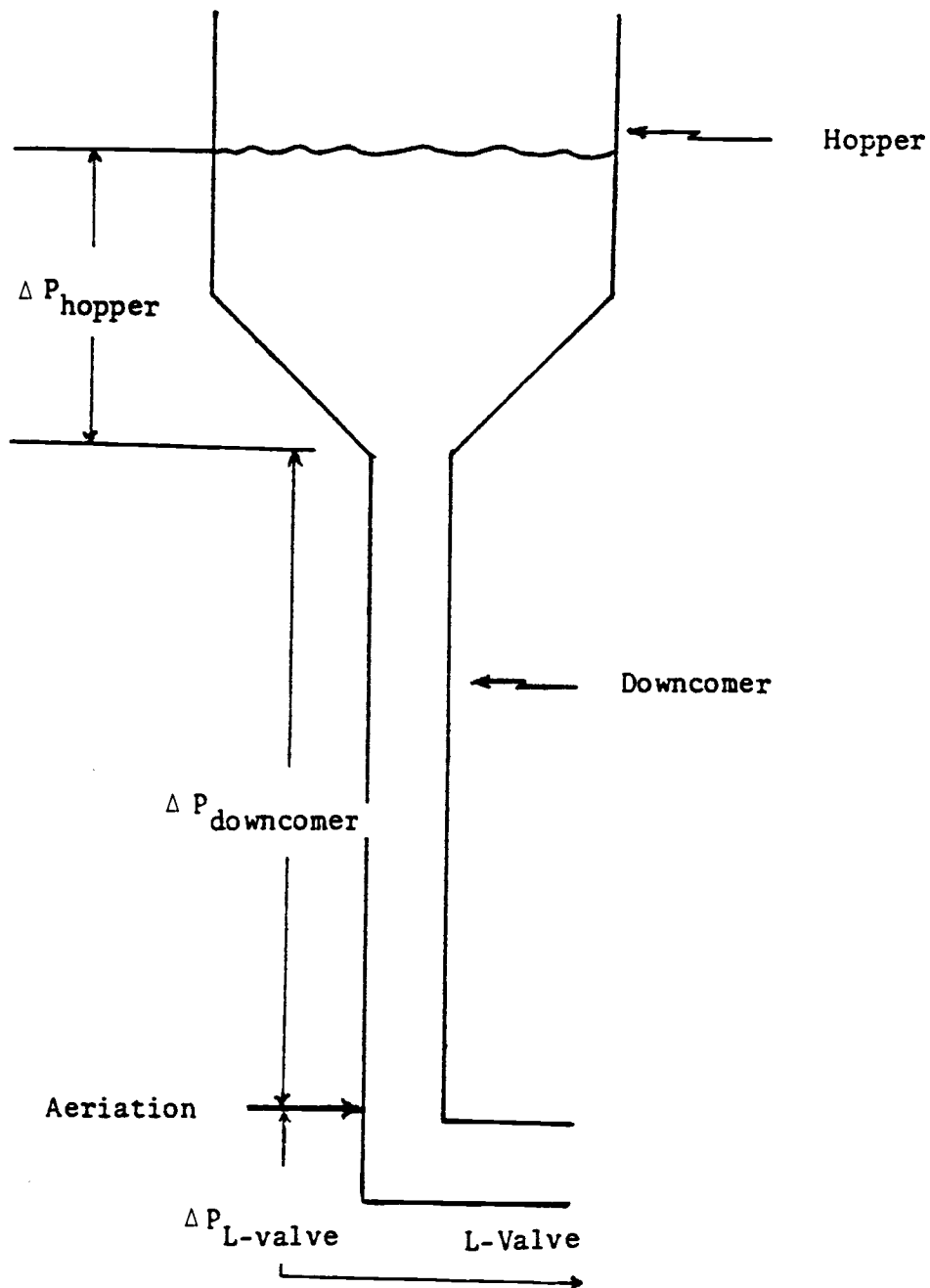


Figure 2.28. Schematic of L-Valve.

The independent pressure drop in the L-valve can be increased by increasing the solids flow rate. The downcomer pressure drop adjusts to balance this increase. If the solids flow rate continues to increase, the downcomer pressure will also keep increasing to balance the pressure drop in the L-valve. This will occur until the  $\Delta P/L$  in the downcomer reaches  $(\Delta P/L)_{mf}$ .

The pressure drop in a downcomer is generated by the relative velocity,  $V_r$ , between the gas and solids in the downcomer. When  $V_r$  reaches the value necessary for minimum fluidization of the solids, a transition from a packed bed to a fluidized bed occurs. Any further increase in  $V_r$  results in the formation of bubbles in the downcomer. These bubbles hinder the flow of solids through the downcomer and thus decrease the solids flow rate.

To determine the minimum downcomer length necessary for an L-valve, it is necessary to know the pressure drop on the independent side of the loop at the solid flow rate desired. The minimum length of downcomer necessary,  $L_{min}$ , is

$$L_{min} = \Delta P_{L\text{-valve}} / (\Delta P/L)_{mf} \quad (11)$$

The actual length of downcomer selected for the L-valve design should be greater than  $L_{min}$  to allow for the possibility of a required increase in the solids flow rate and to act as a safety factor. Typical downcomer lengths might be 1.5 to 2 times  $L_{min}$ .

Unfortunately, at this time there were no published correlations to predict L-valve pressure drop and aeration requirements. The best way to determine these parameters was to estimate them from basic data from

a small L-valve test unit or to extrapolate them (as was done in our case) from the data given by Knowlton.

### Calibration Procedure

A magnetic flow meter like the one shown in Figure 2.19, along with the new electronics instrumentation shown in Figures 2.20, 2.21, and 2.22 was calibrated using the L-valve discussed above. The magnetic flow-meter probe was placed horizontally inside the downcomer of the L-valve. The output signal of the READ coil was monitored at different downward solids flow rates through the downcomer. Upward solids flow was simulated by rotating the magnetic flow-meter probe  $180^\circ$  inside the downcomer of the L-valve.

Iron powder flow rates were determined by measuring the particle velocity at the downcomer wall. The particle velocity at the wall had previously been correlated in a flow test as a function of iron powder flow rate. In this test, the iron powder flow rate was obtained by collecting the iron powder in a container over a measured time interval and then weighing the iron powder. During each solids flow rate measurement, the iron particle velocity at the wall of the clear PVC downcomer was measured by timing a particle as it passed between two marks, 2 feet apart, on the wall of the downcomer.

Before each run 30 data points, at a rate of 1 point/second, of the probe background (i.e., output signal from the READ coil when there is no solid flow) were collected and averaged over time. The consistent background data between the runs were then averaged over the number of runs taken in one solids flow direction.

Each run consisted of collecting 30 data points, at a rate of 1 data point/second. This data was then averaged over time. The average background signal was then subtracted from the average flow signal of each run to give the "actual" flow signal. Table 2.2 contains the results for 14 runs at different downward solids flow and the corresponding averaged output signals. Table 2.3 contains the results for 10 runs of the simulated upward solids flow. Figure 2.29 shows the actual READ coil flow signal versus iron powder mass flux in the downcomer of the L-valve. The inconsistent points at the low mass fluxes of Figure 2.29 are caused by the unsteady flow behavior of the L-valve at low solids velocity. Below a velocity of 0.25 ft/sec, which corresponds to a mass flux of  $50 \text{ lb}_m/\text{ft}^2 \cdot \text{sec}$ , solids tend to flow faster but unsteadily in the middle section of the downcomer than near the walls. If points below  $50 \text{ lb}_m/\text{ft}^2 \cdot \text{sec}$  are ignored, a linear regression fit for the rest of the points yields,

$$\begin{array}{lll} \text{READ coil output signal} = (1.426) \text{ Iron Powder Mass Flux} \\ \text{"Computer Data Units"} & \text{"lb}_m/\text{ft}^2 \cdot \text{sec"} & (12) \end{array}$$

with a correlation coefficient of 0.989.

Table 2.2. Average output signal from a magnetic solid mass flow meter probe for different downward mass flux of solid in the downcomer of the L-valve.

Probe Average Background = -70.20 "Computer Data Units"\*

Run No.	Iron Powder Mass Flux $\text{lb}_m/\text{ft}^2 \cdot \text{sec}$	Average Read Coil Output Signal "Computer Data Units"	Standard Deviation of Output Signal	Average Output Signal - Average Background Signal "Computer Data Units"
1	0.00	- 70.20 (background)	2.85	0.00
2	- 34.40	-147.70	44.10	- 77.50
3	- 41.20	-152.94	36.60	- 82.74
4	- 68.67	-156.70	22.81	- 86.50
5	-123.44	-238.20	30.15	-168.00
6	-146.33	-286.44	21.96	-216.24
7	- 82.40	-197.40	35.00	-127.20
8	- 68.70	-171.74	32.96	-101.54
9	- 51.50	-147.27	29.45	- 77.07
10	-144.20	-280.04	25.91	-209.84
11	- 80.40	-165.74	28.79	- 95.54
12	- 68.67	-160.30	28.76	- 90.10
13	- 68.60	-165.80	33.77	- 95.60
14	- 51.00	-136.97	30.20	- 66.77

\* Data acquisition has been done with the minicomputer of the Chemical Engineering Department of Oregon State University (see next chapter).

1 volt = 200 "Computer Data Units"

Table 2.3. Average output signal from a magnetic solid mass flow meter probe for different simulated upward mass flux of solid in the downcomer of the L-valve.

Probe Average Background = 65.60 "Computer Data Units"

Run No.	Iron Powder Mass Flux $\text{lb}_m/\text{ft}^2\cdot\text{sec}$	Average Read Coil Output Signal "Computer Data Units"	Standard Deviation of Output Signal	Average Output Signal - Average Background Signal "Computer Data Units"
1	0.00	65.50 (background)	3.23	0.00
2	42.75	168.39	38.59	102.89
3	48.47	156.11	26.98	90.61
4	103.00	217.42	30.79	151.92
5	74.91	171.31	34.88	105.81
6	135.22	254.42	30.10	188.92
7	140.37	274.36	25.73	208.86
8	117.71	230.39	22.08	164.89
9	50.50	140.50	27.66	75.00
10	61.80	145.29	26.05	79.79

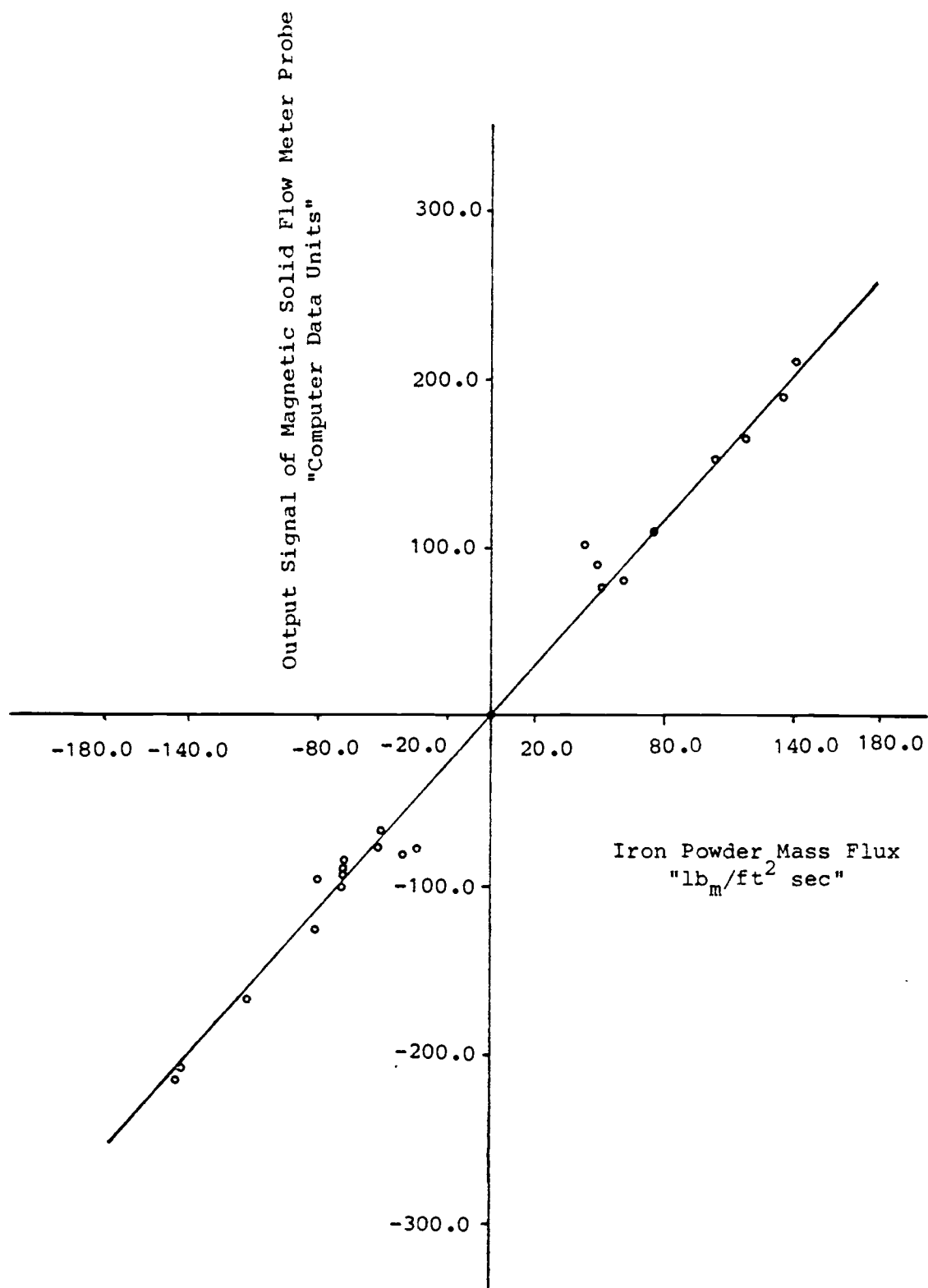


Figure 2.29. Output signal of a magnetic solid flow meter probe vs. iron powder mass flux in L-valve.



### 3. FLUIDIZED BED TEST FACILITY

The fluidized bed experimental facility used for solids movement studies is shown in Figure 3.1. The facility consists of the following systems:

1. The fluidized bed and bed media
2. Air supply systems
3. The probes

These systems plus a data acquisition system are described in this chapter.

#### A. FLUIDIZED BED AND BED MEDIA

##### Fluidized Bed

Experimental measurements of solid mass flow in a fluidized bed were conducted in an 18 in. x 18 in. vessel. The vessel was made of 1 in. thick Plexiglas panels reinforced by steel grids. The front and back panels can be opened to allow the insertion of the dummy heat exchange tube array.

A perforated "sandwich" design plate (Figure 3.2) was used as the gas distributor. The plate consisted of two 1/4" thick PVC plates with a nylon screen (No. 200 Tyler Mesh) between them<sup>4</sup>. The plates had 7/32" diameter holes placed in a triangular pitch. The ratio of the open area of the distributor plate to its total area was 3 percent. The pressure drop across the distributor plate was high enough to achieve

---

<sup>4</sup>It was necessary to use a nonmagnetic plate material due to the proximity of the plate to the bottom probes.

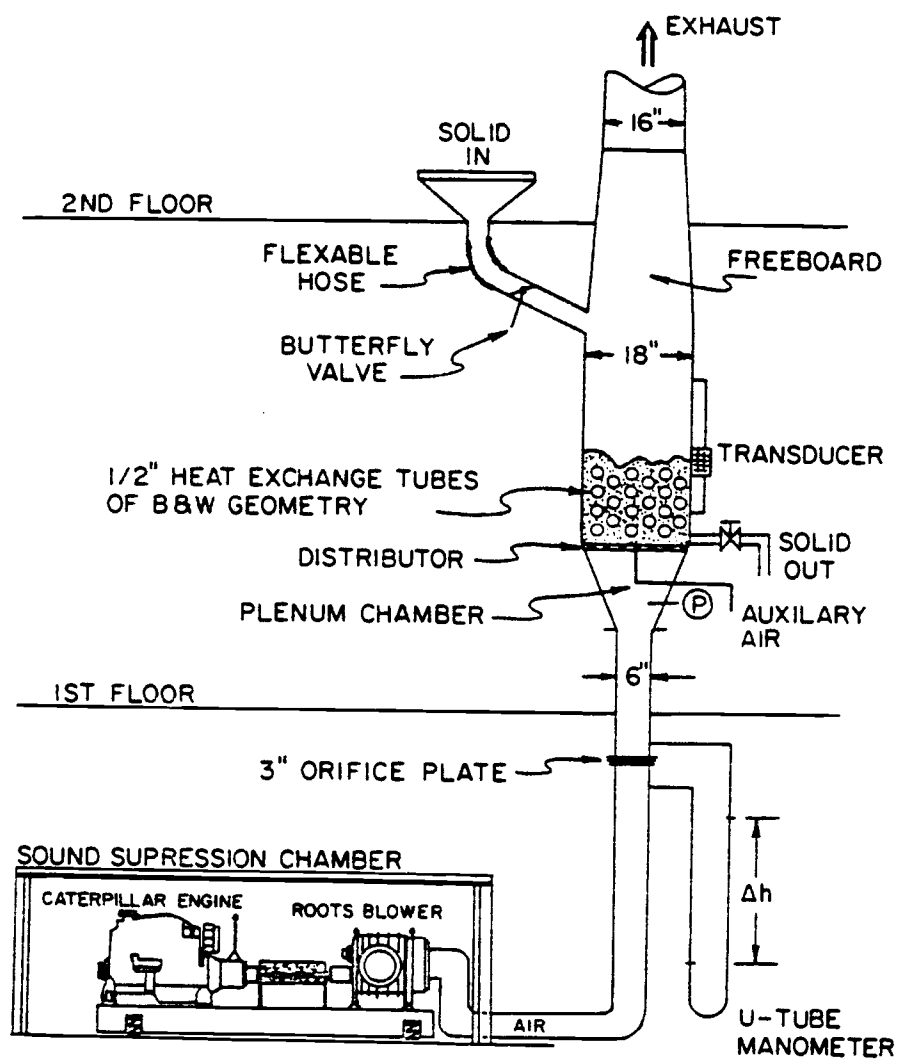


Figure 3.1. A schematic diagram of the 18" x 18" scaled fluidized bed and related facility.

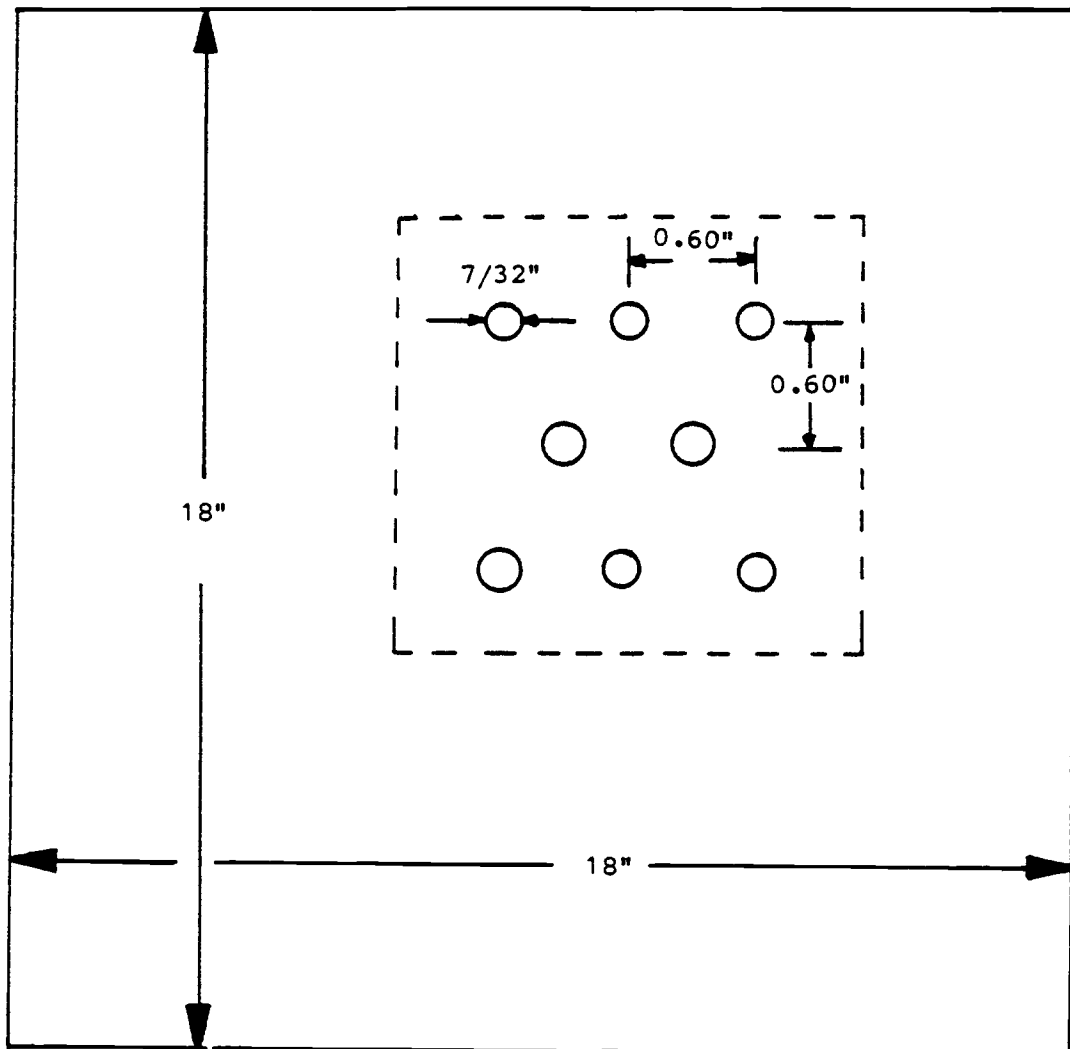


Figure 3.2. The configuration of the distributor plate.

uniform gas flow and, thereby, avoid channeling. The ratio of the pressure drop across the distributor to that across the bed was approximately 30 percent. The bed was equipped with numerous pressure taps connected to the pressure measuring module.

All of the experimental solid flow measurements in the bed were made with one configuration of dummy heat transfer tubes. The tube array was a Plexiglas frame holding 1/2-inch, horizontal, fiberglass tubes. The distance between the distributor plate and the lowest row of tubes was set at 1-1/2 inches. The basic arrangements and dimensions of the tubes inside the bed are given in Figure 3.4.

Solid-particle feed into the fluidized bed was simulated by auxiliary air flowing through a 1-inch i.d. pipe placed at the center of the distributor plate. A 3-inch Plexiglas disk, similar to the one used in the Babcock and Wilcox 6' x 6' hot fluidized bed, was centered above this feed port and immediately underneath the tube array. The purpose of the disk was to enhance the dispersion of the solid particles in the vicinity of the solid feed port. The disk was installed in such a way that it could be easily inserted into or removed from the fluidized bed.

#### Bed Media

The bed media used in this study was iron powder with a surface mean particle diameter of 0.80 mm (0.03 in.), a density of  $6200 \text{ kg/m}^3$  ( $387 \text{ lb/ft}^3$ ) and a minimum fluidization velocity,  $U_{mf}$ , of 2.65 ft/sec. The mean surface particle diameter was determined from sieve analysis and the following formula (26)

$$d_p = \frac{1}{\sum (x_i / d_{pi})} ,$$

where  $x_i$  is the mass fraction of material in size interval  $i$  and  $d_{pi}$  is the average diameter of that size interval.

The density of the iron particles was evaluated from volumetric measurements using water displacement. The height of the slumped bed was maintained at 12 in. above the distributor plate in all of the experiments. The minimum fluidizing velocity was determined by measuring the pressure drop across the bed as a function of superficial gas velocity. These data are shown in Figure 3.3. The experimental value for minimum fluidization was checked against the theoretical equation given by Wen and Yu (27). Excellent agreement was found.

The choice of the bed material was dictated by two important conditions: first, the material had to be magnetizable to be compatible with the magnetic flow meter probes; second, it had to be of such density and size to meet the scale-up criteria of an atmospheric fluidized bed combustor which normally operates at 1550°F with average solid particle density of 160 lb<sub>m</sub>/ft<sup>3</sup> and a surface average particle diameter of 2 mm.<sup>5</sup>

## B. AIR SUPPLY SYSTEMS

The main air needed for fluidization was supplied by a Roots Blower Model 1228. The maximum output from the blower was 8000 cfm at 7.5 psi. The blower was powered by a 325 hp diesel engine (Caterpillar Model 3406T). The blower and engine were located in a soundproof room.

<sup>5</sup> For more details of fluidized bed combustor hydrodynamics, see Ref. (28).

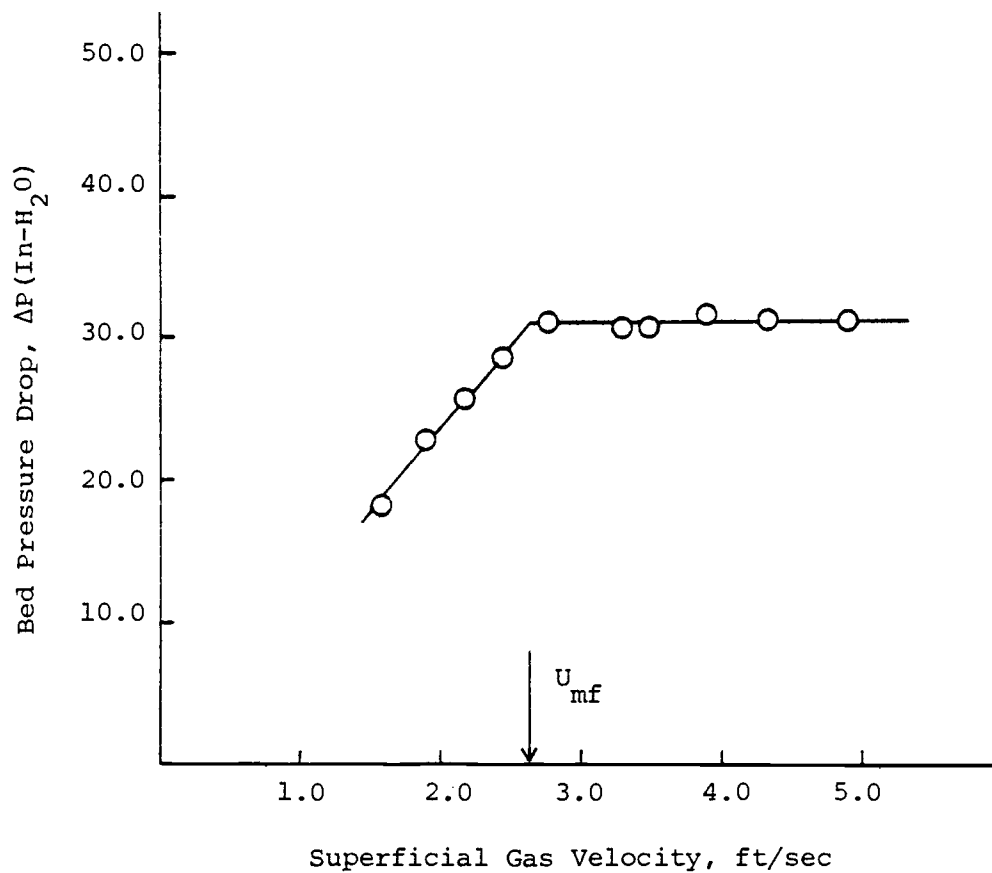


Figure 3.3. Bed pressure drop vs. superficial gas velocity.

The air was directed into a duct system which supplied air to the entire fluidization facility in the Chemical Engineering building. Air flow through the fluidized bed was measured by a previously calibrated orifice flow meter located upstream of the main test facility.

The auxiliary air, needed to simulate solid-particles feed into the fluidized bed, was supplied by a smaller blower powered by a 15 hp electrical motor. Air flow through the solid feed port was measured by a calibrated rotameter.

The fine particles elutriated from the bed were collected by four cyclones. The collected material, however, was not recycled into the bed. All experiments were conducted at atmospheric pressure.

### C. THE PROBES

Fourteen mass-flow probes, identical to that presented in Chapter 2 (refer to Figures 2.19 to 2.22), were used to monitor and measure the magnetic solids movement within the fluidized bed. The arrangement of the tubes and the location of the instrumented tubes (probes) within the array is shown in Figure 3.4. The coils of each of these instrumented tubes were located in the middle section of the tubes.

Each of these probes was calibrated individually by the procedure described in section 2-D. Figure 3.5 shows the calibration points for each of the fourteen probes and their position relative to the smoothed calibration line established in Chapter 2. (Figure 2.29). From the figure it can be seen that all the probes were consistent and gave similar measurements.





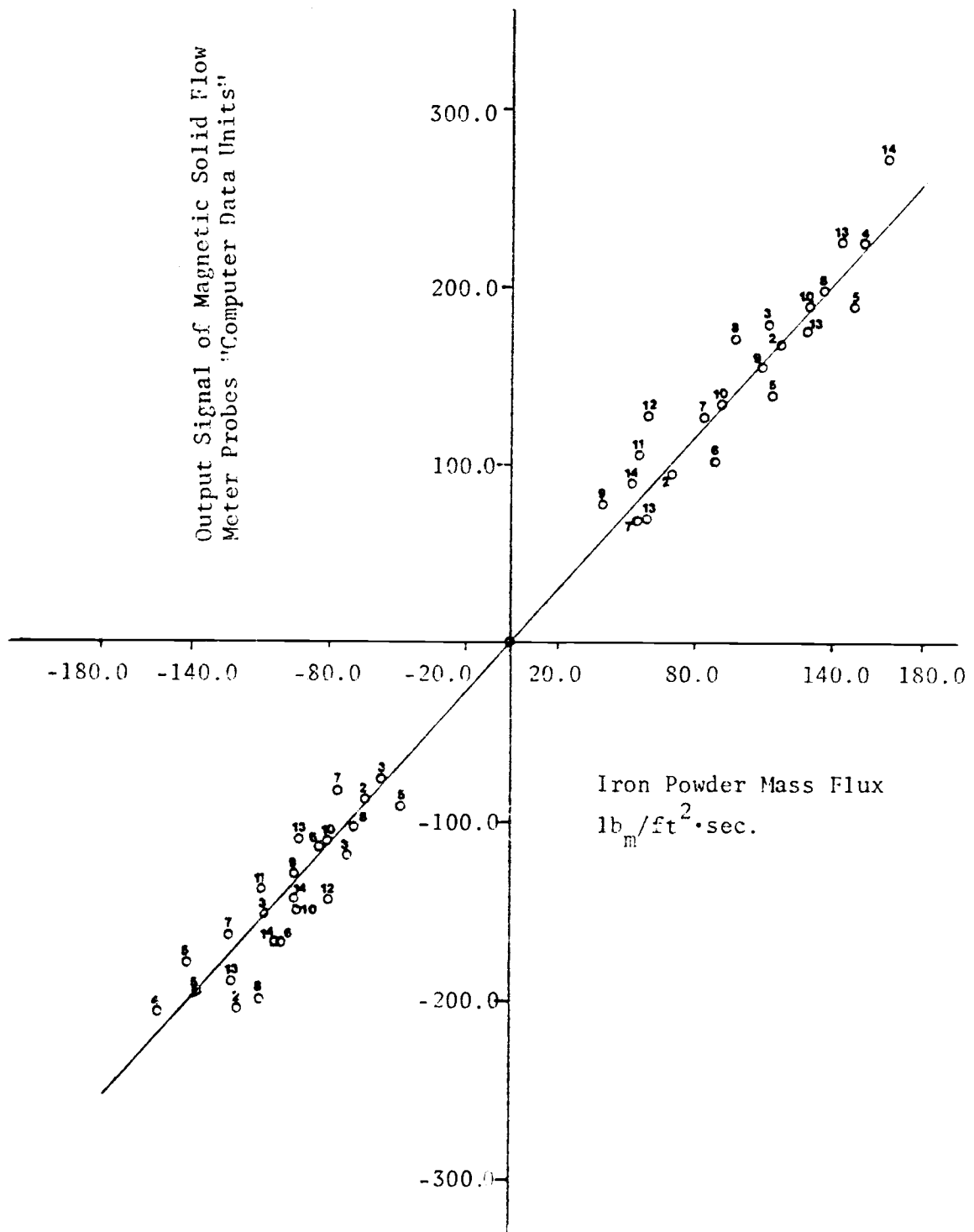


Figure 3.5. Output signal from 14 identical magnetic solid flow probes vs. iron powder mass flux in L-valve.

Two identical channels, each consisting of a WRITE-coil drive circuit and a READ-coil amplification circuit (refer to Figures 2.20, 2.21, and 2.22), were calibrated against each other. These two channels were used to operate two probes simultaneously in all the experimental measurements. The WRITE coils of the operated probes were connected to the WRITE coil drive circuits by 12 gage wires and Amphenol connector placed at the protruding ends of the instrumented tubes. The READ coils and its associated "REED" relays were connected back to the READ coil amplification circuits by a 22 gage individually shielded "BELFOIL" instrumentation cable. The output of the READ coil amplification system was connected to the data acquisition system.

#### D. DATA ACQUISITION SYSTEM

The analog signals from the READ-coil amplification system was sent through the main electronic console to the real-time interface of a Data General 840 Nova minicomputer located in the Chemical Engineering Department. Figure 3.6 shows the block diagram of the computer facility. The NOVA 840 system was used for all data collection, storage, and for most of the data processing. A CYBER computer was used for the development of the more complicated software and for the lengthier calculations and computer graphics.

Oregon State University  
Chemical Engineering Department  
Real-Time Computer Laboratory

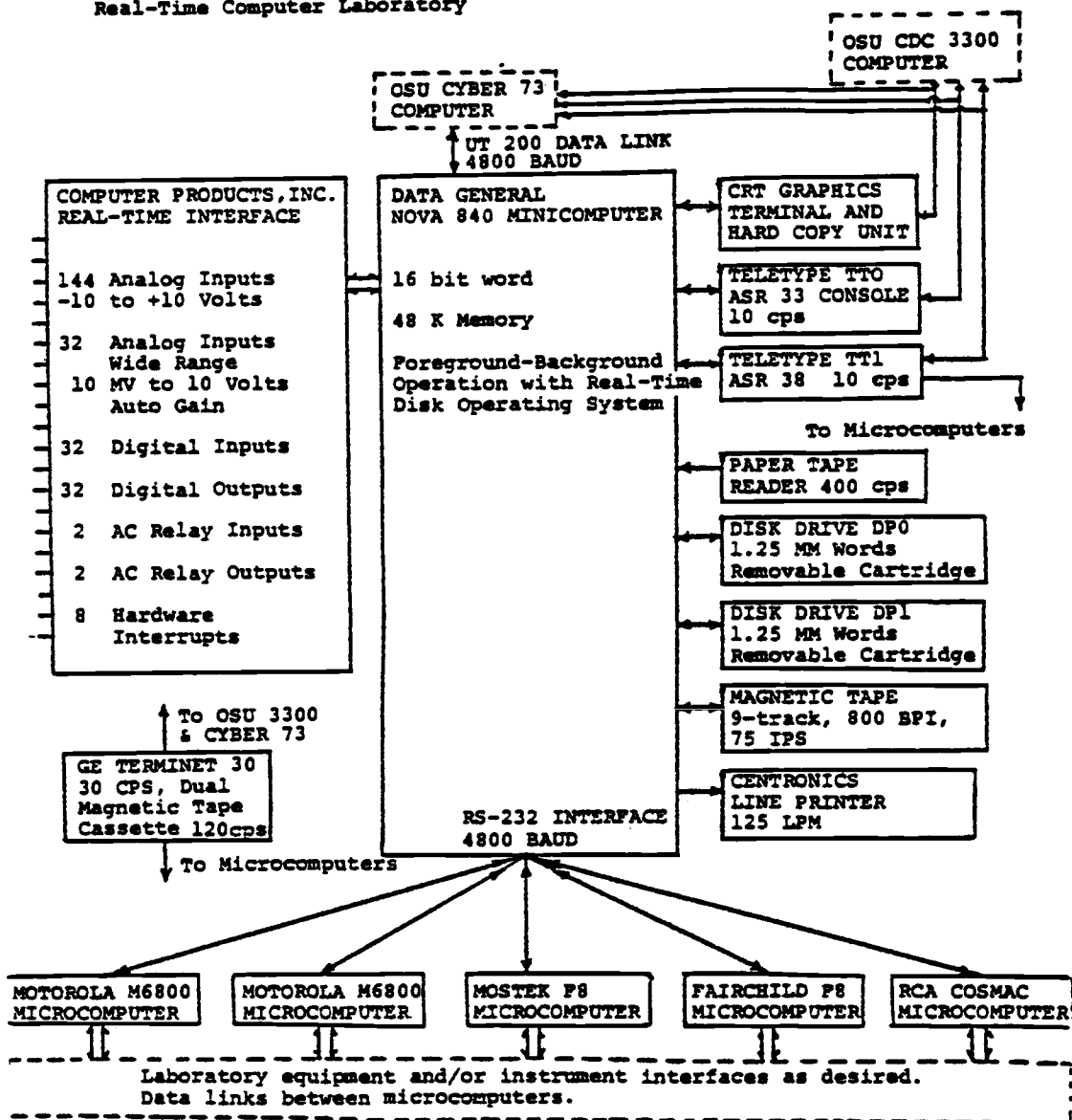


Figure 3.6 Block diagram of the Chemical Engineering Department minicomputer facility.

#### 4. SOLID PARTICLES MOVEMENT IN A FLUIDIZED BED;

##### EXPERIMENTAL RESULTS

###### A. INTRODUCTION

The objective of this experimental study was threefold: a) to study the general mass flow and circulation pattern of the solids in a fluidized bed, b) to study the solids mass flow pattern in the vicinity of a simulated solid feed port, and c) to investigate whether desired solid circulation patterns in the bed can be created by a combination of unequally spaced tubes and uneven gas distribution.

For the first part of this experimental study, the fourteen probes (refer to Figure 3.4) were used to measure the vertical and horizontal components of the mass flow of the solid particles in the immediate vicinity of each location. For the latter two parts of the study, only the bottom probes (probes No. 11, 12, 13, and 14) were used to measure the solids mass flows in their vicinities.

All the probes were installed in such a way that upward flow of solid particles induced a positive signal in the READ coils of the probes, while downward flow induced a negative signal. Horizontal flow measurements were obtained by rotating the probes 90 degrees from their initial position (see Figure 4.1).

Before any experimental data was collected, the background of each of the fourteen probes in each of the two measurement positions was established. This was the signal induced in the READ coils of the probes due to the presence of stationary iron particles around the probes.

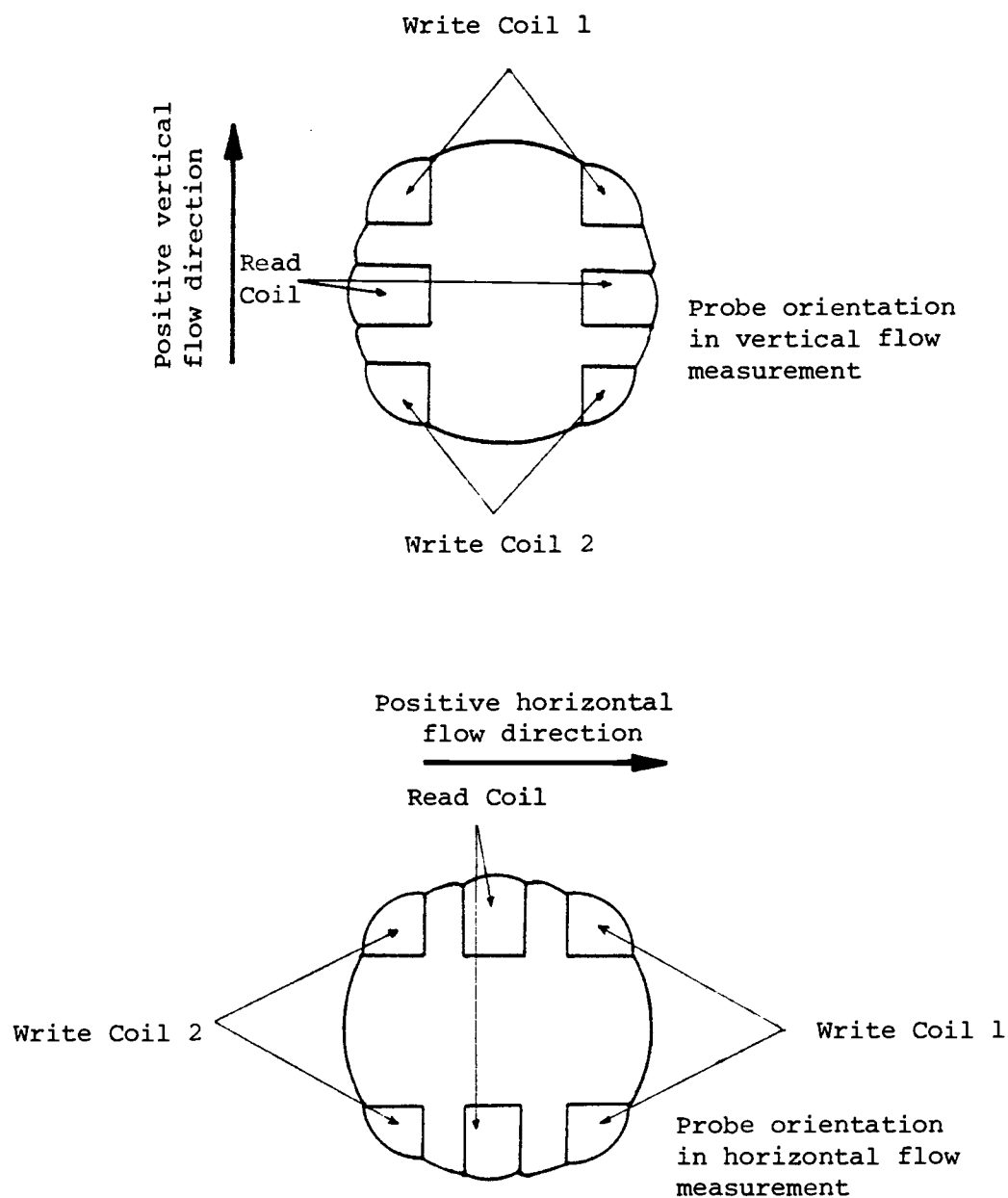


Figure 4.1. Probe orientation in vertical and in horizontal solid flow measurement.

One hundred data points at a rate of 1 data point per second were collected with each probe in each measurement position while the bed was slumped. Figure 4.2 shows a typical plot of this background data for one of the probes when the probe was in a vertical flow measurement position and a horizontal flow measurement position. Of course, if a probe was rotated  $180^\circ$  from its initial position, the same background signal would be obtained but with an opposite polarity. The mean and variance of each probe background signals were then extracted from the collected data.

#### B. EXPERIMENTAL DATA

As has been mentioned before, only two channels were made available to operate two probes simultaneously. Unfortunately, vertical and horizontal solid flow measurements could not be made simultaneously at one location; therefore in each set of experiments, two probes at a time were set to measure the vertical solid flow at their locations until the outputs of all of the probes used in that experiment were recorded. Similar runs under the same set of experimental conditions were then made with the probes set to measure the horizontal component of the solid flow.

Four sets of experiments were conducted in this study. A summary of the experimental conditions investigated is given in Table 4.1. The first two experiments, besides providing data on general solid flow patterns in the bed, can be used as reference conditions for the latter two experiments. In the third experiment, the bottom row of probes was used to study the solid particles flow at a horizontal plane near the solids

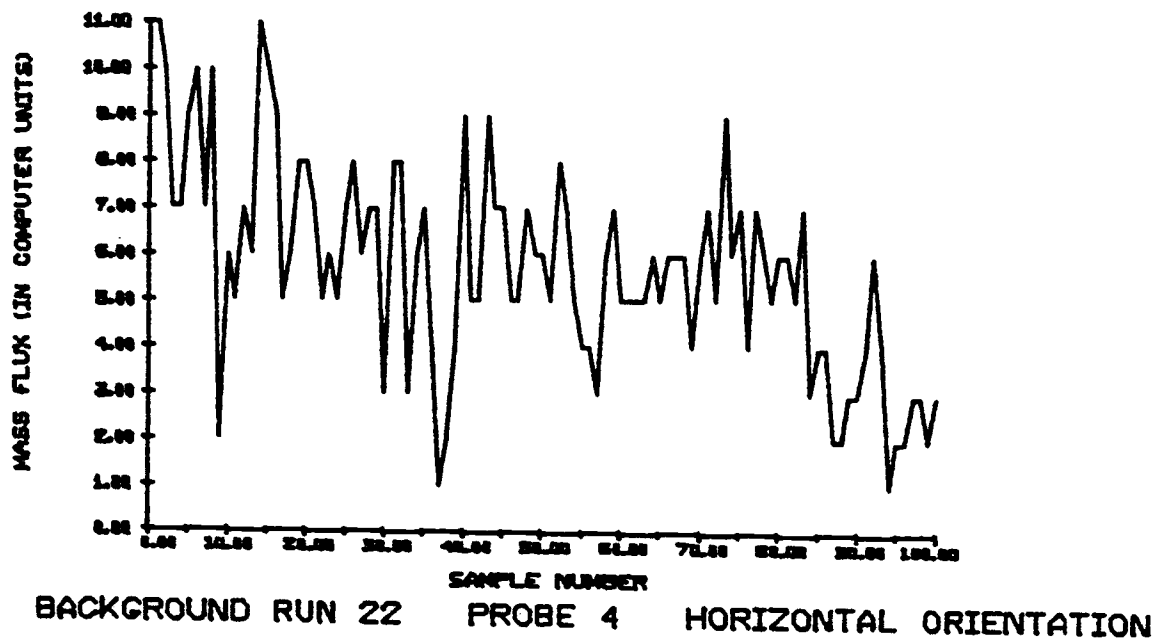
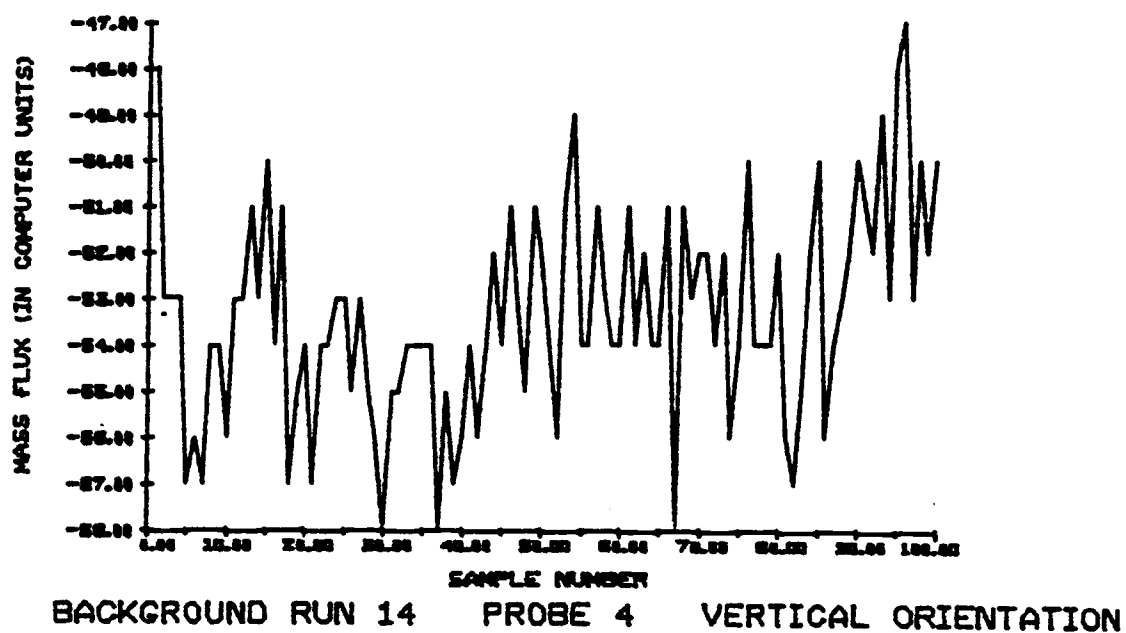


Figure 4.2. Typical plot of the background signals for one of the 14 magnetic solid flow meter probes.

TABLE 4.1 Summary of Experimental Conditions for Solid Particles Movement Experiments.

Experi- ment No.	Objective of experiment	Probes used	Auxiliary air ratio of total air volumetric flow	$U_f$ ft/sec	Circular Disk Placed above Auxiliary air	Tube Array	Distributor Plate
1	To study the general circu- lation pattern of the solids	All 14	0%	3.25	No	See fig. 3.5	See fig. 3.3
2	"	All 14	0%	4.5	Yes	"	"
3	To study solid flow behavior near solid feed port.	Bottom row (11, 12,13, and 14)	10%	4.5	Yes	"	"
4	To study some means of enhancing solid flow near a solid feed port	"	0%	4.5	Yes	See fig. 4.3	Same as fig. 3.3 but with every other row of holes on one side of the plate sealed.



feed port. Solid particle feed was simulated by auxiliary air flowing through the feed port at  $1.0 \text{ ft}^3/\text{sec}$ . The auxiliary air made up about 10 percent of the total air flowing through the bed. The fourth experiment was an attempt to determine if solid circulation near the bottom of the bed and therefore near the solid feed port could be enhanced by using a combination of unequally spaced tube patterns and uneven gas distribution. The tube configuration used here consisted of a closely spaced tube array on one side of the bed and a loosely spaced array on the other (see Figure 4.3). Uneven gas distribution was obtained by sealing every other row of holes in the distributor plate on the widely spaced tube array side of the bed, thus reducing the amount of air flowing through that side of the bed and increasing it on the other.

In all these experiments, each probe used was sampled 1000 times in each directional solid flow measurement at a rate of 1 data point per second. Figure 4.4 shows a representative plot of parts of the mass flux vs. time raw data collected using probe number 5 in test run number 23.

### Histogram Plots

Because plots, such as shown in Figure 4.4, of all the raw data collected would take so much space, and since very little information can be gained directly from such plots, they are not included here. However, more information can be readily deduced from frequency histogram plots of the raw data. Figure 4.5 shows a sample of these plots constructed from the raw data collected using probe number 5 in test run number 23. Histogram plots of the raw data of all the experiments are given in Appendix B. In these plots, the class frequency of every 50-unit class

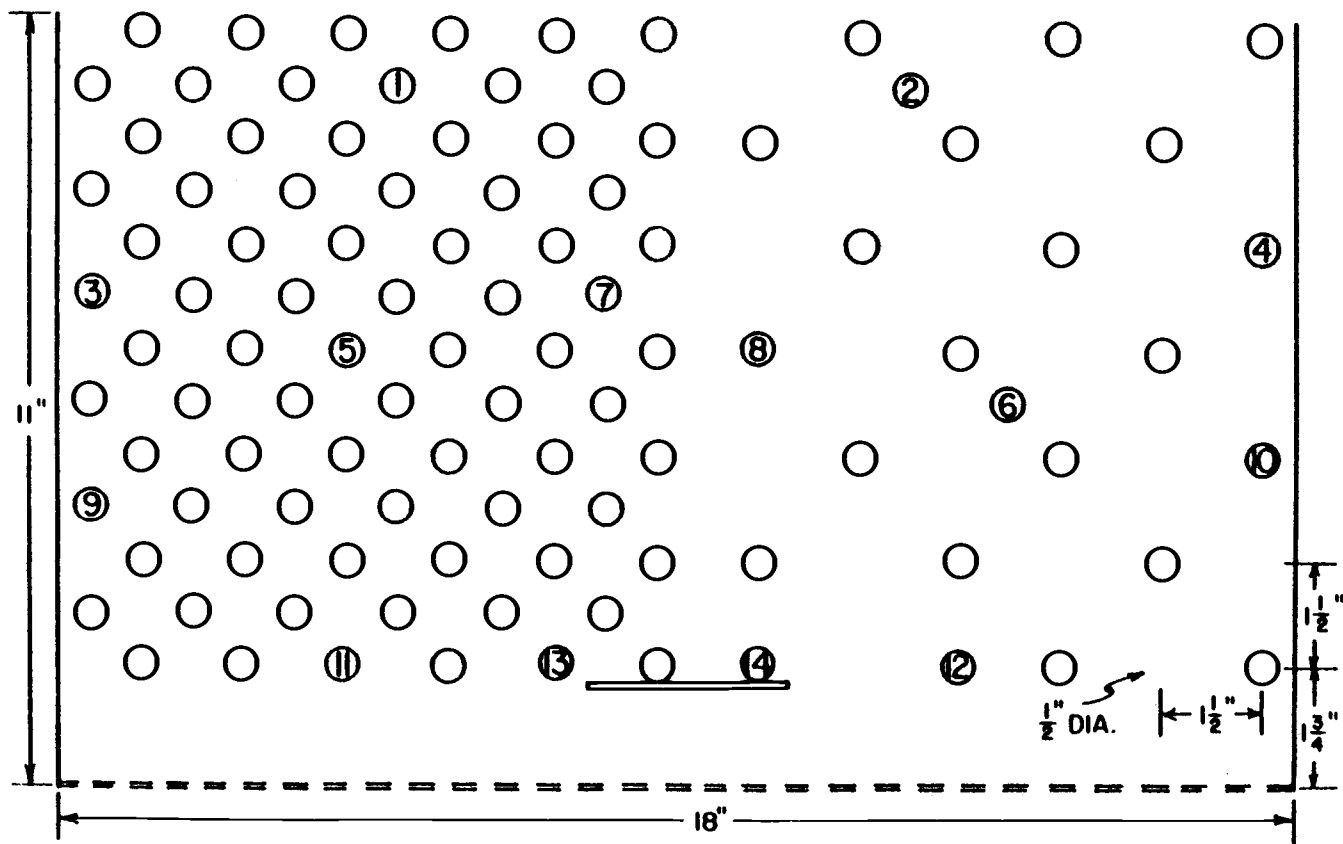


Figure 4.3. The unequally spaced tube pattern used in experiment number 4.

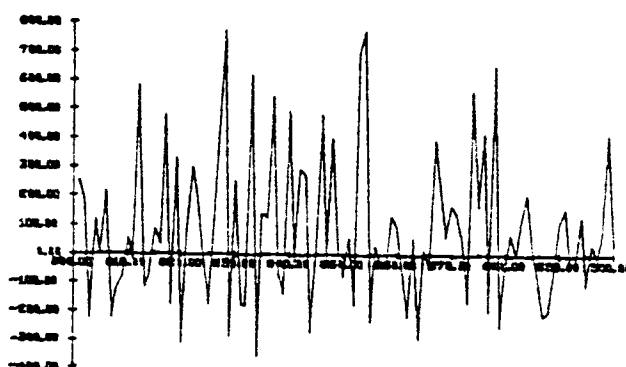
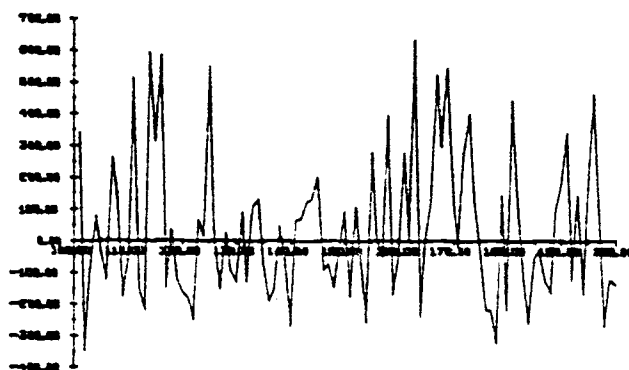
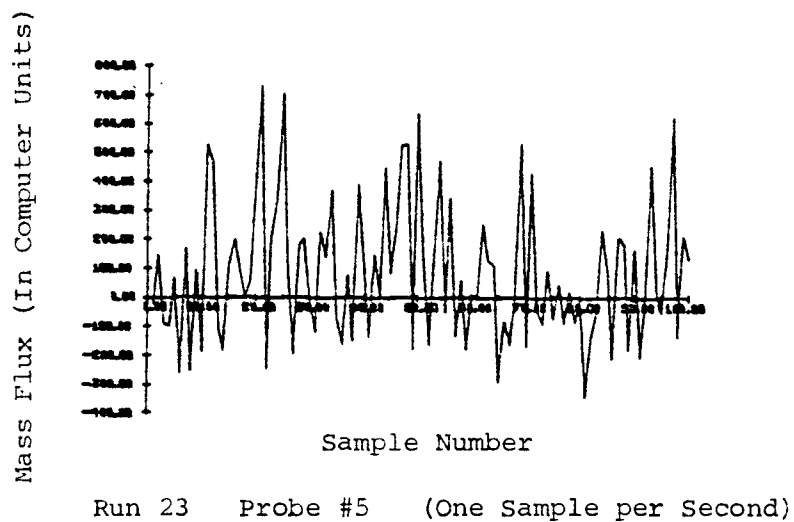


Figure 4.4. A plot of parts of the mass flux raw data collected using one of the 14 probes in one of the test runs.

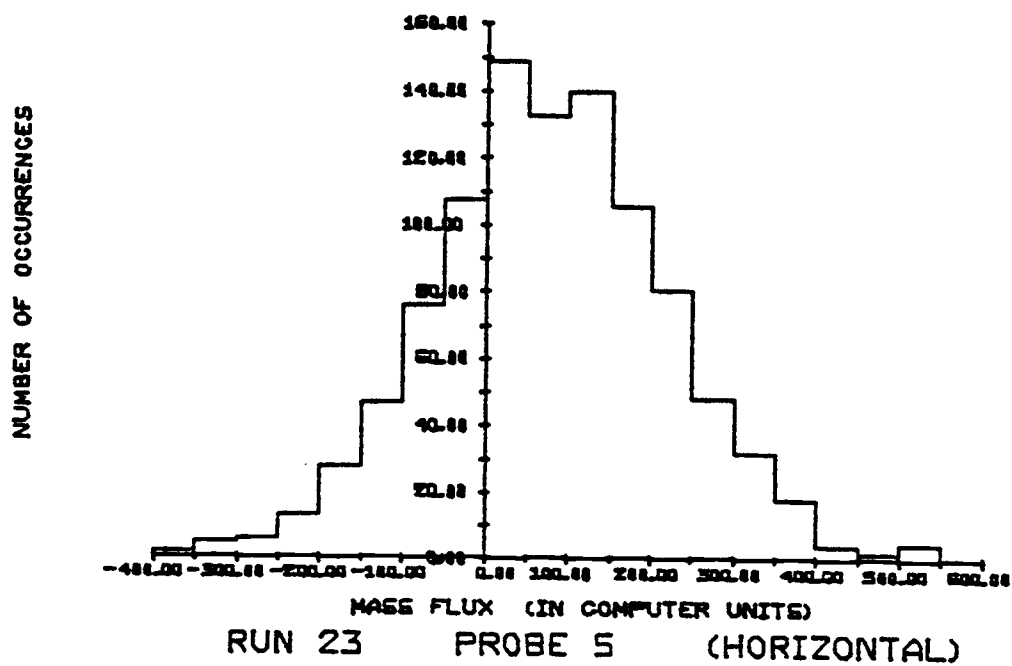
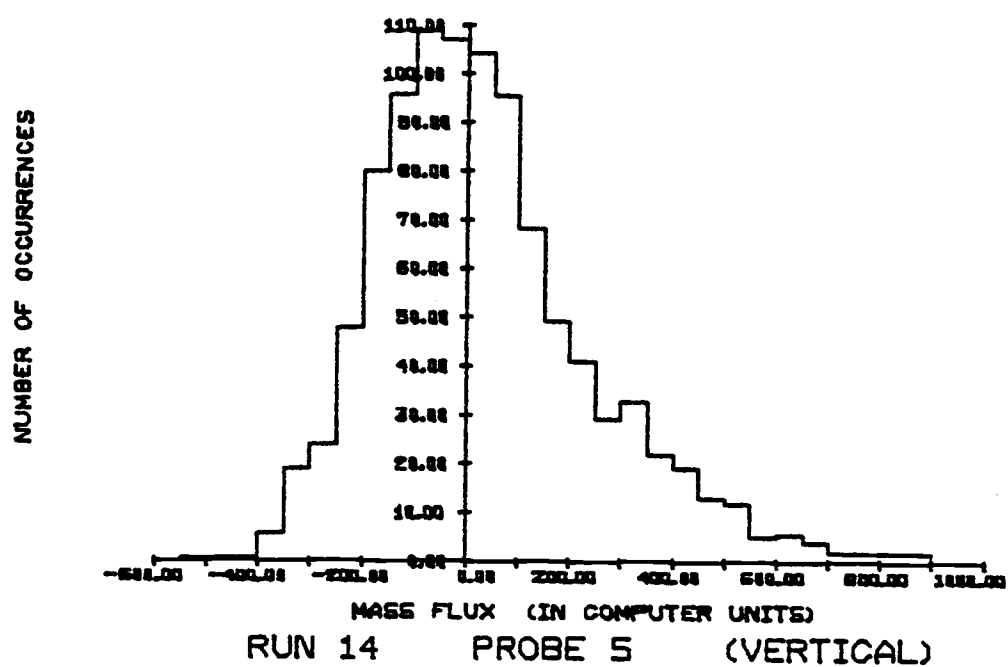


Figure 4.5. A sample histogram plot of mass flux raw data.

interval of mass flux is plotted against the class intervals. Basic statistical information such as the distribution, mode, variance, and the mean of solid-particles local mass fluxes at the various probe locations can be easily deduced from these plots. However, the net solid mass flux at each probe location is of particular interest in this study. This quantity determines the magnitude and direction of the local solid mass flux at each location. Thus, it is possible to map and characterize the solid gross movement inside the bed.

### C. GROSS SOLID CIRCULATION INSIDE THE BED

Figures 4.6, 4.7, 4.8, and 4.9 show the mean and direction of each of the two components of the local solid mass flux measured at the various probe locations in the first, second, third and fourth experiment, respectively. The length of the vector components in these figures is proportional to the mean of the solid mass flux components at the respective probe locations.

From Figures 4.6 and 4.8, a general gross solid circulation pattern inside the bed can be deduced. These figures identify two solid flow regions in the bed.

- a) a freely bubbling region occupying most of the middle section of the bed where solids are transferred upward.
- b) a region adjacent to the bed walls where solid particles travel downward.

Visual observations showed that the region adjacent to the bed walls is seldom disturbed by bubbles.

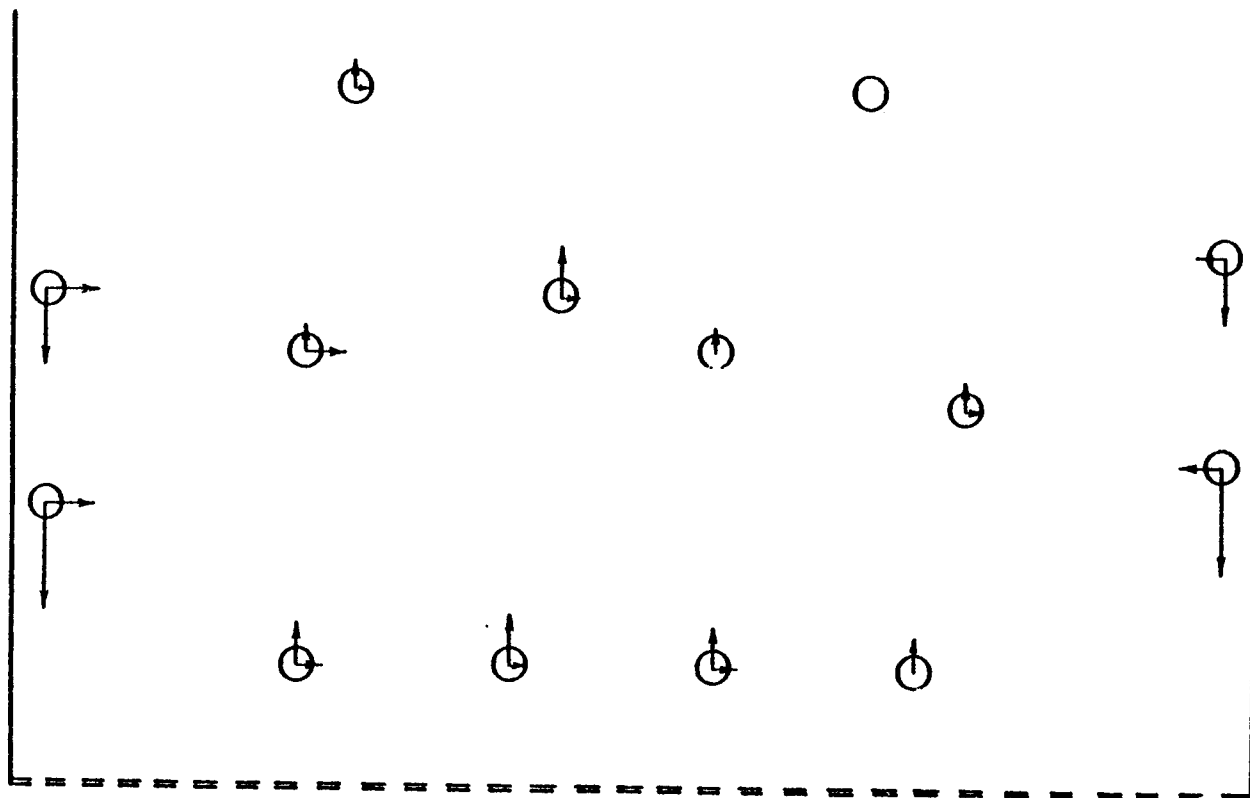


Figure 4.6. The direction of the mean solid mass flux at 14 different probe locations inside the bed for the first experiment. (The vectors length is proportional to the mean solid mass flux.)

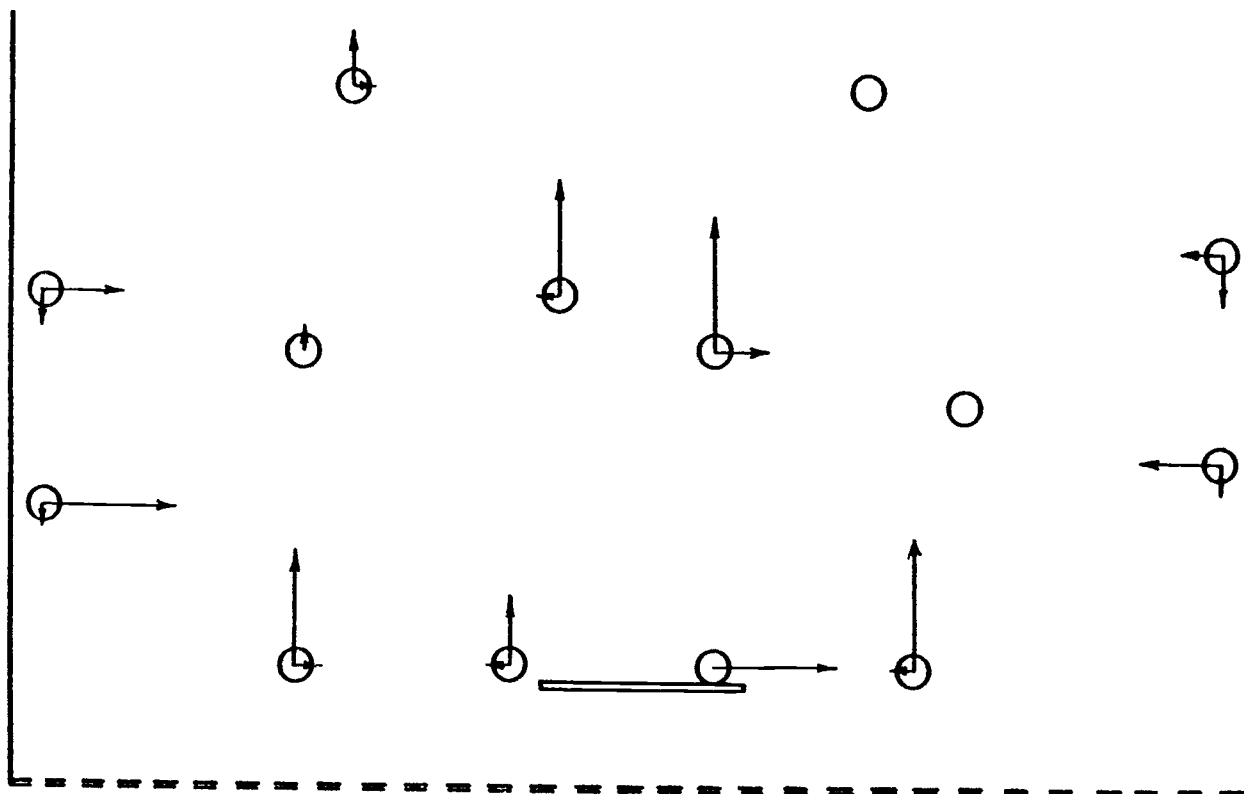


Figure 4.7. The direction of the mean solid mass flux at 14 different probe locations inside the bed for the second experiment. (The vectors length is proportional to the mean solid mass flux.)

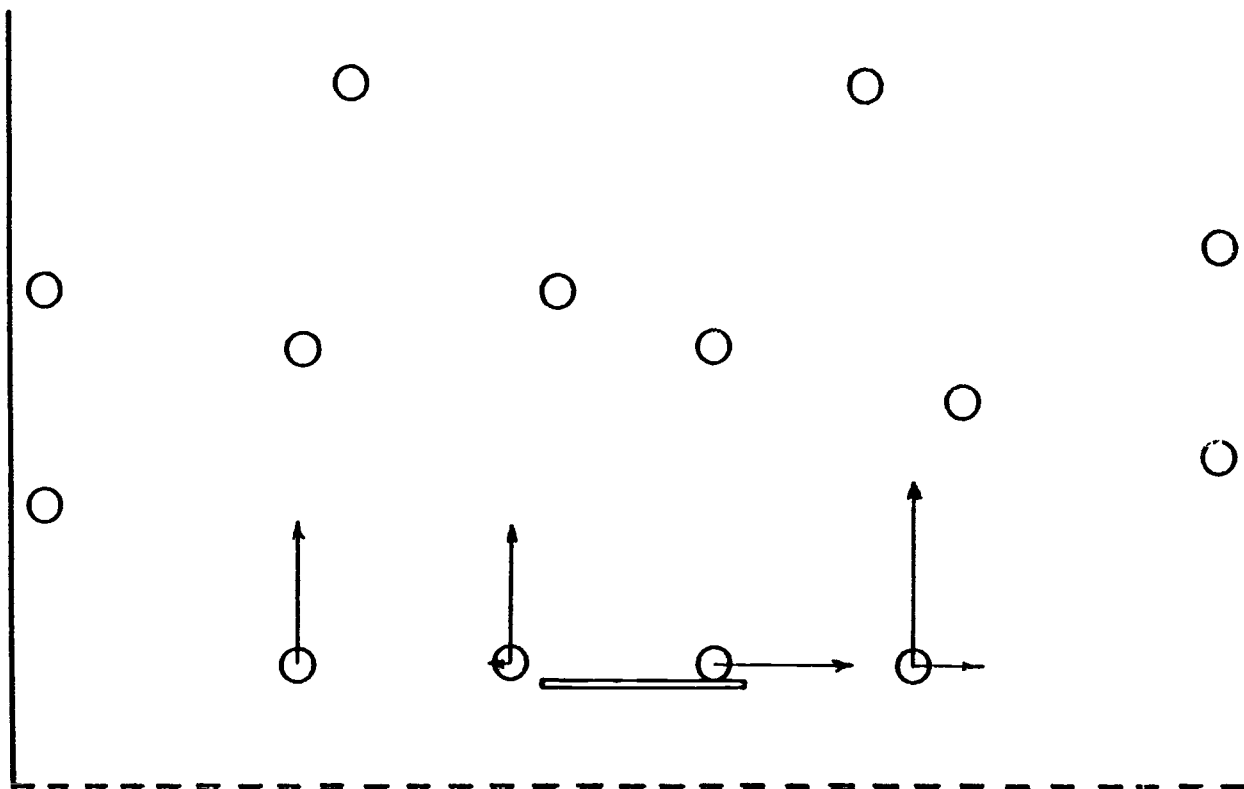


Figure 4.8. The direction of the mean solid mass flux at the four bottom probe locations inside the bed for the third experiment. (The vectors length is proportional to the mean mass flux.)



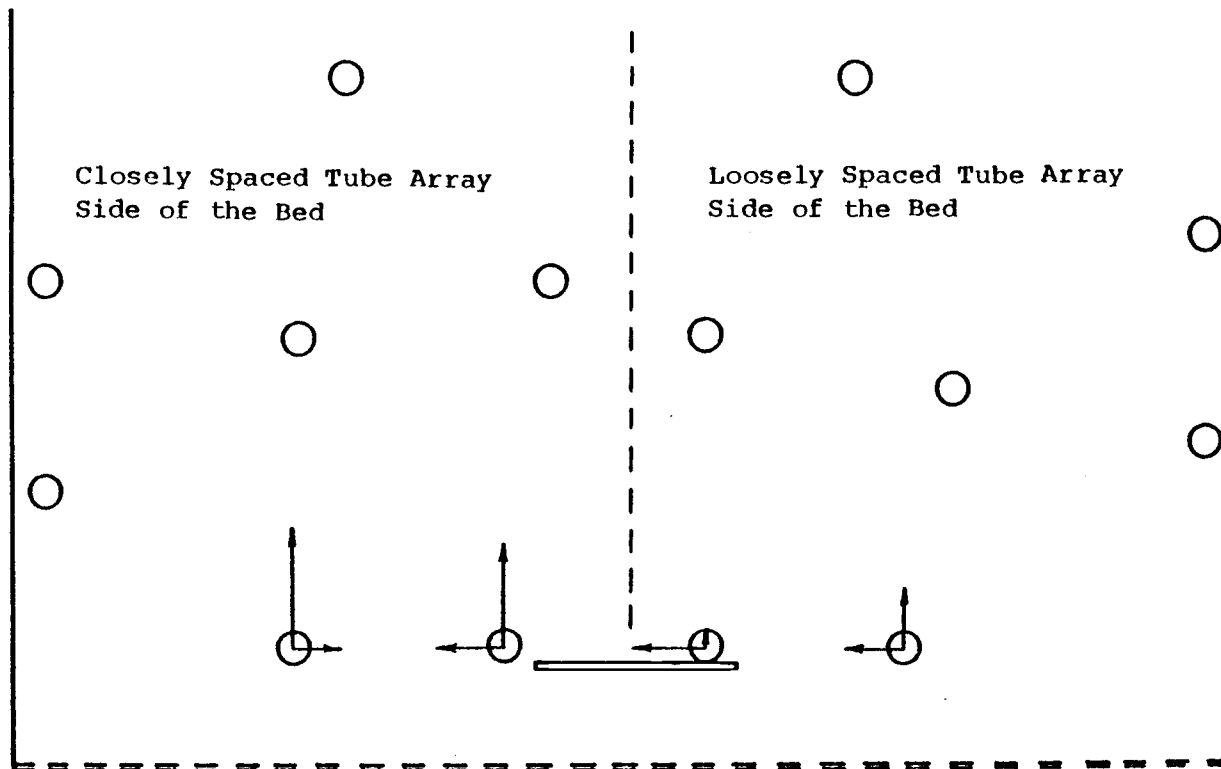


Figure 4.9. The direction of the mean solid mass flux at the four bottom probe locations inside the bed for the fourth experiment.  
(The vectors length is proportional to the mean mass flux.)

These two solid flow regions, and the gross solid flow pattern they indicate inside the bed, have been observed by other investigators also. Cranfield (7) studied individual bubbles injected into an incipiently fluidized bed of large particles and concluded that particles were vertically transported by bubble-induced drift only. In the same study, but in a freely bubbling fluidized bed, Cranfield observed the existence of these two solid flow regions, plus a smaller region just above the distributor plate where solids are randomly mixed by the jetting gas. Cranfield further observed that the descending wall-region material does not mix appreciably into the free bubbling region but re-enters and disperses within it at a level just above the distributor plate. In another study, Marsheck and Gomezplata (19) showed that in a freely bubbling bed particles flow upwards in the regions where bubbles rise and downward elsewhere, and that the bubble flow pattern determines the particles' flow pattern. Merry and Davidson (7) further investigated this phenomenon, and showed that regular circulation of the solid can be induced in a fluidized bed by means of an uneven distribution of the fluidizing fluid supplied to the base. In their experiments, solids particles were forced to flow upwards near the wall region of the bed and downward in the middle section of the bed forming a regular vortex pattern. This was accomplished by supplying more fluid at the base of the bed to the wall region than in the middle of the bed. Thus, bubbles rose in the outer regions of the bed so that there was a central bubble-free region where the solids traveled downwards.

The results of the fourth experiment of this study conducted with an uneven supply of air to the base of the bed and uneven tube arrangement tend to support the findings of these investigators, i.e., the

solid flow pattern inside the bed can be influenced by the distribution of the fluid supply, and hence by the bubbles flow distribution inside the bed. By comparing the net local mass fluxes at the bottom probe locations obtained in the fourth experiment (Figure 4.9) with those obtained in the first experiment (Figure 4.6), it can be seen that not only the lateral particle movement was enhanced at the bottom of the bed in the fourth experiment, but in addition a regular solid flow direction was obtained at that bed level, i.e., solid particles at the bottom of the bed were induced to move from the bubble-poor region into the bubble-rich region of the bed.

Theoretical analysis of the gross solid flow behavior inside the bed which gives rise to a relatively simple mathematical model of this flow behavior for different hydrodynamic conditions is given in the next chapter.

## 5. SOLID PARTICLES CIRCULATION INSIDE A FLUIDIZED BED; DEVELOPMENT OF A THEORETICAL MODEL

### A. INTRODUCTION

An analysis of the motion of fluid and particles in the neighborhood of rising bubbles was first given by Davidson (29). Davidson's model successfully accounted for the movement of both gas and solids in a freely bubbling fluidized bed. In his model, Davidson assumed that the particulate phase behaves as an incompressible fluid that obeys the laws of potential flow and that, relative to the particles, the interstitial fluid velocity is given by Darcy's law. The streamlines followed by the fluid near rising bubbles were derived by Davidson as the central part of his model. However, Davidson's results refer only to the flow outside the rising bubbles. This flow situation represents the so-called fast bubble fluidization regime. A fast bubble regime exists in a fluidized bed in which the gas percolating through the emulsion is moving upward slower than the bubble, or

$$u_f < u_{br}$$

Fast bubbles are characteristic of small particle beds ( $d_p < 0.5$  mm). Row and Partridge (30) have shown that in such beds solids are entrained in the wake (a small turbulent region of solids located immediately underneath a bubble) of the upward rising gas bubbles. The solids are supported under the bubble by upward rising gas. These investigators approximate that the wake of the bubble is 30% of the bubble volume.

Thus, movement of solids results from wake transport, i.e., bubble wake shedding and replenishment, in beds of small particles.

The gas flow theory given by Pyle and Rose (31), describes the gas flow within the rising bubble inside the bed. This flow situation represents the so-called slow bubble fluidization regime. A slow bubble regime is encountered in a bed in which the interstitial velocity of the gas exceeds the rising velocity of the bubble, or

$$u_f > u_{br}$$

Slow bubbles are expected to appear when large particles are fluidized because the interstitial velocity has to be high in order to achieve the fluidization state. Solid movement in this regime has been investigated by Cranfield and Geldart (32), Cranfield (17) and Masson (33). All investigators agree that the main mechanism of particle transport in this regime is by bubble induced drift. In a uniformly fluidized bed, bubbles rise upward through the bed and so particle motion occurs primarily in the upward direction. The net lateral particle displacement induced by a rising bubble is negligible, but considerable lateral displacement of the bed surface material and deposition of underlying material on the surface occurs upon the eruption of bubbles.

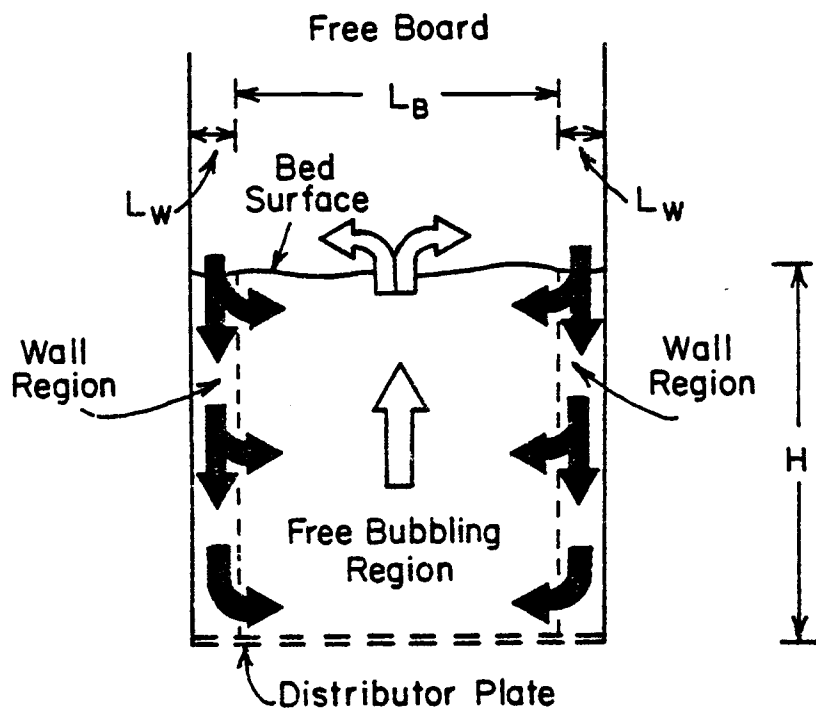
Fitzgerald et al. (34) have developed a criterion, in terms of nondimensional groups, to distinguish between slow and fast bubble fluidization regimes. The criterion is based on experimental observations and theoretical equations and is good for any combination of particle size, density and fluid properties. This criterion was used here to verify that the experiments done in this study are in the slow

bubble regime, and hence the bed expansion correlation developed by Jovanovic (35) for this regime could be used to calculate the average void fraction,  $\epsilon_{av}$  in the bed at a given fluidizing gas velocity. This calculation is given in the next section.

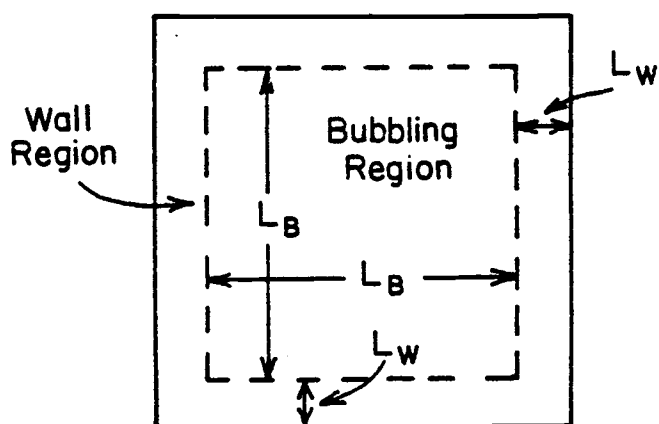
#### B. THE TWO REGION MODEL BED FOR SOLID CIRCULATION

The experimental results on solids movement inside the freely bubbling fluidized bed given in the last chapter along with the results of previous studies by other investigators indicate that under normal operations of the bed, solids tend to follow a preferred track of gross circulation inside the bed. Figure 5.1 illustrates this circulation pattern in which the net solid motion in the bubbling region is in the upward direction. The net lateral movement of solid is not significant in this region. However, considerable lateral displacement of the bed surface material of the region occurs upon the eruption of bubbles at the surface. The descending wall layers, shown in the figure, serve to accommodate most of the blown-up surface material and provide a great proportion of the solid return flow.

To simplify the development of a mathematical model for this solid flow behavior, the bed is visualized as shown in Figure 5.2. In this approach, the four descending wall layers of the bed are lumped into one region interconnected with the upward moving solids of the bubbling region, and solid exchange between the two regions of the model bed is allowed in one dimension only. This approach allows the treatment of a three-dimensional bed by a two-dimensional analysis as will be shown later in this section.

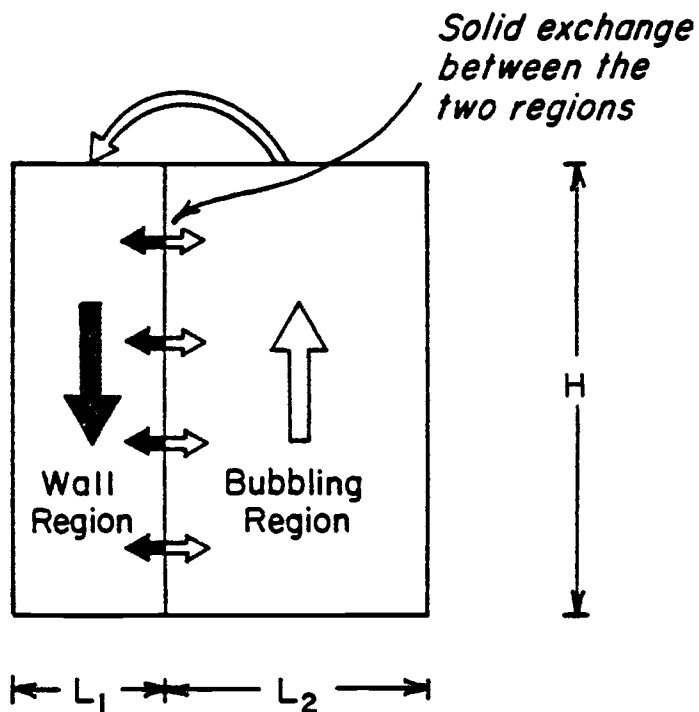


Schematic diagram of a section through the bed showing solid circulation.

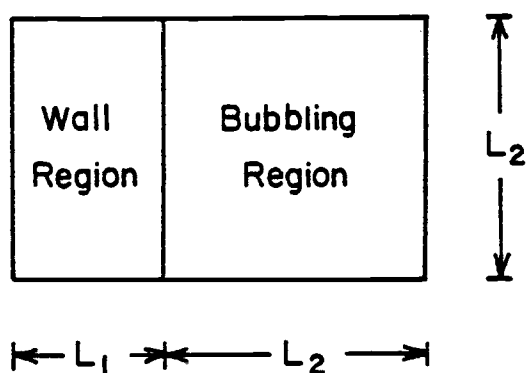


Top view of the bed showing the two solid flowing regions

Figure 5.1. The solid gross circulation pattern inside the bed.



A section through the two region model bed.



Top view of the two region model bed.

Figure 5.2. The two region model bed.



### Assumptions of the Two Region Model Bed

Based on some assumptions about the two region model bed proposed here, a mathematical model of the solid circulation inside a freely bubbling fluidized bed can be derived from a material and momentum balance analysis of the solid flow in each of the two regions of the model. The major assumptions are as follows:

1. The solid particulate phase in each of the two regions of the model behaves as an incompressible fluid of low viscosity. This assumption was verified by Davidson (29) for any particle size fluidized beds. In fact, this fluid-like behavior of the solid phase inside the bed is the reason behind the name for this kind of reactor.
2. Each region has a uniform, constant bulk density. These densities are related to each other through the average bulk density of the bed, at a given fluidizing gas velocity, and an overall mass balance.
3. The void fraction in the wall region is smaller than that in the bubbling region which results in a higher solid bulk density and viscosity in the wall region than that in the bubbling region.
4. The solid flow at any horizontal cross section is uniform within each region, i.e., the flow parameters within each region are dependent only upon the vertical location within that region.
5. Inertia of the fluidizing gas is much smaller than that of the solids, so that its contribution to the momentum

equations of the solid flow can be ignored.

6. The vessel wall shear stresses are ignored.

#### Physical Parameters of the Two Region Model Bed

The average bed void fraction and hence the average bed bulk density, in a given fluidized bed system, can be correlated with the superficial velocity of the fluidizing fluid of the system (see reference 35). For a slow bubble fluidization regime this relation is given by the following equation

$$\frac{\epsilon_{av} - \epsilon_{mf}}{1 - \epsilon_{av}} = \frac{1}{\frac{u_{br}}{u_{mf}} + 2} \frac{u_o - u_{mf}}{u_{mf}} \quad (5-1)$$

The bubble rise velocity in the bed,  $u_{br}$  can be calculated from the equation given by Davies and Taylor (37)

$$u_{br} = 22.25 (d_b)^{.5}, \text{ (in CGS system)}$$

where the bubble diameter,  $d_b$ , can be estimated to be equal to the spacing between the dummy heat transfer tubes inside the bed.

Furthermore, an overall mass balance of the bed material, at a given superficial velocity, offers a simple relationship between the bulk densities of the two regions and this average bulk density of the bed

$$HL_1L_2\rho_s(1 - \epsilon_1) + HL_2^2\rho_s(1 - \epsilon_2) = H(L_1 - L_2)L_2\rho_s(1 - \epsilon_{av})$$

simplifying,

$$L_1 \rho_s (1 - \epsilon_1) + L_2 \rho_s (1 - \epsilon_2) = (L_1 + L_2) \rho_s (1 - \epsilon_{av})$$

or

$$L_1 \rho_1 + L_2 \rho_2 = (L_1 + L_2) \rho_{av} \quad (5-2)$$

The average bed height  $H$ , at a given superficial velocity can be calculated from a mass balance of the bed inventory,

$$H \rho_s (1 - \epsilon_{av}) = H_{mf} \rho_s (1 - \epsilon_{mf})$$

$$H = H_{mf} \frac{1 - \epsilon_{mf}}{1 - \epsilon_{av}} \quad (5-3)$$

The relationship between the dimensions of the two region model and those of the fluidized bed can be obtained by the fact that these systems should have equal cross-sectional area,  $A_t$ . From Figures 5.1 and 5.2 it follows that

$$(L_1 + L_2)L_2 = (L_B + 2L_w)^2 = A_t, \quad (5-4)$$

which gives the following relationship between  $L_1$  and  $L_2$

$$L_1 = \frac{A_t}{L_2} - L_2 \quad (5-5)$$

Furthermore, the bubbling region of the two region model and that of the fluidized bed should have the same cross-sectional area. Thus,

$$L_2 = L_B$$

Substituting in Eq. (5-4), the following relationship between  $L_1$  and  $L_w$  can be obtained

$$L_1 = 4L_w + 4L_w^2/(\sqrt{A_t} - 2L_w)$$

Thus, for a given fluidizing gas superficial velocity,  $\epsilon_{av}$  can be calculated from Eq. (5-1), and the average bed height  $H$  can be calculated from Eq. (5-3). Although values of the physical parameters ( $\rho_1, \rho_2, L_w$ , and  $L_B$ ) could not be directly measured in the bed, for given estimates of  $L_1$  and  $\rho_1$ ,  $L_2$  and  $\rho_2$  can be calculated from Eqs. (5-5) and (5-2), respectively.

### C. MATERIAL AND MOMENTUM BALANCES IN THE TWO REGION MODEL BED

Figure 5.3 shows a fixed control volume in the two region model bed, having unit thickness normal to the paper, over which the following material and momentum balances are made. The origin of the coordinate system shown is at the top surface of the bed and the sign convention is such that solid velocity is positive in the vertical downward direction.

#### Material Balance in the Wall Region

A material balance of the solid flow in the wall region over the control volume shown in Figure 5.3 gives

$$(G_{1y}|_y - G_{1y}|_{y+\Delta y})L_1 + (G_{2x} - G_{1x}) \Delta y = 0$$

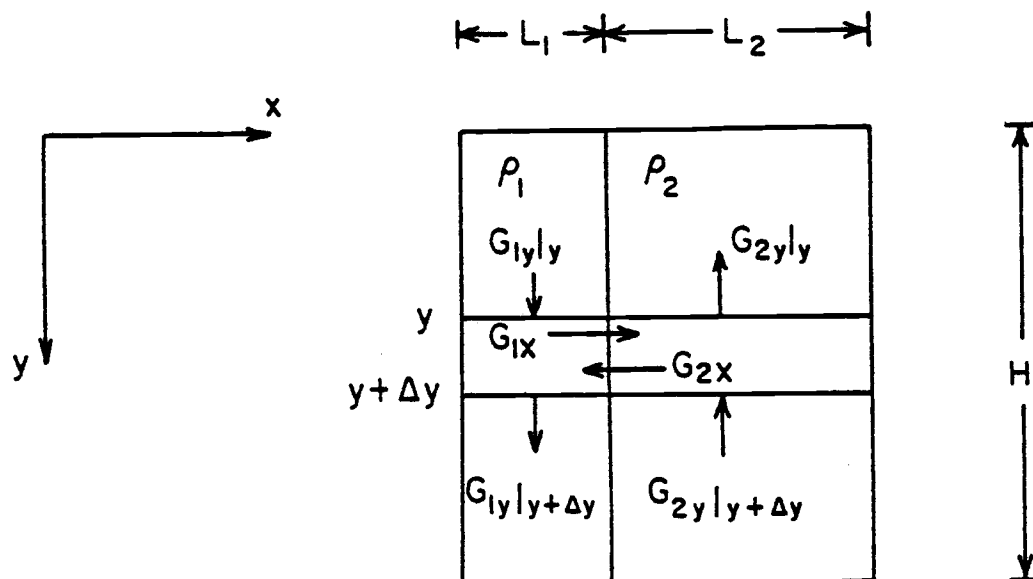


Figure 5.3. Solid mass flux through a fixed differential control volume in the two region model bed.

Dividing by  $\Delta y$  and taking the limit as  $\Delta y$  approaches zero gives the material balance equation in the wall region.

$$\frac{dG_{1y}}{dy} = \frac{1}{L_1} (G_{2x} - G_{1x}) \quad (5-6)$$

#### Material Balance in the Bubbling Region

Similar material balance expressions can be obtained for the solid flow in the bubbling region

$$(G_{2y}|_{y+\Delta y} - G_{2y}|_y)L_2 + (G_{1x} - G_{2x})\Delta y = 0$$

which in turn can be reduced to the following equation

$$\frac{dG_{2y}}{dy} = \frac{1}{L_2} (G_{2x} - G_{1x}) \quad (5-7)$$

Equations (5-6) and (5-7) can be written in terms of the two components of the solid velocities in each region; noting that

$$G_{1y} = \rho_1 V_{1y}, \quad G_{2y} = -\rho_2 V_{2y}, \quad G_{1x} = \rho_1 V_{1x}, \quad \text{and}$$

$$G_{2x} = -\rho_2 V_{2x}$$

substituting in Eq. (5-6) gives

$$\frac{dV_{1y}}{dy} = -\frac{1}{\rho_1 L_1} (\rho_2 V_{2x} + \rho_1 V_{1x}) \quad (5-8)$$

and in Eq. (5-7) gives

$$\frac{dv_{2y}}{dy} = \frac{1}{\rho_2 L_2} (\rho_2 v_{2x} + \rho_1 v_{1x}) \quad (5-9)$$

### X-Component of the Momentum Balance in the Wall Region

Applying the momentum theorem at steady state in the x-direction of the wall region,

$$\begin{aligned} (G_{1y} v_{1x}|_y - G_{1y} v_{1x}|_{y+\Delta y}) L_1 + (-G_{2x} v_{2x} - G_{1x} v_{1x}) \Delta y \\ - (P_1 - P_2) \Delta y = 0 \end{aligned}$$

which can be transformed into the following

$$\frac{d(G_{1y} v_{1x})}{dy} = -\frac{1}{L_1} (G_{2x} v_{2x} + G_{1x} v_{1x}) - \frac{1}{L_1} (P_1 - P_2)$$

Expanding the left hand term gives

$$G_{1y} \frac{dv_{1x}}{dy} + v_{1x} \frac{dG_{1y}}{dy} = -\frac{1}{L_1} (G_{2x} v_{2x} + G_{1x} v_{1x}) - \frac{1}{L_1} (P_1 - P_2)$$

Combining Eq. (5-6) with the above expression and simplifying yields

$$\frac{dv_{1x}}{dy} = -\frac{G_{2x}}{G_{1y} L_1} (v_{1x} + v_{2x}) - \frac{1}{G_{1y} L_1} (P_1 - P_2)$$

Writing the solid mass fluxes in terms of solid velocity components and simplifying gives

$$\frac{dv_{1x}}{dy} = \frac{1}{\rho_1 v_{1y} L_1} [\rho_2 v_{2x} (v_{1x} + v_{2x}) - P_1 + P_2] \quad (5-10)$$

### Y-Component of the Momentum Balance in the Wall Region

Applying the momentum theorem at steady state in the y-direction of the wall region gives

$$\begin{aligned} (G_{1y} V_{1y}|_y - G_{1y} V_{1y}|_{y+\Delta y}) L_1 + (-G_{2x} V_{2y} - G_{1x} V_{1y}) \Delta y \\ + (P_1|_y - P_1|_{y+\Delta y}) L_1 + \rho_1 L_1 g \Delta y = 0 \end{aligned}$$

which yields the following equation

$$\frac{d(G_{1y} V_{1y})}{dy} + \frac{dP_1}{dy} + \frac{1}{L_1} (G_{2x} V_{2y} + G_{1x} V_{1y}) - \rho_1 g = 0$$

Expanding the first term and combining with Eq. (5-6),

$$G_{1y} \frac{dV_{1y}}{dy} + \frac{1}{L_1} (G_{2x} V_{1y} + G_{2x} V_{2y}) + \frac{dP_1}{dy} - \rho_1 g = 0$$

Writing the mass fluxes in terms of velocity components and solving for  $\frac{dP_1}{dy}$  gives

$$\frac{dP_1}{dy} = -\rho_1 V_{1y} \frac{dV_{1y}}{dy} + \frac{\rho_2 V_{2x}}{L_1} (V_{1y} + V_{2y}) + \rho_1 g$$

Combining with Eq. (5-8),

$$\frac{dP_1}{dy} = \frac{V_{1y}}{L_1} (\rho_2 V_{2x} + \rho_1 V_{1x}) + \frac{\rho_2 V_{2x}}{L_1} (V_{1y} + V_{2y}) + \rho_1 g \quad (5-11)$$



### X-Component of the Momentum Balance in the Bubbling Region

Applying the momentum theorem at steady state in the x-direction of the bubbling region,

$$(-G_{2y} V_{2x} \big|_{y+\Delta y} + G_{2y} V_{2x} \big|_y) L_2 + (G_{1x} V_{1x} + G_{2x} V_{2x}) \Delta y + (P_1 - P_2) \Delta y = 0$$

which can be transformed into the following

$$\frac{d(G_{2y} V_{2x})}{dy} = \frac{1}{L_2} (G_{1x} V_{1x} + G_{2x} V_{2x}) + \frac{1}{L_2} (P_1 - P_2)$$

Expanding the left hand term,

$$G_{2y} \frac{dv_{2x}}{dy} + V_{2x} \frac{dG_{2y}}{dy} = \frac{1}{L_2} (G_{1x} V_{1x} + G_{2x} V_{2x}) + \frac{1}{L_2} (P_1 - P_2)$$

Combining with Eq. (5-7)

$$\frac{dv_{2x}}{dy} = \frac{G_{1x}}{G_{2y} L_2} (V_{1x} + V_{2x}) + \frac{1}{G_{2y} L_2} (P_1 - P_2)$$

Writing the solid mass fluxes in terms of solid velocity components and simplifying

$$\frac{dv_{2x}}{dy} = - \frac{1}{\rho_2 V_{2y} L_2} [\rho_1 V_{1x} (V_{1x} + V_{2x}) + P_1 - P_2] \quad (5-12)$$

### Y-Component of the Momentum Balance in the Bubbling Region

Applying the momentum theorem at steady state in the y-direction of the bubbling region,

$$\begin{aligned}
& (-G_{2y} v_{2y}|_{y+\Delta y} + G_{2y} v_{2y}|_y) L_2 + (G_{1x} v_{1y} + G_{2x} v_{2y}) \Delta y \\
& + (P_2|_y - P_2|_{y+\Delta y}) L_2 + \rho_2 L_2 g \Delta y = 0
\end{aligned}$$

which yields the following equation

$$\frac{d(G_{2y} v_{2y})}{dy} + \frac{dP_2}{dy} - \frac{1}{L_2} (G_{1x} v_{1y} + G_{2x} v_{2y}) - \rho_2 g = 0$$

Expanding the first term and combining with Eq. (5-7),

$$G_{2y} \frac{dv_{2y}}{dy} + \frac{dP_2}{dy} - \frac{1}{L_2} (G_{1x} v_{2y} + G_{1x} v_{1y}) - \rho_2 g = 0$$

Writing the mass flux components in terms of velocity components and solving for  $\frac{dP_2}{dy}$ ,

$$\frac{dP_2}{dy} = \rho_2 v_{2y} \frac{dv_{2y}}{dy} + \frac{\rho_1 v_{1x}}{L_2} (v_{1y} + v_{2y}) + \rho_2 g$$

Combining with Eq. (5-9)

$$\frac{dP_2}{dy} = \frac{v_{2y}}{L_2} (\rho_2 v_{2x} + \rho_1 v_{1x}) + \frac{\rho_1 v_{1x}}{L_2} (v_{1y} + v_{2y}) + \rho_2 g \quad (5-13)$$

Equations (5-8) to (5-13) comprise a system of six ordinary differential equations that can be solved simultaneously for  $v_{1y}$ ,  $v_{2y}$ ,  $v_{1x}$ ,  $v_{2x}$ ,  $P_1$ , and  $P_2$  given the appropriate boundary conditions for these equations and the physical parameters  $\rho_1$ ,  $\rho_2$ ,  $L_1$ , and  $L_2$ . However, before these boundary conditions can be established, it should be pointed out that the pressures  $P_1$  and  $P_2$  necessary to bring about the particle

motions defined in Eqs. (5-8), (5-9), (5-10) and (5-12) are not just  $P_f$ , the pressure within the fluidizing fluid in each of the two regions, but include the effect of the particles presence (energy loss by collision and friction among particles) represented by pressures  $P_{1p}$  and  $P_{2p}$ , that is

$$P_1 = P_f + P_{1p} \quad (5-14)$$

and

$$P_2 = P_f + P_{2p} \quad (5-15)$$

This effect in the bubbling region, i.e.,  $P_{2p}$  can be assumed negligible, because of the high void fraction and hence low effect of particle interaction in the region. On the other hand, this effect is relatively larger in the wall region because of the smaller void fraction and hence higher effect of particle interactions in that region. However, as the top of the bed is approached,

$$P_{1p} = P_{2p} = 0, \text{ and } P_1 = P_2 = P_f,$$

as a result of the violent eruptions of bubbles and loose packing of the solid material across the surface of the bed. Thus, from Eqs. (5-14) and (5-15) at the top of the bed,

$$\frac{dP_1}{dy} = \frac{dP_2}{dy} = \frac{dP_f}{dy}$$

From Jovanovic's (35) experimental data of bed expansions in a freely bubbling fluidized bed of large particles,

$$\frac{dp_f}{dy} = \rho_{av} g , \quad (5-16)$$

where  $\rho_{av}$  is the average bulk density of the solids at the given fluidization state.

### Boundary Conditions

The top of the bed is defined here as the height where the pressure in the bed becomes, for all practical purposes, equal to the pressure in the free board. In this case

$$P_1 = P_2 = P_{atm} .$$

At the bottom of the bed,

$$V_{1y} = V_{2y} = 0 .$$

However, the net amount of solids flowing upward in the bubbling region starts to accelerate at the bottom of the bed and reaches a maximum absolute velocity at the bed top. The net amount of solids flowing upwards at that bed level will then get blown out of the bed into the free board. This material is then reintroduced into the bed at the wall region where it starts to decelerate until it reaches zero velocity at the bottom of the bed. Thus, at the top of the bed, since there is no pressure gradient,

$$\frac{dv_{1y}}{dy} = \frac{dv_{2y}}{dy} = 0$$

From Eqs. (5-8) and (5-9) at the top of the bed,

$$\rho_1 V_{1x} + \rho_2 V_{2x} = 0 \quad (5-17)$$

substituting (5-16), and (5-17) into (5-13),

$$\rho_{av} g = \frac{\rho_1 V_{1x}}{L_2} (V_{1y} + V_{2y}) + \rho_2 g$$

solving for  $V_{1x}$ ,

$$V_{1x} = (\rho_{av} - \rho_2) L_2 g / \rho_1 (V_{1y} + V_{2y})$$

Substituting (5-11) and (5-12) into (5-6),

$$\rho_{av} g = \frac{\rho_2 V_{2x}}{L_1} (V_{1y} + V_{2y}) + \rho_1 g$$

Solving for  $V_{2x}$ ,

$$V_{2x} = (\rho_{av} - \rho_1) L_1 g / \rho_2 (V_{1y} + V_{2y})$$

Thus, the governing differential equations for the solid circulation model and their boundary conditions are again as follows

$$\frac{dv_{1y}}{dy} = - \frac{1}{\rho_1 L_1} (\rho_2 V_{2x} + \rho_1 V_{1x}) \quad (5-8)$$

$$@ y = H, V_{1y} = 0$$

$$\frac{dv_{2y}}{dy} = \frac{1}{\rho_2 L_2} (\rho_2 v_{2x} + \rho_1 v_{1x}) \quad (5-9)$$

$$@ y = H, v_{2y} = 0$$

$$\frac{dv_{1x}}{dy} = \frac{1}{\rho_1 v_{1y} L_1} [\rho_2 v_{2x} (v_{1x} + v_{2x}) - P_1 + P_2] \quad (5-10)$$

$$@ y = 0, v_{1x} = (\rho_{av} - \rho_2) L_2 g / \rho_1 (v_{1y} + v_{2y})$$

$$\frac{dv_{2x}}{dy} = - \frac{1}{\rho_2 v_{2y} L_2} [\rho_1 v_{1x} (v_{1x} + v_{2x}) + P_1 - P_2] \quad (5-12)$$

$$@ y = 0, v_{2x} = (\rho_{av} - \rho_1) L_1 g / \rho_2 (v_{1y} + v_{2y})$$

$$\frac{dP_1}{dy} = \frac{v_{1y}}{L_1} (\rho_2 v_{2x} + \rho_1 v_{1x}) + \frac{\rho_2 v_{2x}}{L_1} (v_{1y} + v_{2y}) + \rho_1 g \quad (5-11)$$

$$@ y = 0, P_1 = P_{atm}$$

$$\frac{dP_2}{dy} = \frac{v_{2y}}{L_2} (\rho_2 v_{2x} + \rho_1 v_{1x}) + \frac{\rho_1 v_{1x}}{L_2} (v_{1y} + v_{2y}) + \rho_2 g \quad (5-13)$$

$$@ y = 0, P_2 = P_{atm}$$

This parametric system of differential equations with split boundary conditions was solved using numerical methods (see Appendix C). The vertical and horizontal solid mass-flux gradients in each region of the model were then extracted from the corresponding gradients of the solid velocity in each region. In addition, the net horizontal mass flux gradient in the two regions, i.e.,

$$\rho_1 V_{1x} + \rho_2 V_{2x} ,$$

was also calculated. These results are given next.

#### D. RESULTS OF CALCULATIONS AND LIMITS OF THE MODEL

The solid-particles circulation model derived in the last section was solved for the two fluidizing gas superficial velocities used in the experiments of this study (see Chapter IV), and several values of the parameters  $\rho_1$  and  $L_1$ . Table 5.1 gives a summary of the values of  $L_1$  and the corresponding values of  $L_2$  used in these calculations. Figures 5.4 (a, b, and c) show the effect of  $L_1$  on the solid-particles mass fluxes in the two regions of the bed when the gas superficial velocity in the bed is 3.25 ft/sec., and the void fraction in the wall region,  $\epsilon_1$ , is kept equal to that of the bed at minimum fluidization (the lower limiting value of  $\epsilon_1$ ). Figures 5.5 (a, b, and c) show these solid mass fluxes for the same fluidizing gas superficial velocity and the same values of  $L_1$ , but for a higher value of the void fraction in the wall region. Figures 5.6 (a, b, and c) show the effect of the wall region void fraction,  $\epsilon_1$ , on these solid mass fluxes in the two regions of the bed. Figures 5.7 (a, b, and c), Figures 5.8 (a, b, and c), and Figures 5.9 (a, b, and c) show the results for similar calculations of the solid mass fluxes in the two regions of the model bed when the fluidized bed is operating at 4.5 ft/sec. gas superficial velocity.

The aforementioned figures show that, at a given gas superficial velocity and a wall region void fraction in the bed, the vertical solid mass flux in the wall region decreases by increasing  $L_1$  until a minimum

Table 5.1. Summary of the dimensions of the model bed used in solid mass flux calculations.

$L_1$ "ft"	$L_2$ "ft"	$A_1/A_2\%$	$A_1/A_t\%$	$L_w$ "ft"
0.143	1.430	10%	9.1 %	0.035
0.210	1.399	15%	13.0 %	0.051
0.274	1.369	20%	16.67%	0.065
0.335	1.342	25%	20.0 %	0.079
0.613	1.225	50%	33.33%	0.138



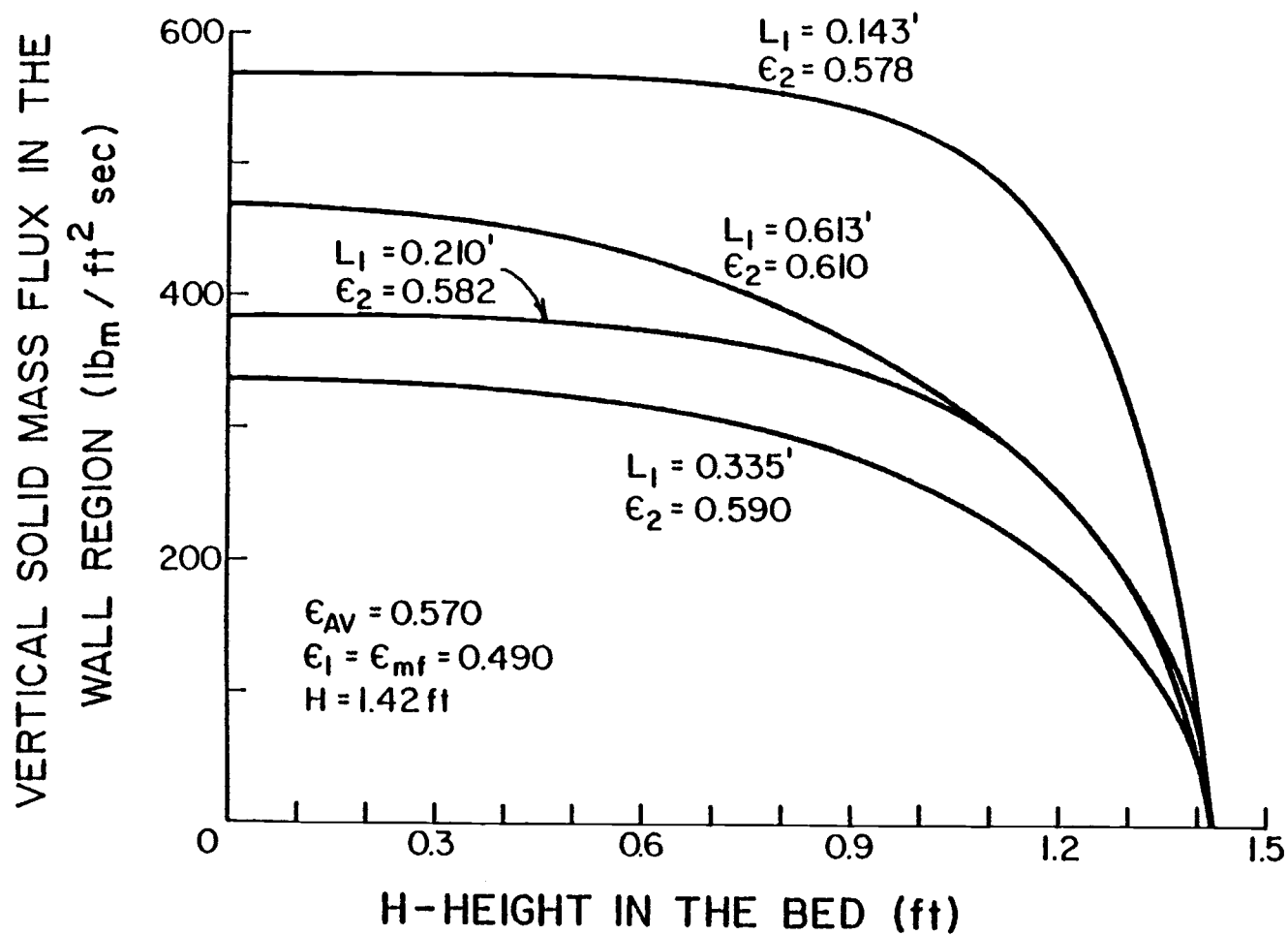


Figure 5.4a. Vertical solid mass flux in the wall region of the model bed as a function of height in the bed and wall region thickness for  $U_o = 3.25$  ft/sec and  $\epsilon_1 = 0.49$ .

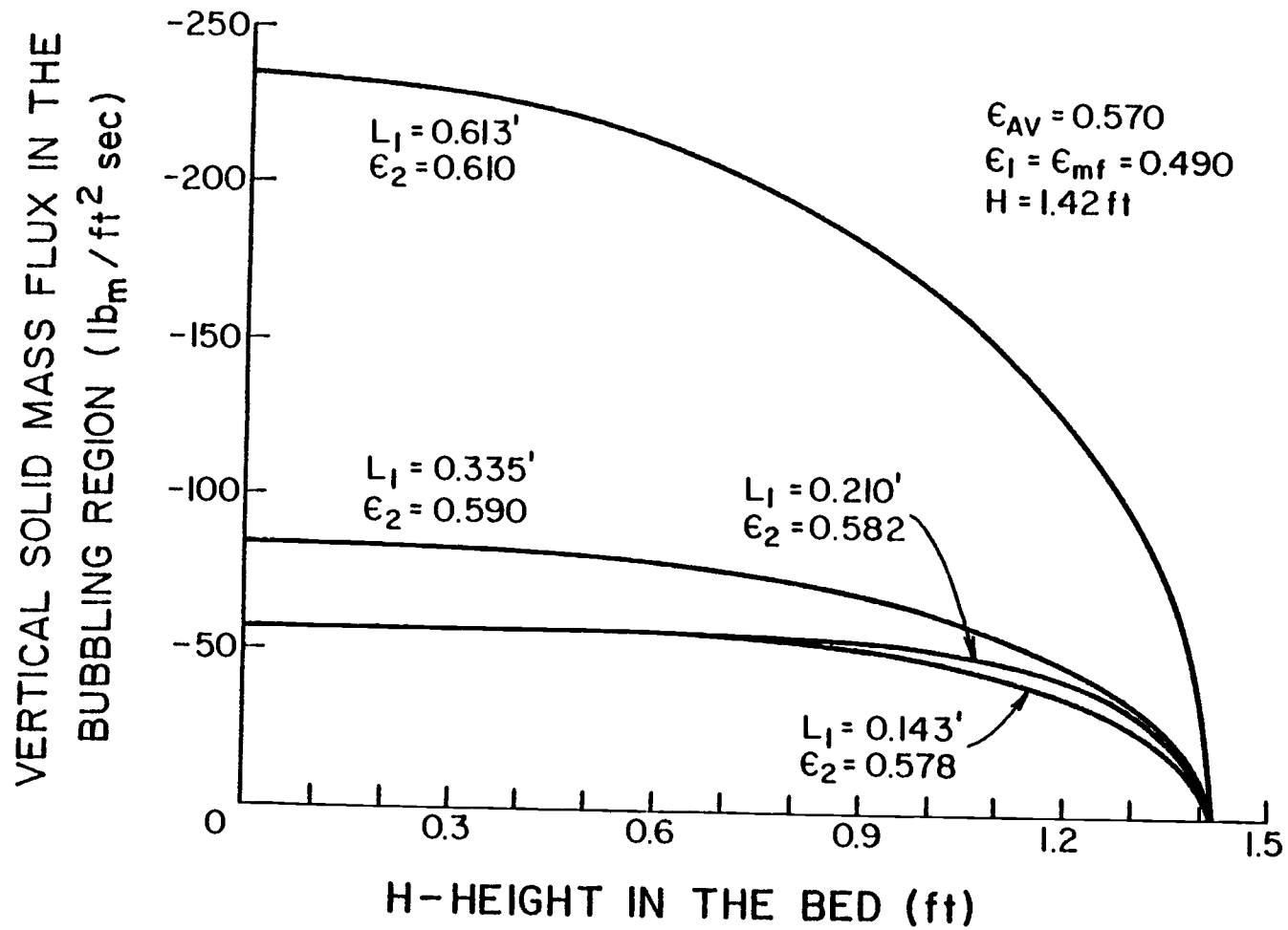


Figure 5.4b. Vertical solid mass flux in the bubbling region of the model bed as a function of height in the bed and wall region thickness for  $U_o = 3.25$  ft/sec and  $\epsilon_1 = 0.490$ .

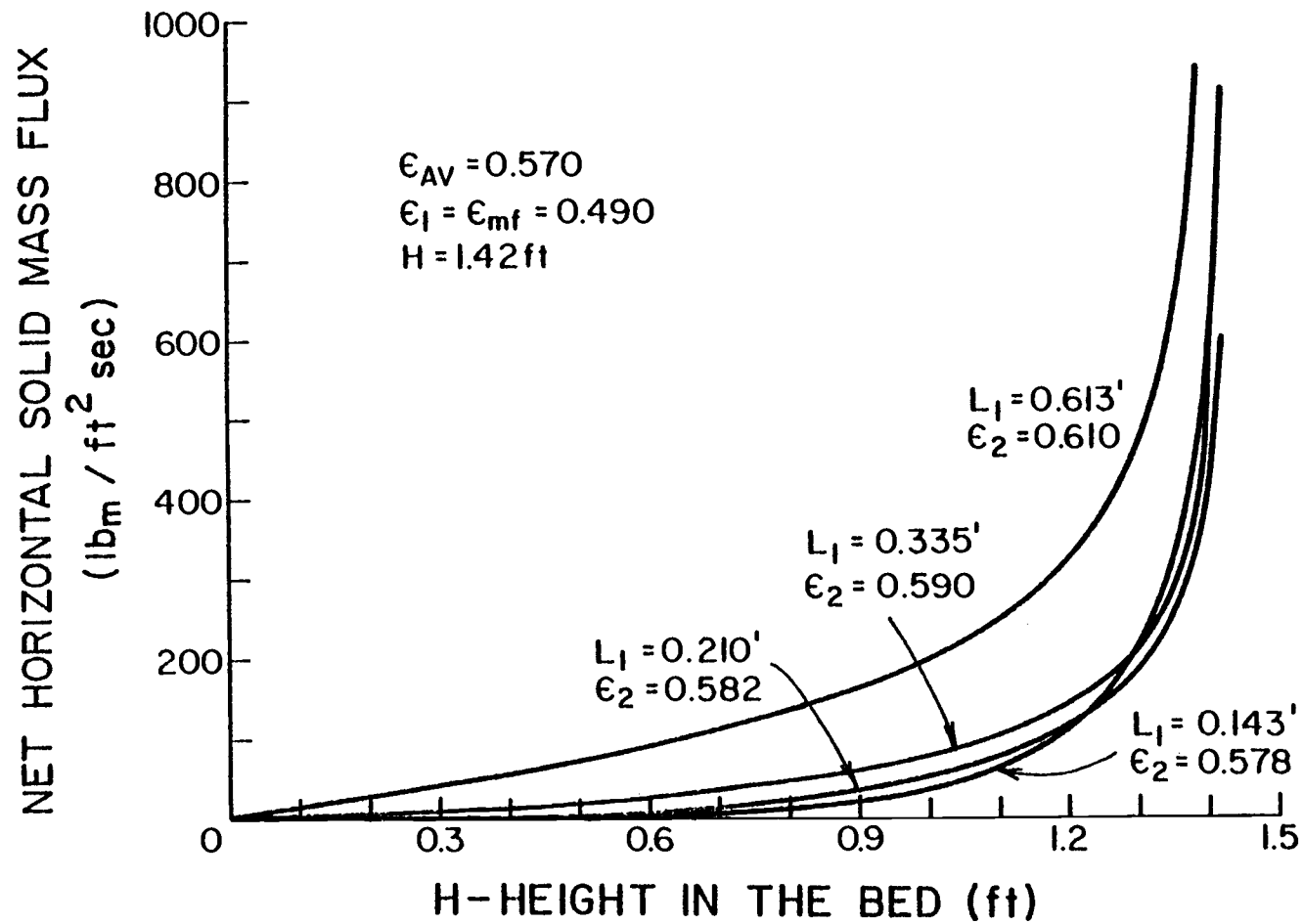


Figure 5.4c. Net horizontal solid mass flux between the two regions of the model bed as a function of height in the bed and wall region thickness for  $U_o = 3.25 \text{ ft/sec}$  and  $\epsilon_1 = 0.49$ .

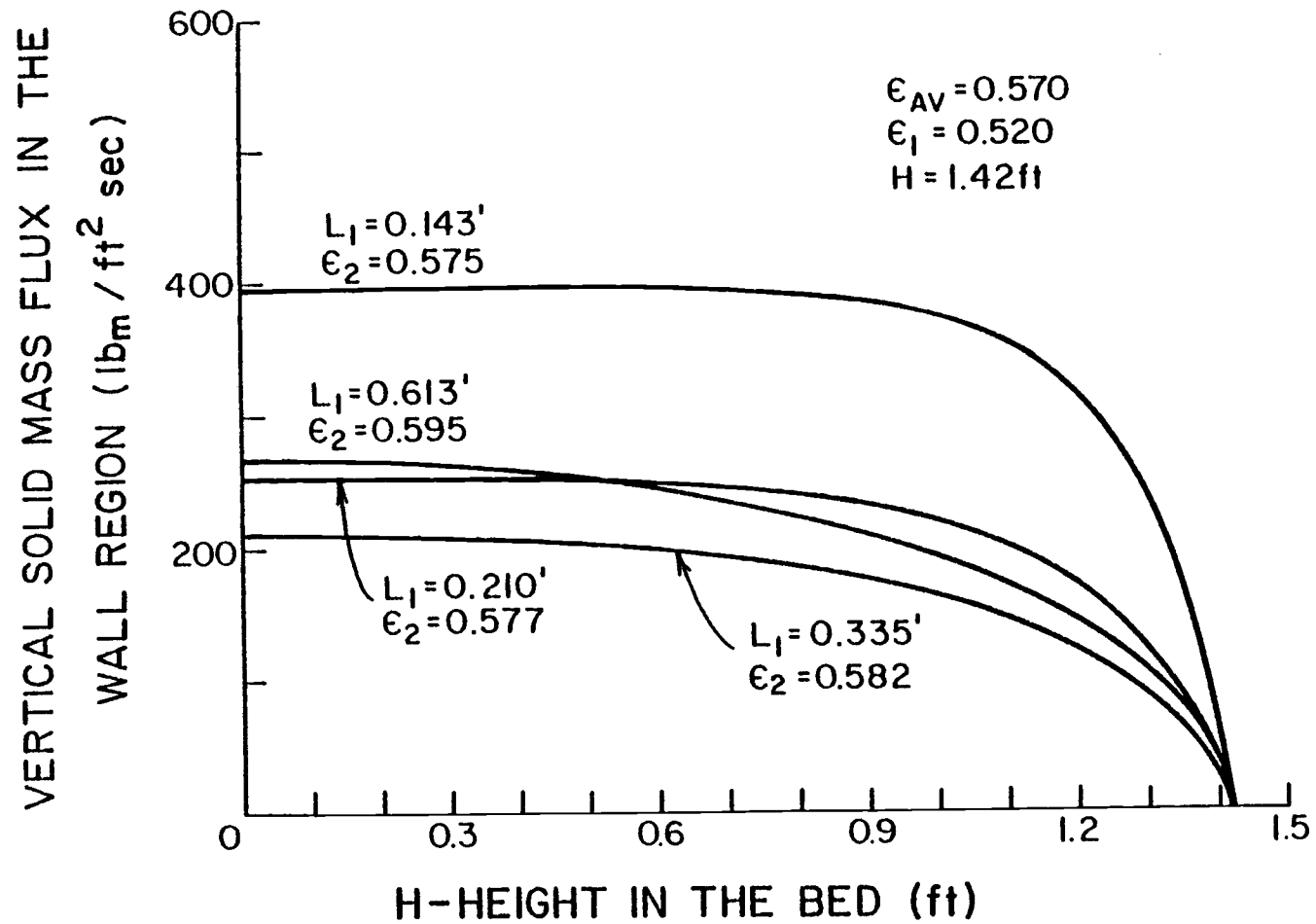


Figure 5.5a. Vertical solid mass flux in the wall region of the model bed as a function of height in the bed and wall region thickness for  $U_o = 3.25$  ft/sec and  $\epsilon_1 = 0.520$ .

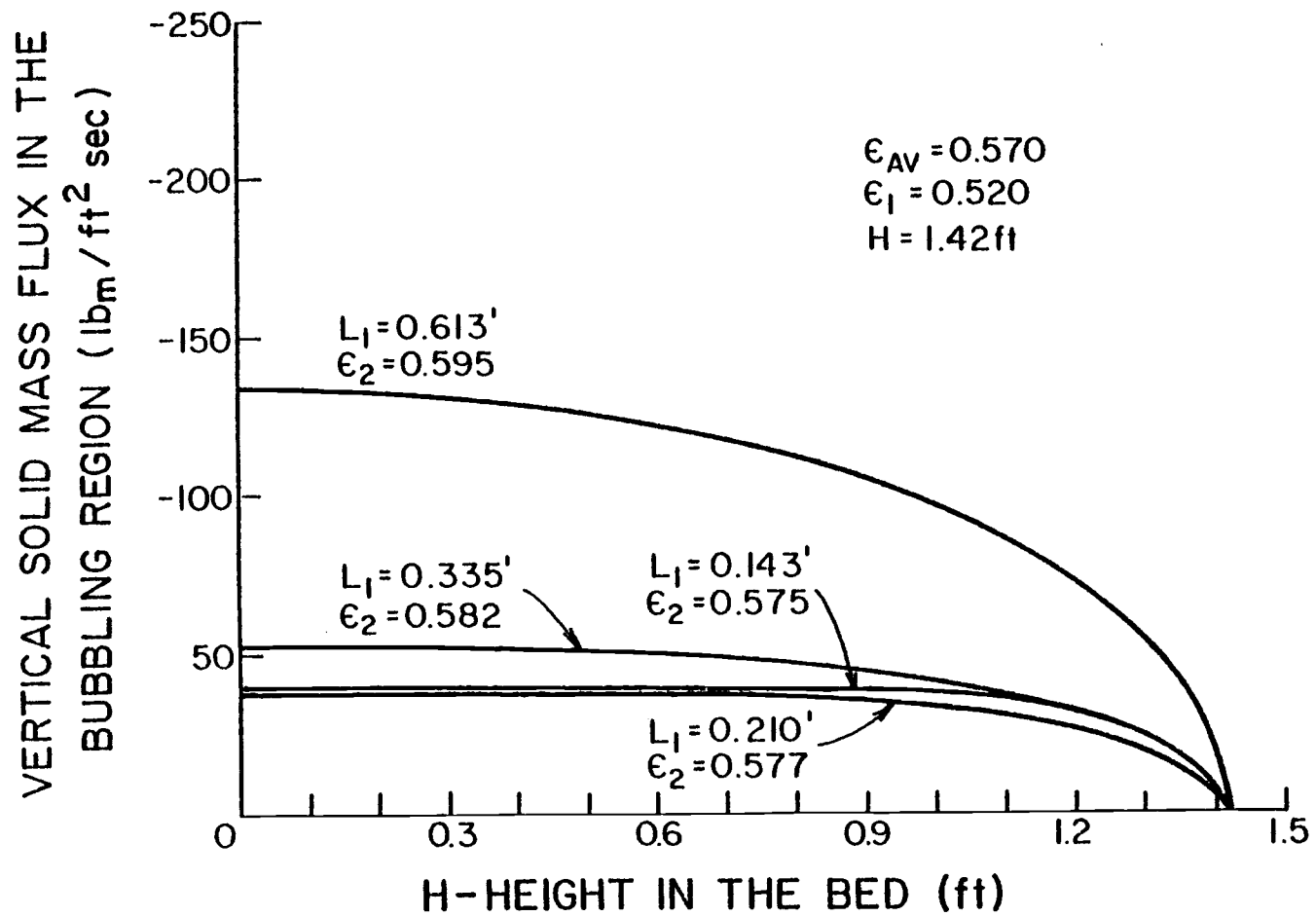


Figure 5.5b. Vertical solid mass flux in the bubbling region of the model bed as a function of height in the bed and wall region thickness for  $U_o = 3.25 \text{ ft/sec}$  and  $\epsilon_1 = 0.520$ .

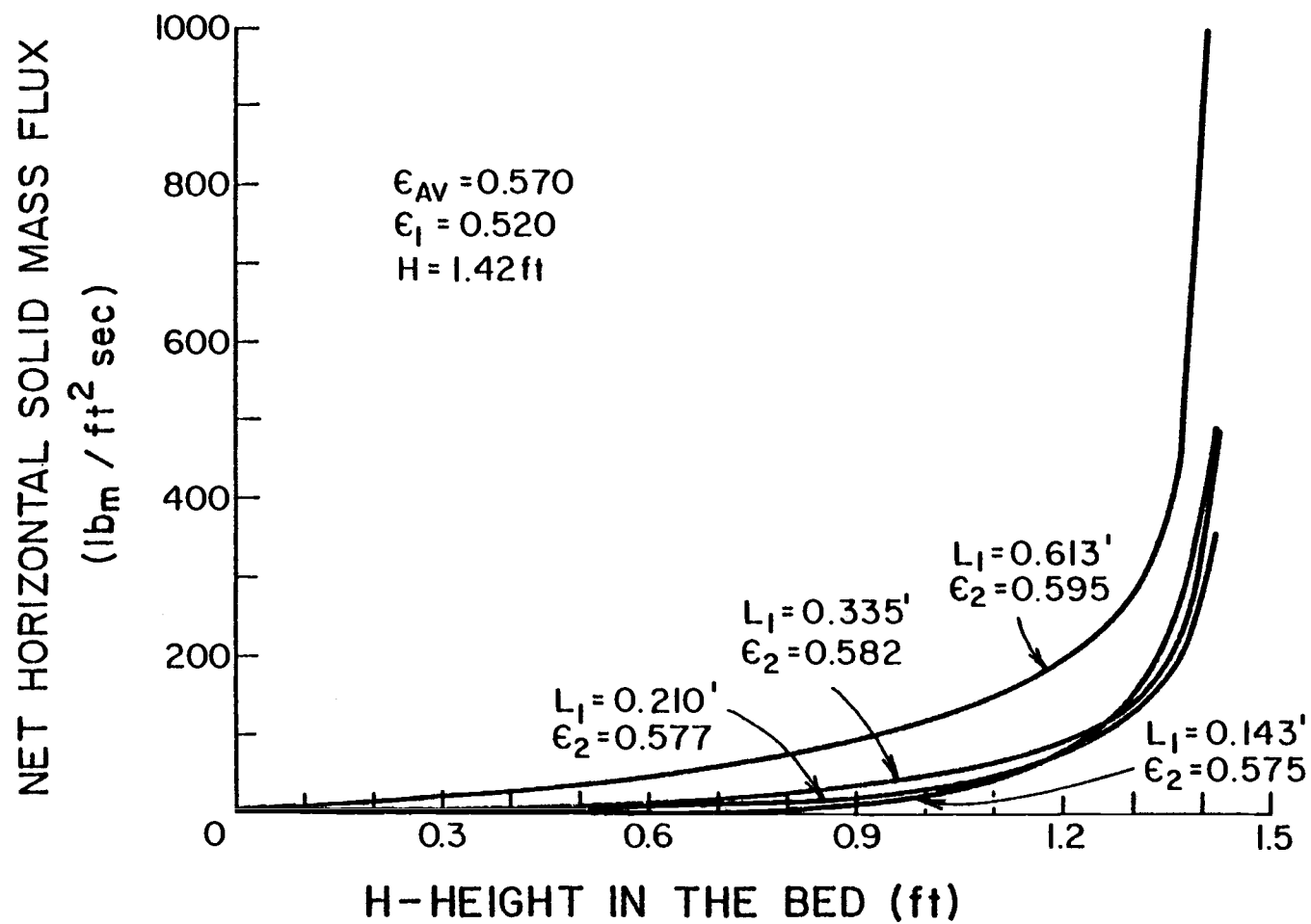


Figure 5.5c. Net horizontal solid mass flux in the two regions of the model bed as a function of height in the bed and wall region thickness for  $U_o = 3.25$  ft/sec and  $\epsilon_1 = 0.520$ .

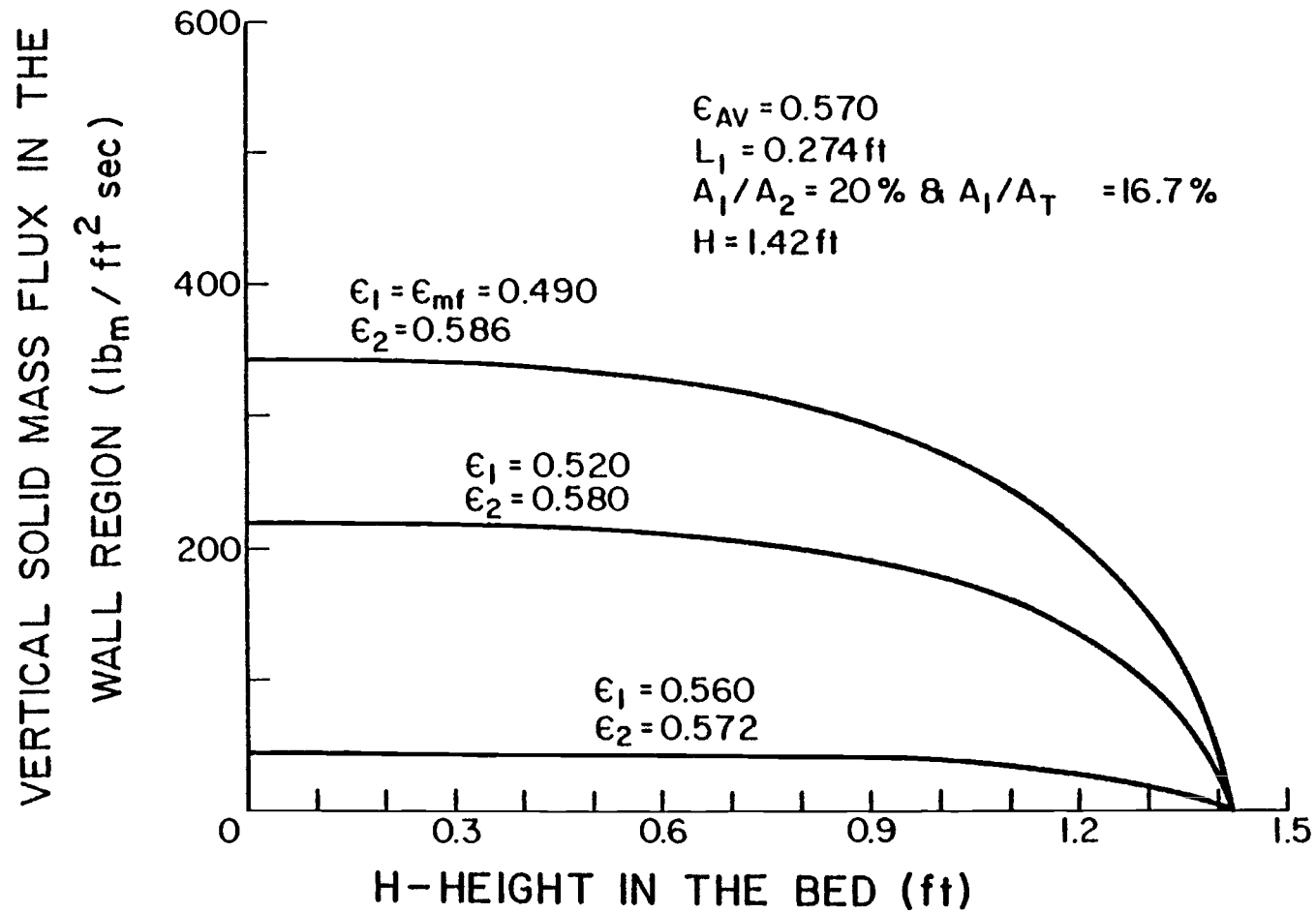


Figure 5.6a. Vertical solid mass flux in the wall region of the model bed as a function of height in the bed and wall region void fraction for  $U_o = 3.25 \text{ ft/sec}$ .

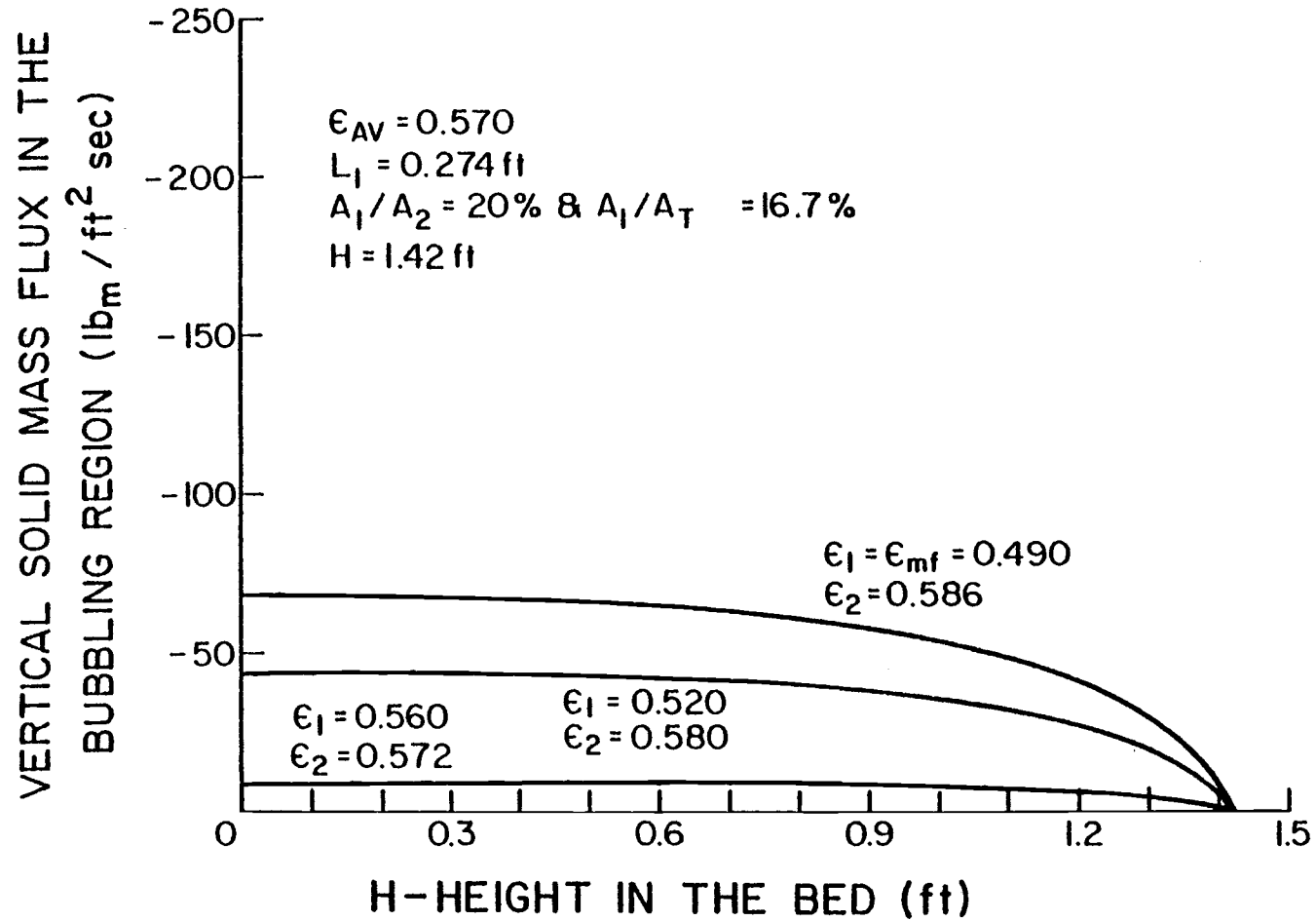


Figure 5.6b. Vertical solid mass flux in the bubbling region of the model bed as a function of height in the bed and wall region void fraction for  $U_o = 3.25 \text{ ft/sec}$ .



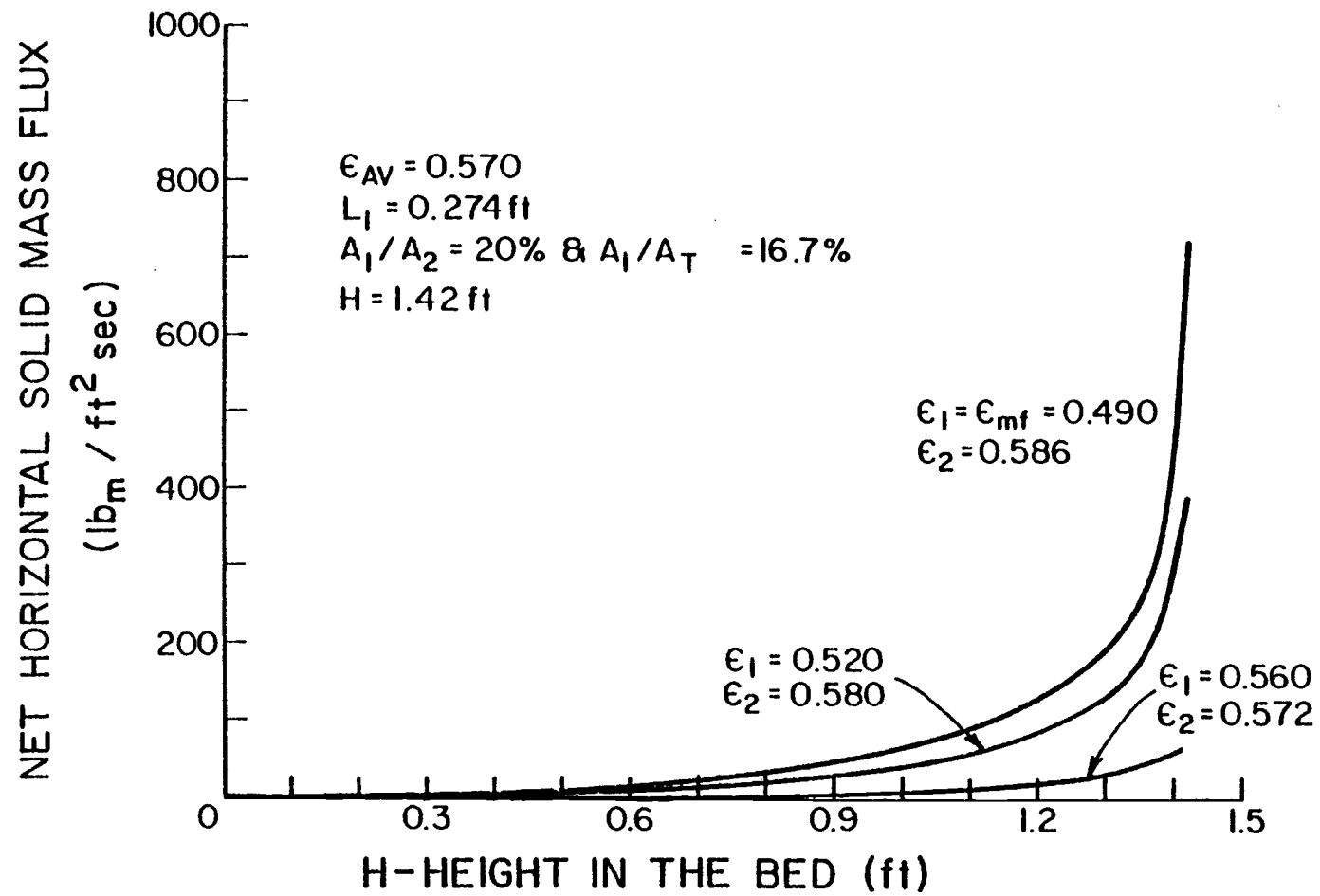


Figure 5.6c. Net horizontal solid mass flux between the two regions of the model bed as a function of height in the bed and wall region void fraction for  $U_o = 3.25 \text{ ft/sec}$ .

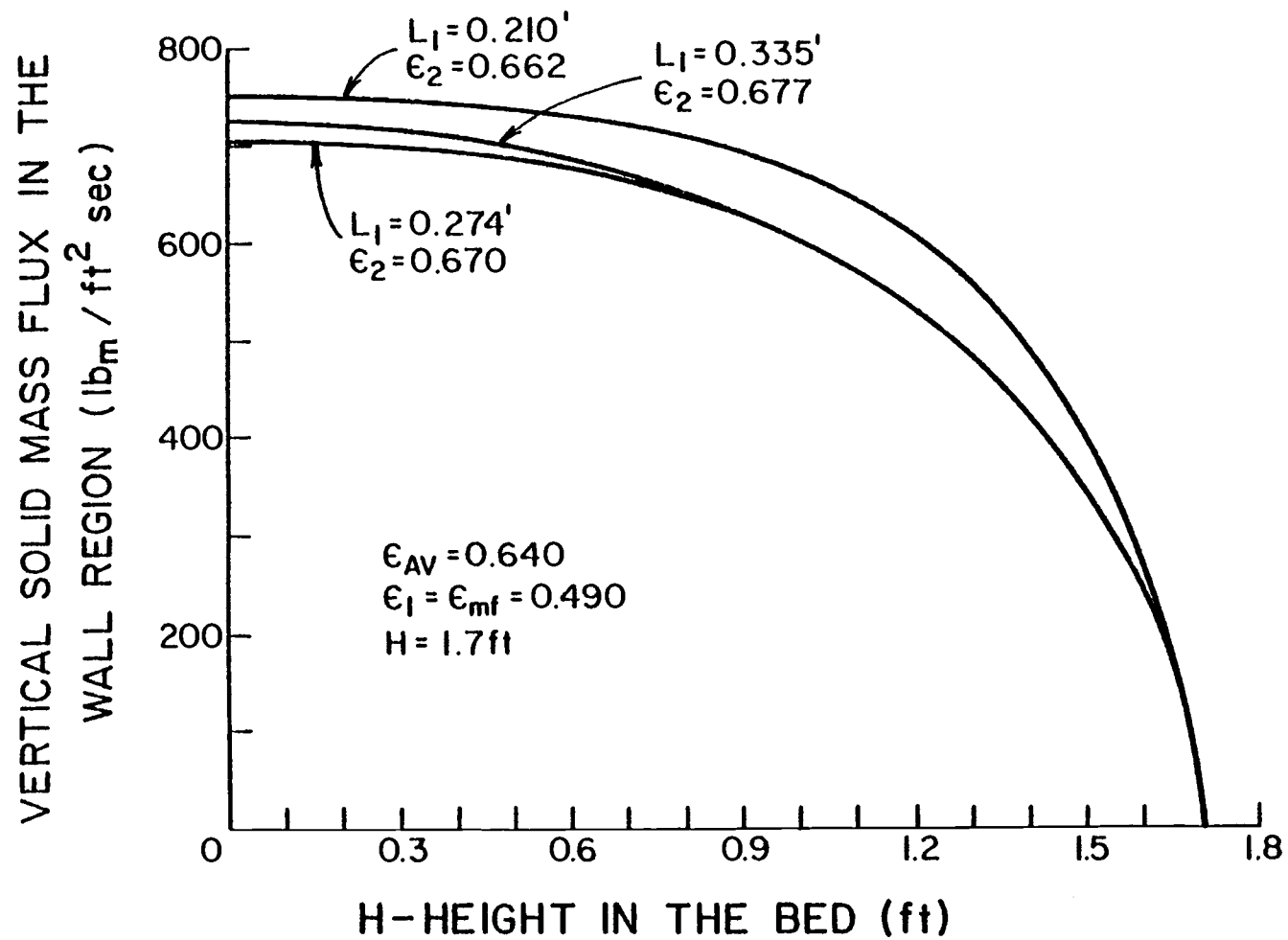


Figure 5.7a. Vertical solid mass flux in the wall region of the model bed as a function of height in the bed and wall region thickness for  $U_o = 4.5 \text{ ft/sec}$  and  $\epsilon_1 = 0.49$ .

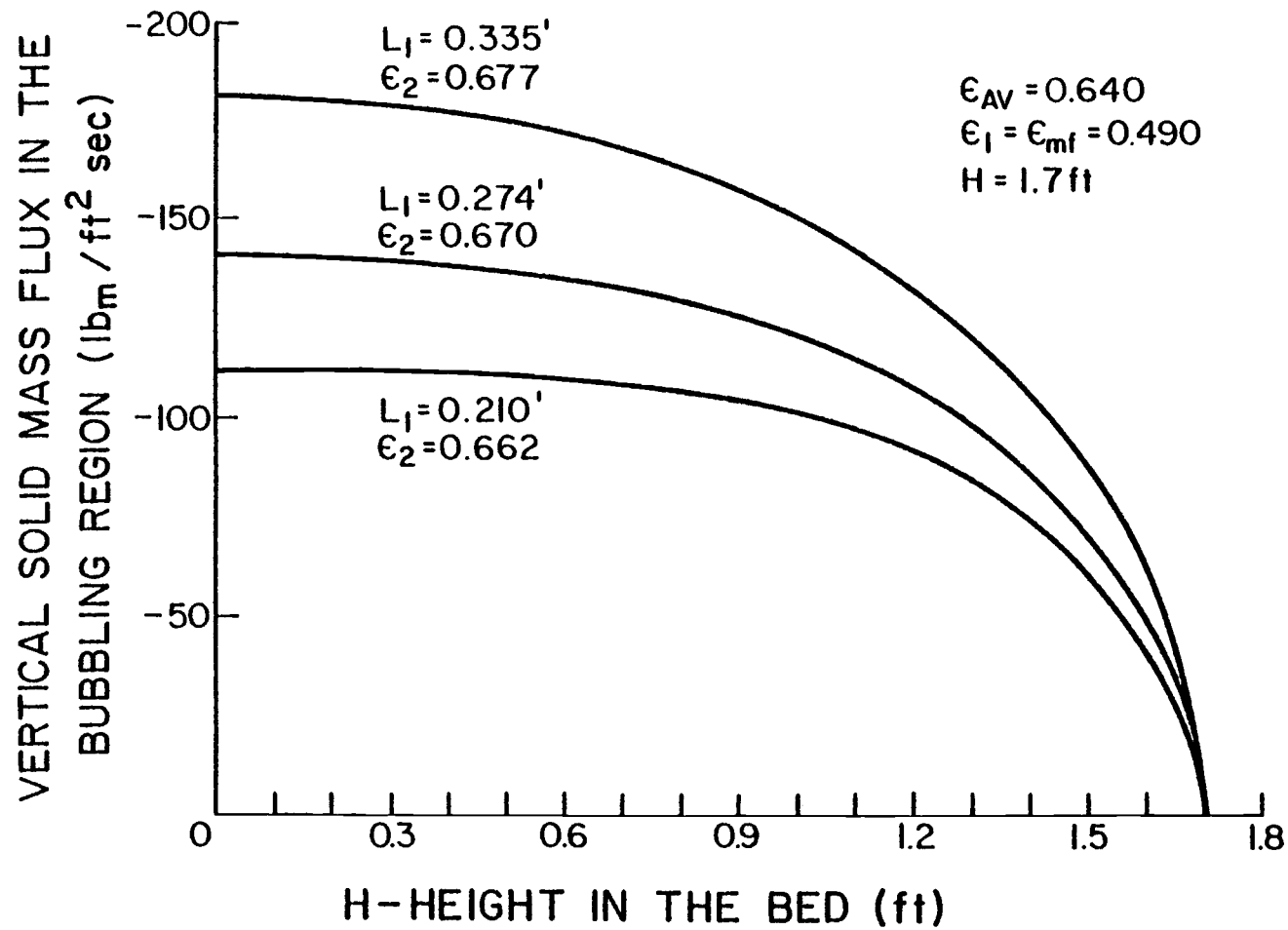


Figure 5.7b. Vertical solid mass flux in the bubbling region of the model bed as a function of height in the bed and wall region thickness for  $U_o = 4.5$  ft/sec and  $\epsilon_1 = 0.49$ .

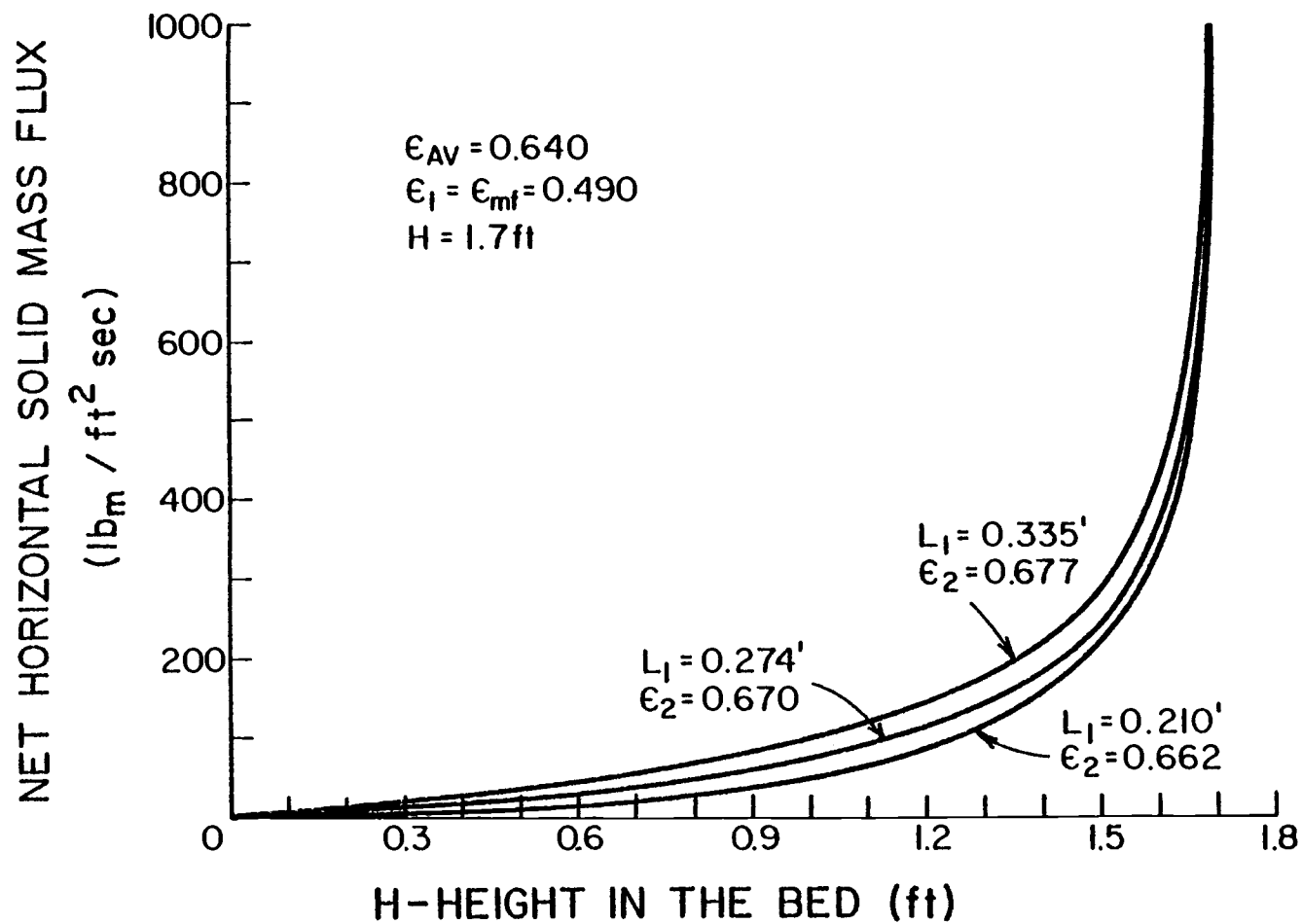


Figure 5.7c. Net horizontal solid mass flux between the two regions of the model bed as a function of height in the bed and wall region thickness for  $U_o = 4.5 \text{ ft/sec}$  and  $\epsilon_1 = 0.49$ .

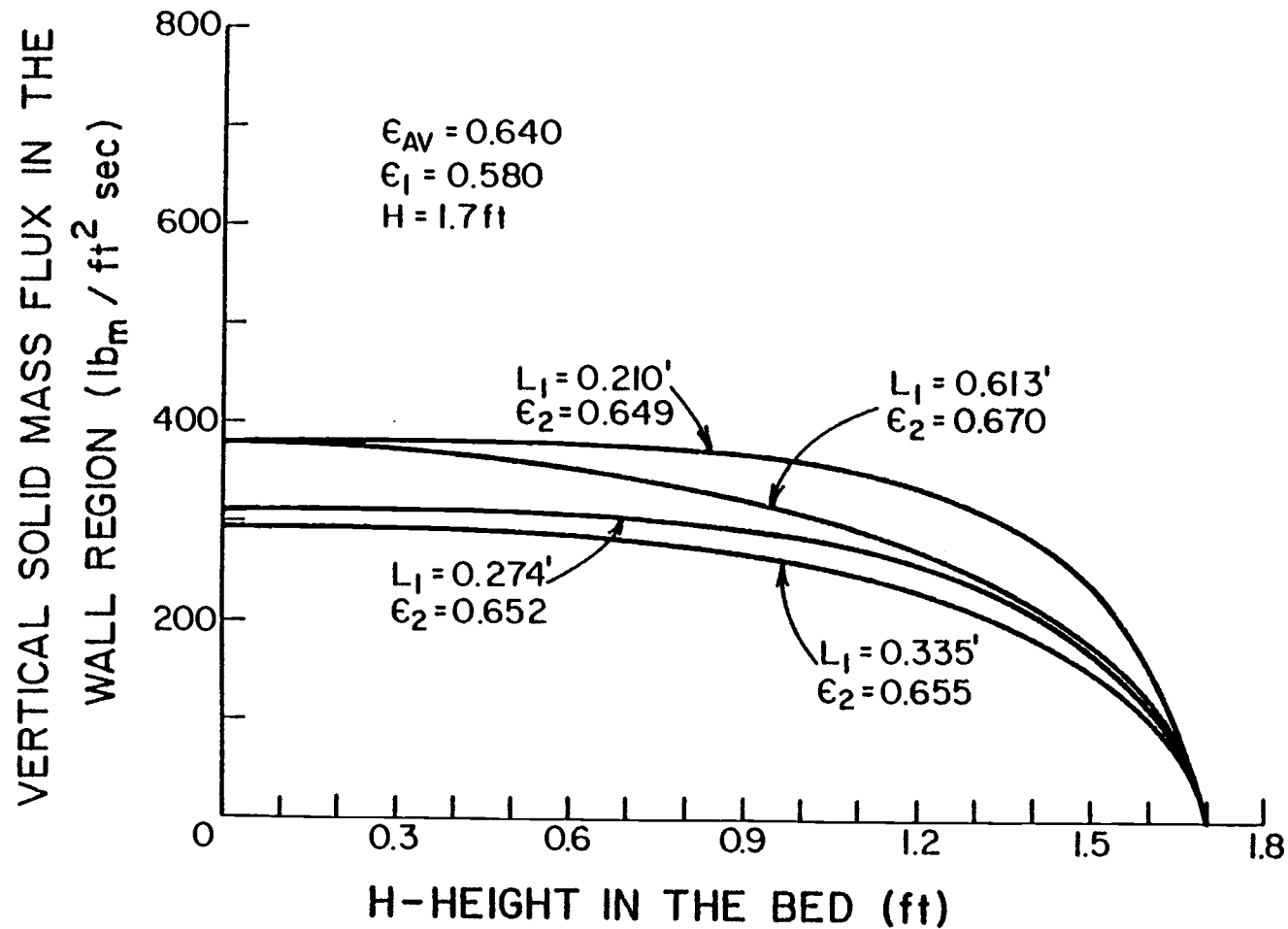


Figure 5.8a. Vertical solid mass flux in the wall region of the model bed as a function of height in the bed and wall region thickness for  $U_o = 4.5 \text{ ft/sec}$  and  $\epsilon_1 = 0.580$ .

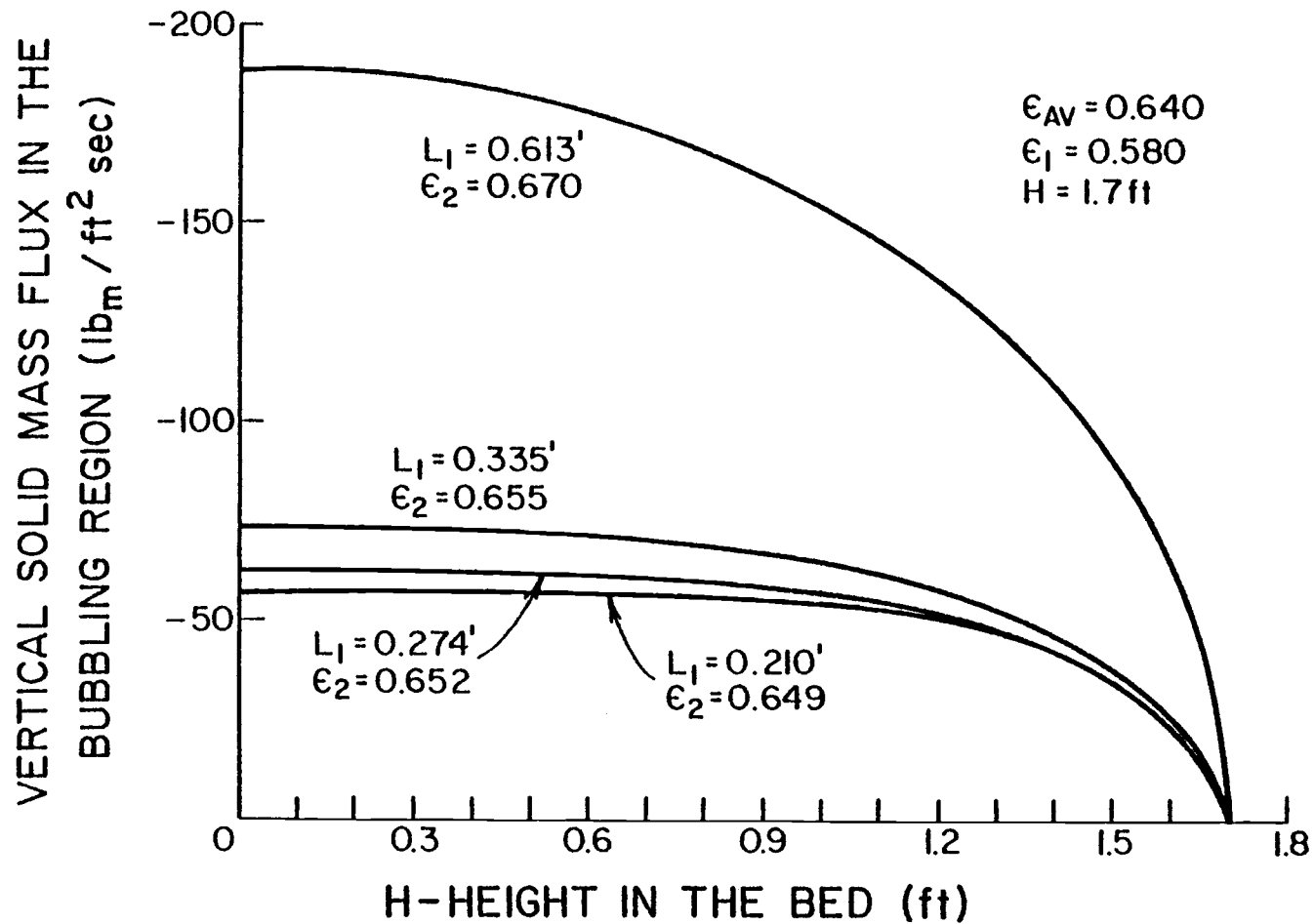


Figure 5.8b. Vertical solid mass flux in the bubbling region of the model bed as a function of height in the bed and wall region thickness for  $U_o = 4.5$  ft/sec and  $\epsilon_1 = 0.580$ .

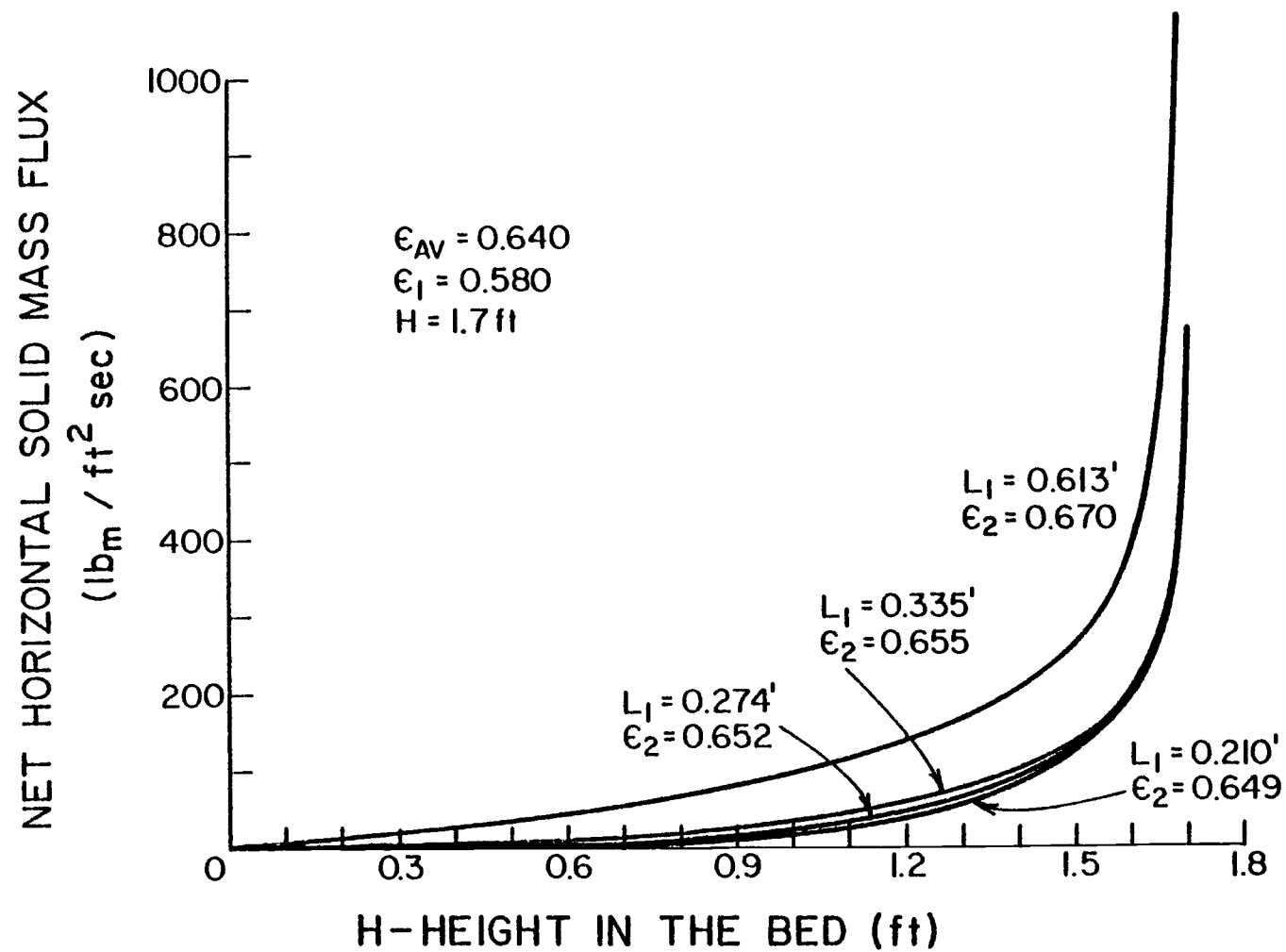


Figure 5.8c. Net horizontal solid mass flux between the two regions of the model bed as a function of height in the bed and wall region thickness for  $U_o = 4.5 \text{ ft/sec}$  and  $\epsilon_1 = 0.580$ .

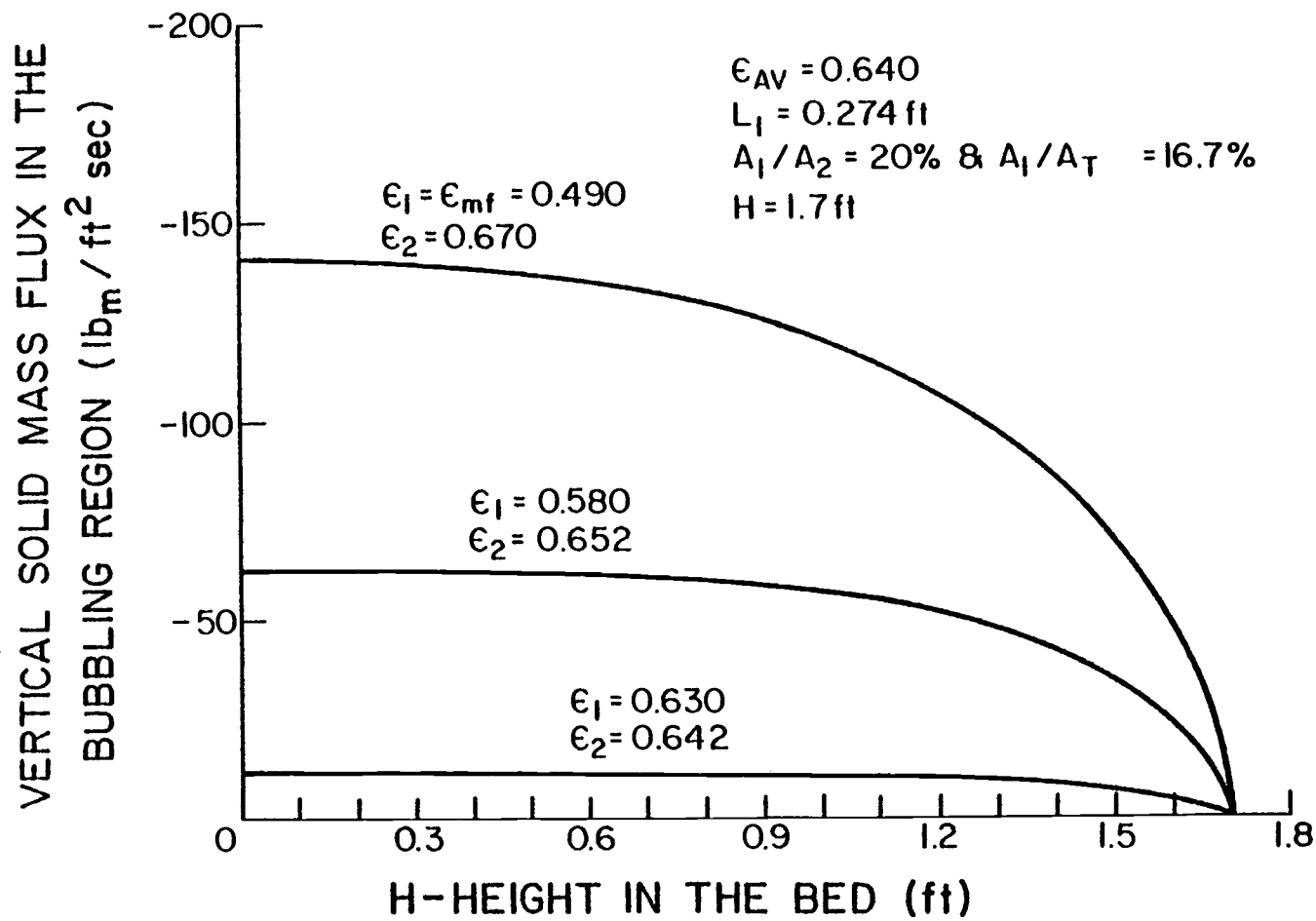


Figure 5.9a. Vertical solid mass flux in the wall region of the model bed as a function of height in the bed and wall region void fraction for  $U_o = 4.5$  ft/sec.



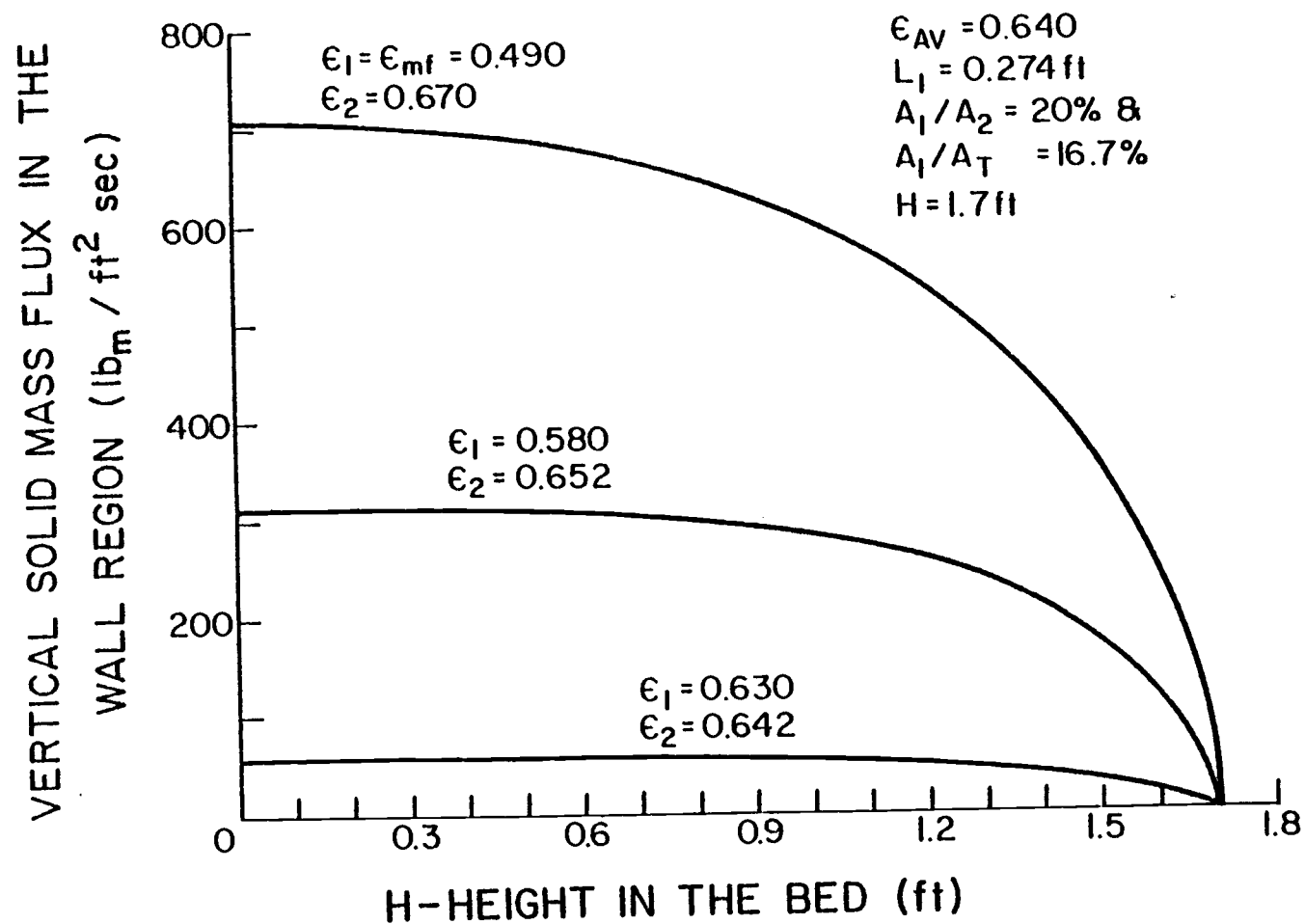


Figure 5.9b. Vertical solid mass flux in the bubbling region of the model bed as a function of height in the bed and wall region void fraction for  $U_o = 4.5$  ft/sec.

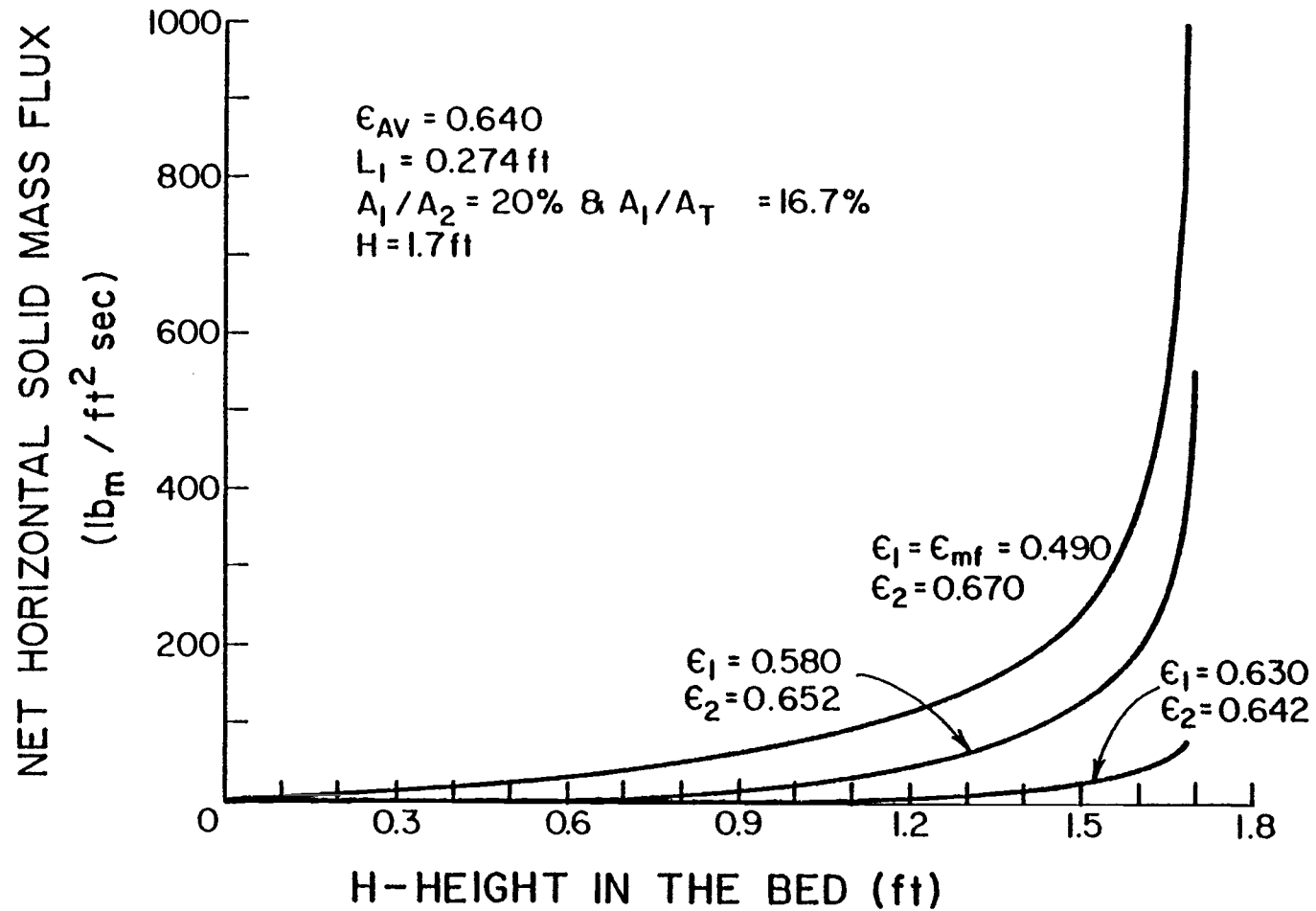


Figure 5.9c. Net horizontal solid mass flux between the two regions of the model bed as a function of height in the bed and wall region void fraction for  $U_o = 4.5 \text{ ft/sec}$ .

value is reached beyond which this vertical solid mass flux increases with an increase in  $L_1$ . On the other hand, for the values of  $L_1$  used in these calculations, the vertical solid mass flux in the bubbling region increases monotonically with  $L_1$ . These figures also show that although the net horizontal mass flux between the two regions is significant only towards the bottom of the bed, this net horizontal mass flux increases by increasing  $L_1$ . These changes in the solid mass fluxes in the bed with  $L_1$  can be explained by examining the effect of  $L_1$  and  $L_2$  coupled with effect of  $\rho_2$  on the material and momentum balance equations of the solid flow in the two regions of the model bed.

The figures also show that the effect of the void fractions in the two regions of the bed on the solid circulation is such that increasing the difference between these two parameters at a given gas superficial velocity and given  $L_1$  and  $L_2$  results in an increase in the solid mass fluxes in the two regions of the bed. Thus, reducing the void fraction in the wall region at a given gas superficial velocity in the bed (for example by reducing the amount of gas going through that region) or increasing the gas superficial velocity in the bed while maintaining a constant wall region void fraction, or both, would increase the difference between the void fractions in the two regions and hence enhance the solid flow circulation in the bed.

#### Limits of the Model

The results of the two-region model bed calculations suggest that the solid flow circulation inside a freely bubbling fluidized bed can be enhanced by one or a combination of the following factors inside the bed: 1) increasing the gas fluidizing velocity; 2) increasing the dif-

ference between the void fractions in the two regions of the bed; and 3) increasing the width of the descending wall layers. However, all of these factors are limited to a certain range, depending on the fluidized bed system, beyond which the bed no longer operates as a freely bubbling fluidized bed. As the gas fluidizing velocity, in a given fluidized bed system operating in the slow bubble regime, is increased beyond a certain value the bed would undergo a transition from the slow bubble fluidization regime into the exploding bubble regime and for sufficiently high velocity into the turbulent regime (see reference 34) for which the assumptions of the two-region model would no longer hold. On the other hand, increasing the thickness of the wall region is limited by the fact that the solid flow characteristics in this region are influenced by the bubble flow in the region, or more accurately by the lack of it, and hence by the amount of gas flowing through the region (see references 7, 17, 19, and 32). Thus, increasing this parameter in the bed at a given gas superficial velocity means increasing the amount of gas flowing in the middle (bubbling) section of the bed, which would eventually lead to channeling of the gas through the bed and poor gas-solid contact (see reference 26).

The two-region solid circulation model therefore suggests that optimum solid circulation inside a freely bubbling fluidized bed system can be obtained by operating the bed at the highest allowable gas velocity for that particular system and at the highest values of  $L_1$  and  $\epsilon_2/\epsilon_1$  that would still give uniform fluidization in the bed system without gas channeling and defluidization of the wall region.

#### E. COMPARISON BETWEEN MODEL PREDICTIONS AND EXPERIMENTAL RESULTS

The qualitative agreement between the model predictions for the gross solid circulation flow inside a freely bubbling fluidized bed with the experimental observations of this flow behavior was shown in the last section. However, in order to make a conclusive test on the model predictions for the solid mass fluxes in the bed against those obtained experimentally, the actual values of the physical parameters  $\rho_1$  and  $L_1$  of the bed have to be known. Unfortunately, direct physical measurements of these parameters are practically impossible to make in the bed. Another method of testing the validity of the predictions of the proposed model is to fit it to experimental data of the local solid mass fluxes in the bed, and thus find the best estimate of the parameters  $\rho_1$  and  $L_1$  of the model that would minimize the difference between the model predictions and the experimental data at the various locations in the bed. However, because of the nonlinearity of the model, this procedure requires data on the local solid mass fluxes at more vertical locations inside the bed than what is available from the experiments of this study. Another factor that adds to the complications of the quantitative testing of the model with this study's experimental data is the presence of the tube array in the bed - a factor which is not accounted for in the model. The tube array could be considered here to act as a low pressure drop distributor for both the gas and solid phases of the bed, and hence should not have much influence on the gross solid circulation inside the bed. However, the horizontal orientation of this tube array inside the bed creates a difference between the wall-layer local solid mass fluxes at any two walls perpendicular to each other in the

bed. This effect makes it inaccurate to calculate the local solid mass fluxes in the wall region of the model bed from this study's experimental measurements of the local solid mass fluxes at two parallel walls.

Nevertheless, the model predictions for the vertical solid mass fluxes in the bubbling region of the bed show a reasonable agreement with the experimental measurements of these mass fluxes at the two fluidizing velocities used in this study. Figures 5.10 and 5.11 show a comparison between the theoretical predictions and the experimental measurements of these mass fluxes in the bubbling region for the low and high gas velocities used, respectively. Without specifying optimum values for the physical parameters in the bed for each fluidization condition, these figures show that the model predictions for the solid mass fluxes in the bed are of the same order of magnitude as the experimental measurements. These comparisons, however, are not adequate to fully verify the model. More data under more controlled and suitable conditions inside the bed are still needed to establish the relationships between the physical parameters of the model and size and hydrodynamic conditions of the bed.

At the onset of this investigation, very little was known about the solid flow behavior inside a large-particle fluidized bed. Useful data on the subject were scarce and not adequate to guide the experimental program of the study. Thus, the experimental program was designed to meet general goals. The global goal was to gather basic data on the solid movement inside a large-particle bed that could be used to map and characterize this movement, and hence to better understand the basic phenomena that take place in fluidized beds of large particles. The theoretical model derived here was later conceived and based on the information gathered on the gross solid circulation inside the bed.

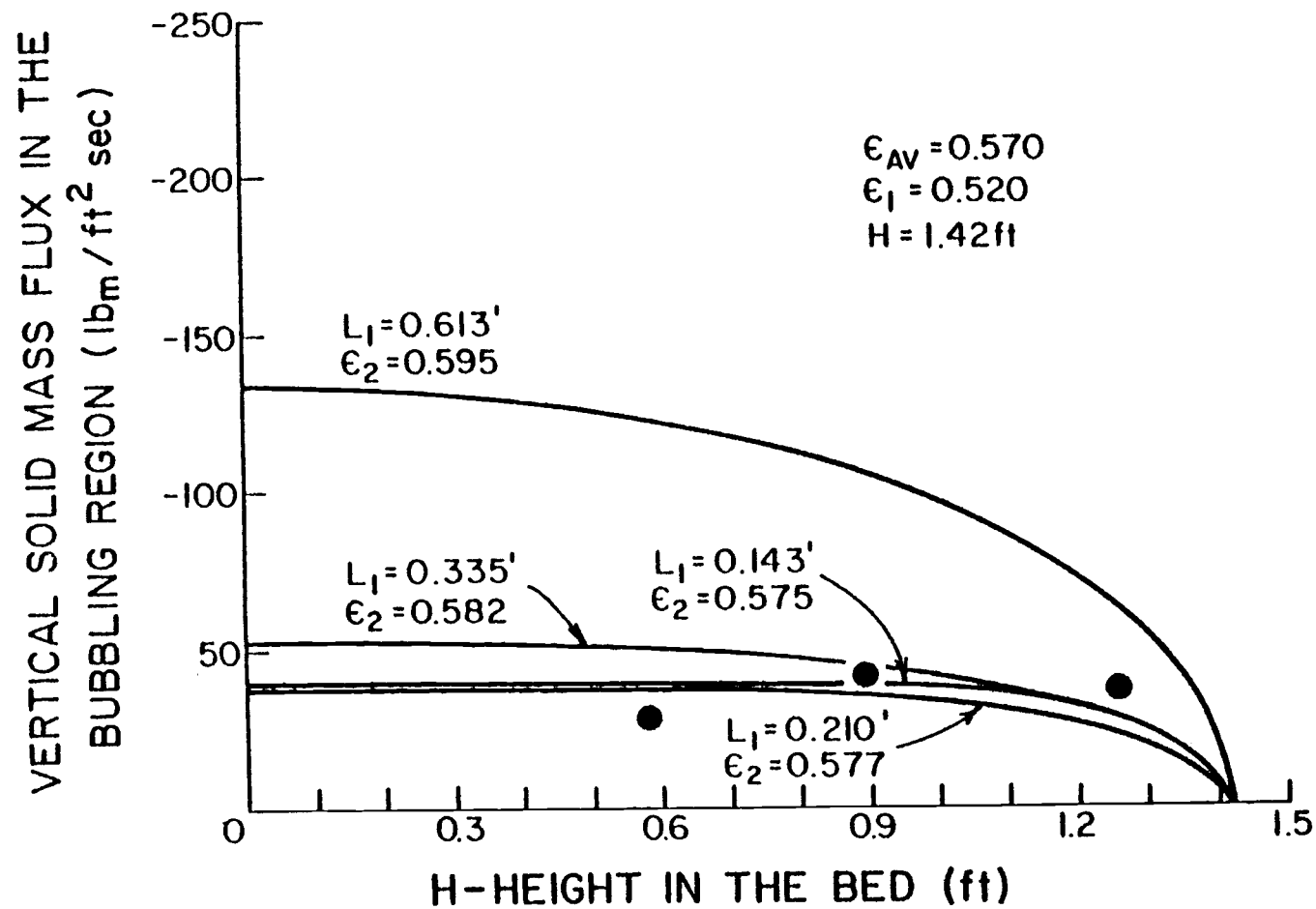


Figure 5.10. Comparison between theoretical and measured values of vertical solid mass flux in the bubbling region of the bed for  $U_o = 3.25 \text{ ft/sec}$ .

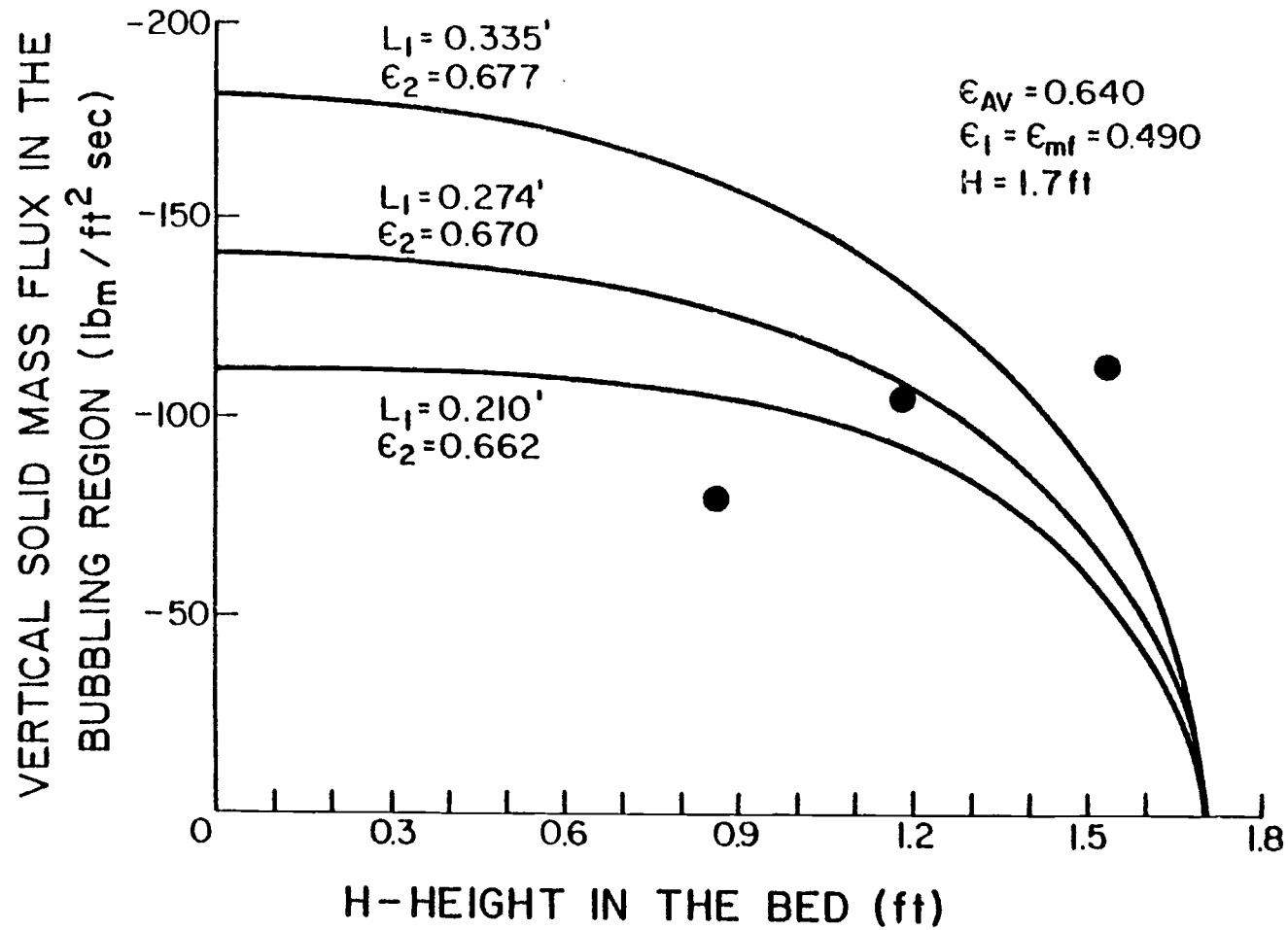


Figure 5.11. Comparison between theoretical and measured values of vertical solid mass flux in the bubbling region of the bed for  $U_o = 4.5 \text{ ft/sec}$ .



Although the model is not fully verified here, it should set the "stage", and provide guidance for further studies and more specific experiments on the solid movements inside fluidized beds. Recommendations for basic designs of further experiments are given in the next chapter.

## 6. SUMMARY AND CONCLUSIONS

Understanding the characteristics of the solid movement and gross circulation inside a fluidized bed is important to the design and operation of a fluidized bed reactor. This solid flow behavior has a very significant effect on the performance of a fluidized bed coal combustor. It is critically important to have a nearly uniform combustion throughout the bed. Gross fuel-rich and fuel-lean regions must be avoided. They would lead to lower fuel efficiency, decreased sulfur retention, difficult erosion problems, and possibly combustion in the free board above the bed with a sufficient temperature rise to melt or sinter the ash produced by the coal.

Previous studies on solid movement inside fluidized beds were hampered, in great part, by inadequate instrumentation and methods of solid flow measurements. A review of the various methods and instrumentation used in previous studies, along with the still unanswered questions on the scale-up of results obtained from small beds to large beds was given in Chapter I.

A major contribution of this work to the study of solid movements inside fluidized beds is the development of new instrumentation that overcomes the limitations and uncertainty of previous studies. The new instrument is capable of measuring local solid mass fluxes in two dimensions inside a bed consisting entirely of magnetic solid particles. The bed material should not impose any limitations on future studies on solids movement inside fluidized beds, since magnetic solid particles of different sizes and densities are commercially available or can be easily fabricated to suit the needs of the particular study. Chapter II

gave the basic principles and development of the magnetic solid particle mass flow meter. The basic principles of the instrument can also be implemented in different application of magnetic solid mass flow measurements, such as measurements of solid mass flow in vertical pipes and downcomers, and the calibration of mechanical or magnetic solid flow control valves such as studied by Levenspiel, et al. (39). Coil designs similar to those used on the initial tests on the magnetic solid particles mass flow meter (Figure 2.9) are suitable for such applications.

Chapter III described the fluidized bed test facility used to obtain data on solid movement inside a tube-filled fluidized bed with atmospheric air as the fluidizing gas. Fourteen probes such as described in Chapter II were located in various locations inside a bed (18 in. x 18 in. in cross-section). The bed was scaled down from the Babcock and Wilcox 6 ft. x 6 ft. fluidized bed combustor using the scaling criteria described by Scharff, et al. (6).

Chapter IV presented the experimental results on solid mass flow measurements inside a freely bubbling fluidized bed operating in the slow bubble regime. Two gas superficial velocities were used (3.25 and 4.5 ft./sec.). The experimental results suggest the following conclusions about the solid flow behavior inside a freely bubbling fluidized bed:

- a) Solid particles follow a preferred track of gross circulation such that the net solid motion in the middle bubbling region of the bed is in the upward direction while adjacent to the bed walls the net solid flow is in the downward direction.
- b) The net lateral particle motion is not significant in the bubbling middle region of the bed. However, solid particles

flowing in the wall region undergo a significant net lateral displacement towards the middle region of the bed as the bottom of the bed is approached.

- c) Increasing the gas superficial velocity in the bed results in an increase in the net vertical mass flow of the solid in the bubbling region and the net lateral mass flow in the wall region.
- d) Significant lateral particle motion near a solid feed port at the bottom of the bed can be induced by an uneven gas velocity distribution inside the bed. More bubbles form where more gas is supplied, and the lateral motion is induced by the buoyancy force created by the uneven voidage distribution inside the bed.

In Chapter V, a theoretical model for the gross solid circulation observed in freely bubbling fluidized beds was proposed. The model was derived from basic material and momentum balance analyses of the net solid circulation flow inside the bed. At this stage, the model's main value is in giving a qualitative picture of this solid flow behavior. Its quantitative predictions could not be fully tested with the experimental data of this study. This requires data on a bed in which the solids movement in the wall layers is not affected by the bed internal tube array.

To minimize the difference in local solid mass fluxes at two perpendicular walls inside the bed, solid mass flow measurements should be made in a bed without an internal tube array. Thus, one instrumented tube (probe) should be used to measure local solid mass fluxes at three or more vertical locations close to one of the bed walls. Similar

measurements should be made in the middle bubbling region of the bed. Local solid mass fluxes in the wall region of the two-region model bed can be extrapolated from such data with minimum error.

This study was conducted on one size scaled bed. Further similar studies are necessary to test the scaling criteria and to establish the relationship between bed size and wall layer thickness before the solid circulation patterns in industrial-scale units can be predicted.

## BIBLIOGRAPHY

1. Walker, P. L., "Kinetics of Coal Pyrolysis and Gasification," Quarterly Technical Progress Report, April-June (1980). Coal Research Station, The Pennsylvania State University.
2. Park, D., Levenspiel, O., and Fitzgerald, T. J., "The Plume Model for Large Utility Scale Atmospheric Fluidized Bed Combustors," The Proceedings of the Sixth International Conference of Fluidized Bed Combustion, Vol 3 p. 791, Atlanta, GA, August (1980).
3. Van Deemter, J. J., "Mixing Patterns in Large-scale Fluidized Beds," Fluidization, edited by J. R. Grace and J. M. Matsen, Plenum (1980).
4. Martin-Gautier, A. F. L. and Pyle, D. C., "The Fluid Mechanics of Single Bubbles," In Fluidization Technology, edited by D. L. Keairns, McGraw-Hill (1976).
5. Fitzgerald, T. J. and Crane, S. D., "Cold Fluidized Bed Modeling," The Proceedings of the Sixth International Conference on Fluidized Bed Combustion, Vol. 3, p. 815, Atlanta, GA, August (1980).
6. Scharff, M. F. et al., of Jaycor. Final Report to U.S. Department of Energy, Morgantown Energy Research Center, Contract EY-77-C-21-8156, "Project to provide an Experimental Plan for the Merc 6'x6' Fluidized Bed Cold Test Model," (1977).
7. Merry, J. M. D. and Davidson, J. F., "Gulf Stream Circulation in Shallow Fluidized Beds," Trans. Inst. Chem. Engrs., Vol. 51, (1973).
8. Mori, Y. and Nakamura, K., "Particle Movement in a Gas-Solid Fluidized Bed," J. of Chem. Eng. of Japan, Vol. 1, No. 2 (1968).
9. Kondukov, N. B., et al., "An Investigation of the Parameters of Moving Particles in a Fluidized Bed by a Radioisotope Method,"

- Int. Chem. Eng., Vol. 4, No. 1 (1964).
10. Leva, M., Fluidization, McGraw-Hill, N.Y. (1959).
  11. Chen, M. M., Lyn, J., and Chao, B. T., "Computer Aided Particle Tracking, A Technique for Studying Solid Particle Dynamics in Gas or Liquid Fluidized Bed," AIChE Annual Meeting, New Orleans (1981).
  12. Highley, J. and Merrick, D., "The Effect of the Spacing Between Solid Feed Points on the Performance of a Large Fluidized Bed Reactor," AIChE Symposium Series, No. 116, Vol. 67 (1980).
  13. Katz, S. and Fenz, F. A., "Application of Radioactive Tracers," Petrol. Refiner., 33, 203 (1954).
  14. May, W. G., Chem. Eng. Progr., 55, 49 (Dec. 1959).
  15. Haines, A. K., King, R. A., and Woodburn, E. T., AIChE J. 18, 591 (1972).
  16. Blickle, T., Borlai, O., and Hodany, L., International Congress on Fluidization and Its Applications, Toulouse, France, 1973.
  17. Cranfield, R. R., "Solids Mixing in Fluidized Beds of Large Particles," AIChE Symp. Series, Vol. 74, No. 176 (1978).
  18. Fitzgerald, T., et al., "Cold Modeling of Fluidized-Bed Combustors," EPRI CS-1476, Project 315-1 Final Report, August (1980).
  19. Marsheck, R. M. and Gomezplata, A., "Particle Flow Patterns in a Fluidized Bed," AIChE J., Vol. 11, No. 1, (1965).
  20. Rozenbaum, R. B., Todes, O. M. and Fainshtein, L. N., J. of Engr. Phys., Vol. 25, No. 4 (1975).
  21. Heerties, P. M., Verloop, J. and Willems, R., Powder Tech., 4 (1970/71).
  22. Oki, K., Wolawender, W. P. and Fan, L. T., "The Measurement of Local

- Velocity of Solid Particles," Powder Technology, 18 (1977).
23. Ishide, M., Nishwaki, A. and Shirai, T., "Movement of Solid Particles Around Bubbles in a Three-Dimensional Fluidized Bed at High Temperatures," Fluidization, edited by J. R. Grace and J. M. Matsen, Plenum, (1980).
  24. Colonias, John S., Particle Accelerator Design: Computer Programs, Academic Press, 1974.
  25. Knowlton, T. M. and Hirsan, T., "Wet and Dry Limestone Feeding Using an L-Valve," The Proceedings of the Sixth International Conference on Fluidized Bed Combustion, Vol. II, Atlanta, GA, August (1980).
  26. Kunii, D. and Levenspiel, O., Fluidization Engineering, Wiley, New York, 1969.
  27. Wen, C. Y. and Yu, Y.H., "A Generalized Method for Predicting the Minimum Fluidization Velocity," AIChE J., 12 610 (1966).
  28. Fitzgerald, T. J., "Fundamentals of Fluidized Bed Hydrodynamics as Applied to FBC System Design," Proceedings of DOE/WVU Conference on Fluidized Bed Combustion System, Design and Operation, october 27-29, Morgantown, WV, (1980).
  29. Davidson, J.F. and Harrison, D., Fluidized Particles, Cambridge University Press, Cambridge (1963).
  30. Row, P.N. and Partridge, B.A., Particle Movement Caused by Bubbles in a Fluidized Bed, Third Congress of European Federation of Chemical Engineers, London, June 2, 1962.
  31. Pyle, D.L. and Rose, P.L., Chemical Reaction in Bubbling Fluidized Beds, Chem. Eng. Sci., 20,25 (1965).
  32. Cranfield, R.R. and Geldart, D., Large Partical Fluidization, Chem. Eng. Sci., 29, 935 (1974).



33. Masson, H., Solid Circulation Studies in a Gas Solid Fluid Bed, AIChE J., 33, 621 (1977).
34. Catipovic, N.M., Jovanovic, G.N. and Fitzgerald, T.J., Regimes of Fluidization for Large Particles, AIChE J., 3 (1978).
35. Jovanovic, G.N., Gas Flow in Fluidized Beds of Large Particles; Experiment and Theory, Ph.D. Thesis, Oregon State University, 1979.
36. IMSL Library Reference Manual, Chapter D; Volume 1, 8th Edition, June 1980.
37. Davis, R.M. and Taylor, G.I., Proc. Roy. Soc., A200, 375, (1950).
38. The Babcock and Wilcox Company, Annual Report, 1978, prepared for The Electric Power Research Institute (RP-718-2).
39. Levenspiel, O., et al., A Magnetic Control Valve for Flowing Solids: Exploratory Studies, Ind. Eng. Chem. Proc. Des. Dev., Vol. 21, No. 4, (1982).
40. Carnahan, B., Luther, H.A., and Wilkes, J.O., Applied Numerical Methods, John Wiley & Sons, Inc., New York (1969).

## APPENDICES

## APPENDIX A

Schematic Drawing of the Electronic Instrumentation of the  
Magnetic Solid Particle Mass Flow Meter

Figure A.1 shows a detailed schematic drawing of the electronic circuits of the magnetic solid particle mass flow meter. One of two identical channels used for the experimental measurements in the bed is shown. Each channel consists of a WRITE coil drive circuit and a READ coil signal-amplification circuit. Both channels, however, were controlled by the same time control circuit.

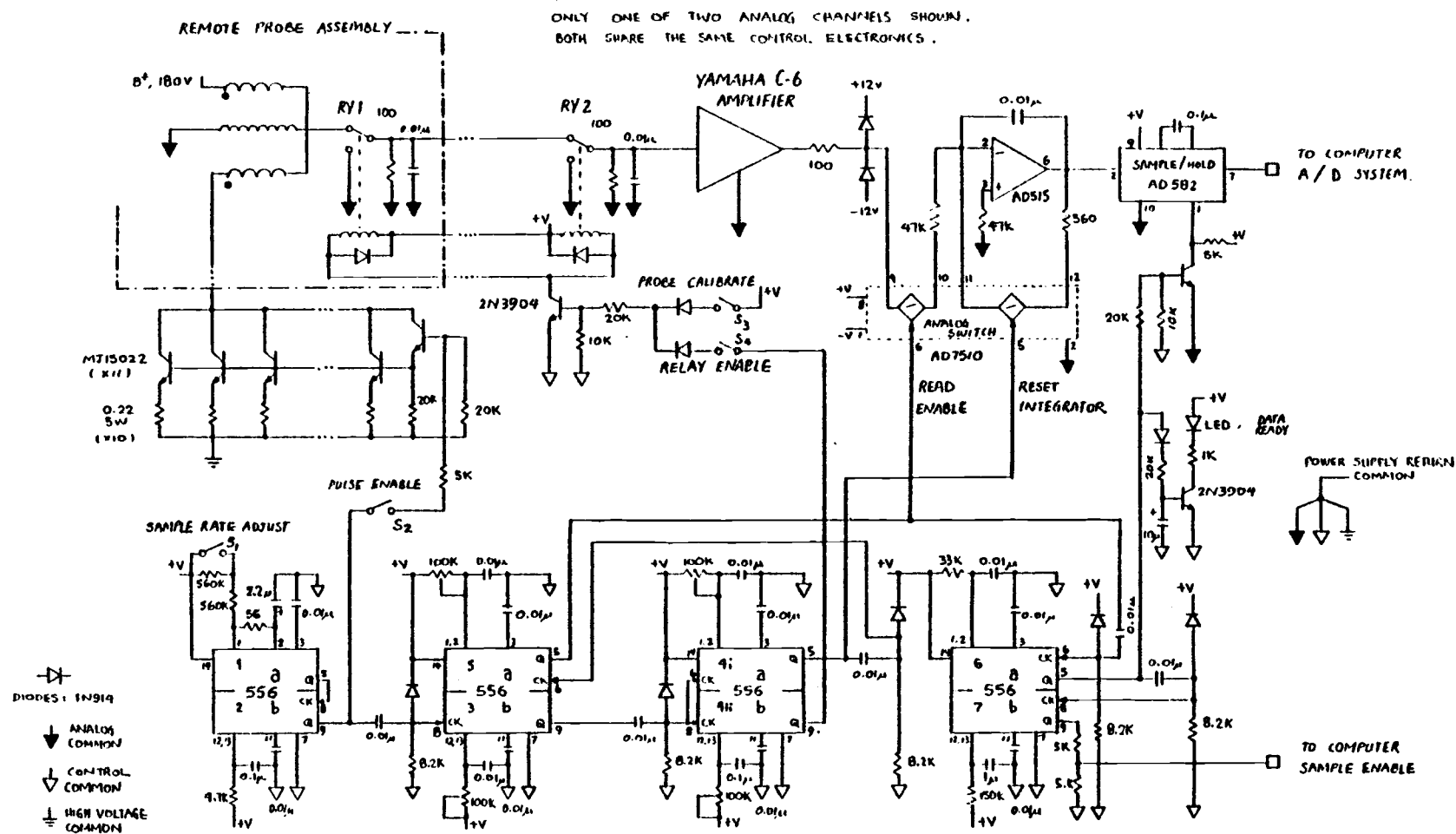


Figure A.1. Detailed schematic drawing of the electronic circuits of the magnetic solid particle mass flow meter.

## APPENDIX B

## Histogram Plots of Raw Data

Figures B.1, B.2, B.3 and B.4 show frequency histogram plots constructed from the raw data of the first, second, third, and fourth experiment respectively. Such representation of the data facilitates comparison between the behavior of local solid mass flux inside the bed under different fluidization conditions. Furthermore, it provides an additional tool to compare the hydrodynamic behavior of two different size beds.

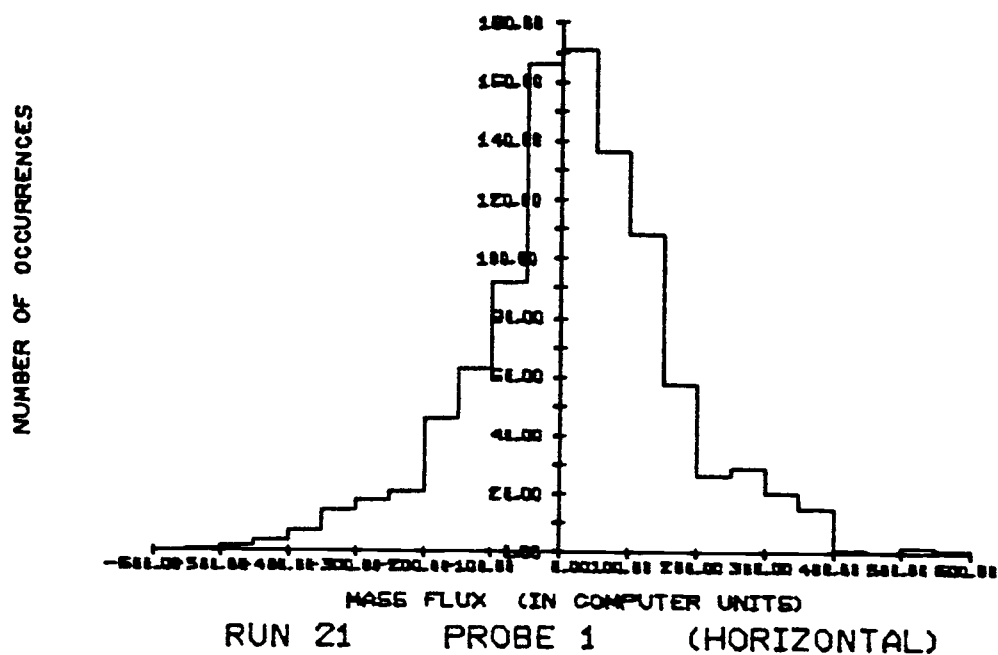
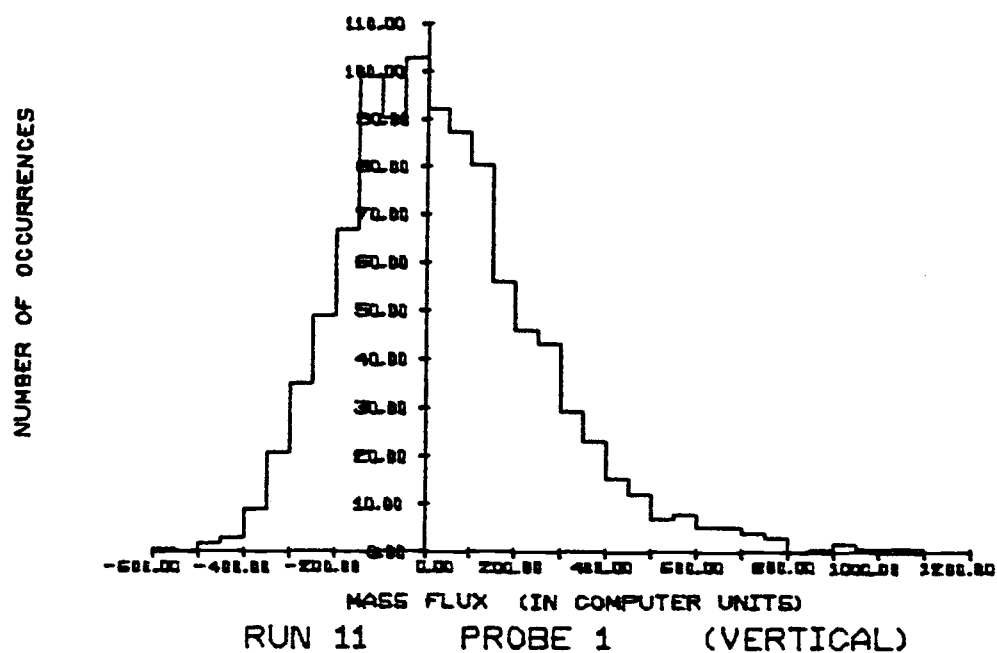


Figure B.1. Frequency histogram plots for the data of the first experiment.

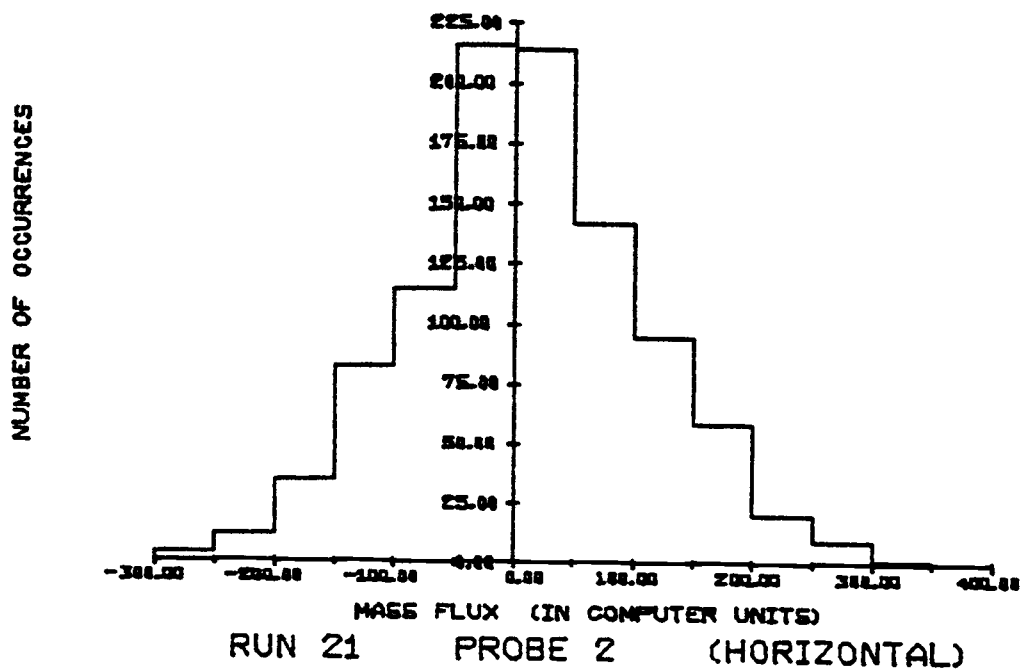
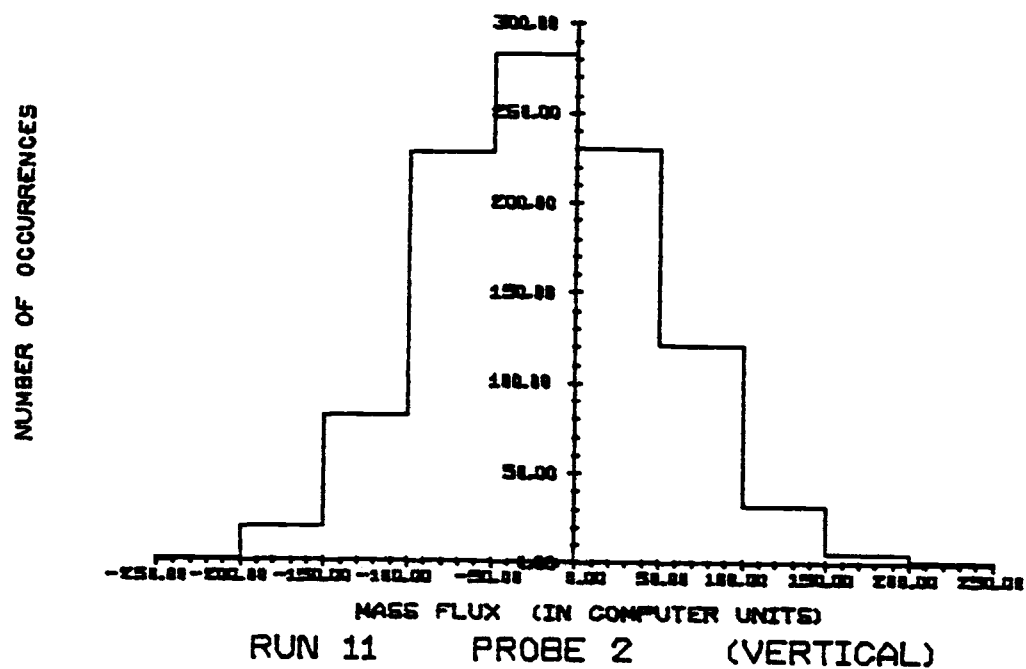


Figure B.1. (continued)

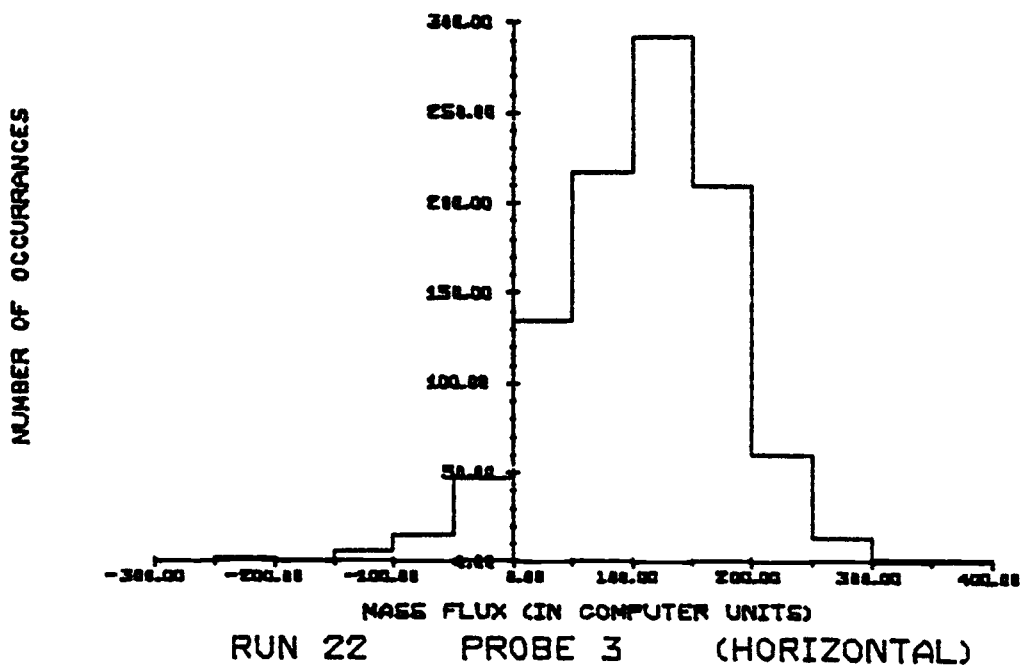
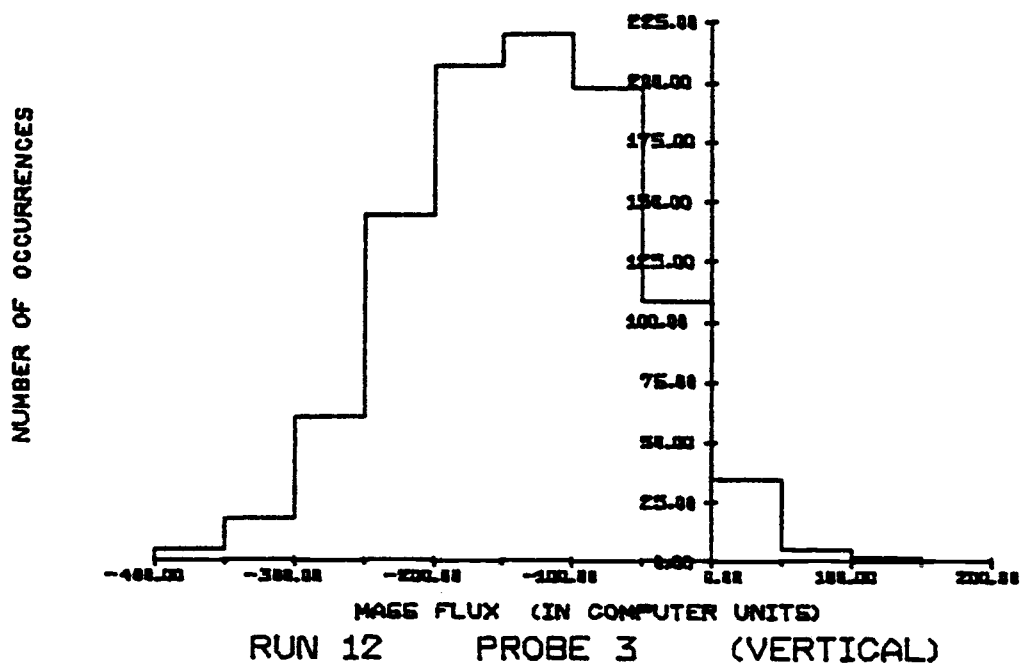


Figure B.1. (continued)



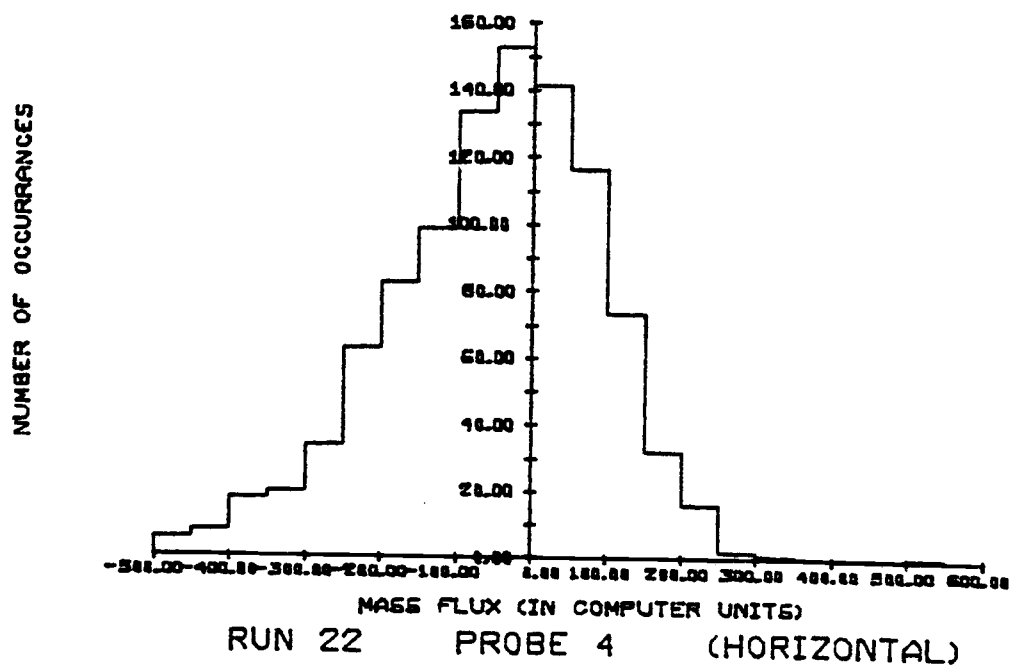
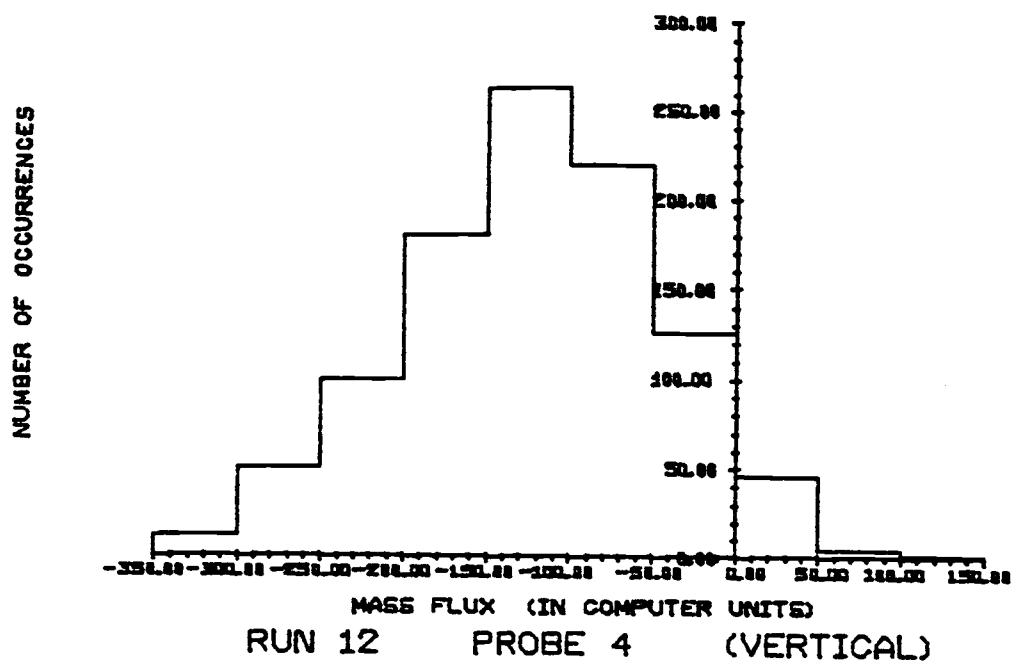


Figure B.1. (continued)

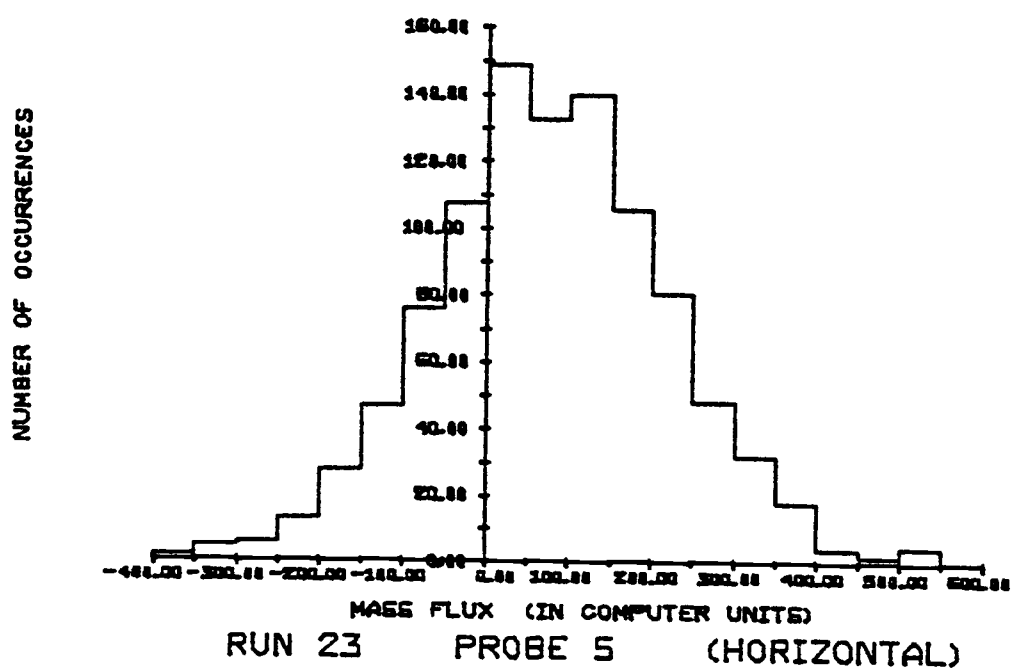
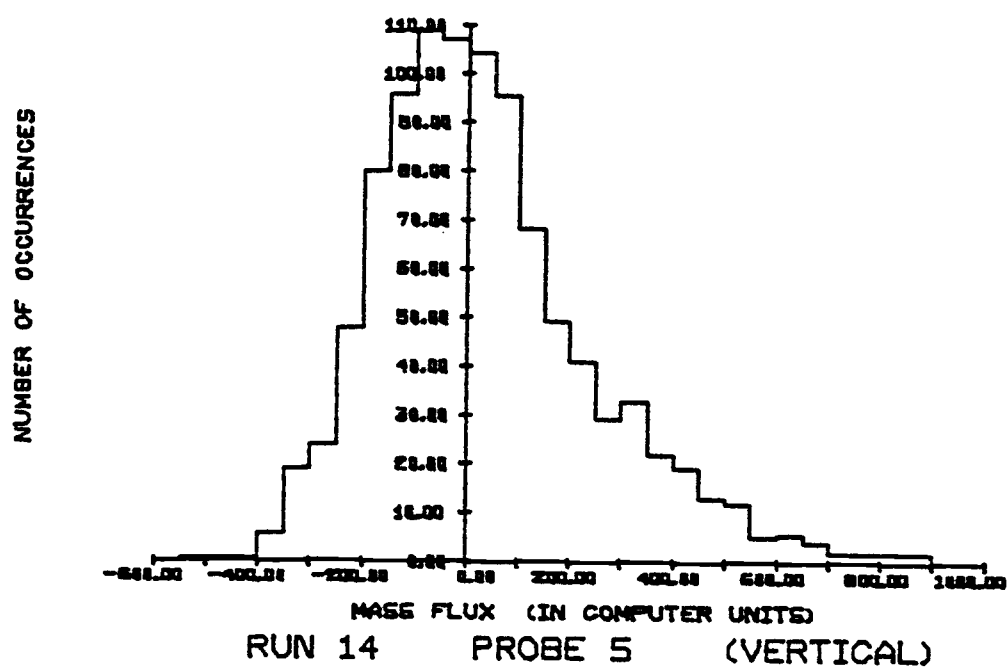


Figure B.1. (continued)

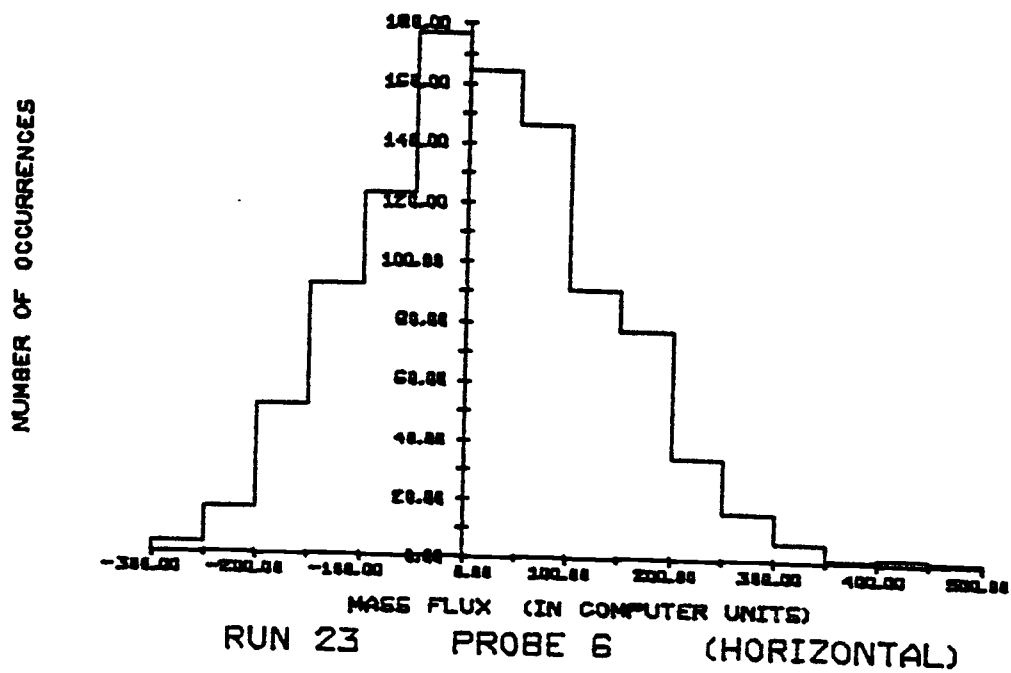
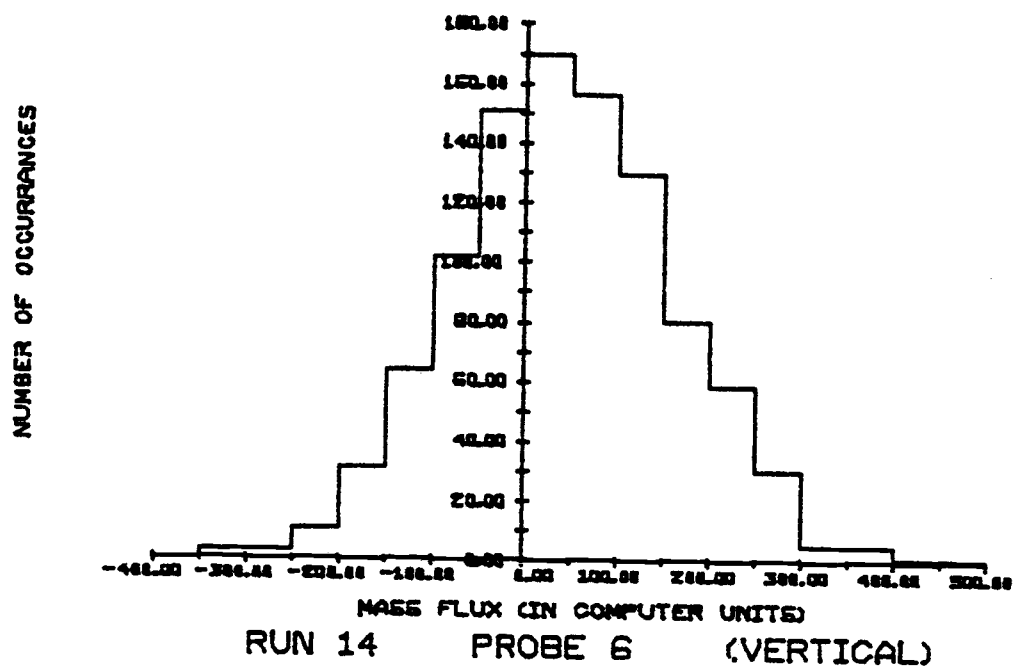


Figure B.1 (continued)

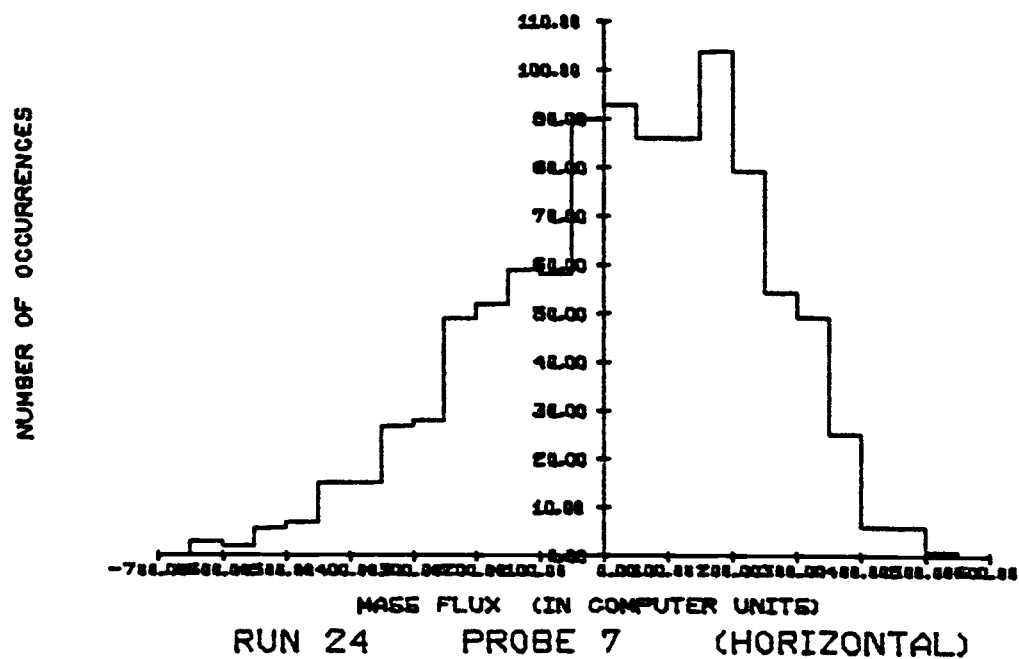
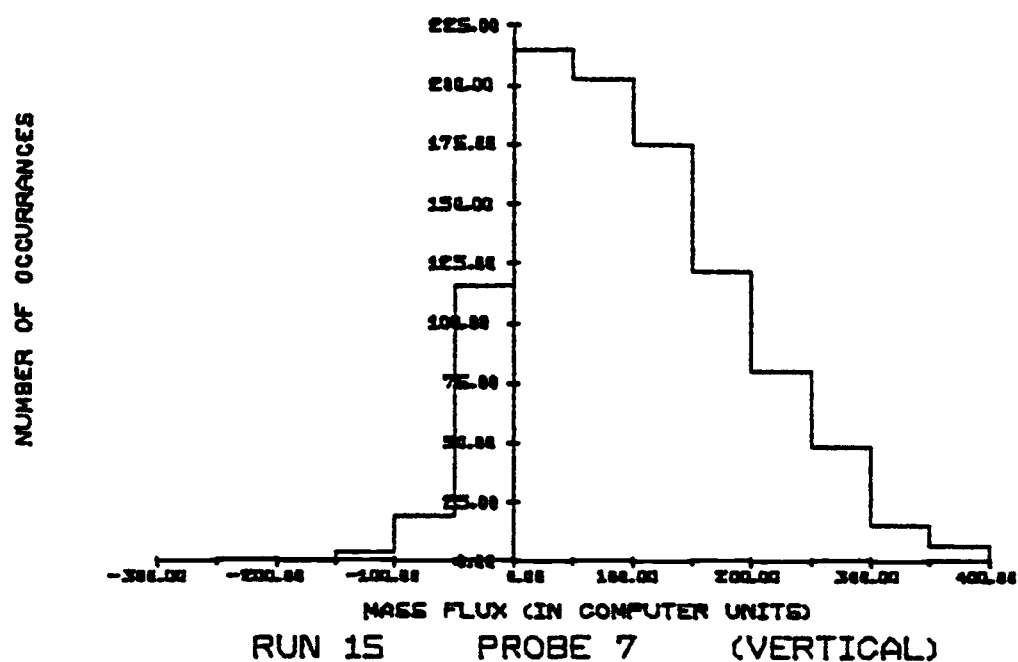


Figure B.1. (continued)

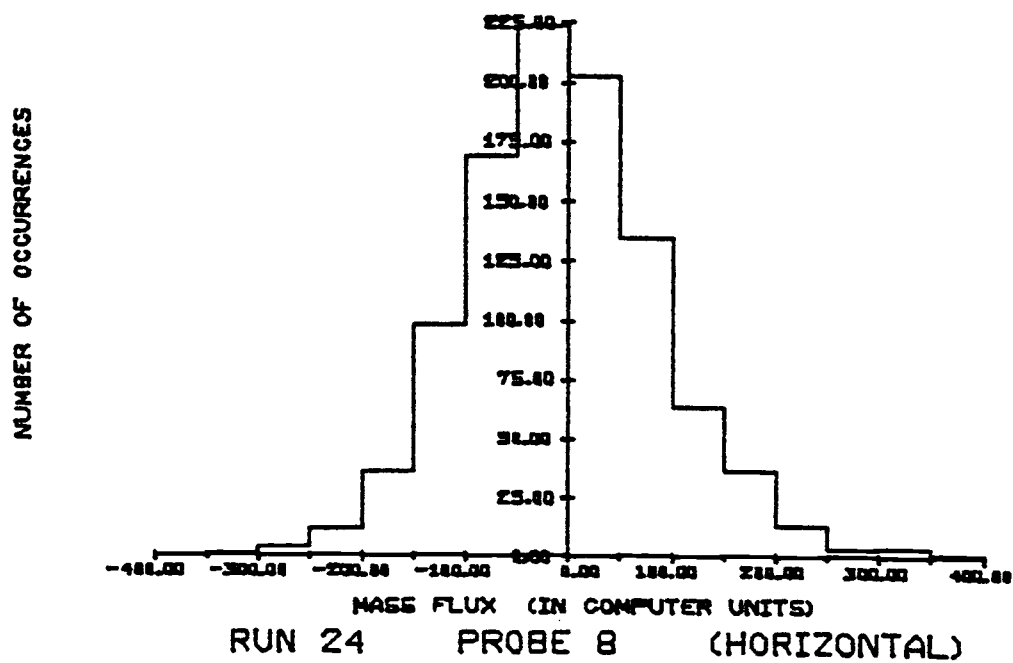
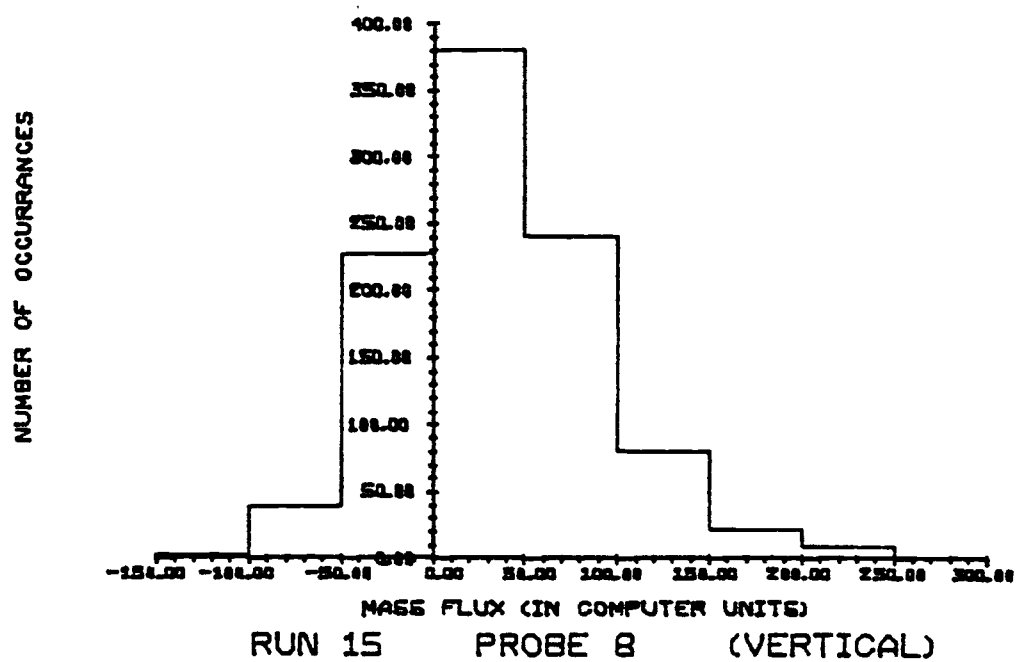


Figure B.1. (continued)

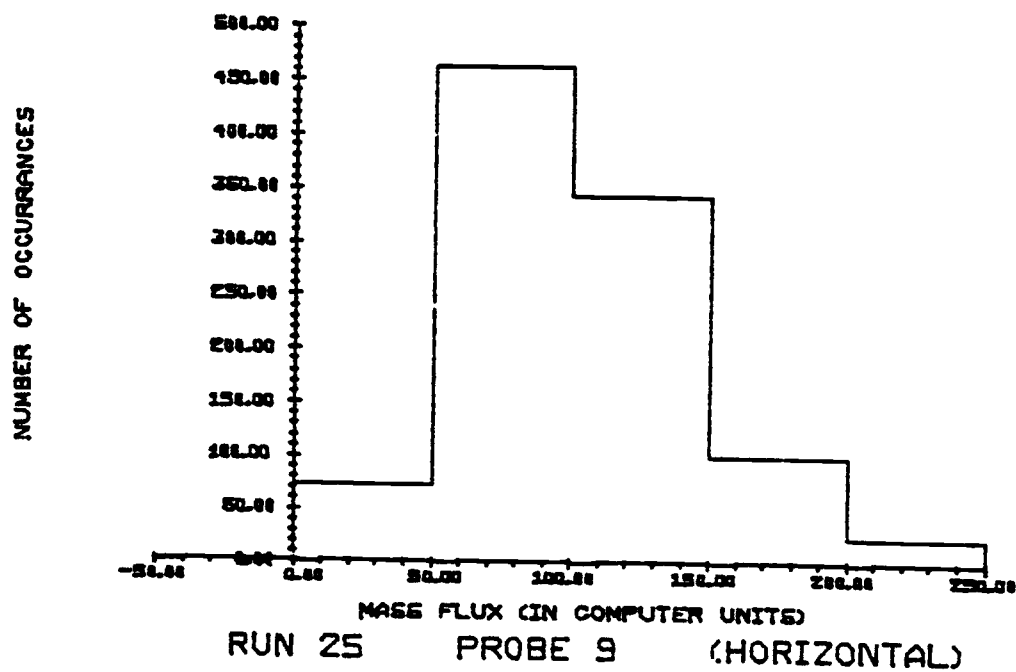
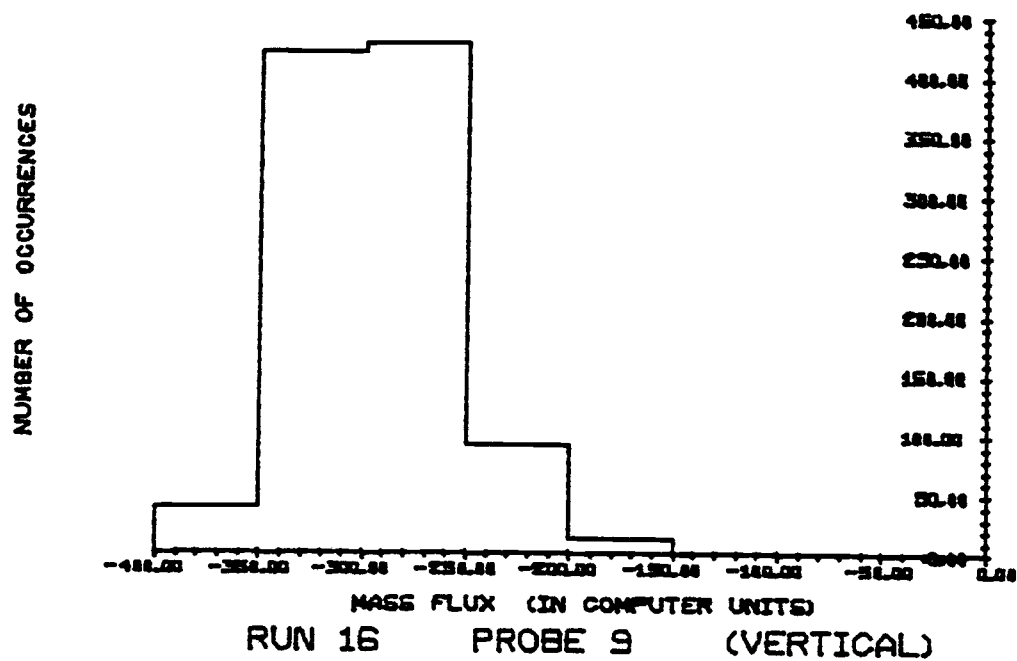


Figure B.1. (continued)

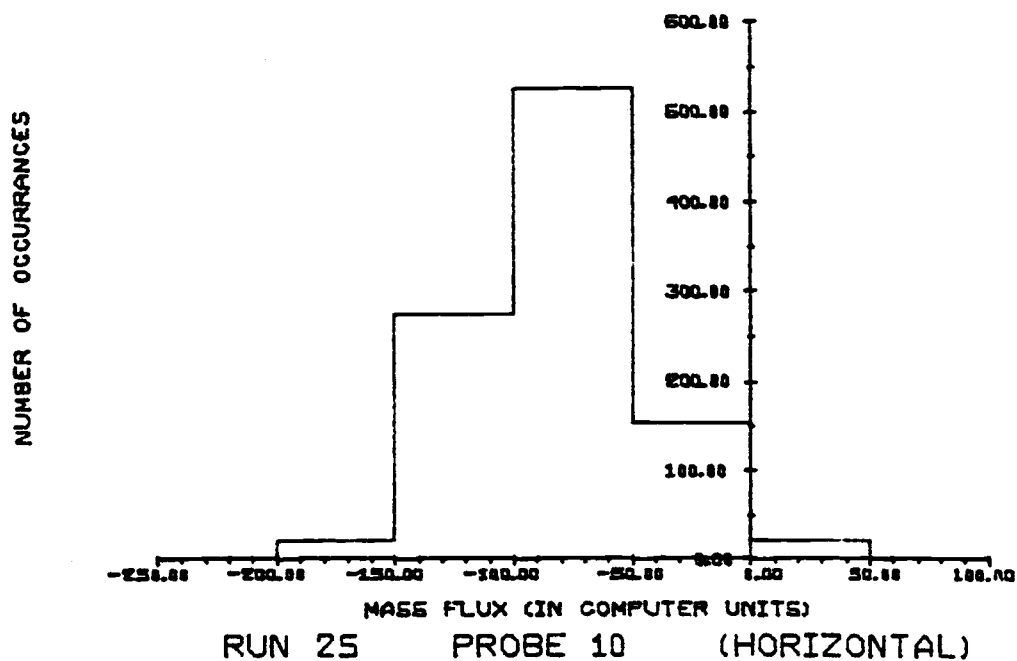
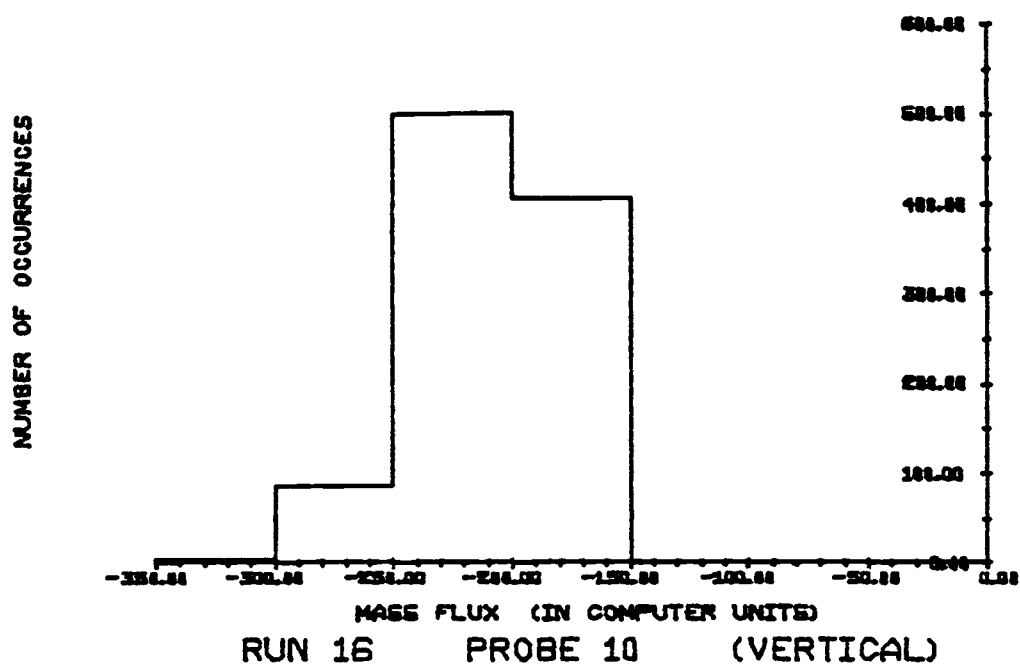


Figure B.1. (continued)

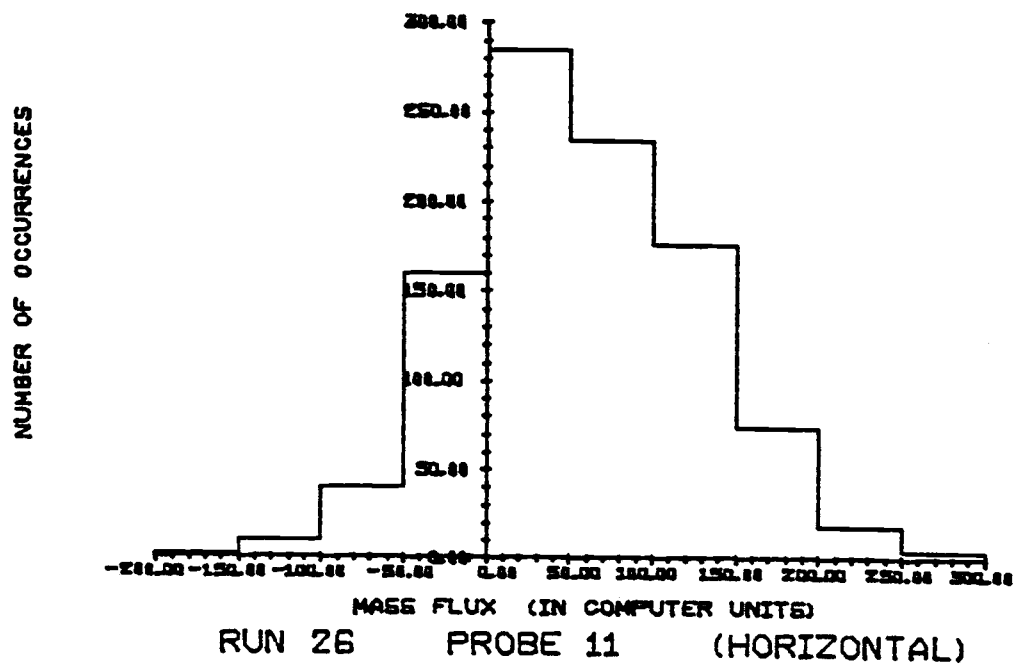
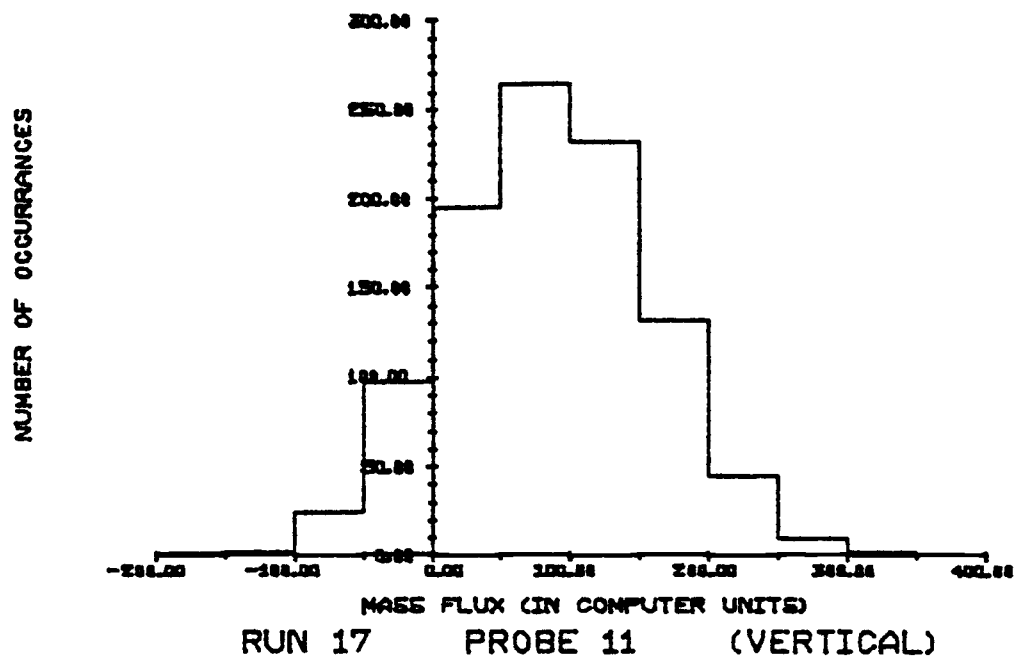


Figure B.1. (continued)



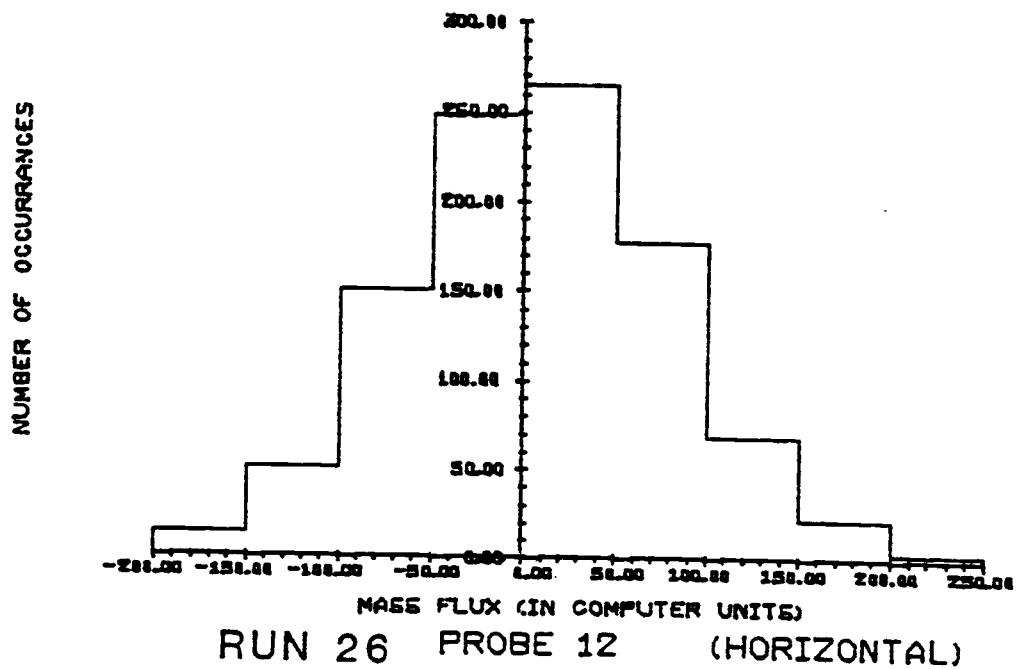
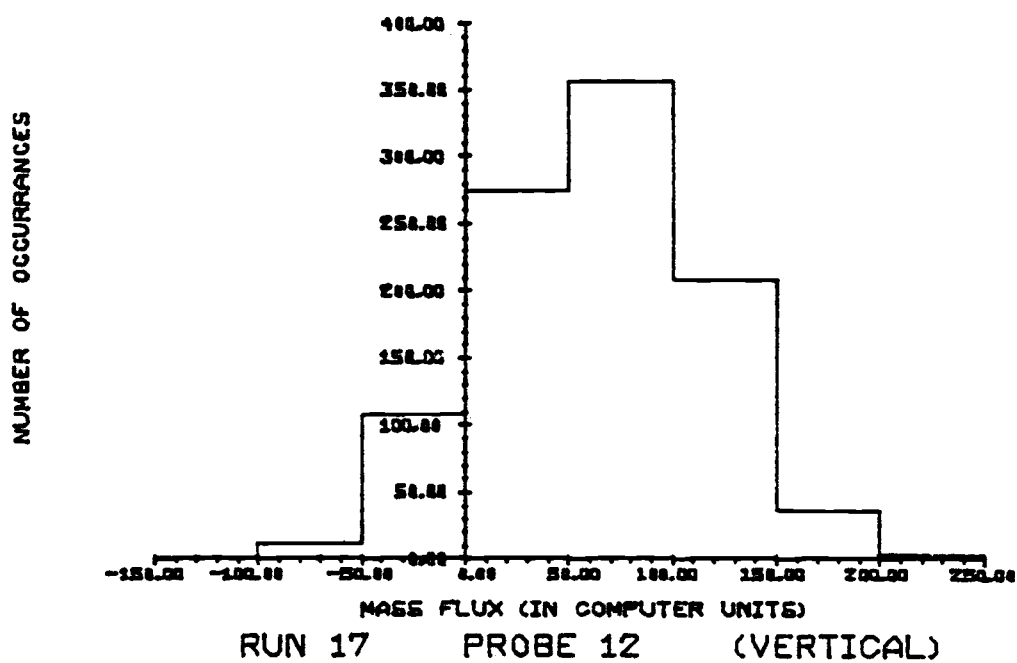


Figure B.1. (continued)

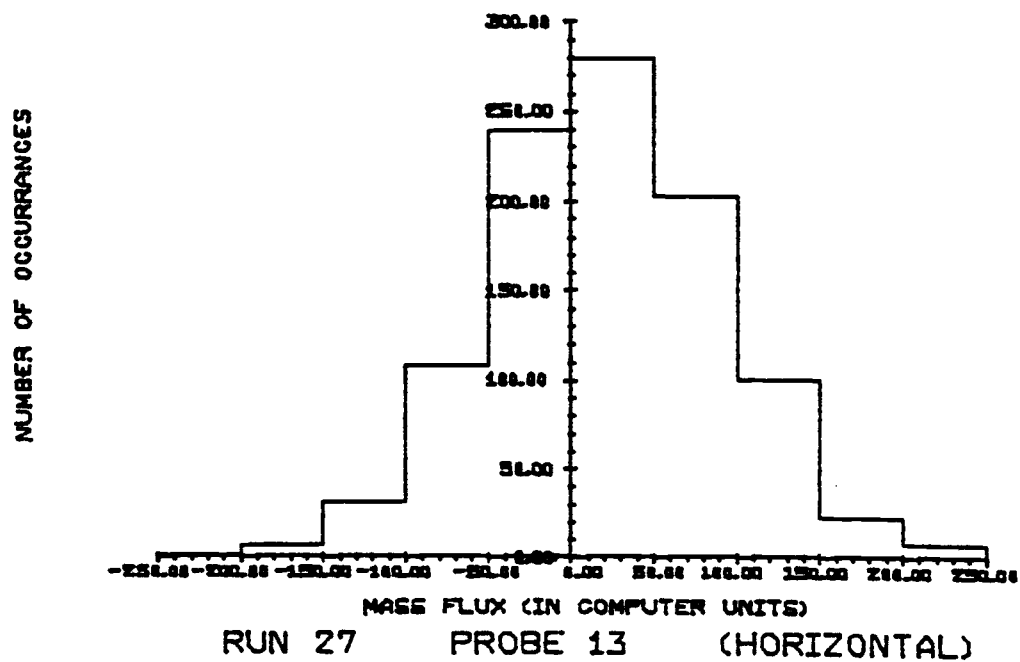
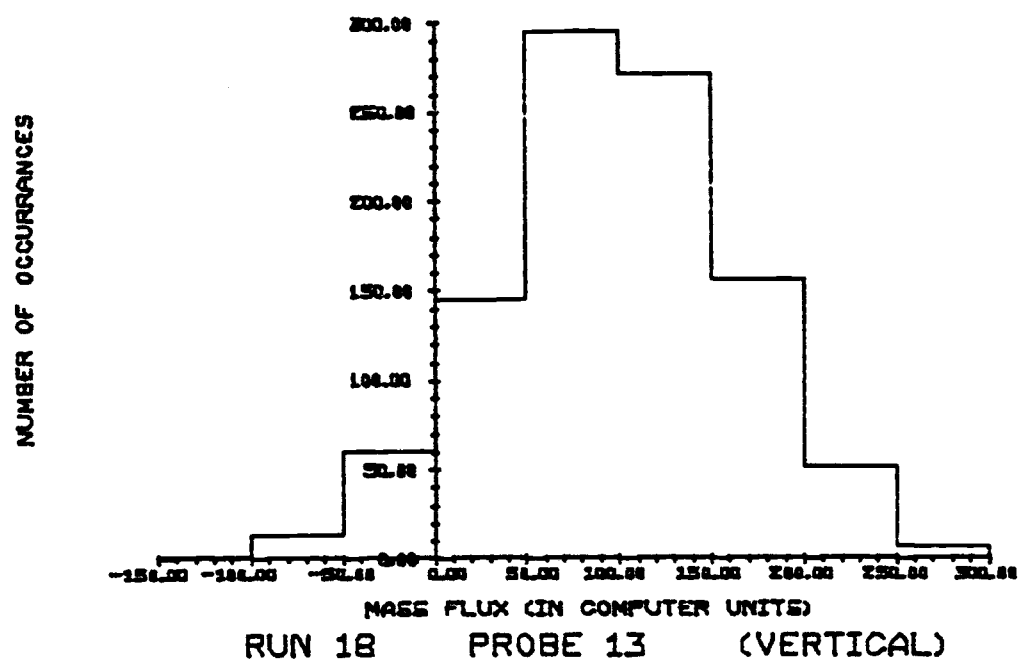


Figure B.1. (continued)

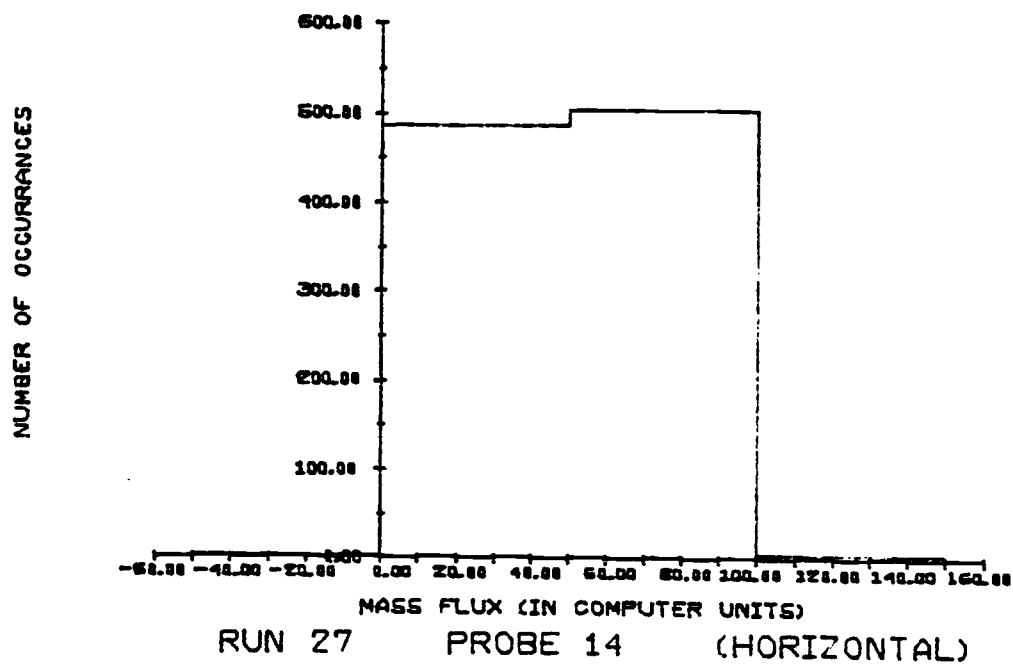
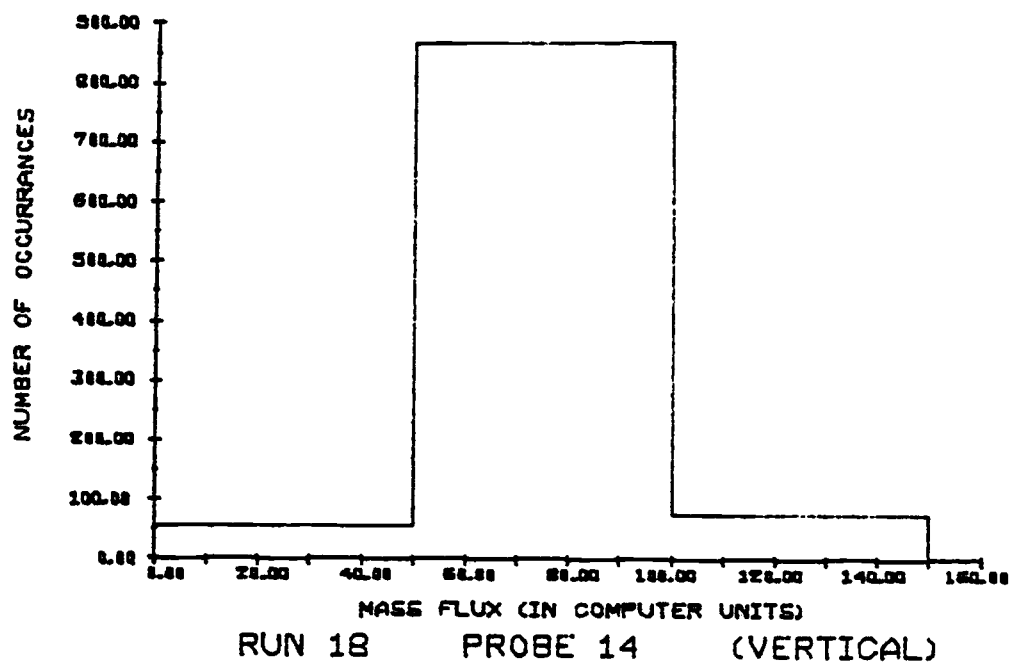


Figure B.1. (continued)

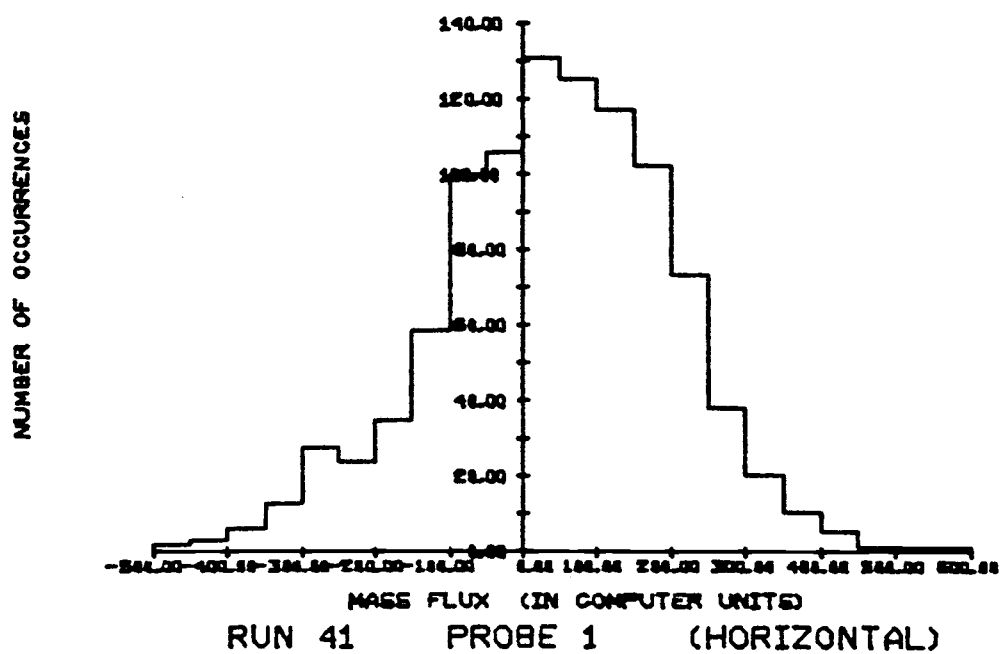
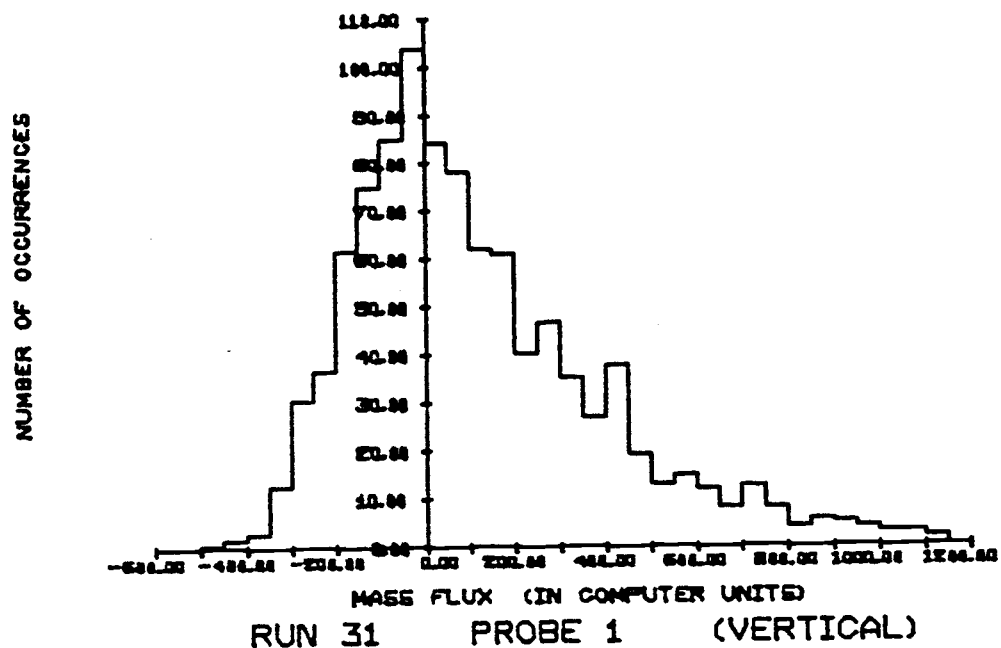


Figure B.2. Frequency histogram plots for the data of the second experiment.

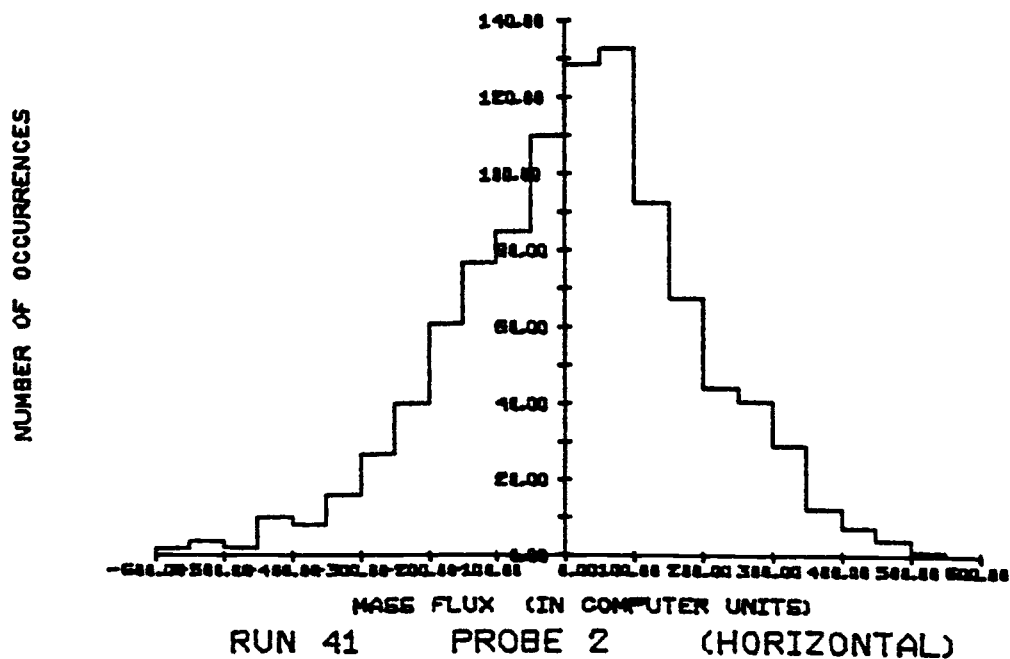
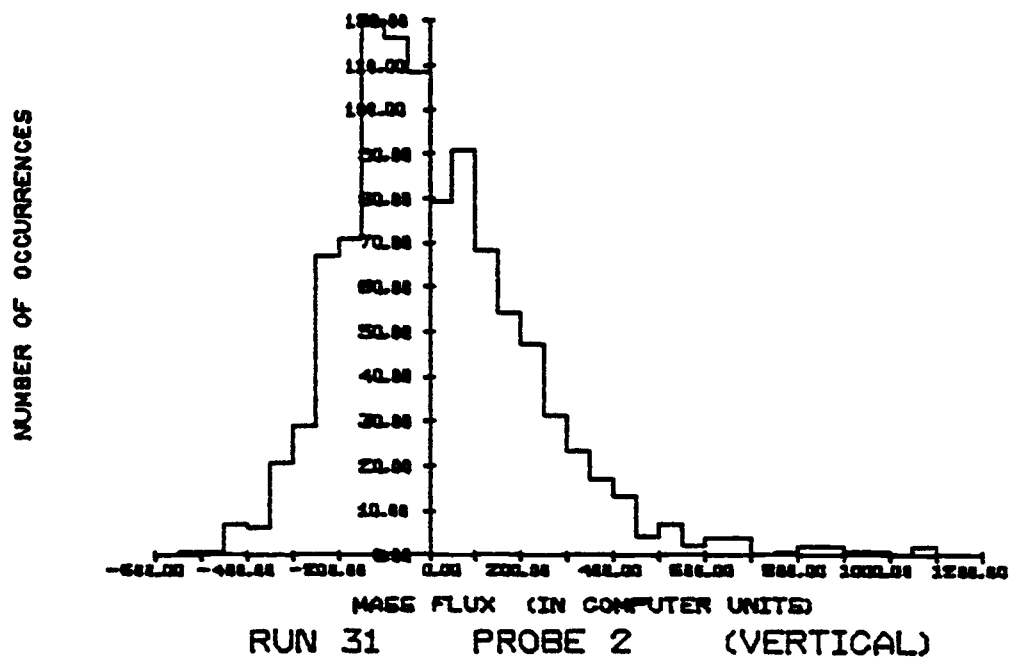


Figure B.2. (continued)

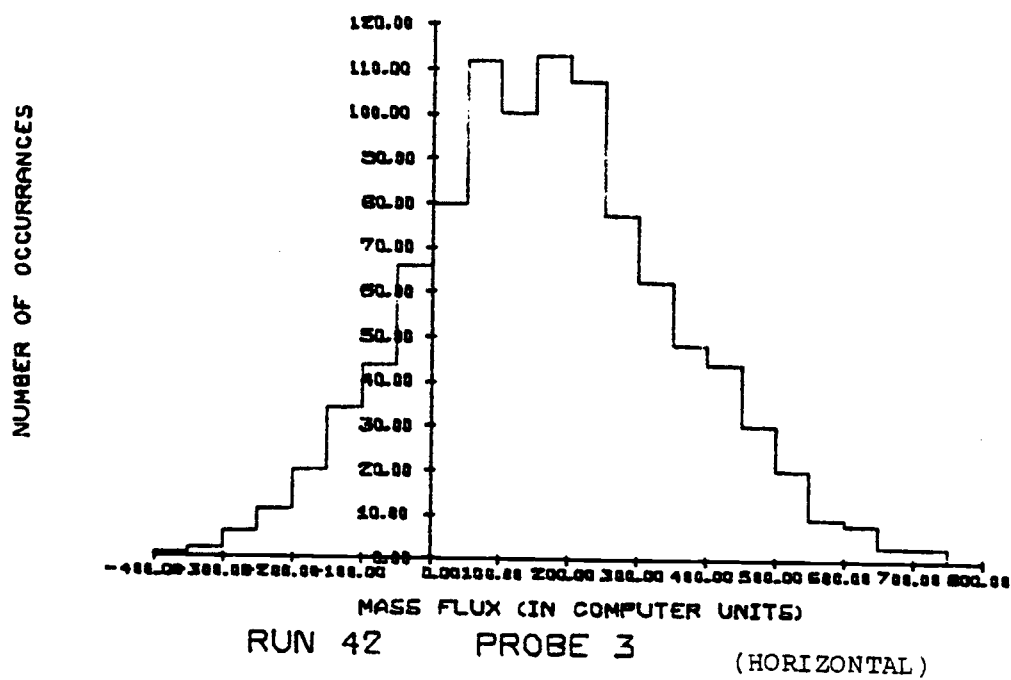
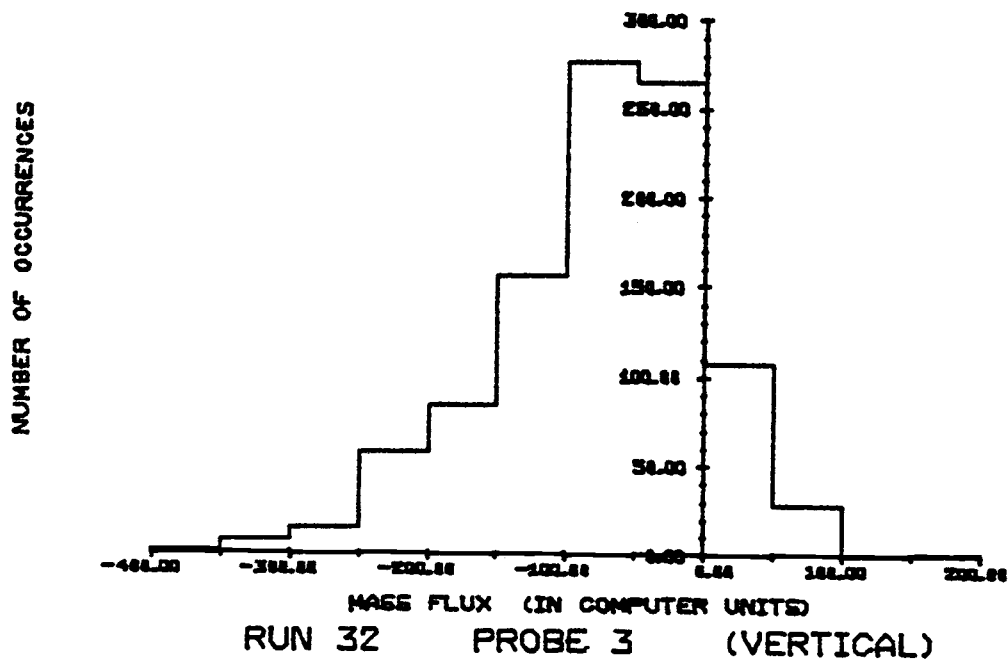


Figure B.2. (continued)

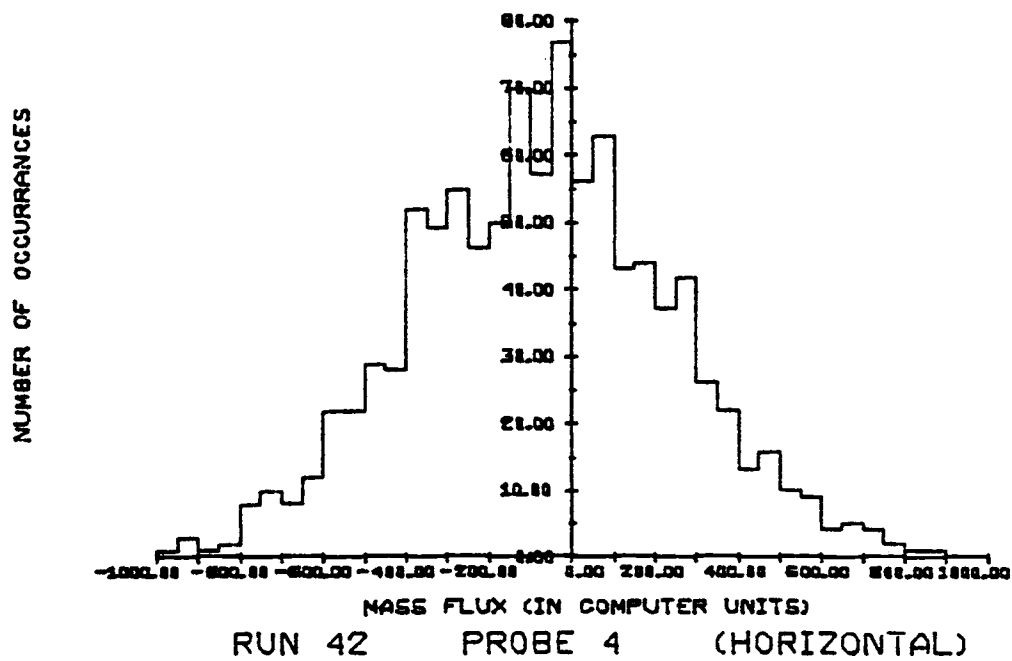
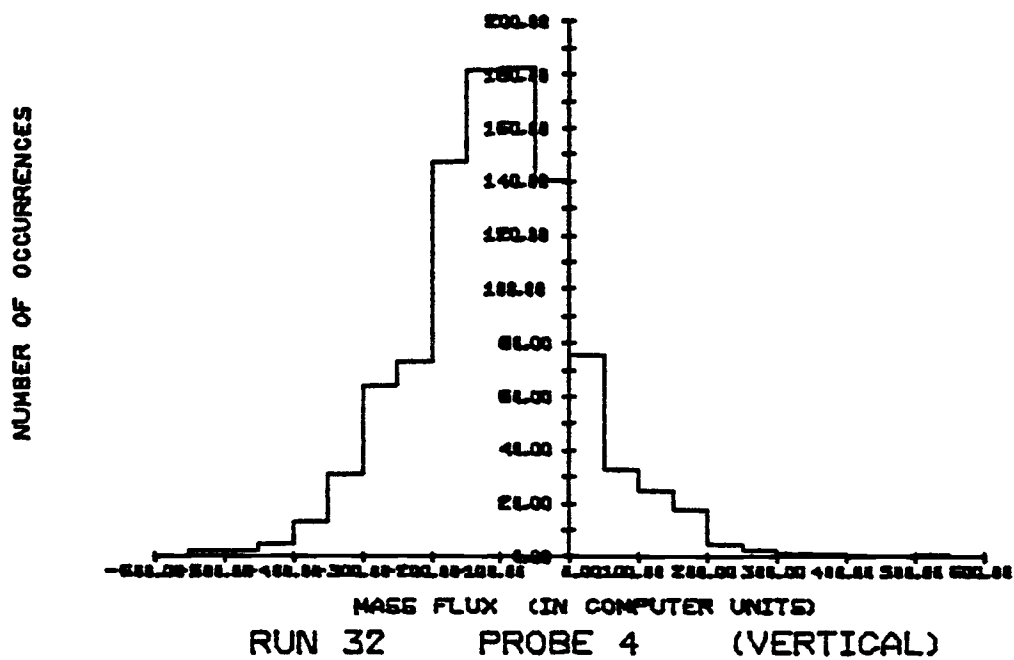


Figure B.2. (continued)

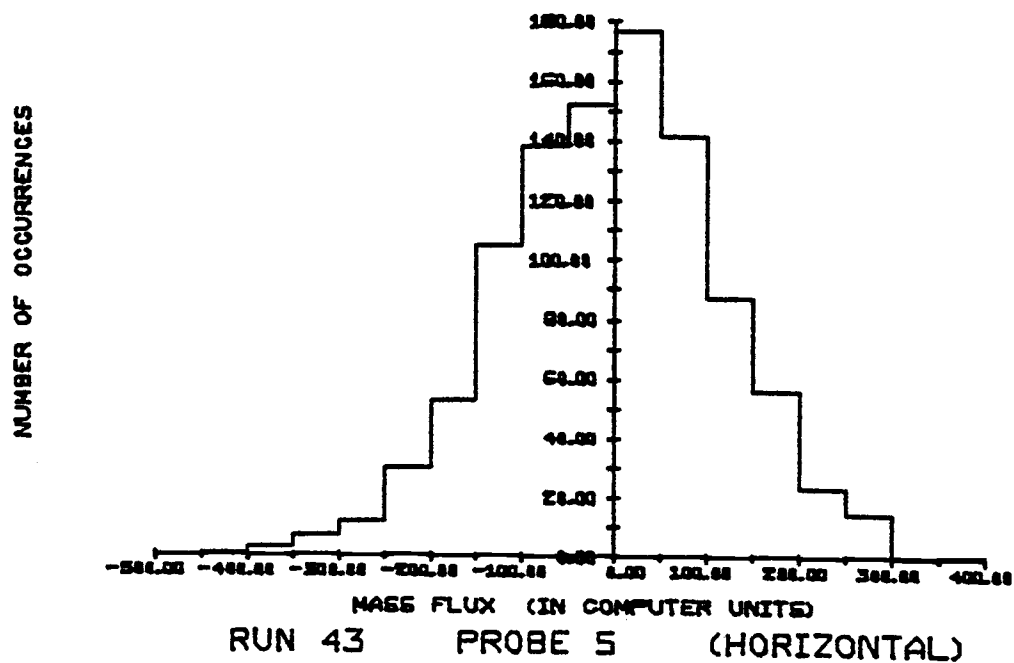
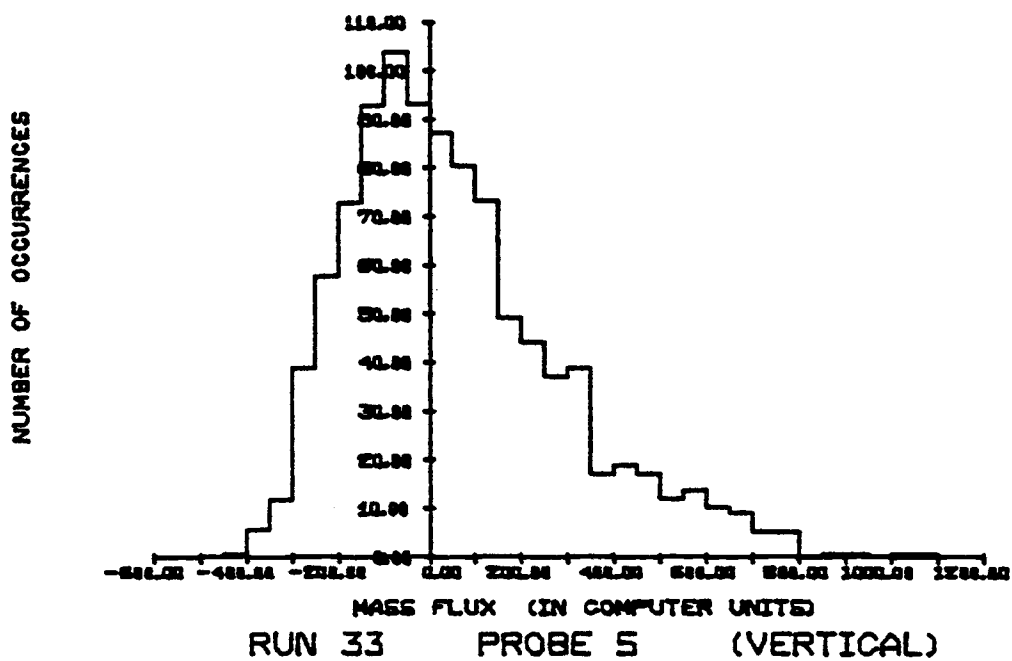


Figure B.2. (continued)



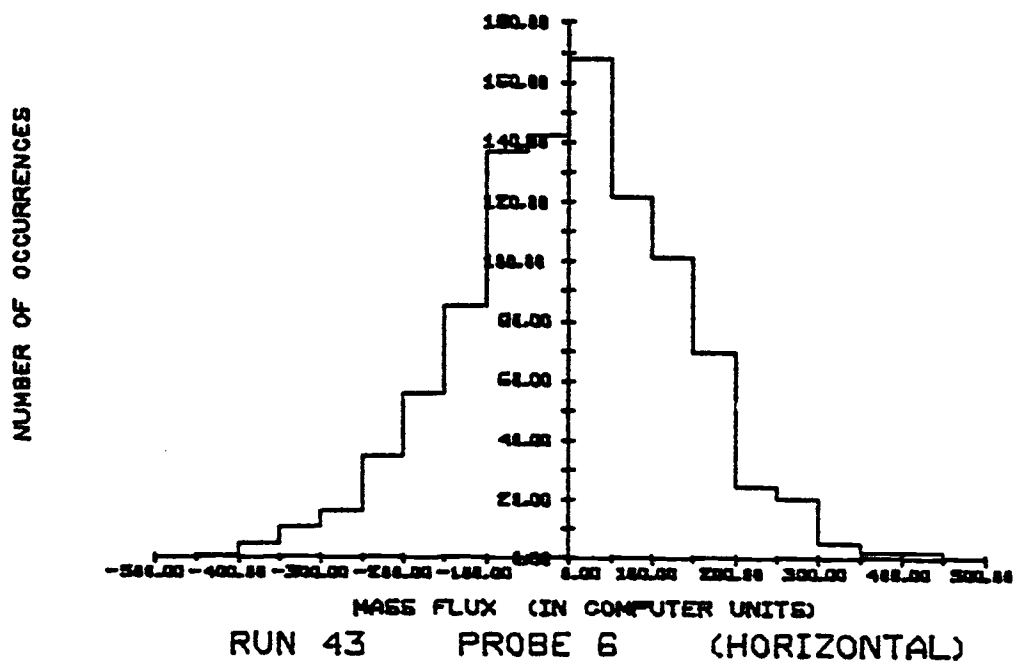
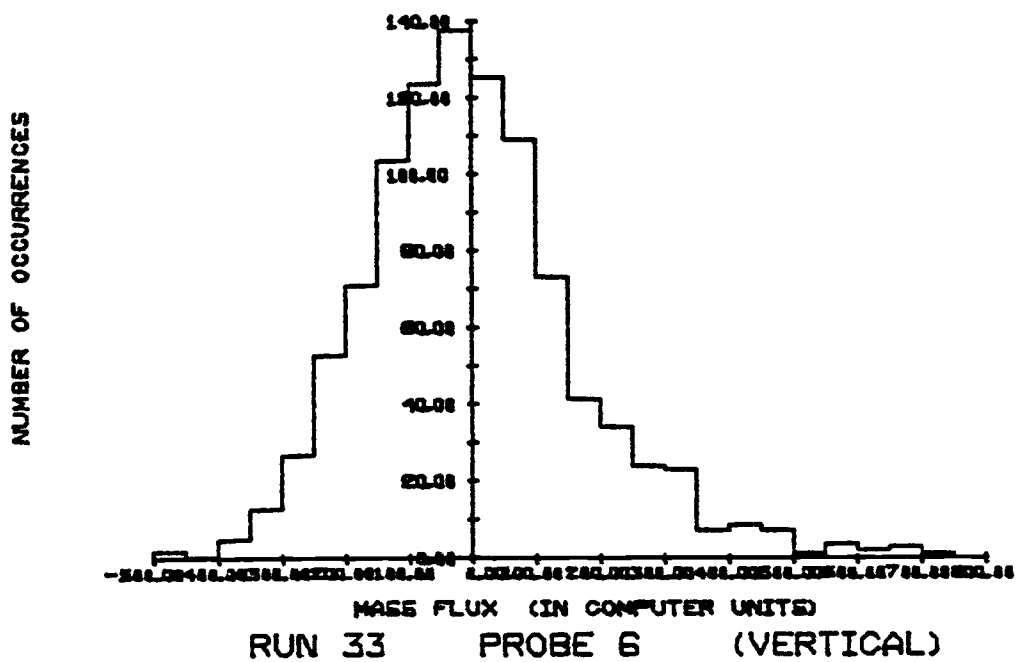


Figure B.2. (continued)

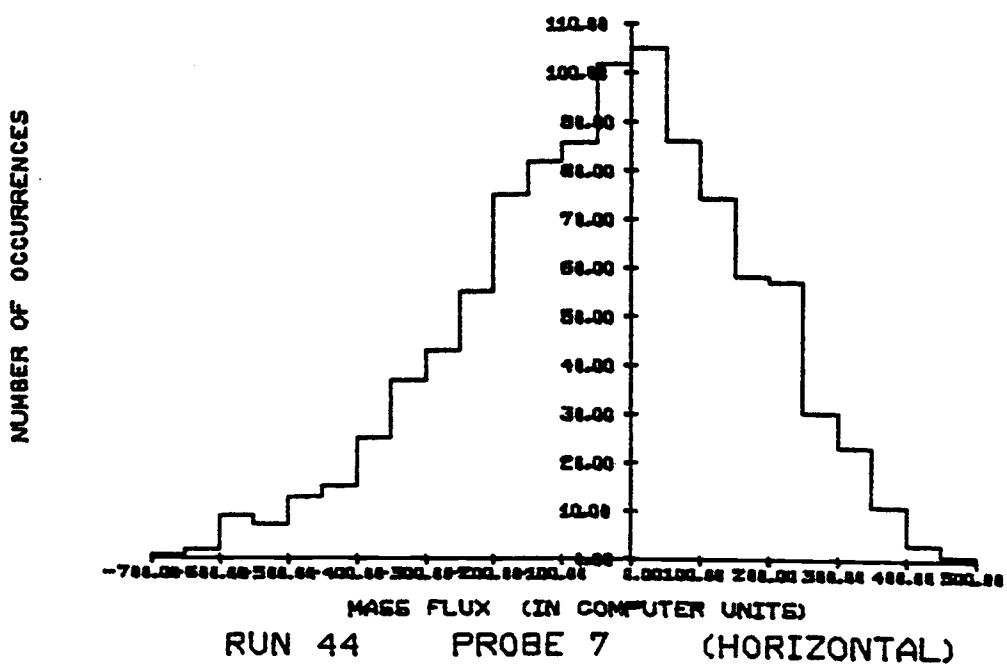
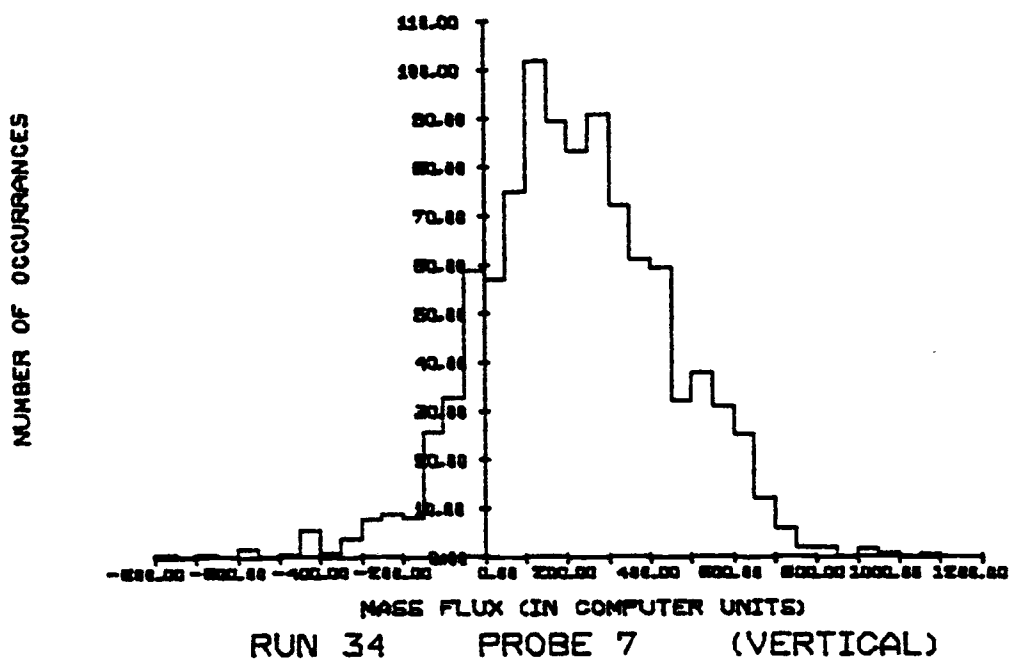


Figure B.2. (continued)

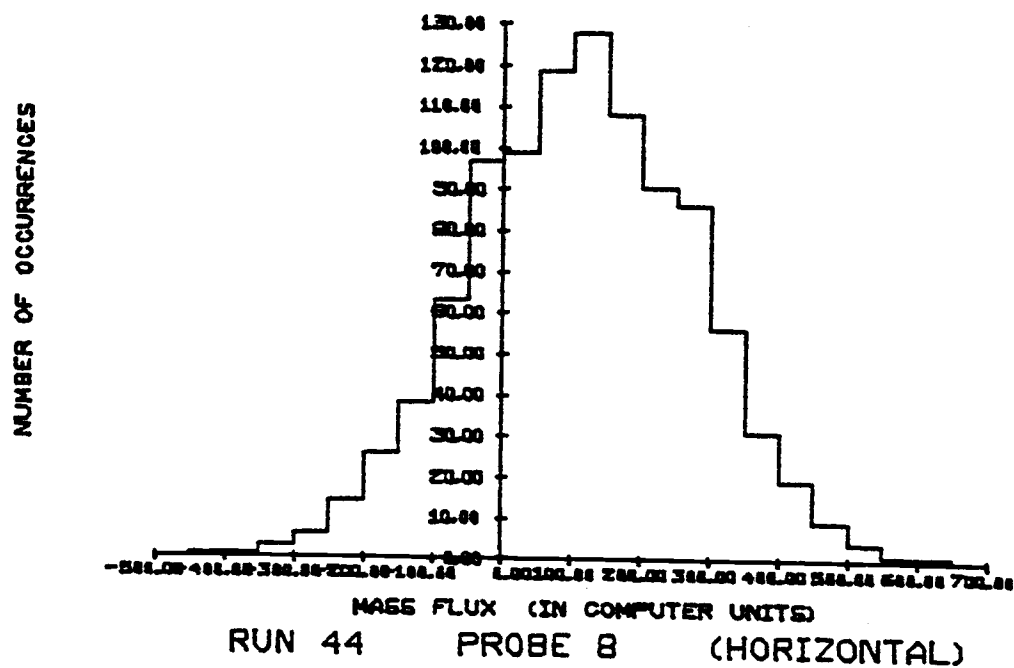
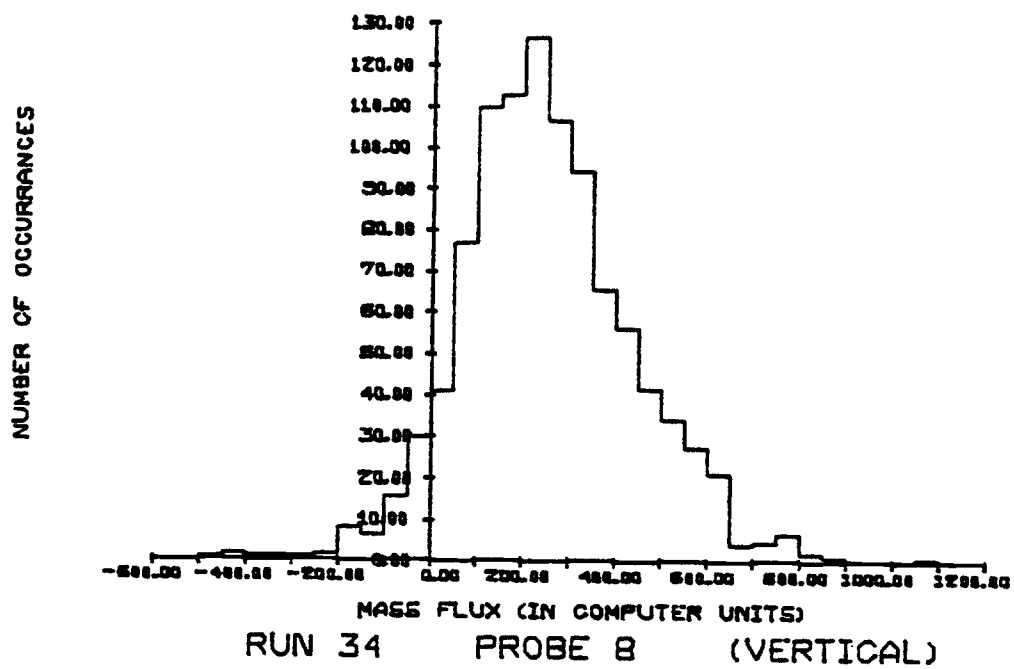


Figure B.2. (continued)

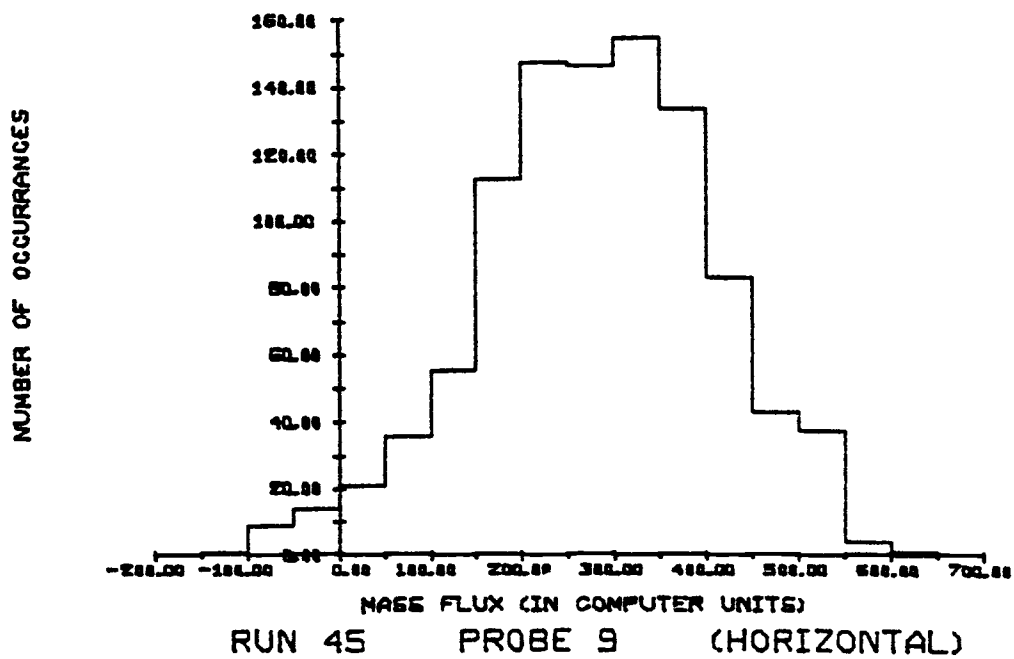
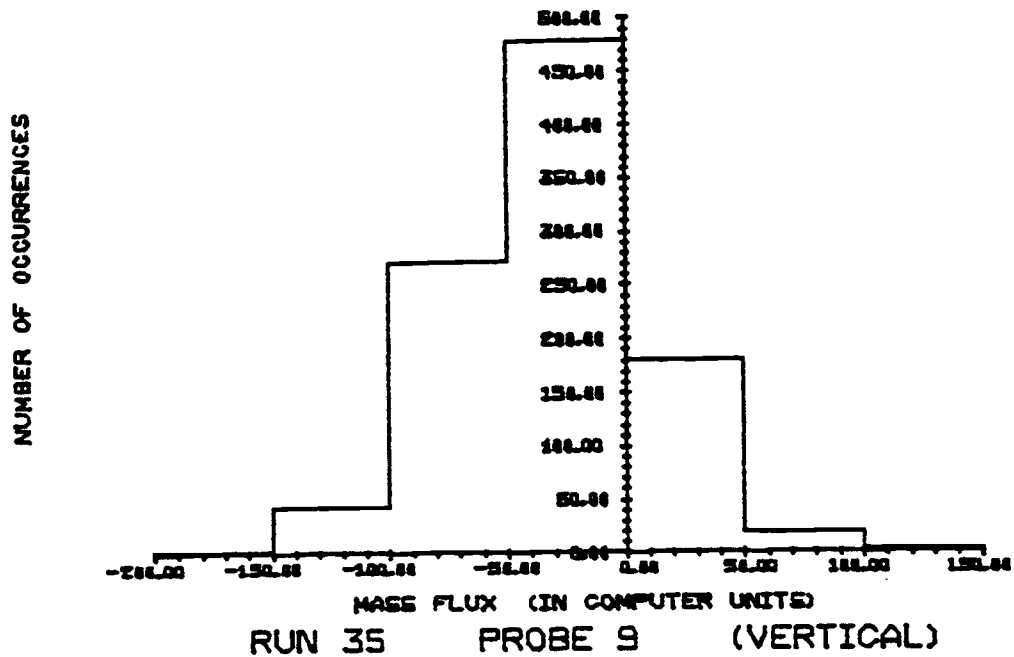


Figure B.2. (continued)

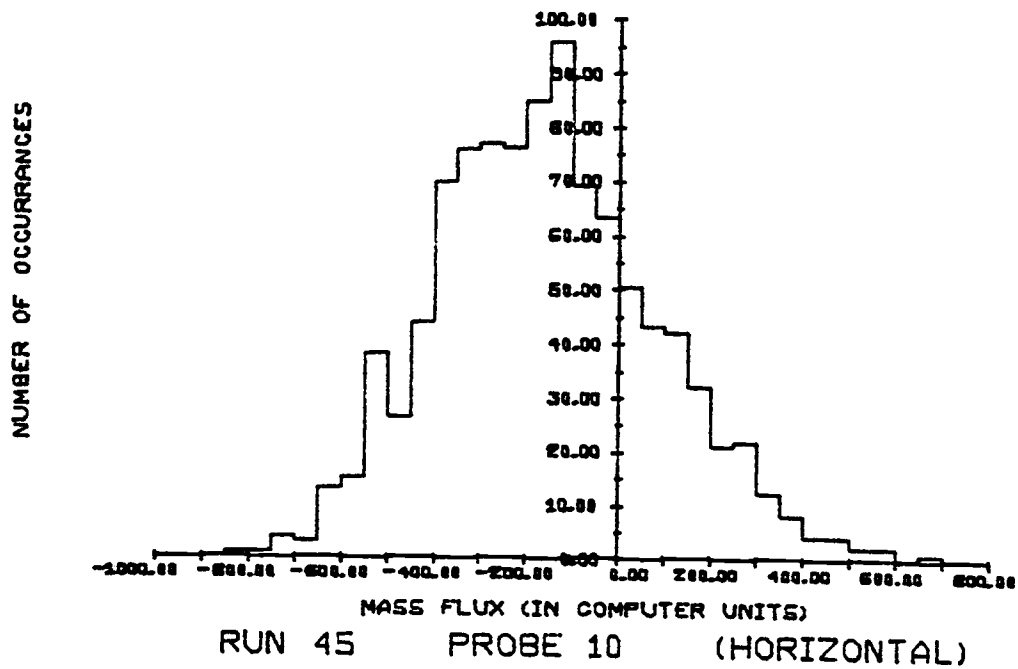
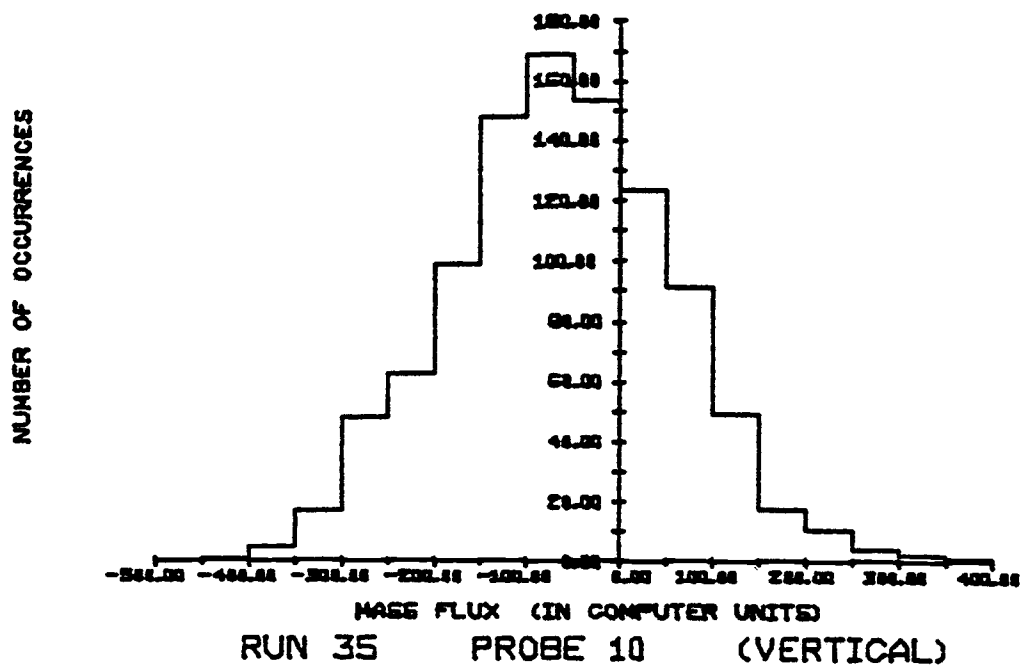


Figure B.2. (continued)

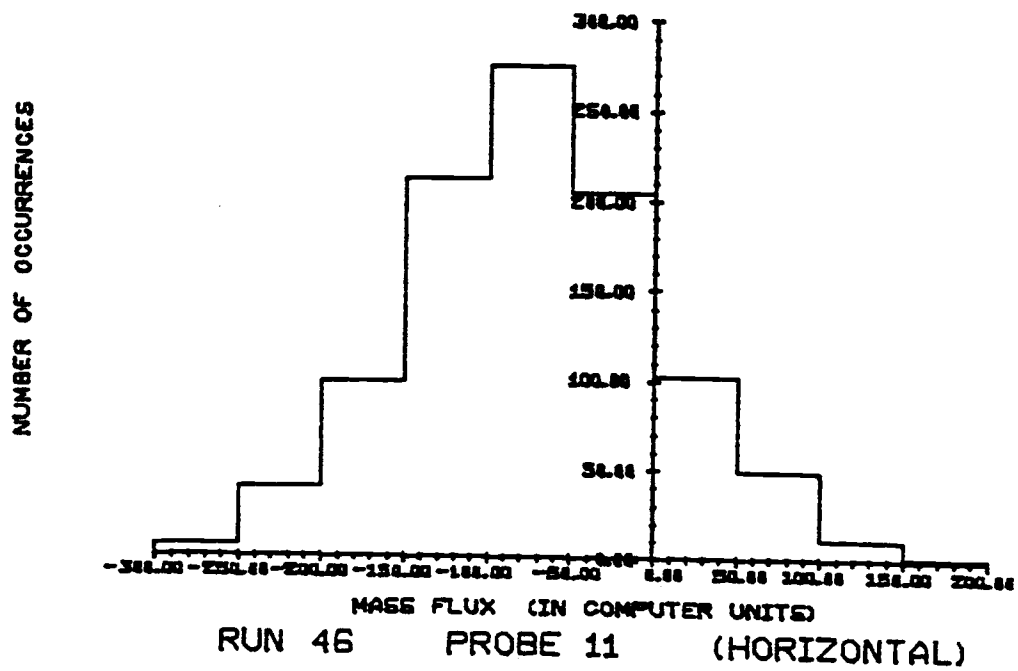
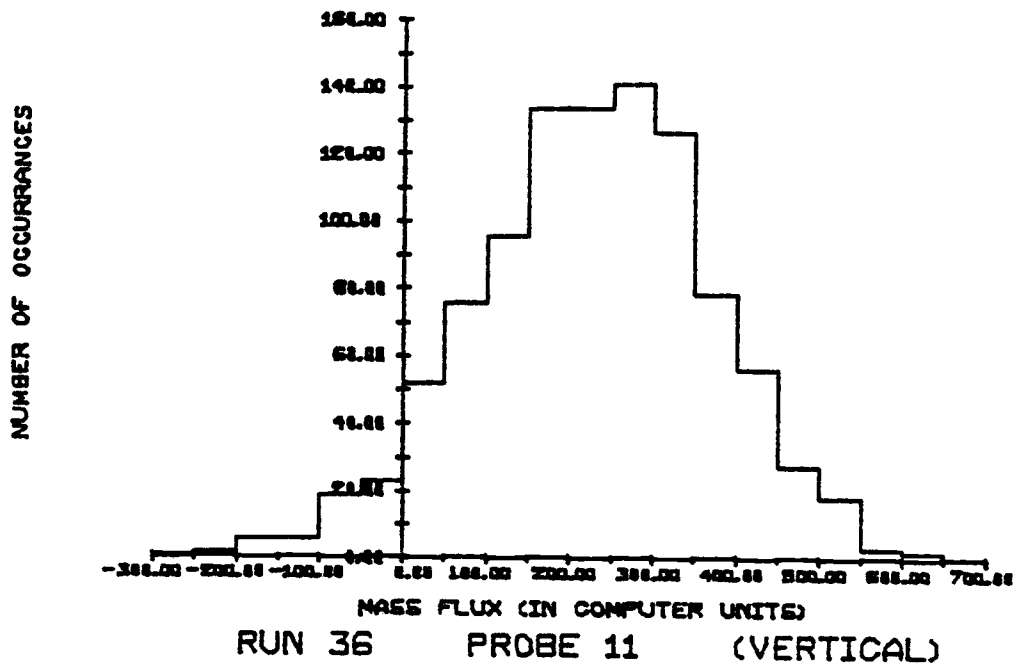


Figure B.2. (continued)

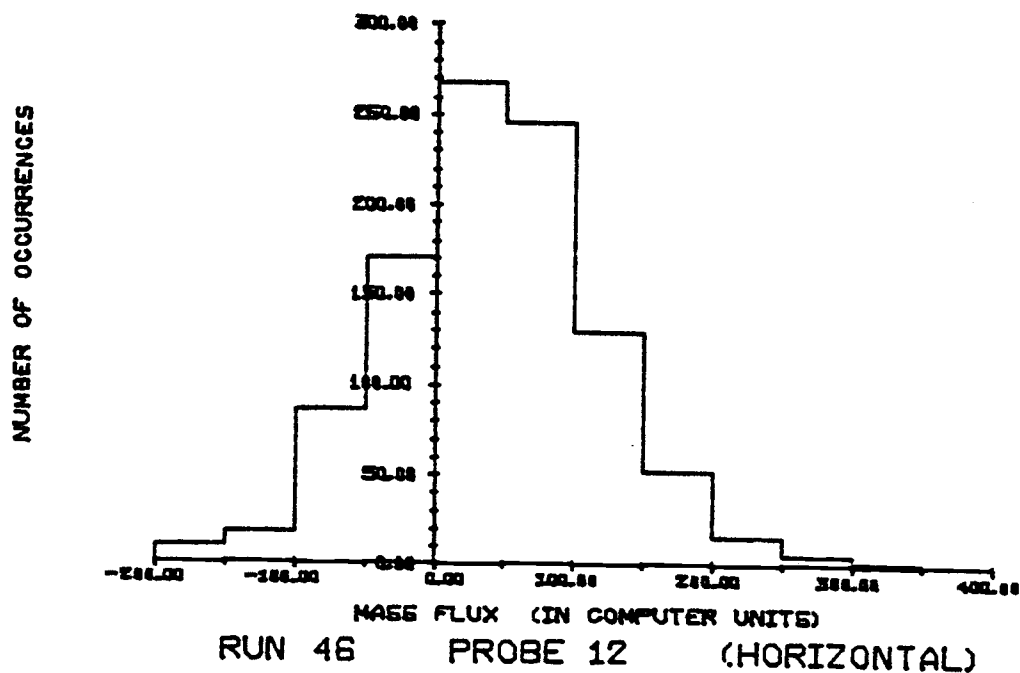
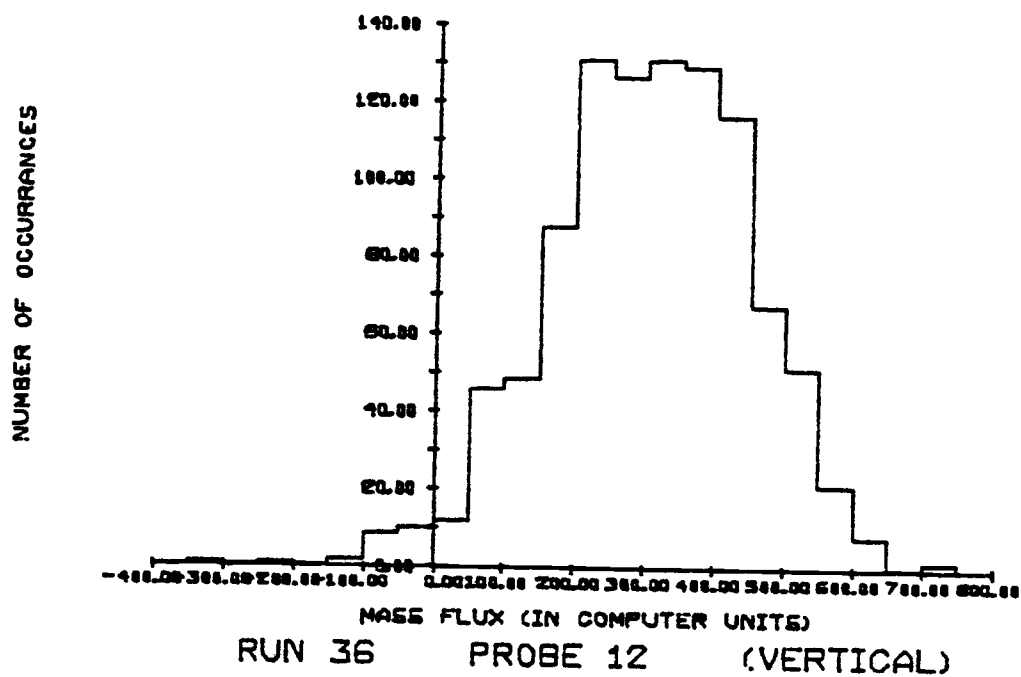


Figure B.2 (continued)

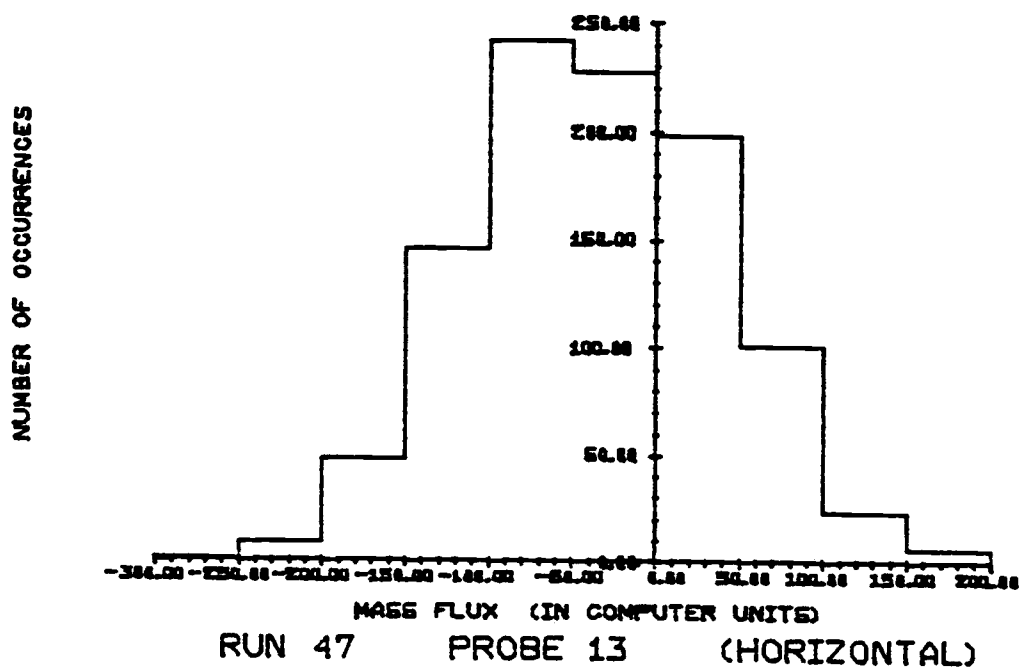
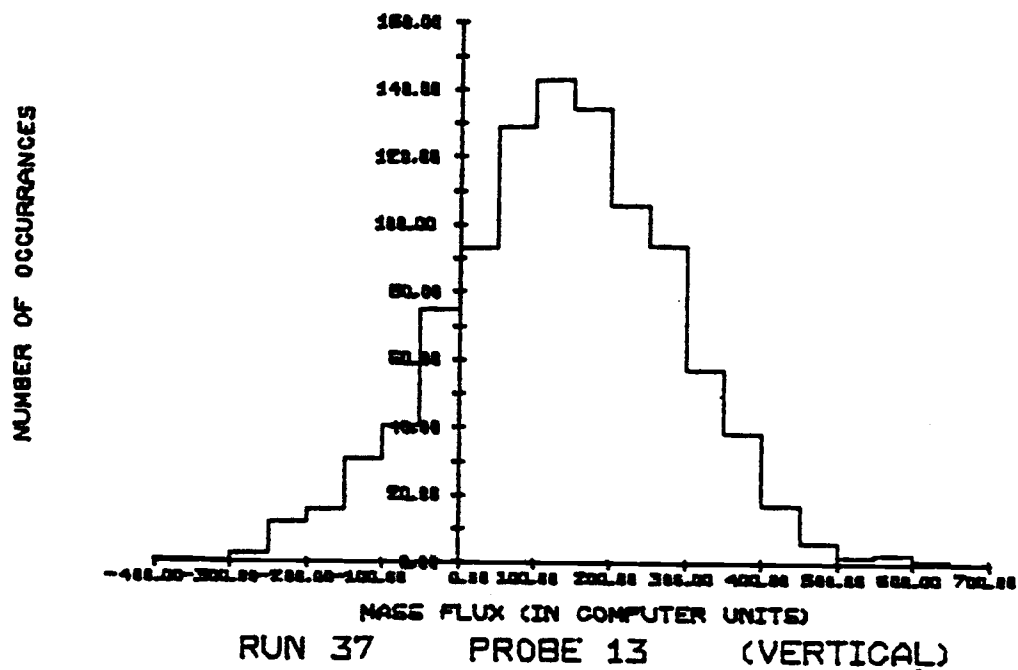


Figure B.2. (continued)



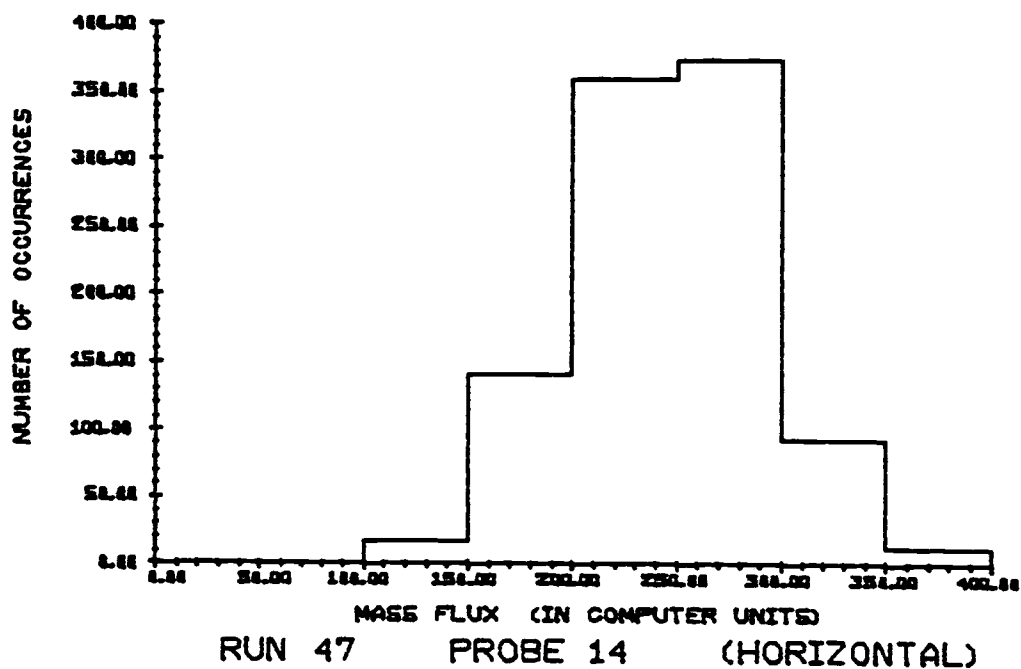
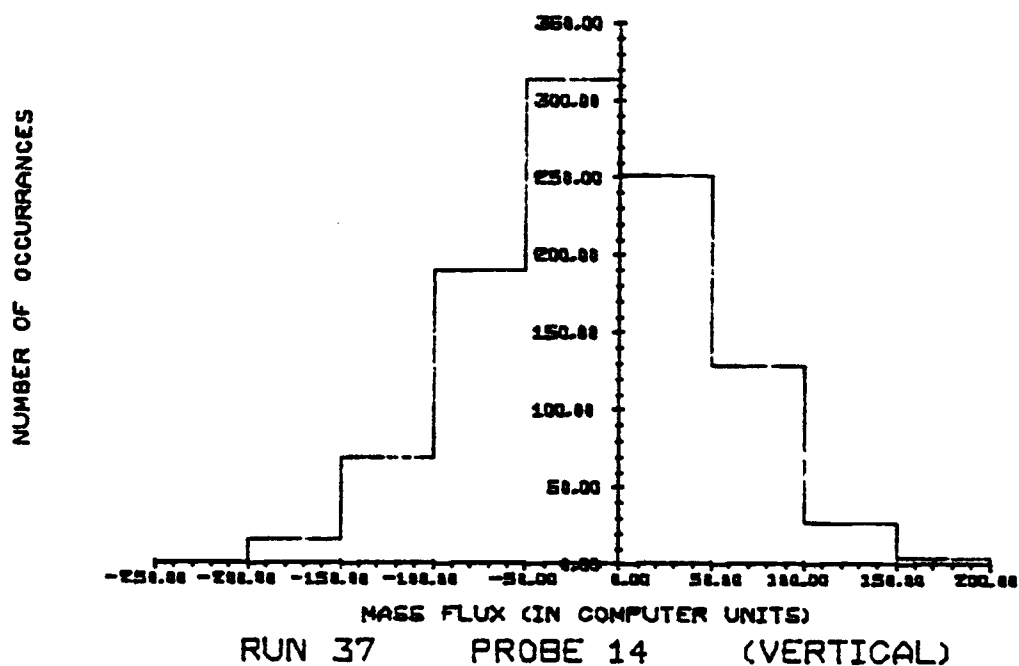


Figure B.2. (continued)

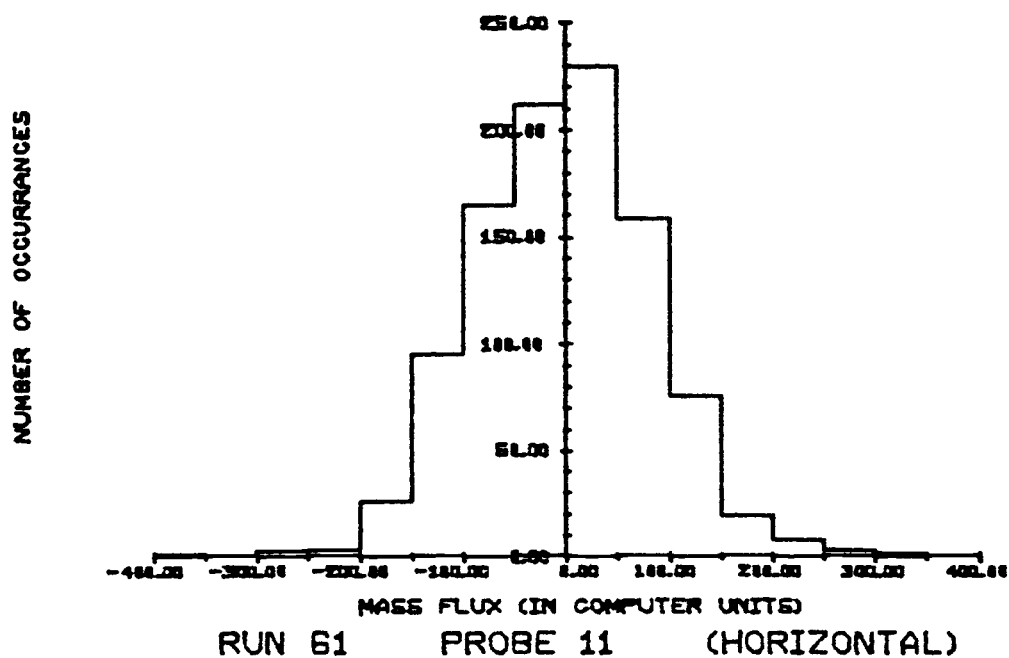
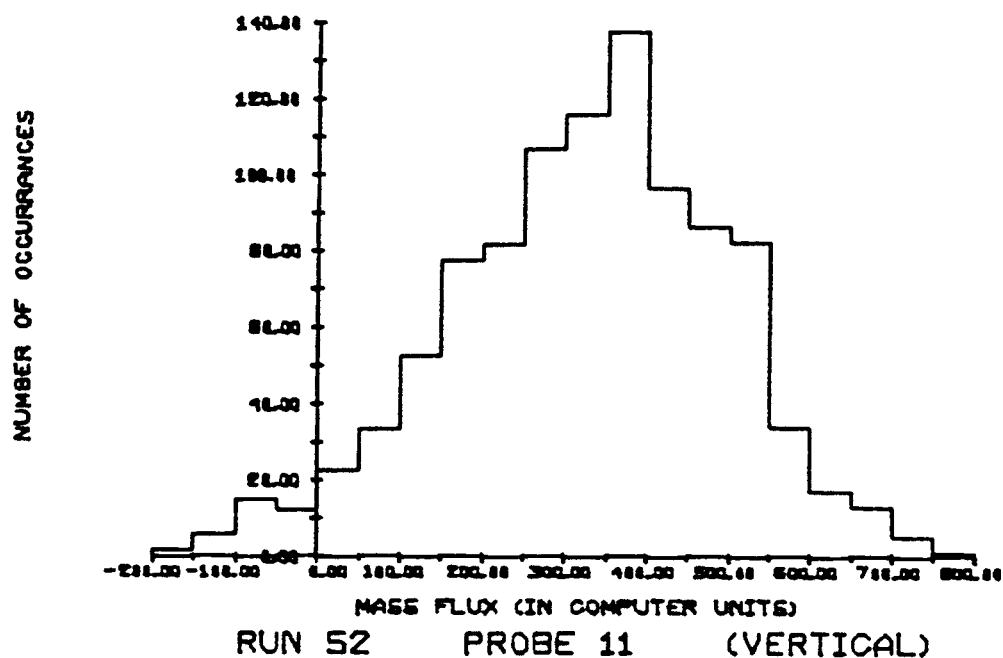


Figure B.3. Frequency histogram plots for the data of the third experiment.

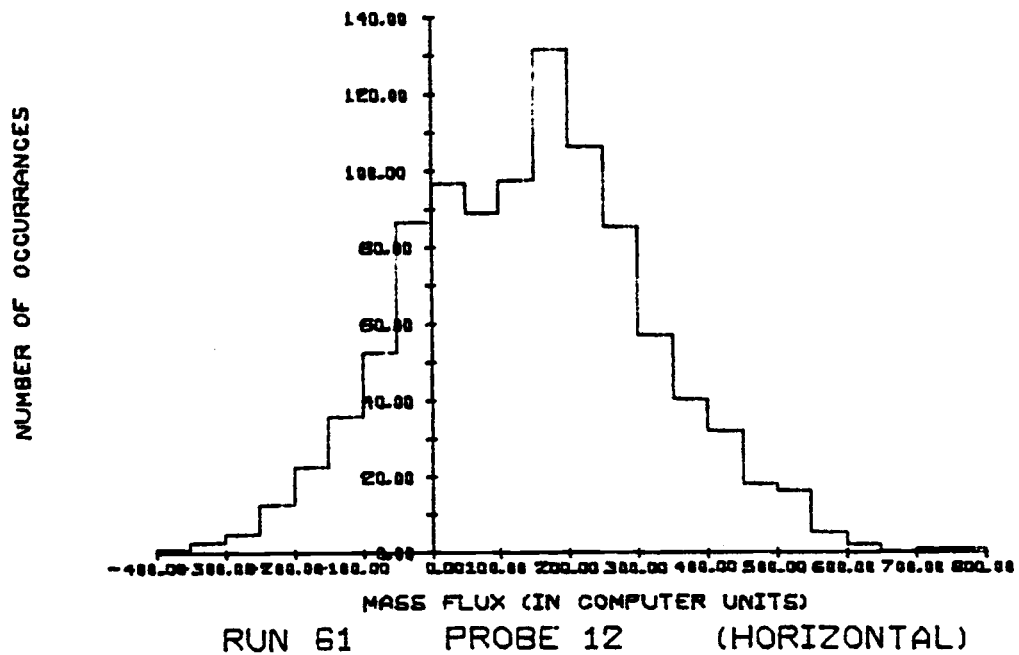
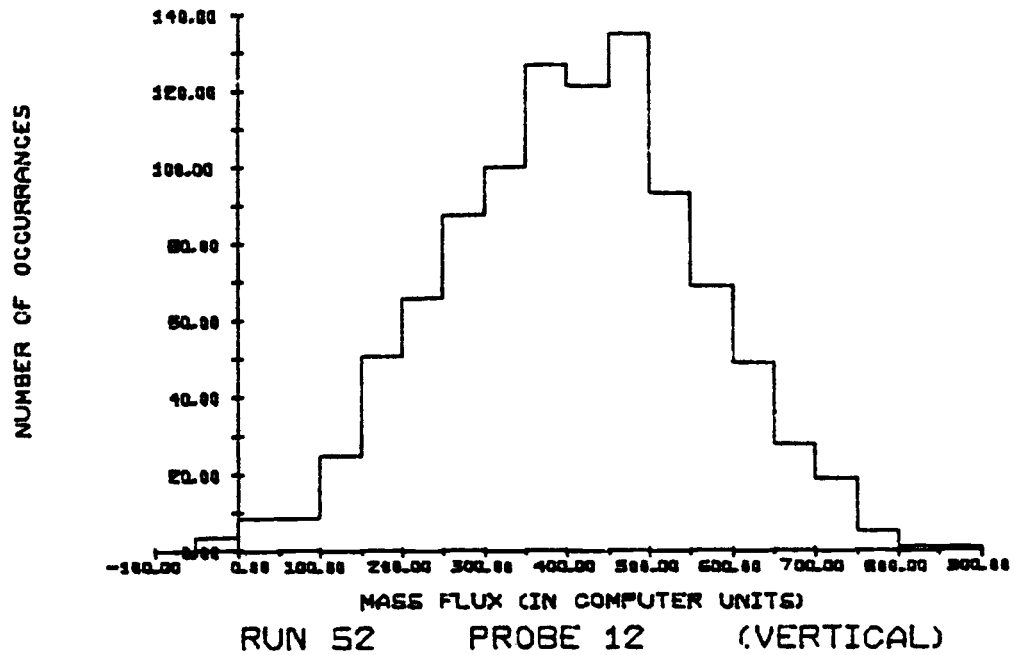


Figure B.3. (continued)

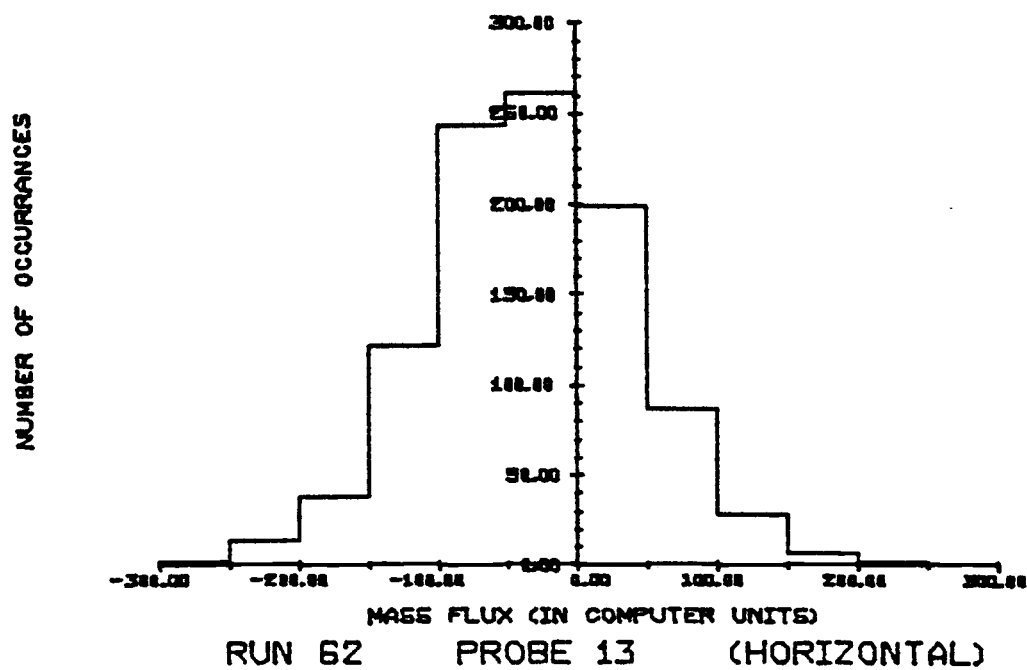
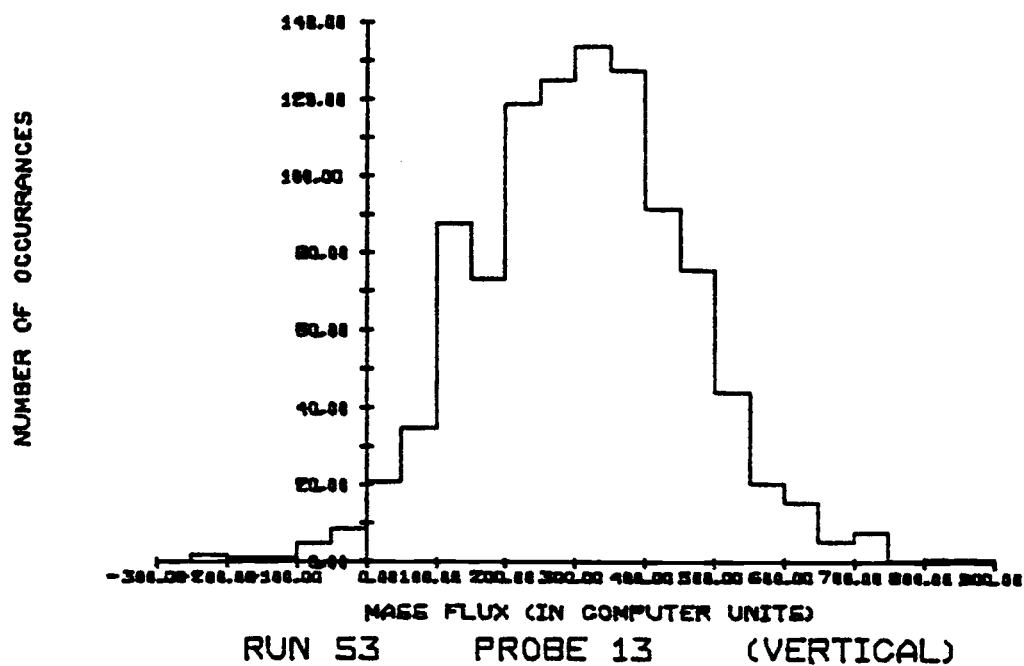


Figure B.3. (continued)

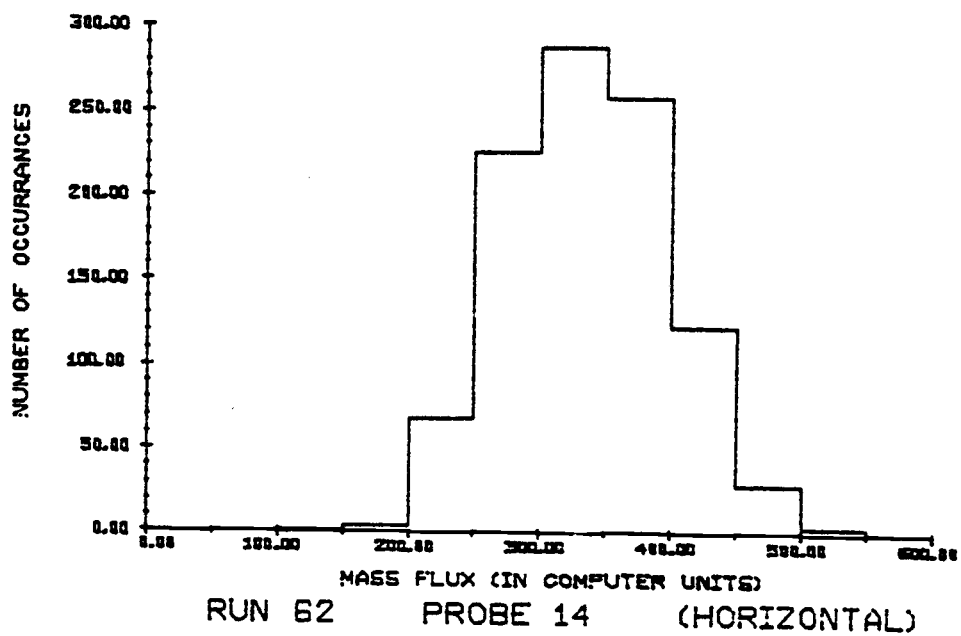
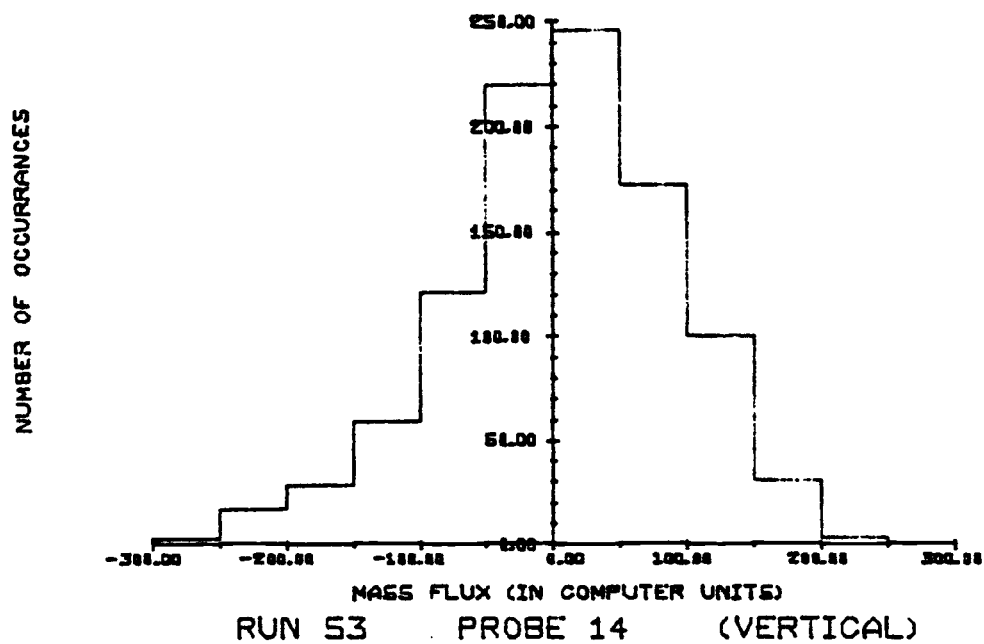


Figure B.3 (continued)

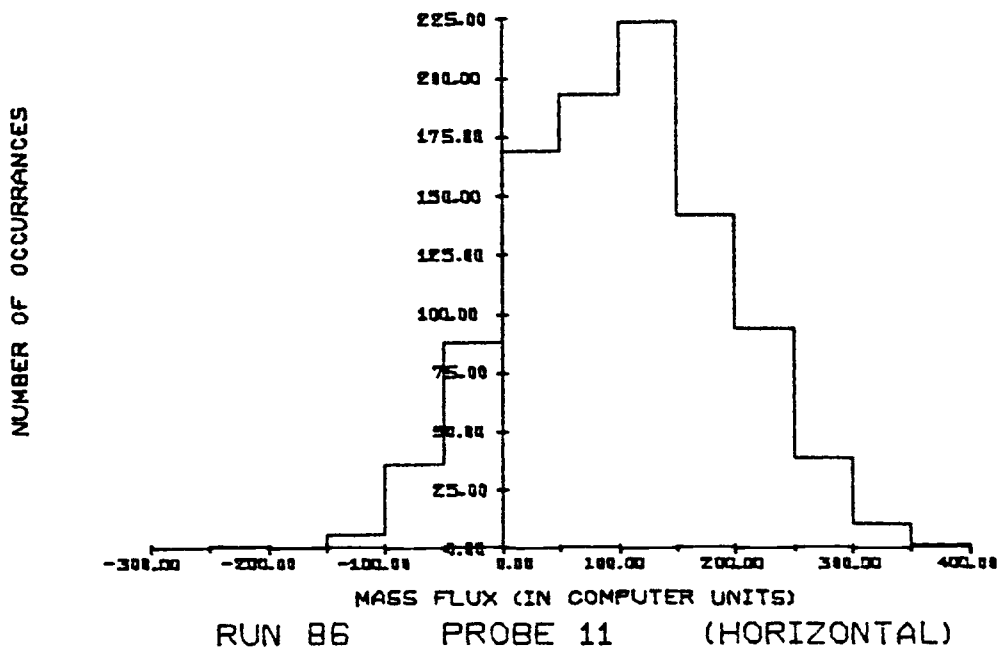
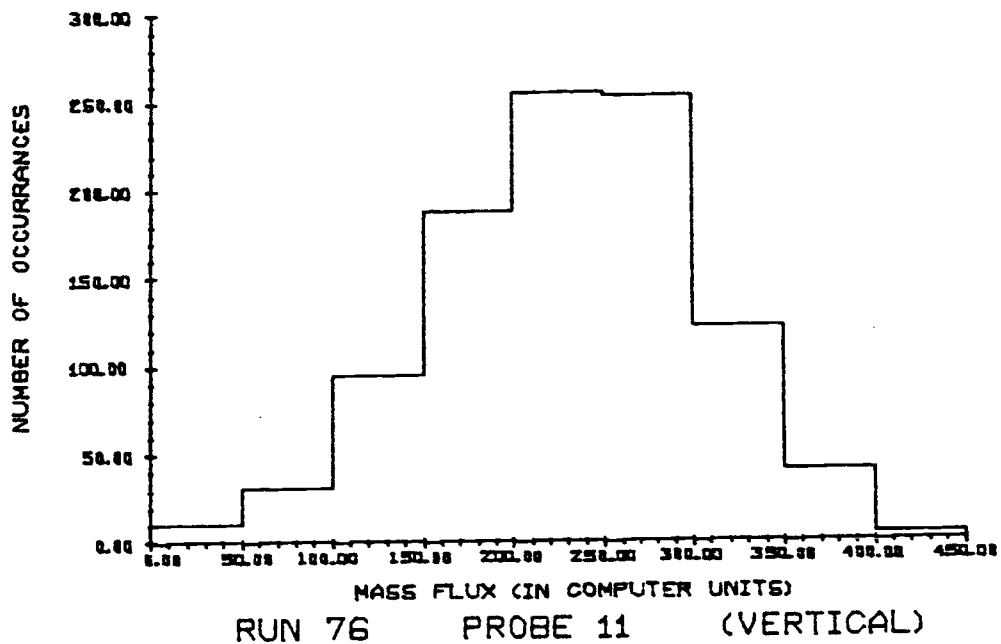


Figure B.4. Frequency histogram plots for the data of the fourth experiment.

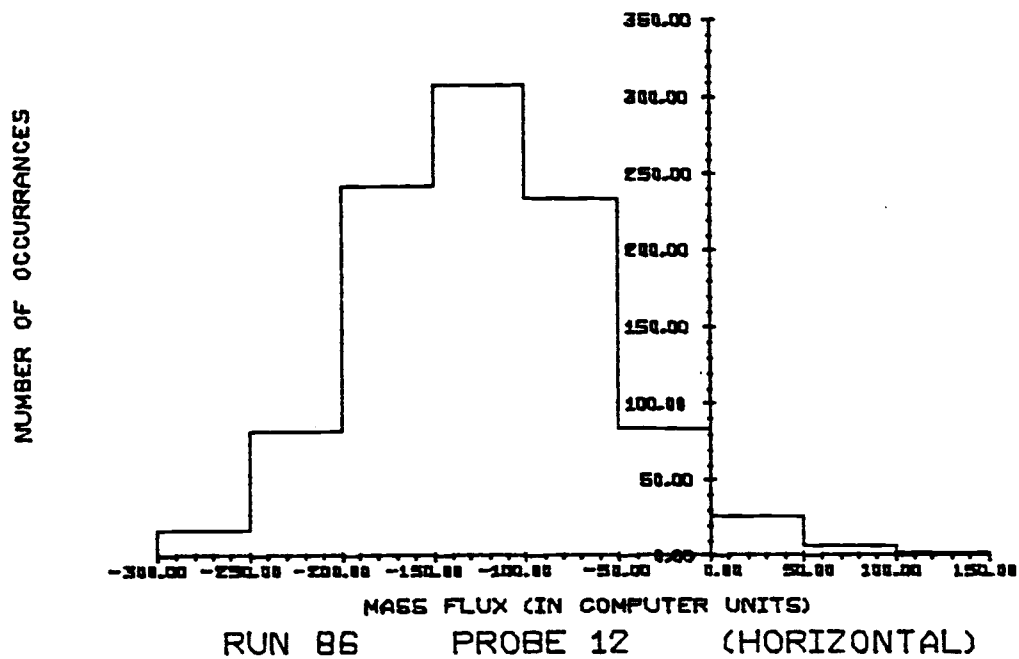
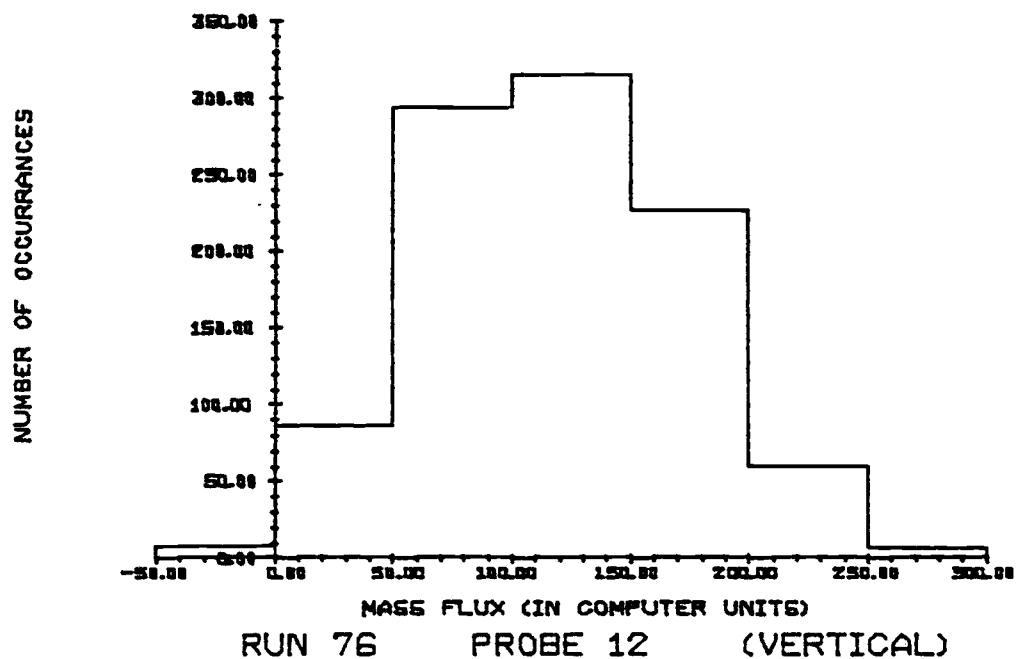


Figure B.4. (continued)

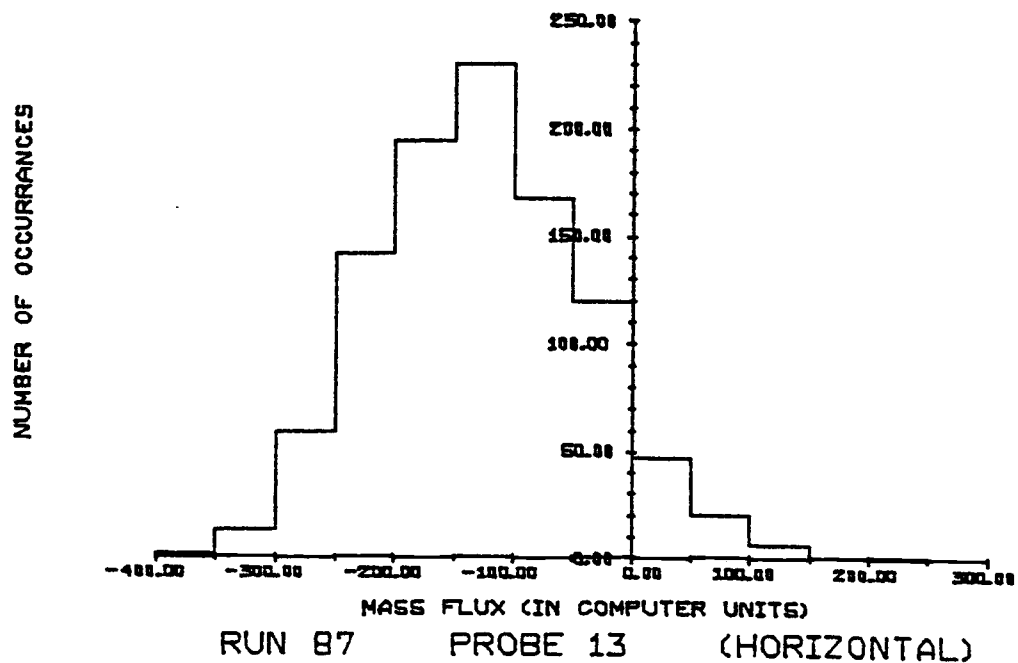
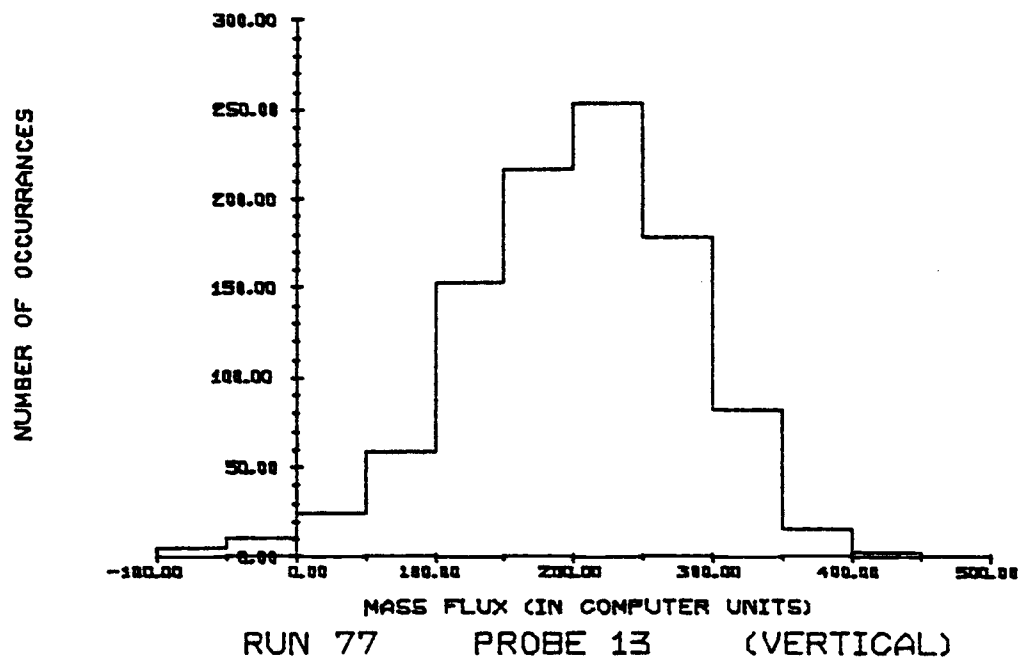


Figure B.4. (continued)



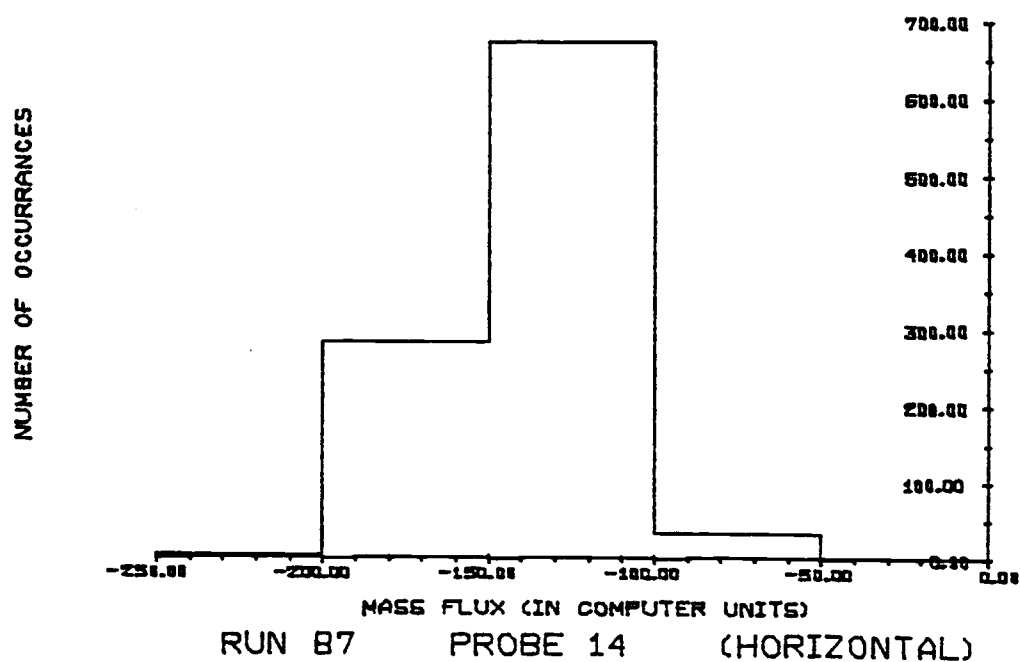
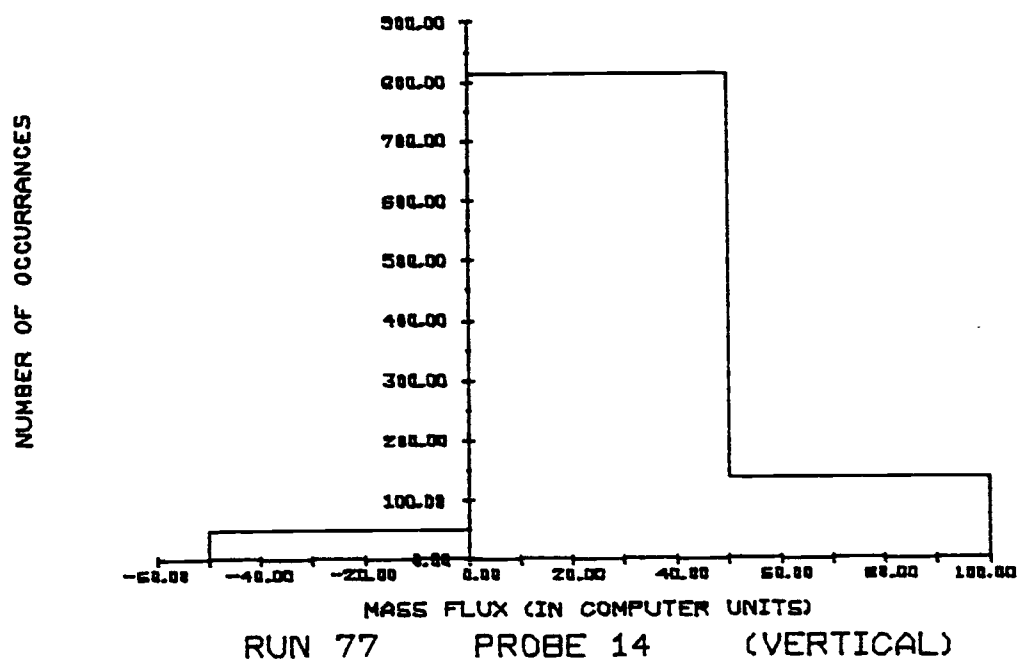


Figure B.4. (continued)

## APPENDIX C

Numerical Solution for System of Differential Equations in the  
Two-Region Model Bed

The system of ordinary differential equations in the two-region model bed was solved using the Runge Kutta Fifth and Sixth Order Method.\* Since the system of equations have split boundary conditions, an interval halving shooting method was used to determine the missing initial conditions on  $V_{1y}$  and  $V_{2y}$ . Details of the method algorithm can be found in reference (40). Figure C.1 shows the Fortran code encompassing the above algorithms.

---

\*Subroutine DVERK of the International Mathematical and Statistical Libraries was used. The subroutine is based on this method of finding approximations to the solutions of a system of first order O.D.E., with initial conditions. For details of the algorithm of the subroutine see reference (36).

```

PROGRAM MODEL7(INPUT,OUTPUT,TAPE5=INPUT,TAPE6=OUTPUT,TAPE2)
REAL V(6),G(7),C(24),W(6,Y),Y,TOL,YEND
INTEGER N,IND,NU,IER
COMMON/VAL1/ XL1,XL2,ROAV,R01,R02,GRAV
COMMON/VAL2/ N,NU,IND,IER,TOL
EXTERNAL FUNC1,FCN

C
C SYSTEM PARAMETERS FOR DVERK
C
      N=6
      NU=6
      TOL=0.00001
      Y=0.
      YEND=0.

C
C ENTER SYSTEM FIXED CONSTANTS
C
      R05=387.055
      EPS1=.56
      GRAV=32.174

C
C ENTER SYSTEM CHANGING PARAMETERS
C
      WRITE(6,100)
      READ(5,*)XL1,EPSAV,VLOW,VHIGH

C
C CALCULATE THE REST OF THE SYSTEM PARAMETERS
C
      XL2=(-XL1+SQR(XL1**2+9.))/2.
      ROAV=R05*(1.-EPSAV)
      R01=R05*(1.-EPS1)
      R02=(ROAV*(XL1+XL2)-R01*XL1)/XL2

C
C CALL THE SHOOTING ROUTINE HALF TO CALCULATE V(1) AT
C THE TOP OF THE BED.
C
      CALL HALF(VLOW,VHIGH,FUNC1,VAHS,.001,10,1,IER)
      IF(IND.LT.0.OR.IER.GT.0)GO TO 10
      IF(IEER.GT.1)GO TO 10

C
C CALCULATE THE INITIAL CONDITIONS OF THE 6 DIFF. EQ.
C
      V(1)=VAHS
      V(2)=-R01*XL1+V(1)/(R02+XL2)
      V(3)=2116.8
      V(4)=2116.0
      V(5)=GRAV*XL2*(ROAV-R02)/(R01*(V(1)+V(2)))
      V(6)=GRAV*XL1*(ROAV-R01)/(R02*(V(1)+V(2)))

C
C CALCULATE THE INITIAL CONDITIONS IN TERMS OF MASS FLUX
C
      G(1)=R01*V(1)
      G(2)=R02*V(2)
      G(3)=V(3)
      G(4)=V(4)
      G(5)=R01*V(5)
      G(6)=R02*V(6)
      G(7)=G(5)+G(6)

C
C WRITE THE INITIAL CONDITIONS IN TERMS OF MASS FLUX
C
      WRITE(6,110)Y,(G(1),I=1,7)
      WRITE(2,110)Y,(G(1),I=1,7)

C
C SOLVE THE SYSTEM OF ODE'S USING DVERK AT EACH YEND
C
      IND=1
      DO 5 J=1,71
      YEND=YEND+0.02
      CALL DVERK(N,FCN,Y,V,YEND,TOL,IND,C,NU,W,IER)
      IF(IND.LT.0.OR.IER.GT.0)GO TO 6

C
C OBTAIN MASS FLUXES AT YEND FROM VELOCITIES AT YEND
C
      G(1)=R01*V(1)
      G(2)=R02*V(2)
      G(3)=V(3)
      G(4)=V(4)
      G(5)=R01*V(5)
      G(6)=R02*V(6)
      G(7)=G(5)+G(6)

C
C WRITE THE MASS FLUXES AT EACH YEND ON TERMINAL & TAPE2
C
      WRITE(6,110)Y,(G(1),I=1,7)
      WRITE(2,110)Y,(G(1),I=1,7)
5     CONTINUE
      GO TO 10
6     CONTINUE
      WRITE(6,120)IND,IER
      CONTINUE
100    FORMAT(' ENTER XL1,EPSAV,VLOW,VHIGH :')
110    FORMAT(10.2,2X,'(F10.4,2X)')
120    FORMAT(' ERROR FROM DVERK; SOURCE: MAIN PROGRAM',//,
15X,' IND=',13,5X,' IER=',13)
      STOP
      END

```

Figure C.1. Fortran code for calculation procedure of the system of Eqs. (5-8) to (5-13).

```

SUBROUTINE FUNC(VIAT0,VIN1)
REAL V(6),C(24),W(6),Y,T,TOL,LEND
INTEGER N,IND,NV,IER
COMMON/VAL1/XL1,XL2,KOAV,KO1,KO2,GRAV
COMMON/VAL2/N,NV,IND,IER,TOL
EXTERNAL FCN
IND=1
Y=0.
YEND=1.42
V(1)=VIAT0
V(2)=-KO1*XL1+V(1)/(KO2*XL2)
V(3)=2116.0
V(4)=2116.8
V(5)=GRAV*XL2*(KOAV-KO2)/(KO1*(V(1)+V(2)))
V(6)=GRAV*XL1*(KOAV-KO1)/(KO2*(V(1)+V(2)))
CALL BULK(N,FCN,Y,V,YEND,TOL,IND,C,NV,W,IER)
IF(IND.LT.0.OR.IER.GT.0)GO TO 10
VIAT1=V(1)
RETURN
10 WRITE(6,100)IND,IER
100 FORMAT(' ERROR FROM BULK; SOURCE: FUNC',/,5X,
1' IND=',13,5X, IER=',13)
RETURN
END
SUBROUTINE FCN(N,Y,V,VPRIME)
COMMON /VAL1/XL1,XL2,KOAV,KO1,KO2,GRAV
REAL V(N),VPRIME(N),DRTST
INTEGER N
DRTST=ABS(KO2*XL2*(V(2)/(KO1+V(5))))
VPRIME(1)=-((KO2+V(6)+KO1+V(5))/(KO1*XL1)
VPRIME(2)=(KO2+V(6)+KO1+V(5))/(KO2*XL2)
VPRIME(3)=(2.*KO2+V(6)+V(1)+KO1+V(5)+V(1)+KO2+V(6)+V(2)
1/XL1+KO1*GRAV
VPRIME(4)=(2.*KO1+V(5)+V(2)+KO1+V(5)+V(1)+KO2+V(2)+V(6))
1/XL2+KO2*GRAV
IF(DRTST.LE.0.001)GO TO 11
VPRIME(5)=(KO2+V(6)+(V(5)+V(6))-V(3)+V(4))/(KO1*XL1+V(1))
VPRIME(6)=-((KO1+V(5)+(V(5)+V(6))+V(3)-V(4))/(KO2*XL2+V(2))
RETURN
11 CONTINUE
VPRIME(5)=V(5)
VPRIME(6)=-V(5)
RETURN
END
SUBROUTINE HALF(X1,X2,FUNC,XANS,EPS,NMAX,IURT,ICRR)

```

```

C THIS SUBROUTINE FINDS THE LOCAL ZERO CROSSING OF A
C FUNCTION BY INTERVAL HALVING.
C THE ARGUMENTS HAVE THE FOLLOWING DEFINITION.
C X1 - LOWER BOUND OF FUNCTION
C X2 - UPPER BOUND OF FUNCTION
C FUNC - NAME OF FUNCTION SUBROUTINE (EXTERNAL TO MAIN PROGRAM)
C FVAL(X,F) - THE FUNCTION VALUE F AT X
C XANS - FINAL VALUE RETURNED
C NMAX - MAXIMUM NUMBER OF ITERATIONS
C EPS - STOPPING CRITERION FOR CONVERGENCE AS ABSOLUTE FRACTION
C CHANGE IN X OR IN FUNC. LOG(1/EPS) IS APPROXIMATELY THE
C NUMBER OF SIGNIFICANT FIGURES.
C EPS SHOULD BE GREATER THAN (X2-X1)/(2**NMAX)
C IURT - SELECTS PRINT ITERATION (OUTPUT TO 6)
C 0 - NO PRINTING
C N - PRINT EVERY N(TH) ITERATION
C IERR - ERROR RETURNED ON COMPLETION OF CALL
C 1 - CALL SUCCESSFUL
C 2 - FUNCTION VALUES AT END POINTS ARE NOT OF
C OPPOSITE SIGN F(X1)+F(X2).GT.0.0
C 3 - DID NOT CONVERGE IN NMAX ITERATIONS
C NO IS OUTPUT DEVICE
C NO=6
C FMIN AND XMIN ARE THE POINTS WHERE CONVERGENCE
C CHECK SWITCHES FROM RELATIVE TO ABSOLUTE
C FMIN=1.0E-4
C XMIN=1.0E-4
C ICNT=0
C IFLG=IURT
C IF(IFLG.LE.0)IFLG=2*NMAX
C A=X1
C B=X2
C CALL FUNC(A,FA)
C CALL FUNC(B,FB)
C IF(IURT.GT.0) WRITE(NO,150) ICNT,A,FA,B,FB
C CHECK END POINTS FOR OPPOSITE SIGN
C IF(FA*FB.LE.0.0) GO TO 5
C IERR=2
C RETURN
5 DO 25 ICNT=1,NMAX
C CHECK FOR CONVERGENCE
C FN=FA
C IF((N.LT.FMIN) FN=1.0
C IF(ABS((FA+FN)/FN).GT.EPS) GO TO 10
C AN=A

```

```

      IF (ABS(XNIR) .GT. 1.0
      IF (ABS((A-B)/A) .GT. EPS) GO TO 10
      GO TO 30
C   CALCULATE MIDPOINT AND REPEAT
10  C=(A+B)/2.09
      CALL FUNC(C,FC)
      IF (FA*FC .GT. 0.0) GO TO 20
      FB=FC
      B=C
      GO TO 24
20  FA=FC
      A=C
24  IF (MOD(ICNT,IFLG) .EQ. 0) WRITE(ND,15) ICNT,A,FA,B,FB
25  CONTINUE
      XANS=(A+B)/2.0
      IF (IWK1 .GT. 0) WRITE(ND,15) NMAX
      IERR=3
      RETURN
30  XANS=(A+B)/2.0
      ICI=ICNT-1
      IF (IWK1 .GT. 0 .AND. MOD(ICI,IFLG) .NE. 0) WRITE(ND,15) ICI,A,FA,B,FB
      IERR=1
      RETURN
150 FORMAT(32H PRINTING FROM SUBROUTINE HALF ,/
      2 6H ITER,7X,20X1,10X,5H (X1),11X,20X2,10X,5H (X2),1X,14,4L14.4)
151 FORMAT(1X,14,4L14.4)
152 FORMAT(21H DID NOT CONVERGE IN ,14,12H ITERATIONS )
      END

```